Modeling the Dynamics of the Mixture Effects of Organic Micropollutants in Rivers

Dissertation

der Mathematisch-Naturwissenschaftlichen Fakultät

der Eberhard Karls Universität Tübingen

zur Erlangung des Grades eines

Doktors der Naturwissenschaften

(Dr. rer. nat.)

vorgelegt von

Ran Wei

aus Changsha/China

Tübingen

2024

Gedruckt mit Genehmigung der Mathematisch-Naturwissenschaftlichen Fakultät der Eberhard Karls Universität Tübingen.

Tag der mündlichen Qualifikation:	29.05.2024
Dekan:	Prof. Dr. Thilo Stehle
1. Berichterstatter/-in:	Prof. Dr. Christiane Zarfl
2. Berichterstatter/-in:	Prof. Dr. Beate I. Escher
3. Berichterstatter/-in:	Prof. Dr. Holger Pagel

Abstract

River water quality is under heavy impact from anthropogenic activities. Organic anthropogenic pollutants that are present at low concentrations in river water and range from nanogram per liter to microgram per liter are categorized as organic micropollutants. Traditional wastewater treatment plants (WWTPs) have limited capabilities to efficiently remove micropollutants before releasing treated water into the receiving rivers. WWTPs are one of the main point sources of micropollutants in rivers. Hence, the micropollutants from WWTPs directly impact the receiving waterbodies, particularly in small rivers where the surrounding areas are densely populated, and the WWTPs' effluents make up a considerable amount of the river discharge during baseflow conditions. The threat to river water quality from the presence of micropollutants in rivers is elevated during heavy rain events. Untreated wastewater enters rivers at larger quantities than during the baseflow conditions. Storms also provide micropollutants with various sources and dispersive entry routes into the receiving water. The level of impact from micropollutants is dictated by their fate in rivers. Therefore when we evaluate, monitor, and improve river water quality, it becomes crucial to understand the source(s), and the in-stream reactive transport processes of micropollutants, which characterize their fate in rivers.

Micropollutants present in river water are composed of a wide range of substances, collectively referred to as micropollutant mixtures. It is impossible to identify every individual substance in the mixture. Previous studies used 1) chemical analysis to investigate the individually detected micropollutants in the mixture with regards to their concentrations; 2) *in vitro* bioassays to quantify the overall effects of the mixture with regards to their endpoints; 3) numerical models to study the in-stream processes of single substances.

The goal of this thesis is to provide a quantitative understanding of the in-stream processes of the micropollutant mixture effects, which is still lacking in previous studies. To fill this knowledge blank, I hypothesized that the in-stream processes of the mixture effects are governed by the advection-dispersion-reaction equation (ADR). I tested the hypothesis by investigating the following three perspectives:

1) the in-stream processes of the mixture effects, for which I developed a convolution-based one-dimensional reactive transport model that is computationally cheap and is suitable to couple with Metropolis–Hastings Markov chain Monte Carlo algorithm for parameter estimates and computing ensemble model results. I parameterized the model to quantify the in-stream processes of individual micropollutants and their mixture in the Steinlach river near Tübingen, Southern Germany. The results show that our model parameterization can characterize the in-stream processes of the individual micropollutants and their mixture well. The low computational cost of the convolution enables modeling the fate of large numbers of substances, as well as many iterations of model runs during the Monte Carlo process.

2) the transferability of the ADR under different flow conditions for the mixture effects, for which I further developed a partial differential equation (PDE)-based one-dimensional transient reactive transport model and applied the model to a storm event, during which the mixture effects were sampled from the Ammer river, Tübingen, Southern Germany and quantified in *in vitro* bioassays. I introduced the stochastic elements into the model by using Gaussian Process Regression (GPR) to construct the model inputs. The conditional realizations from GPR enabled the model to efficiently generate ensemble results with deterministically calibrated parameter values while explicitly expressing the known physical

processes. I showed GPR is a robust method to characterize the temporal in-stream dynamics of the mixture effects.

3) the potential to combine numerical approaches with machine learning methods to solve the ADR and estimate parameter values for the mixture effects, for which I applied the deep learning-based Bayesian optimization method, simulation-based inference (SBI), to obtain the parameter posterior distributions of a PDE-based one-dimensional reactive transport model. I also applied the physics-informed neural network (PINN) to obtain the solution of the same model. The two approaches were applied to model the in-stream processes of mixture effects sampled in the Ammer river during the baseflow conditions. I compared the results of modeled mixture using SBI coupled with standard PDE model to that obtained with PINN. I showed the potential of deep learning methods aiding the process-based reactive transport modeling, demonstrating the advantages and disadvantages of both approaches, concluding that the preference of one over the other is a heavily objective-oriented choice.

To my knowledge, this is the first work that uses process-based models to quantitatively characterize the in-stream processes of the organic micropollutant mixture effects. My key results show the applicability of the mass conservation law to mixture effects quantified in *in vitro* bioassays, approving the validity of using mixture effects as a novel state variable for the future water quality modeling, as well as highlighting the possibility and advantages to merge traditional process-based models with deep learning methods for the future study on mixture effects.

Zusammenfassung

Die Qualität von Flusswasser wird stark von anthropogenen Aktivitäten beeinflusst. Organische anthropogene Schadstoffe, die in Flüssen mit geringen Konzentrationen im Bereich von Nanogramm pro Liter bis Mikrogramm pro Liter vorkommen, werden als Mikroschadstoffe bezeichnet. Die Möglichkeiten von traditionellen Kläranlagen (KKAs), Mikroschadstoffe effizient zu entfernen, bevor das behandelte Wasser in Flüsse eingeleitet wird, sind begrenzt. KKAs sind eine der Hauptquellen für Mikroschadstoffe in Flüssen. Unter Basisabflussbedingungen nimmt der Einfluss von Mikroschadstoffen aus KKAs auf kleine Gewässer zu. Dies gilt vor allem für dicht besiedelte Gebiete, bei denen Kläranlagenabflüsse einen erheblichen Anteil des Flusswassers ausmachen. Die Gefährdung der Flusswasserqualität durch das Vorhandensein von Mikroschadstoffen nimmt während starker Regenereignisse zu. Unbehandeltes Abwasser gelangt dann in größeren Mengen in die Flüsse als unter Basisabflussbedingungen. Stürme bieten Mikroschadstoffen außerdem verschiedene Quellen und Verbreitungspfade in die empfangenden Gewässer. Der Schweregrad des Einflusses der Mikroschadstoffe ist von ihrem Verhalten in den Flüssen abhängig. Daher ist es bei der Bestimmung, Überwachung und Verbesserung der Flusswasserqualität entscheidend, die Quelle(n) und die flussinternen reaktiven Transportprozesse von Mikroschadstoffen zu verstehen, welche über ihr Schicksal in den Flüssen entscheiden.

Mikroschadstoffe im Flusswasser bestehen aus einer breiten Palette von Substanzen, die als Mikroschadstoffmischung bezeichnet wird. Es ist unmöglich, jede einzelne Substanz in der Mischung zu identifizieren. Frühere Studien verwendeten 1) chemische Analysen, um die individuell nachgewiesenen Mikroschadstoffe in der Mischung hinsichtlich ihrer Konzentrationen zu untersuchen; 2) *in vitro* Bioassays, um die Gesamtwirkungen der Mischung hinsichtlich ihrer Endpunkte zu quantifizieren; 3) numerische Modelle, um die flussinternen Prozesse einzelner Substanzen zu untersuchen.

Diese Dissertation hat zum Ziel, ein quantitatives Verständnis der flussinternen Prozesse der Mikroschadstoffmischungseffekte zu liefern, was in bisherigen Studien fehlt. Um diese Wissenslücke zu schließen, bin ich davon ausgegangen, dass die flussinternen Prozesse der Mischungseffekte von der Advektions-Diffusions-Reaktions-Gleichung (ADR) bestimmt sind. Ich habe diese Hypothese mit den drei Ansätzen untersucht:

1) für die flussinternen Prozesse der Mischungseffekte habe ich ein eindimensionales reaktives Transportmodell auf Basis der mathematischen Faltung entwickelt, das wenig Rechenressourcen benötigt und sich gut mit dem Metropolis-Hastings Markov-Ketten-Monte-Carlo Algorithmus koppeln lässt. Dieser erlaubt Parameterabschätzungen und die Berechnung von Ensemblemodellergebnissen. Ich habe die Parameter des Modells angepasst, um die flussinternen Prozesse einzelner Mikroschadstoffe und ihrer Mischung im Fluss Steinlach bei Tübingen in Süddeutschland zu quantifizieren. Die Ergebnisse zeigen, dass die Modellparametrisierung die flussinternen Prozesse der einzelnen Mikroschadstoffe und ihrer Mischung gut abbilden kann. Aufgrund des geringen Rechenaufwands der Faltung kann bei der Modellierung eine große Anzahl von Substanzen berücksichtigt werden, sowie eine hohe Anzahl an Modelliterationen im Monte-Carlo-Prozesses erreicht werden.

2) die Anwendbarkeit der ADR auf Mischungseffekte unter verschiedenen Abflussbedingungen, wofür ich ein eindimensionales, instationäres reaktives Transportmodell auf der Grundlage partieller Differentialgleichungen (PDE) entwickelt habe. Mit diesem Mod-

ell habe ich ein Unwetterereignis im Fluss Ammer in Tübingen (Süddeutschland) simuliert, um die Auswirkungen von Schadstoffmischungen auf *in vitro*-Bioassays zu bestimmen. Das Modell berücksichtigt dabei stochastische Modelleingabewerte über Gauß-Prozess Regression (GPR). Die konditionierten Realisationen aus der GPR ermöglichen es dem Modell, effizient Ensembles mit deterministisch kalibrierten Parameterwerten zu erzeugen und gleichzeitig die bekannten physikalischen Prozesse explizit zu berücksichtigen. Ich habe gezeigt, dass GPR eine robuste Methode ist, um die zeitliche Dynamik der flussinternen Mischungseffekte zu charakterisieren.

3) die Möglichkeit, numerische Ansätze mit Methoden maschinellen Lernens zu kombinieren, um die ADR zu lösen und Parameterwerte für Mischungseffekte abzuschätzen. Dafür habe ich die simulationsbasierte Inferenz (SBI), eine bayesianische Optimierungsmethode basierend auf *Deep Learning*, angewendet, um die *A-posteriori*-Wahrscheinlichkeitsverteilungen der Parameter eines PDE-basierten eindimensionalen reaktiven Transportmodells zu erhalten. Ich habe dasselbe Modell außerdem über ein physikalisch basiertes neuronales Netzwerk (PINN) lösen lassen. Ich habe beide Methoden auf Daten zu Mischungseffekten im Fluss Ammer angewendet, die unter Basisabflussbedingungen gewonnen wurden. Ich habe die modellierten Mischungsergebnisse aus dem SBI-Standard-PDE-Modell mit denen aus dem PINN-Ansatz verglichen. Ich habe das Potenzial von *Deep Learning* methoden zur Unterstützung der prozessbasierten reaktiven Transportmodellierung gezeigt und die Vor- und Nachteile beider Ansätze herausgearbeitet. Ich komme dabei zu dem Schluss, dass die Präferenz für einen der beiden Ansätze stark von der jeweiligen Fragestellung abhängt.

Nach meinem Wissen ist dies die erste Arbeit, die prozessbasierte Modelle verwendet, um die flussinternen Prozesse der Mischungseffekte organischer Mikroschadstoffe quantitativ zu charakterisieren. Meine wichtigsten Ergebnisse zeigen die Anwendbarkeit des Massenerhaltungsgesetzes auf Mischungseffekte, die mit *in vitro* Bioassays quantifiziert werden. Die Ergebnisse bestätigen die Gültigkeit der Verwendung von Mischungseffekten als neue Zustandsvariable für die zukünftige Wasserqualitätsmodellierung. Sie betonen auch die Möglichkeit und die Vorteile der Verknüpfung traditioneller prozessbasierter Modelle mit *Deep Learning* methoden für zukünftige Untersuchungen zu Mischungseffekten.

Acknowledgments

It's okay to struggle, but it's not okay to give up.

Gabriele Ivy Grunewald
1986 – 2019

Looking at the finally compiled PDF file, I truly think this is a long and bumpy journey. There are a thousand difficulties from scientific perspectives, and there are another thousand from somewhere else. But only in the darkness, can men see the stars. Through all the difficulties and time, I definitely learned a lot, and I think I am a slightly better scientist now than when I started. I am grateful for the years in the beautiful Tübingen. *Vielen Dank, Tübingen!*

However, I stood on the shoulders of others. Without their support, patience, and encouragement, I would not be here today.

I thank my two supervisors, Christiane Zarfl and Beate Escher, for their detailed yet different genres of feedback giving throughout the years. One is always gentle and the other brutally critical. However, missing one of the two, the paper would not be published. I also thank Holger Pagel for being my external examiner, and I hope our scientific paths will cross in the future.

I thank my colleagues in the environmental systems analysis group including Ana, Jonas, Lana, Matthias, and Rebecca. I enjoyed our weekly group meetings and our diverse scientific backgrounds.

I thank Olaf Cirpka for acquiring the grant for forming the Research Training Group 'Integrated Hydrosystem Modelling' (RTG), Monika Jekelius for managing all the detailed yet important paperworks in RTG.

Max Müller, thanks for providing me the invaluable laboratory data used in my model, and for your support at some of the most difficult times at the early stage of my Ph.D.. I still remember you told me to 'chin up'!

Yan Liu, thanks for your help when I started my Ph.D., even during some of your busiest days.

Reynold, thank you for being a big brother at the beginning of my Ph.D.. I felt your support even when you were not smiling. But the strongest support comes when you are not showing.

Gaëlle and Victor, thanks for being cool office mates and your emotional support during the lockdown!

Al, thanks for proof-reading my thesis and hanging out!

Cora, thanks for your tips about the transient model!

Marie-Madeleine, thanks for translating my abstract!

Clarissa, big thanks for your support, encouragement, help in the field, discussing the results, writing, talking, and everything, throughout the years!

Amir and Binlong, you are the best office mates I could ever ask for. Thanks for all the intensive scientific and non-scientific discussions, and intensive laughs! I wish we knew each other a couple of years earlier. But more importantly, you were there when I felt the lowest.

I want to thank friends on the sixth floor: Anh, Luise, Michał, Natalia, Steffi and Felix plus small Tim and Jakob, Timm, and Simon! We had some great time together and you carried me through the tough ones.

I am extremely grateful and proud to be a member of the third generation of the RTG. It was the smartest group of people I have ever met, yet no one was arrogant in the slightest way. Great scientific minds without those attitude. The most helpful colleagues anyone could ever ask for. Because of you, I have an extremely high standard to match with. You also made me feel that I was not alone, especially during the pandemic. So thank you: Anna, Elena, Hemanti, Ishani, Jonas, Julia, Luciana, Michelle, and Philipp, for teaching me the basics: being scientific, modest, and kind!

I also want to thank my friends outside of the institute, Dario, Davide, Julien, Kübra, LJ, Lorenzo, Martina, and Oksana. For some of you, we met at the very beginning in Tübingen, some back in Boulder, and I cherish our friendship spanning over the years. For all of you, you gave me shelters when science became too harsh.

At last I deeply thank and hug my mom and dad, for supporting me, the only kid, in studying and living across the land and ocean since 2014. 爸，妈，多谢你们多年的支持。太久不见，我很抱歉!

魏然
15.01.2024, Tübingen

Acronyms

ADR advection, dispersion and reaction equation.

ANN artificial neural network.

AS auto-sampler.

BME Bayesian model evidence.

CA concentration addition.

CEST central European summer time.

CI confidence interval.

DOC dissolved organic carbon.

EC effect concentration.

ECd electrical conductivity.

EU effect unit.

FDM finite difference method.

GPR Gaussian process regression.

IC inhibition concentration.

KDE kernel density estimation.

MH-MCMC Metropolis-Hastings Markov Chain Monte Carlo.

MS measuring station.

MSE mean squared error.

NPE neural posterior estimation.

NRMSE normalized root mean square error.

ODE ordinary differential equation.

PAH polycyclic aromatic hydrocarbon.

PCP personal care product.

PDE partial differential equation.

PI posterior interval.

PINN physics-informed neural network.

REF relative enrichment factor.

SBI simulation-based inference.

TU toxic unit.

WWTPs wastewater treatment plants.

Contents

List of Figures

List of Tables

List of Algorithms

Statement of Contributions

This thesis is based on three chapters (one published and two unpublished). I was mainly responsible for model parameterization, implementation in MATLAB and Python, results analysis and visualization, and paper writing. I am the first author on each chapter. Chapter 2 is based on and reprinted with permission from the publication:

Wei, R., Escher, B. I., Glaser, C., König, M., Schlichting, R., Schmitt, M., Störiko, A., Viswanathan, M., and Zarfl, C.. Modeling the Dynamics of Mixture Toxicity and Effects of Organic Micropollutants in a Small River under Unsteady Flow Conditions. *Environ. Sci. Technol.*, 56(20):14397–14408, 2022. ISSN 0013-936X. doi: 10.1021/acs.est.2c02824.

In Chapter 2, I contributed 70% scientific ideas, 10% data generation, 90% analysis and interpretation, and 80% paper writing. The authors contributed as follow:

- Scientific ideas: Ran Wei, Christiane Zarfl, and Beate I. Escher
- Data generation: Ran Wei, Clarissa Glaser, Maria König, Rita Schlichting, and Markus Schmitt
- Analysis & interpretation: Ran Wei, Anna Störiko, and Michelle Viswanathan
- Paper writing: Ran Wei, Christiane Zarfl, Beate I. Escher, Maria König, Rita Schlichting, Markus Schmitt, Anna Störiko, and Michelle Viswanathan

Chapter 1

Introduction

1.1 Background

Organic micropollutants comprise a wide spectrum of substances, such as pharmaceuticals (Jaeger et al., 2018), personal care products (PCPs) (Jaeger et al., 2018; Kim and Zoh, 2016), polycyclic aromatic hydrocarbon (PAHs) (Wicke et al., 2021) and pesticides (Moschet et al., 2015). They appear in the environment at low concentration levels ranging from ng L^{-1} to μg L^{-1}. Due to the wide categories of substances that are used for various anthropogenic purposes, they enter rivers via diverse sources and routes, leading to their ubiquitous presence in river water (Desiante et al., 2021). Conventional wastewater treatment plants (WWTPs) have limited ability to efficiently remove micropollutants from the discharged wastewater (Loos et al., 2013), making wastewater treatment plants effluent one of the major point sources of micropolluants in rivers (Jaeger et al., 2018; Loos et al., 2013; Reemtsma et al., 2016). During rain events, a broader range of routes are facilitated by storm water for micropollutants to enter river channels. Typical entry routes include runoff from urban surfaces (Dittmer et al., 2020) that contains substances from building materials (Müller et al., 2019; Gasperi et al., 2014), vehicle tire materials (Klöckner et al., 2020), the washout of pesticides from agricultural fields (Neumann et al., 2002) and animal farms (Kim and Zoh, 2016), and combined sewage overflow (Launay et al., 2016).

The ubiquitous presence of micropollutants in surface water poses a threat to water quality, aquatic life and human health, causing acute and chronic negative effects at both organ and population levels (Varga et al., 2019). Previous studies reported various potential adverse effects caused by micropollutants: reproduction failure in fish caused by steroid hormones (Nash et al., 2004; Ojoghoro et al., 2021); Bacteria in wastewater resistant to antibiotics (Costanzo et al., 2005; Rodríguez-Molina et al., 2019). Potential long-term toxicity caused by pharmaceuticals in the surface water is also reported (Luo et al., 2014; Fent et al., 2006).

Studying the in-stream processes and the fate of the micropollutants provides quantitative information regarding the level of their presence in rivers over space and time. Various studies (Kunkel and Radke, 2012; Barber et al., 2013; Hanamoto et al., 2013; Schwientek et al., 2013; Li et al., 2016; Jaeger et al., 2018) investigated the presence and quantities (e.g., concentration, mass flux) of a large sets of micropollutants in rivers, where the WWTPs are the major releasing point source. These studies rely on data from field sampling and focus on individual micropollutant's concentration dynamics. The Lagrangian sampling

scheme (Antweiler et al., 2014; Schwientek et al., 2016) has proved to be an effective tool to capture the in-stream solute transport dynamics, providing time-series signals traveling along the river course by aiming to track the same water parcels. The challenge arises from the fact that there are unknown numbers of micropollutants in each sample of the Lagrangian sampling scheme, and it is not possible to identify all individual micropollutants, let alone quantifying their concentrations. The mixture effects of the micropollutants in the collected samples, quantified by *in vitro* biossays (Escher et al., 2021), on the other hand represents the overall impact of the micropollutants in the sample with respect to certain endpoints. The mixture effects can be categorized into specific effects and cytoxicity. The former is expressed as effect unit (EU) quantified from any non-lethal endpoint (Escher et al., 2021). The latter is expressed as toxic unit (TU) that is quantified from apical lethal point. EU and TU can also be used to characterize the effects of individual compounds. In mixtures where a large number of compounds are present at very low concentrations, the synergistic (Cedergreen, 2014) or antagonistic (Marx et al., 2015) mixture effects are usually unnoticed (Escher et al., 2020). Under such circumstances, the concentration addition (CA) concept (Cedergreen, 2014; Escher et al., 2020) can be applied to calculate the effects of the unknown micropollutants in the mixture. Various studies (Neale et al., 2017; König et al., 2017; Müller et al., 2018, 2020; Zhi et al., 2020; Lee et al., 2022) investigated the mixture effects of the WWTP-induced micropollutants in river water. The measured total mixture effects are orders of magnitude higher than the sum effects from the individually detected and activated micropollutants, indicating the majority of the mixture effects are coming from unknown micropollutants in the samples. Therefore, the combination of chemical analysis and *in vitro* bioassays presents a comprehensive picture regarding the quantitative level of presence of micropollutants in river water.

Process-based models provide quantitative knowledge about real-world systems that are under investigation. Figure 1.1 illustrates the overall scheme for applying process-based models to real-world environmental systems. The general type of thinking in process-based modeling is to parameterize the model (Figure 1.1C) such that it represents the underlying controlling processes in the real-world environment (Figure 1.1A). Samples are collected in the environment and the data is measured in the laboratory (Figure 1.1A–B), and it is used for constructing model input (e.g., boundary and initial conditions), as well as evaluating the parameterization when such parameterization is used to explain the data. Conditioned on data, process-based models are used to obtain parameter values of the system, particularly those parameters that are difficult to measure directly (Figure 1.1D). A well-parameterized process-based model, meaning that the processes in the model are defined as realistically as possible to that of the real-world system, can be further used to conduct scenario analysis, aiding the planning of laboratory experiments and field campaigns.

The mass conservation law describes the solute transport using the continuity equation (Clement, 1978). By adding source or sink terms, and considering the compressibility of the fluid that carries the solute (John et al., 2017), the continuity equation can be reformulated to the advection-dispersion-reaction equation (ADR) (Carrera et al., 2022), in which the intensive quantity e.g., concentration or temperature, is the state variable. The ADR is the governing equation of process-based reactive transport models. Therefore, applying the process-based reactive transport model to micropollutants concentration data from field campaigns allows us to quantitatively describe the in-stream processes of the micropollutants, obtaining their physical and reactive parameters through calibration. Vari-

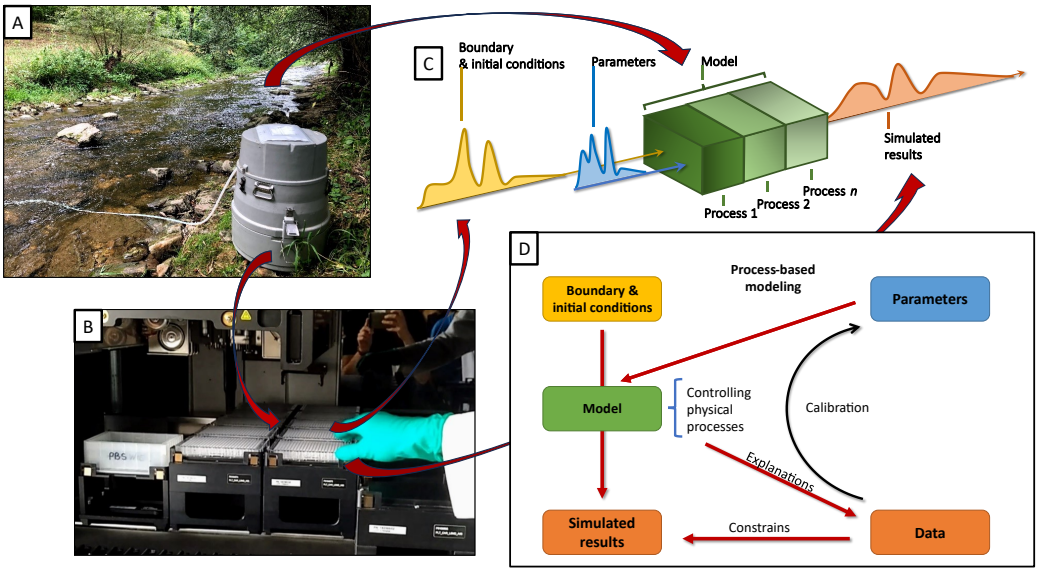

Figure 1.1: Scheme of the overall approach: the environment (e.g., river (A)) provides samples to be measured to produce data (B). The data provides quantitative information for constructing model input (boundary and initial conditions), and evaluating model output, thus physical parameter estimation. The process-based model presents the controlling processes in the environment (C). The relationship among process-based models, parameters, data, and environmental systems form a complete feedback loop (D).

ous studies (Riml et al., 2013; Guillet et al., 2019; Liu et al., 2019) successfully applied the reactive transport model to individual micropollutants concentration data in rivers, quantitatively characterizing complex processes such as light dependent dissipation, mass exchange between water and transient storage phase. There is a lack of quantitative knowledge about the in-stream processes of the mixture effects. On the other hand the mixture effects, EU and TU, are quantified as concentration equivalent (König et al., 2017; Escher et al., 2018, 2021), indicating that the in-stream processes of the mixture effects can be described by the ADR. Therefore, similar to concentrations, applying the reactive transport model to the mixture effects data allows us to quantitatively understand their in-stream processes.

Uncertainty from model parameterization (conceptualization), initial and boundary conditions, data, and numerical approximation (integration in time and descritization in space) influences the model prediction, compromising our quantitative understanding of the system under investigation. Calibrating the model against informative data would improve the model prediction by quantifying the parameter uncertainty. In practice when modeling a complex reactive system, ensemble results from stochastic processes, typically Bayesian inference, e.g., Markov Chain Monte Carlo (MCMC) (Spade, 2020), are often needed or preferred (Chavez Rodriguez et al., 2020; Störiko et al., 2021, 2022; Schwarz et al., 2022; Wei et al., 2022), particularly when results from deterministic parameter estimate methods, e.g., trust-region-reflective (Liu et al., 2020) and Levenberg-Marquardt (Levenberg, 1944; Marquardt, 1963), could not fully represent the observed dynamics. Both deterministic and stochastic calibrations require iterative model forward runs. One of the main challenges in uncertainty quantification for process-based models is the trade-off between

model complexity and practicality. The process-based model is a simplified representation of the real-world system. While parameterizing more complex processes adds extra details to the model, the complexity imposes constraints on the forward run efficiency during calibrations. Such constraints become even more critical when applying MCMC that needs a large number (from thousands to tens of thousands) of iterative model forward runs. Another challenge the process-based model frequently faces is to achieve solutions that are as close as possible to the meaningful and complex information from the measurements under the known and parameterized physical processes. Even the most well-parameterized model can still yield discrepancy with the data since there are always hidden processes in the environment that characterize the behaviours of the data but the modelers failed to formulate, thus are not present in the models. The recently rapidly advanced deep learning methods, e.g., the Artificial Neural Network, showed the potential to overcome this challenge when embedding with the existing knowledge regarding the processes in the environment. In particular, the urge to achieve more accurate (than numerical methods) modeled results while presenting interpretable physical processes (thus not purely data-driven), and efficiently quantifying parameter uncertainty prompt the development of the physics-informed neural network (PINN) (Raissi et al., 2019) and simulation-based inference (SBI) (Greenberg et al., 2019).

In this thesis, the transport of extensive quantities, e.g., mass, in rivers is assumed to be one-dimensional. The lateral exchange is neglected. We calibrate the model against data from the Lagrangian sampling campaigns, where the same water parcels are assumed to be tracked, while facing the limitations that samples occasionally are missing, measurement errors are always present, and measuring stations are scarce considering the distance of the study sites. Our process-based models are developed upon those assumptions and aim to overcome those limitations, meaning our models operate on the "conundrum" that the conceptual uncertainty in the description of a dynamic reactive system is inevitable to begin with. We justify our overall modeling approach based on the following principles:

1. not all uncertainty introduced by the known processes influence the overall system behavior, since the overall system behavior is typically represented by the measurements that potentially provide only limited information. Therefore we identify and focus on the controlling processes of the studied reactive systems.

2. focusing on the controlling processes allows us to reformulate the governing equations of the model into other forms, e.g., convolution in Chapter 2, which in return accelerates the model forward runs.

3. there are enough existing tools that can be used to solve the problems we are facing. By combing the merits of numerical methods, Bayesian inference, and deep learning, we are able to integrate the models with the data that is available, presenting quantitative information regarding the controlling processes.

1.2 Hypothesis & Aims

The main hypothesis of this thesis is that the mixture effects quantified in *in vitro* bioassays are intensive state variables equivalent to, e.g., concentrations. Thus, the mixture effects follow the mass conservation laws. In rivers, the in-stream processes of the mixture effects can be described by the advection-dispersion-reaction equations (ADR).

Under the main hypothesis, we aim to gain quantitative understandings of:

1. the in-stream processes of the mixture effects.
2. the transferability of the ADR from steady-state flow to transient flow conditions for the mixture effects.
3. the potential to achieve accurate solutions and efficient parameter posterior approximation by deep learning methods for solving the ADR and estimating parameter values integrating the mixture effects field data.

1.3 Theory & Modeling Methods

1.3.1 The state variable

Effect unit and toxic unit. The specific effects and cytotoxicity of river water samples are expressed as effect unit (EU) for specific effects and toxic unit (TU) for cytotoxicity (non-specific effect). EU and TU can be used to characterize the effects of individual chemicals (Eq. 1.1 and Eq. 1.2),

$$EU_{\text{chem}_i,\text{assay}_j} = \frac{C_{\text{chem}_i}}{EC_{k,\text{chem}_i,\text{assay}_j}} \tag{1.1}$$

$$TU_{\text{chem}_i,\text{assay}_j} = \frac{C_{\text{chem}_i}}{IC_{k,\text{chem}_i,\text{assay}_j}} \tag{1.2}$$

where C_{chem_i} [ng L^{-1}] is the concentration of the individual detected compound. EC_{k,chem_i} [ng L^{-1}] and IC_{k,chem_i} [ng L^{-1}] are the compound specific effect concentration (EC) and inhibition concentration (IC) that causes k effects of specific endpoints and cell death (cytotoxicity), respectively. i and j are individual compounds' and bioassays' indices, respectively. Further details are in Section 2.2 of Chapter 2.

Mixture effects. EU and TU can be used to characterize the mixture effects of all detected and activated chemicals in the sample, $EU_{\text{chem,assay}_j}$ (Eq. 1.3) and $TU_{\text{chem,assay}_j}$ (Eq. 1.4), which are the sum of the individual compounds' effects (CA concept).

$$EU_{\text{chem,assay}_j} = \sum_{i=1}^{n} \frac{C_{\text{chem}_i}}{EC_{k,\text{chem}_i,\text{assay}_j}} \tag{1.3}$$

$$TU_{\text{chem,assay}_j} = \sum_{i=1}^{n} \frac{C_{\text{chem}_i}}{IC_{k,\text{chem}_i,\text{assay}_j}} \tag{1.4}$$

The EU and TU describing the mixture effects of the micropollutants extracted from the water samples are EU_{bio_j} [$L_{\text{bioassay}} \cdot L_{\text{water}}^{-1}$] (Eq. 1.5) and TU_{bio_j} [$L_{\text{bioassay}} \cdot L_{\text{water}}^{-1}$] (Eq. 2.6), respectively.

$$EU_{\text{bio}_j} = \frac{1}{EC_{k,\text{assay}_j}} \tag{1.5}$$

$$TU_{\text{bio}_j} = \frac{1}{IC_{k,\text{assay}_j}} \tag{1.6}$$

EC_{k,assay_j} and IC_{k,assay_j} are the ECs and ICs of the extracts from the water sample that trigger k effects and cytotoxicity, respectively. The units of EC and IC are relative enrichment factor (REF [L_{water} $L^{-1}{}_{bioassay}$]) (Escher et al., 2021). For TU of the whole bioactive mixture (TU_{bio}), the measured TU_{bio} values in different bioassays are relatively similar since TUs are quantified based on the same endpoint. The mean TU_{bio} of different bioassays was used in this study. i and j are individual compounds' and bioassays' indices, respectively. n is the number of the compounds detected in the water sample and activating in the corresponding assay j. The corresponding effect units EU_{bio} (Eq. 1.5) and toxic units for cytotoxicity TU_{bio} (Eq. 1.6) are mathematically equivalent to bioanalytical equivalent concentrations (Escher et al., 2018, 2021; König et al., 2017) and can be seen as concentrations, which makes EU_{bio} and TU_{bio} valid state variables for process-based modeling that would normally be focused on concentrations of individual chemicals. Further details are in Section 2.2.

1.3.2 Mass conservation and continuity equation

Mass is conserved over time in a closed system. The transport of an extensive state variable, e.g., mass, can be described by the continuity equation (Clement, 1978), of which the general differential form is expressed as Eq. 1.7,

$$\frac{\partial c}{\partial t} = -\nabla \cdot \mathbf{j} + S \tag{1.7}$$

where c is the intensive state variable, e.g., volumetric density. $\mathbf{j}$ is the flux density. $\nabla\cdot$ is the divergence. S represents the sink and source term. t is the time. By differentiating the transport processes, we arrive at Eq. 1.8,

$$\frac{\partial c}{\partial t} = -\nabla \cdot (\mathbf{v}c) + \nabla \cdot (\mathbf{D}\nabla c) + S \tag{1.8}$$

where $\nabla\cdot(\mathbf{v}c)$ (divergence of the advective flux) describes the advection that is caused by the bulk movement of the fluid with which the solute is carried. $\mathbf{v}$ is the velocity field. $\nabla\cdot(\mathbf{D}\nabla c)$ (divergence of the dispersive flux) describes the dispersion (diffusion) phenomenon that is caused by the gradient of the intensive state variable. $\mathbf{D}$ is the dispersion tensor. ∇ is the gradient.

1.3.3 One-dimensional reactive transport

In rivers, it is common to consider the transport of the solute as one-dimensional, since the magnitude of the longitudinal travel is usually much higher than that of the lateral travel. It is also commonly assumed that the fluid, e.g., water, is incompressible, leading the divergence of the velocity to zero (Eq. 1.9) (John et al., 2017).

$$\nabla \cdot \mathbf{v} = 0 \tag{1.9}$$

Therefore, Eq. 1.8 can be simplified to Eq. 1.10 to describe the one-dimensional transport of the solute.

$$\frac{\partial c}{\partial t} = -v(t) \cdot \frac{\partial c}{\partial x} + D_L(t) \cdot \frac{\partial^2 c}{\partial x^2} + S \tag{1.10}$$

where $D_L(t)$ is the longitudinal dispersion coefficient, e.g., [m^2 s^{-1}]. x is the space coordinates. $D_L(t)$ is expressed as in Eq. 1.11,

$$D_L = v(t) \cdot \alpha + D^* \tag{1.11}$$

where α, e.g., [m], denotes the dispersivity. $v(t) \cdot \alpha$, e.g., [m^2 s^{-1}], is the hydrodynamic dispersion. D^*, e.g., [m^2 s^{-1}], is the pore-diffusion coefficient. When the velocity is assumed to be steady over time, Eq. 1.10 is simplified to Eq. 1.12.

$$\frac{\partial c}{\partial t} = -v \cdot \frac{\partial c}{\partial x} + (v \cdot \alpha + D^*) \cdot \frac{\partial^2 c}{\partial x^2} + S \tag{1.12}$$

Eqs. 1.8, 1.10 and 1.12 are often referred to as Advection-Dispersion-Reaction equations (ADR).

1.3.4 Combining mixture effects with one-dimensional reactive transport model

The mixture effects, EU and TU defined in Eqs. 1.1 - 1.6, are quantified as concentration equivalent (Escher et al., 2021). From the mass balance point of view, the ADR (Eq. 1.12) holds for the mixture effects, and is applied to quantitatively characterize the in-stream processes of the mixture effects (Eq. 1.13).

$$\frac{\partial EU_{\text{bio}}}{\partial t} = -v \cdot \frac{\partial EU_{\text{bio}}}{\partial x} + (v \cdot \alpha + D^*) \cdot \frac{\partial^2 EU_{\text{bio}}}{\partial x^2} + S_{\text{bio}} \tag{1.13}$$

1.3.5 Solving the one-dimensional reactive transport equation

The one-dimensional reactive transport equations, Eqs. 1.8, 1.10 and 1.12, are partial differential equations (PDE). It is often impossible to solve them analytically due to the complexity in the source and sink term S, as well as boundary conditions. For the models in Chapter 2, I used the convolution method to approximate their solutions. To solve the ADRs in Chapter 3 and Chapter 4, I used the finite difference method (FDM) (Noye and Tan, 1989) to discretize the spatial domain, coverting the PDEs to a series of ordinary differential equations (ODE), solving them using the numerical ODE solver *ode15s* (Shampine and Reichelt, 1997) in MATLAB and the ODE solver *solve_ivp* (explicit Runge-Kutta method of order 5(4) (Dormand and Prince, 1986)) from the *SciPy* library (Virtanen et al., 2020) in the open-source programming language Python, respectively.

The gradient for the advective transport is discretized as in Eq. 1.14,

$$\left.\frac{\partial c}{\partial x}\right|_i = \frac{c_i - c_{i-1}}{\Delta x} \tag{1.14}$$

where i is the spatial index for the nodes in the discretized domain. The dispersive transport is discretized as in Eq. 1.15.

$$\left.\frac{\partial^2 c}{\partial x^2}\right|_i = \frac{c_{i+1} - 2c_i + c_{i-1}}{\Delta x^2} \tag{1.15}$$

1.3.6 Bayesian inference for parameter estimates

Bayesian calibration was used to estimate the model parameters in Chapter 2 and Chapter 4. Bayesian inference itself is a statistical inference that provides uncertainty quantification of model parameter from a stochastic point of view, meaning instead of deriving deterministic values, the estimated model parameter values are characterized by probability density functions. The estimated probability density function (posterior) is based

on the prior knowledge (prior), e.g., physical and empirical constraints or literature information, without the influence from the data, and the likelihood of the data (likelihood) conditioned on the parameters. Quantitatively Bayes rule states that given the data $\boldsymbol{y}$, the posterior probability density of parameter $\boldsymbol{\theta}$, $p(\boldsymbol{\theta}|\boldsymbol{y})$, is the product of the prior parameter probability density $p(\boldsymbol{\theta})$ and the likelihood of the data $p(\boldsymbol{y}|\boldsymbol{\theta})$ divided by the marginal likelihood of the data $p(\boldsymbol{y})$ (Eq. 1.16):

$$p(\boldsymbol{\theta}|\boldsymbol{y}) = \frac{p(\boldsymbol{y}|\boldsymbol{\theta}) \cdot p(\boldsymbol{\theta})}{p(\boldsymbol{y})} \tag{1.16}$$

$p(\boldsymbol{y})$ is the so-called Bayesian model evidence (BME) that is the integral of the likelihood over the entire parameter space Ω as in Eq. 1.17 (Schwindt et al., 2023; Morales Oreamuno et al., 2023):

$$p(\boldsymbol{y}) = \int_{\Omega} p(\boldsymbol{y}|\boldsymbol{\theta}) p(\boldsymbol{\theta})\, d\boldsymbol{\theta} = \mathbb{E}_{\text{prior}}[p(\boldsymbol{y}|\boldsymbol{\theta})] \tag{1.17}$$

$p(\boldsymbol{y})$ is constant, meaning it does not influence the posterior $p(\boldsymbol{\theta}|\boldsymbol{y})$. Therefore, Eq. 1.16 is simplified to Eq. 1.18:

$$p(\boldsymbol{\theta}|\boldsymbol{y}) \propto p(\boldsymbol{y}|\boldsymbol{\theta}) \cdot p(\boldsymbol{\theta}) \tag{1.18}$$

Likelihood function. One of the most commonly used likelihood functions is the Gaussian likelihood. If $\boldsymbol{\theta} = [\boldsymbol{\theta}_{\text{model}}, \sigma_{\epsilon,j}]$ is the parameter vector, $\boldsymbol{y}_{\text{obs}}$ is the observation vector, then the likelihood function $\mathcal{L} = p(\boldsymbol{y}|\boldsymbol{\theta})$ is defined as (Eq. 1.19):

$$\mathcal{L}(\boldsymbol{\theta}|\boldsymbol{y}_{\text{obs}}) = \prod_{i=1}^{n} \frac{1}{\sqrt{2\pi\sigma_{\epsilon}^2}} \exp\left(-\frac{1}{2}\frac{[y_{\text{model},i}(\boldsymbol{\theta}_{\text{model}}) - y_{\text{obs},i}]^2}{\sigma_{\epsilon}^2}\right) \tag{1.19}$$

where $\boldsymbol{\theta}_{\text{model}}$ is the model parameter vector, i [-] the observation index, and n [-] the total number of the observations. σ_{ϵ} is the standard deviation in the likelihood function.

Posterior sampling. An analytical expression for the posterior is typically difficult to derive. Alternatively, Markov chain Monte Carlo that draws samples from the approximated posterior (Eq. 1.18) is usually used. The Metropolis–Hastings Markov chain Monte Carlo (MH-MCMC) algorithm was used to obtain samples of the posterior parameter distribution in Chapter 2. The Simulation-based inference (SBI) was used to obtain the Neural Posterior Estimation (NPE) in Chapter 4.

1.4 Studied Rivers

In this thesis, I applied the reactive transport models to data collected from two rivers: the Steinlach River (2020-08-19 – 2020-08-21 in Chapter 2) and the Ammer River (2019-07-27 – 2019-07-28 in Chapter 3, 2018-06-19 – 2018-06-20 in Chapter 4). Both rivers are located in the state of Baden-Wüttemberg, southwest Germany.

The Steinlach River The Steinlach River is a 25.9 km long 4th-order river that starts from the valley of the Eckenbachgraben near the town of Mössingen, passing through the southern part of Tübingen city, draining into the Neckar River of the Rhine basin in the state of Baden-Württemberg, Germany. It flows through the catchment of 140 km² (Schwientek et al., 2016), of which the use is 49% agriculture, 39% forest and 12% urban (Schwientek

et al., 2013; Guillet et al., 2019). The Steinlach River has a mean discharge (as of March 1, 2016) of 1.84 $m^3\ s^{-1}$ (https://www.hvz.baden-wuerttemberg.de/). However the discharge varies seasonally that it can reach 15 $m^3\ s^{-1}$ in December (Schwientek et al., 2013) and drop to 0.1 $m^3\ s^{-1}$ - 0.2 $m^3\ s^{-1}$ during the dry period (Liu et al., 2018). The river stretch we were focusing on in Chapter 2 was fed by one main tributary Ehrenbach and four small creeks. A constructed diversion (Mühlbach) takes the water out of the main channel at approximately 1 km downstream of the wastewater treatment plant (WWTP) and flows into the Neckar River without returning to the main channel. Further information regarding the fluvial geomorphology can be found in Schwientek et al., 2016. Figure 1.2 shows the sampling site.

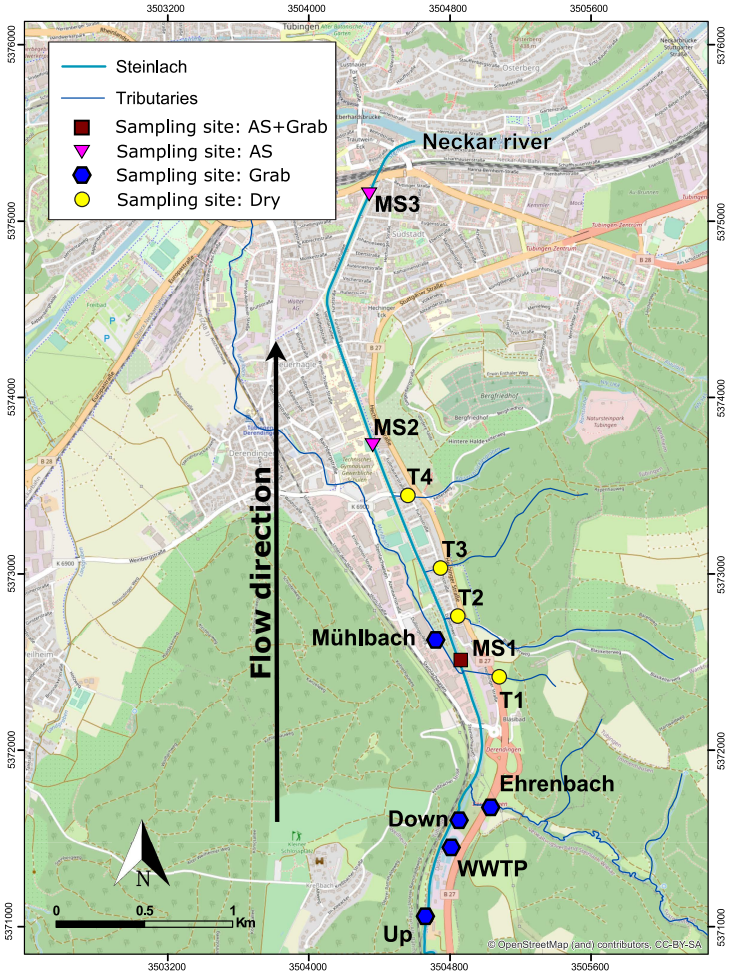

Figure 1.2: Steinlach River sampling site. Water in the main channel flows from the south to the north. Three measuring stations (MS 1–3) were set along the river main channel for collecting time-series samples. MS– measuring station; Grab – grab samples; AS – auto-sampler. Map made by Victor Carvalho Cabral.

The Ammer River. The Ammer River is a 4th-order river and starts from the city of Herrenberg, flowing over a distance of approximately 22 km and through an catchment area of 134 km^2, and merges with the Neckar River in the city of Tübingen. The mean

discharge is 0.87 $m^3 s^{-1}$ (gauge Pfäffingen (https://www.hvz.baden-wuerttemberg.de/). The largest WWTP (80000 personal equivalents (PE)) in the catchment is located downstream of Herrerberg and directly releases water into the Ammer river. The second WWTP (9000 PE, located in Hailfingen) releases water into the tributariy Kochhart Creek that flows into the Ammer River main channel near the city of Reusten. The river stretch we are focusing on in Chapter 3 and Chapter 4 is 7.7 km long, starting 250 m downstream of the first WWTP and ends near Pfäffingen. Further information regarding the fluvial geomorphology can be found in Glaser et al., 2020. Figure 1.3 shows the sampling site.

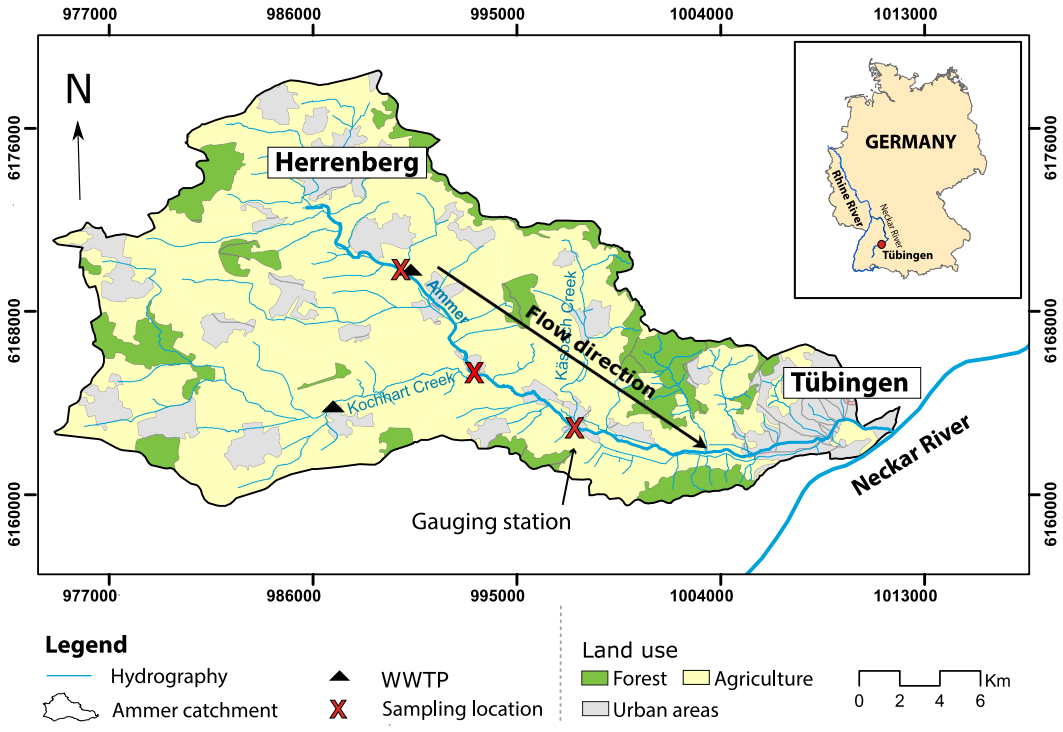

Figure 1.3: Ammer River sampling site. The middle sampling site was not used during the campaign in Chapter 3. All three sampling sites were used in the campaign in Chapter 4. Map made by Victor Carvalho Cabral.

1.5 Thesis Structure

To quantitatively understand the in-stream processes of effects of single organic micropollutants and their mixture, I divided my process-based model applications into three chapters.

1. In Chapter 2, I implemented convolution-based models and applied them to data obtained under unsteady flow conditions. I addressed the model parameter uncertainties for the mixture effects using Bayesian inference. Parameter posterior and ensemble output were computed using Metropolis–Hastings Markov Chain Monte Carlo (MCMC) to address the noisy mixture effects observations.

2. In Chapter 3, I updated the steady-state flow condition reactive transport model with transient terms and applied to mixture effects data collected from a storm event. In parallel, a flood routing model was implemented to compute the discharge wave propagation during the storm event. To properly process the noisy time-series signals and include the measurement uncertainties, I introduced the stochastic elements into the deterministic models by implementing Gaussian Process Regression (GPR) to characterize the inflow boundary condition.

3. In Chapter 4, I implemented the physics-informed neural network (PINN) in the machine learning framework *PyTorch* to solve standard reactive transport model, training the PINN model using real-world mixture effects observations from a field campaign. I also applied the simulation-based-inference (SBI) to obtain the neural posterior for the model parameters. Integrating, stochastic input from GPR, parameters from neural posteriors, and the 1-D reactive transport model was able to efficiently compute the ensemble mixture effect output. I compared the two approaches in terms of the final prediction accuracy, estimated parameter values, as well as computational efforts and summarize the advantage and disadvantages of each approach with respect to the modeling purposes.

4. In Chapter 5, I summarized how the main research questions of this thesis are addressed, highlighting the major outcome from the process-based modeling on the mixture effects of micropollutants in rivers. With a brief overview of the recent development of open-source programming language libraries, I outlined the potential future application directions for the reactive transport and other process-based modeling.

Chapter 2

Modeling the dynamics of mixture toxicity and effects of organic micropollutants in a small river under unsteady flow conditions

This chapter is based on and reprinted with permission from: Wei, R., Escher, B. I., Glaser, C., König, M., Schlichting, R., Schmitt, M., Störiko, A., Viswanathan, M., and Zarfl, C.. Modeling the Dynamics of Mixture Toxicity and Effects of Organic Micropollutants in a Small River under Unsteady Flow Conditions. *Environ. Sci. Technol.*, 56(20):14397–14408, 2022. ISSN 0013-936X. doi: 10.1021/acs.est.2c02824.

Abstract

The presence of anthropogenic organic micropollutants in rivers poses a long-term threat to surface water quality. To describe and quantify the in-stream fate of single micropollutants, the advection-dispersion-reaction (ADR) equation has been used previously. Understanding the dynamics of the mixture effects and cytotoxicity that are cumulatively caused by micropollutant mixtures along their flow path in rivers requires a new concept. Thus, we extended the ADR from single micropollutants to defined mixtures, then to the measured mixture effects of micropollutants extracted from the same river water samples. Effects (single and mixture) are expressed as effect units (EU) and toxic units (TU), the inverse of effect concentrations and inhibitory concentrations, respectively, quantified with a panel of *in vitro* bioassays. We performed a Lagrangian sampling campaign under unsteady flow, collecting river water that was impacted by a wastewater treatment plant (WWTP) effluent. To reduce the computational time, the solution of the ADR was expressed by a convolution-based reactive transport approach, which was used to simulate the dynamics of the effects. The dissipation dynamics of the individual micropollutants were reproduced by the deterministic model following first-order kinetics. The dynamics of experimental mixture effects without known compositions were captured by the model ensemble obtained through Bayesian calibration. The highly fluctuating WWTP effluent discharge dominated the temporal patterns of the effect fluxes in the river. Minor inputs

likely from surface runoff and pesticide diffusion might contribute to the general effect and cytotoxicity pattern but could not be confirmed by the model-based analysis of the available effect and chemical data.

2.1 Introduction

Organic micropollutants like pharmaceuticals, personal care products (PCPs) (e.g., fragrances), detergents, industrial chemicals (e.g., for roof sealing), pesticides and substances induced by combustion of organic materials (e.g., polycyclic aromatic hydrocarbons (PAHs)) have been found ubiquitously at low concentration levels (typically in a $ng \cdot L^{-1}$-range) in surface waters. The diverse physicochemical properties of these micropollutants can adversely affect their biological and chemical removal efficiencies in the secondary treatment of the wastewater treatment plants (WWTPs) (Petrovic et al., 2009). Even the WWTPs equipped with advanced processes have difficulties to completely eliminate all the micropollutants (Kim and Zoh, 2016; Radjenović et al., 2009; Guillossou et al., 2019). Treated and untreated wastewater has been viewed as one of the main sources of organic micropollutants in rivers (Mandaric et al., 2018; Neale et al., 2017). Especially in small rivers where the surrounding areas are densely populated and the WWTPs' effluent makes up a significant share of the river water, partly depending on the season and weather conditions, the downstream river water quality will be adversely impacted by the WWTPs' effluent (Li et al., 2016; Jaeger et al., 2018; Schaper et al., 2019; Müller et al., 2020).

To understand the micropollutant dynamics and their potential risk, some previous studies applied a Lagrangian sampling scheme with high temporal resolution to collect composite samples in rivers. The Lagrangian scheme captures the in-stream dynamics of the micropollutants by tracking the same water packages from upstream to downstream locations (Schwientek et al., 2016; Glaser et al., 2020; Guillet et al., 2019; Antweiler et al., 2014). These studies were purely focusing on the concentrations of the micropollutants, inorganic ions and dissolved organic carbon (DOC). Numerous studies have also been conducted on individual and mixture effects (specific effects and cytotoxicity) from WWTPs-emitted micropollutant mixtures (Neale et al., 2015, 2017) in rivers. A main question these studies try to answer is the identification of the micropollutants in the complex mixtures (Escher et al., 2021) and their individual contributions to the overall mixture effects. It is not possible to identify every single compound in the complex mixture that potentially consists of hundreds and thousands of chemicals. The effects stemming from the individual compounds, as well as the ones driving the overall mixture, can be quantified in the panels of *in vitro* bioassays. When thousands of compounds are present at very low concentrations in mixtures, their interactions that might cause synergistic or antagonistic mixture effects are usually not dominant and therefore not noticeable (Escher et al., 2020). Under such circumstances, the concentration addition (CA) concept (Escher et al., 2020) can be applied with which the effects of the unknown micropollutants in the mixture can be calculated.

The fast changing in-stream dynamics of individual and mixture effects have been studied by Müller and coworkers (Müller et al., 2018, 2020). Mixture effects are regarded as indicator for the sum of effective chemicals and thus quantified as concentration equivalents. It is also assumed that chemicals that trigger the same endpoint in the same bioassay will undergo similar processes that impact the actual effectiveness of the compounds in the river (environment). However, there is a lack of quantitative understanding of the

in-stream transport mechanisms and reactive processes that the mixture effects undergo.

A process-based mathematical modeling approach is needed to gain quantitative insights of in-stream mechanisms of the mixture effects. Liu et al., 2020 studied the in-stream fate of a few pharmaceuticals using a one-dimensional reactive transport model. The computational expense of the model is already relatively high due to the complex parameterization and spatial discretization. Uncertainties originating from the measurement of the total mixture effects also impair the understanding of mechanisms and processes. For example, unclear transport patterns in the mixture effects data are potentially caused by uncertainties, which could arise from various sources: e.g., measurements, temporal resolutions of observations, simplified characterizations of the real-world processes (Höge et al., 2019), actual natural variability. To address these uncertainties and to display levels of belief in the modeled results (as well as the model structure), ensemble results from "stochastification" (Höge et al., 2019) are particularly useful by addressing the randomness of a system. Coupled with stochastic methods, the measurement uncertainties are taken into account when approximating the model parameters' distributions, from where ensemble results can be computed. Thus, the computational costs increase with the complexity of the mixtures that contain a large number of micropollutants, of which the individual and total mixture effects are quantified in multiple bioassays. The simulation time can be the limiting factor to run the model when hundreds of thousands of model runs are needed for each mixture effect during stochastic simulation.

The present study intended to evaluate if a one-dimensional model based on the advection-dispersion-reaction equation (ADR) is able to characterize the in-stream dynamics of specific effects and of the cytotoxicity of both individual compounds and the total bioactive micropollutant mixture. We tested our hypothesis by combining a Lagrangian sampling campaign in a WWTP-influenced river with the measurement of chemical mixtures and their effects. Measured and predicted mixture effects were compared before setting up the model describing the in-stream dynamics, first, for single chemicals, second, the known mixtures, and finally the measured bioassay responses. Sample effects were quantified with *in vitro* bioassays covering four different modes of action that had been demonstrated previously to be very relevant for water quality assessment and responding to a wide range of organic micropollutants (Escher et al., 2021). We implemented a computationally cheap convolution-based (a solution of the ADR (Cirpka and Valocchi, 2007; Toride et al., 1993)) transport model to simulate the unsteady discharge in the river main channel caused by the WWTP's highly dynamic outflow. Adding first-order reaction kinetics, the convolution-based reactive transport model was applied to the individual compounds' effects. For the measured mixture effects of all micropollutants in water samples, modeled ensemble time series were computed within Bayesian inference to account for measurement and parameter uncertainties and overcome the noisy transport patterns in the observations.

2.2 Theory

Effect unit and toxic unit. The specific effects relate to any non-lethal endpoints, e.g., estrogenic effects, triggered by binding of micropollutants and natural hormones to the estrogen receptor (Escher et al., 2021). Cytotoxicity, in our case, is the toxicity that refers to apical lethal endpoints. Specific effects and cytotoxicity in the WWTP-impacted river water were quantified with *in vitro* bioassays and expressed as effect unit (EU) for specific ef-

fects and toxic unit (TU) for cytotoxicity (non-specific effect). Both EU and TU can be used to characterize the effects of individual chemicals ($EU_{\text{chem}_i,\text{assay}_j}$, Eq. 2.1 and $TU_{\text{chem}_i,\text{assay}_j}$, Eq. 2.2), the mixture effects of the detected chemicals in the sample ($EU_{\text{chem,assay}_j}$ and $TU_{\text{chem,assay}_j}$), as well as the experimentally quantified mixture effects (EU_{bio} and TU_{bio}).

$$EU_{\text{chem}_i,\text{assay}_j} = \frac{C_{\text{chem}_i}}{EC_{k,\text{chem}_i,\text{assay}_j}} \tag{2.1}$$

$$TU_{\text{chem}_i,\text{assay}_j} = \frac{C_{\text{chem}_i}}{IC_{k,\text{chem}_i,\text{assay}_j}} \tag{2.2}$$

C_{chem_i} [ng L^{-1}] is the concentration of the individual detected compound. EC_{k,chem_i} [ng L^{-1}] and IC_{k,chem_i} [ng L^{-1}] are the compound specific effect concentration (EC) and inhibition concentration (IC) that causes k effects (k typically is 10 % of the maximum effect (Escher and Neale, 2021) or the induction ratio (IR) of 1.5, which is 50% over unexposed cells of IR 1 (Escher and Neale, 2021; Müller et al., 2018).) of specific endpoints and cell death (cytotoxicity), respectively. i and j are individual compounds' and bioassays' indices, respectively.

The mixture effects of all detected and activated compounds, $EU_{\text{chem,assay}_j}$ (Eq. 2.3) and $TU_{\text{chem,assay}_j}$ (Eq. 2.4), are the sum of the individual compounds' effects (CA concept).

$$EU_{\text{chem,assay}_j} = \sum_{i=1}^{n} \frac{C_{\text{chem}_i}}{EC_{k,\text{chem}_i,\text{assay}_j}} \tag{2.3}$$

$$TU_{\text{chem,assay}_j} = \sum_{i=1}^{n} \frac{C_{\text{chem}_i}}{IC_{k,\text{chem}_i,\text{assay}_j}} \tag{2.4}$$

The EU and TU describing the mixture effects of the micropollutants extracted from the water samples are EU_{bio_j} [$L_{\text{bioassay}} \cdot L_{\text{water}}^{-1}$] (Eq. 2.5) and TU_{bio_j} [$L_{\text{bioassay}} \cdot L_{\text{water}}^{-1}$] (Eq. 2.6), respectively.

$$EU_{\text{bio}_j} = \frac{1}{EC_{k,\text{assay}_j}} \tag{2.5}$$

$$TU_{\text{bio}_j} = \frac{1}{IC_{k,\text{assay}_j}} \tag{2.6}$$

EC_{k,assay_j} and IC_{k,assay_j} are the ECs and ICs of the extracts from the water sample that trigger k effects and cytotoxicity, respectively. The units of EC and IC are relative enrichment factor (REF [$L_{\text{water}}\ L^{-1}{}_{\text{bioassay}}$]) (Escher et al., 2021). For TU of the whole bioactive mixture (TU_{bio}), the measured TU_{bio} values in different bioassays should be relatively similar since TUs are quantified based on the same endpoint. The mean TU_{bio} of four bioassays (bioassay details in Section 3.2.1) was used in this study. i and j are individual compounds' and bioassays' indices, respectively. n is the number of the compounds detected in the water sample and activating in the corresponding assay j. The corresponding effect units EU_{bio} (Eq. 2.5) and toxic units for cytotoxicity TU_{bio} (Eq. 2.6) are mathematically similar to bioanalytical equivalent concentrations (Escher et al., 2018, 2021; König et al., 2017) and, in principle, can be regarded as concentrations, which makes units EU_{bio} and TU_{bio} amenable to the model calculations that would normally be based on concentrations of individual chemicals.

Effect unit and toxic unit fluxes. The fluxes $F_q(t)$ of the EU ($q = EU_{\text{chem}i,\,\text{assay}\,j}$; $EU_{\text{bio}\,j}$) and the TU ($q = TU_{\text{chem}i,\,\text{assay}\,j}$; $TU_{\text{bio}\,j}$) are defined by the products of the effect units and toxic units, respectively, with the corresponding discharge (Q in [$m^3\ s^{-1}$]) at time t (Eq. 2.7. EU is replaced by TU when computing the cytotoxicity flux).

$$F_q(t) = EU_{\text{chem}i,\,\text{assay}\,j}(t) \cdot Q(t) \tag{2.7}$$

Conservative transport of electrical conductivity. The electrical conductivity (ECd) in rivers is assumed to behave identically to the conservative compounds or ideal tracer (Schwientek et al., 2016; Glaser et al., 2020). Therefore, the ECd time series can be used to determine the hydrological parameters values, i.e., the mean water travel time and the lumped advection and dispersion coefficient (Schwientek et al., 2016; Glaser et al., 2020; Maloszewski and Zuber, 1993) by fitting the modeled ECd to the measurements (fitting details in Section 2.3.3). In general, the one-dimensional transport of a time series signal in rivers can be described by a linear time-invariant system and its impulse response in the time domain. The essence is that the output signal is the integral of the product of the input signal and a transfer function. This operation is named convolution and can be expressed for the ECd by Eq. 2.8,

$$ECd_{\text{down}}(t) = \int_0^{t_{max}} ECd_{\text{up}}(t-\tau)g(\tau)d\tau \tag{2.8}$$

where ECd_{up} [mS cm^{-1}] and ECd_{down} [mS cm^{-1}] are the ECd time series at the upstream and the downstream locations of the studied river stretch, respectively. t is the sampling time point. t_{max} is the integral time interval. τ is the travel time of the individual water parcel, and $g(\tau)$ is the transfer function.

Conservative transfer function. The impulse response of a linear time-invariant system is the transfer function, which is a probability density function (PDF) that characterizes the distribution of the travel times (τ) of the water parcels and produces the downstream signal from the upstream signal via convolution. Assuming ECd behaves conservatively, the transfer function consists of advection and dispersion terms (Małoszewski and Zuber, 1982; Schwientek et al., 2016; Glaser et al., 2020), and is expressed as Eq. 2.9,

$$g(\tau) = \frac{1}{\tau\sqrt{\frac{4\pi D\tau}{\Delta t_{\text{ECd}}}}} \exp\left[-\frac{(1-\frac{\tau}{\Delta t_{\text{ECd}}})^2}{\frac{4D\tau}{\Delta t_{\text{ECd}}}}\right] \tag{2.9}$$

which is parameterized by the dimensionless dispersion coefficient D [-] and the mean travel time Δt_{ECd}.

Strictly speaking, for the ADR to be expressed by eqs. 2.8 – 2.9, a steady-state condition is required. However, the convolution could still be applied under unsteady condition when, e.g., the mean fluctuation period of the velocity is short in comparison with the time scale of advection or dispersion (Boudreau, 1997); the time scale of flow velocity fluctuation is smaller than the travel time (Cirpka et al., 2007). In our study, no cross-sectional area data along the river course could be obtained. Thus, the flow velocity (the travel time) was approximated by a mean value.

Unsteady discharge propagation. Measuring downstream discharge (Q_{down} [m^3 s^{-1}]) was not possible due the lack of a reliable rating curve. For approximating discharge time series $Q_{\text{down}}(t)$ under unsteady flow conditions, an earlier approach for steady state conditions by Schwientek et al., 2016 was adopted in Eq. 2.10,

$$Q_{\text{down}}(t) = \int_0^{t_{max}} Q_{\text{up}}(t-\tau)q(\tau)d\tau \tag{2.10}$$

where $Q_{\text{up}}(t)$ [m^3 s^{-1}] is the discharge time series at the upstream location (Q_{up} calculation in Appendix A.1).

The unsteady discharge follows the travel phenomenon of the kinematic wave in the open channel. Since the studied river stretch approximates a rectangular cross-section area and the water depth is shallow relative to the channel width, the definition of the celerity $c_{\text{kn,wave}}$ [m s^{-1}] of the wave in relation to the mean velocity of the ECd v_{ECd} [m s^{-1}], can be simplified to Eq. 2.11 (Glaser et al., 2020; Schwientek et al., 2016),

$$c_{\text{kn,wave}} = \frac{5}{3}v_{\text{ECd}} \tag{2.11}$$

which yields to Eq. 2.12,

$$\Delta t_{\text{kn,wave}} = \frac{3}{5}\Delta t_{\text{ECd}} \tag{2.12}$$

where $\Delta t_{\text{kn,wave}}$ is the mean kinematic wave travel time. The transfer function $q(\tau)$ needs to be adjusted as Eq. 2.13.

$$q(\tau) = \frac{1}{\tau\sqrt{\frac{20\pi D\tau}{3\Delta t_{\text{ECd}}}}} \exp\left[-\frac{(1-\frac{5\tau}{3\Delta t_{\text{ECd}}})^2}{\frac{20D\tau}{3\Delta t_{\text{ECd}}}}\right] \tag{2.13}$$

The sorption – desorption process that could influence the mean travel estimate for the solutes transport was not included. Good results regarding the mean travel time estimate using ECd without considering the sorption – desorption process in the similar segment of the same river could be seen in Guillet and coworkers (Guillet et al., 2019). The study segment of the Steinlach river is a relatively straight artificial channel that creates neither enough hyporheic zones nor enough heads gradient to enhance hyporheic exchange. Under such conditions, sorption to the riverbed and suspended sediments can be neglected.

Reactive transport of the effects from individual chemicals and mixture. In addition to the transport processes described above for the EU and TU, these effects undergo exponential first-order decay. The transient storage part (needed under low flow conditions (Liu et al., 2020)) of the model was ignored in this case. Therefore, the transport of the EU and TU is complemented by a description of the lumped loss process following first-order kinetics (Eq. 2.14 – 2.17),

$$EU_{\text{chem}_i,\text{assay}_j,\text{down}}(t) = \int_0^{t_{max}} EU_{\text{chem}_i,\text{assay}_j,\text{up}}(t-\tau)r_{\text{chem}_i}(\tau)d\tau \tag{2.14}$$

$$TU_{\text{chem}_i,\text{assay}_j,\text{down}}(t) = \int_0^{t_{max}} TU_{\text{chem}_i,\text{assay}_j,\text{up}}(t-\tau)r_{\text{chem}_i}(\tau)d\tau \tag{2.15}$$

$$EU_{\text{bio}_j,\text{down}}(t) = \int_0^{t_{max}} EU_{\text{bio}_j,\text{up}}(t-\tau) r_{\text{bio}_j,\text{spec}}(\tau) d\tau \tag{2.16}$$

$$TU_{\text{bio}_j,\text{down}}(t) = \int_0^{t_{max}} TU_{\text{bio}_j,\text{up}}(t-\tau) r_{\text{bio}_j,\text{cyto}}(\tau) d\tau \tag{2.17}$$

where the $EU_{\text{chem}_i,\text{assay}_j}$, $TU_{\text{chem}_i,\text{assay}_j}$, EU_{bio_j} and TU_{bio_j} are time series of the state variables defined in Eq. 2.1 – 2.6. $r_{\text{chem}_i}(\tau)$, $r_{\text{bio}_j,\text{spec}}(\tau)$ and $r_{\text{bio}_j,\text{cyto}}(\tau)$ are compound and assay specific reactive transfer functions, respectively, that relate to the conservative transfer function $g(\tau)$ (Eq. 2.9) through Eq. 2.18 – 2.20.

$$r_{\text{chem}_i}(\tau) = g(\tau)\exp(-\lambda_{\text{chem}_i}\tau) \tag{2.18}$$

$$r_{\text{bio}_j,\text{spec}}(\tau) = g(\tau)\exp(-\lambda_{\text{bio}_j,\text{spec}}\tau) \tag{2.19}$$

$$r_{\text{bio}_j,\text{cyto}}(\tau) = g(\tau)\exp(-\lambda_{\text{bio}_j,\text{cyto}}\tau) \tag{2.20}$$

where λ_{chem_i}, $\lambda_{\text{bio}_j,\text{spec}}$ and $\lambda_{\text{bio}_j,\text{cyto}}$ are the compound-specific and assay-specific reaction rate constants $[\tau^{-1}]$ that are, for the purpose of reducing computational costs, assumed to be constant over time.

2.3 Materials & Methods

General approach. A model-aided scenario analysis (Appendix A.2) was conducted prior to the sampling and a Lagrangian sampling scheme that follows the same water parcel along the course of the river was applied in the Steinlach River in Tübingen (southwestern Germany). The studied river stretch is under direct impact of a WWTP effluent. Three auto-samplers (AS) were installed (1.086 km, 2.249 km and 3.754 km downstream of the WWTP, respectively) for 46 hours to collect two-hour interval composite time series water samples. Each composite sample consisted of eight sub-samples taken every 15 minutes. One grab sample each was taken upstream of the WWTP, in the tributary Ehrenbach, at the WWTP's effluent and in the tributary Mühlbach. Three grab samples were taken at measuring station 1 (MS1). Samples from the field were analyzed for organic micropollutants' concentrations (80 targeted micropollutants) and effects (four different *in vitro* bioassays). The one-dimensional convolution-based reactive convolution model (with interpolated signals from MS1 (Figure A.1) as model input) was implemented for describing the fate of individual effects along the river. Within Bayesian inference, the model was used for describing the fate of the mixture effects.

2.3.1 Field campaign

The underlying sampling campaign took place in summer (June to August) 2020 at the Steinlach River with a mean discharge of 1.83 $m^3\ s^{-1}$ and a WWTP effluent of 0.26 $m^3\ s^{-1}$ close to the city of Tübingen, Germany. More details on the field site and the sampling campaign can be found in Appendix A.3.

Mean travel time. Prior to the sampling, it was crucial to estimate the mean water parcel travel time so that the starting time of the auto-samplers at different sampling sites could be determined. ECd time series signal was measured prior to and during the sampling period. We assumed that 1) the ECd behaves conservatively, 2) it reflects the temporal variation resulting from the effluent flow of the WWTP, 3) the measured ECd values are a result of the existing inorganic substances in the water and are much higher than the background ECd values in the main channel and 4) the fluctuations of the flow velocity over time can be approximated by a mean value because the mean fluctuation period of the velocity is short in comparison with the time scale of advection or dispersion. To quantitatively obtain the flow velocity fluctuations, continuous measurements of cross-sectional areas of the river channel over time are required. The mean travel time Δt_{ECd} and the lumped dispersion coefficient D estimation method presented by Schwientek et al., 2016 and Glaser et al., 2020 was modified by implementing the MultiStart algorithm to find the global solution in this study (Section 2.3.3). ECd measurement prior to the sampling and correcting scheme are described in Appendix A.4 in Figure A.2 – Figure A.5.

2.3.2 Laboratory work

A brief description of the chemical analysis of the micropollutants (previously published by Schmitt et al., 2021) like pharmaceuticals, fungicides and herbicides can be found in the Supporting Information (Appendix A.5). Dissolved organic carbon (DOC) and pH of the water samples were also measured.

***In vitro* bioassays.** The enriched extracts from the 1L water sample were tested on four *in vitro* bioassays named AhR-CALUX for aryl hydrocarbon receptor induction, PPARγ-GeneBLAzer for peroxisome proliferator-activated receptor activity, ERα-GeneBLAzer for estrogenicity and AREc32 for oxidative stress. Examples of inducing compounds for the four bioassays are polycyclic aromatic hydrocarbons (PAHs), fibrate pharmaceuticals, endocrine-disrupting compounds and pharmaceuticals that could produce reactive oxygen species, respectively (Escher et al., 2021). In each cell line, the cytotoxicity was also measured. The effect concentration and inhibitory concentration (EC_{10} and IC_{10}) that cause 10% of the effects were quantified by fitting a simple linear regression in the concentration-response curve (Escher et al., 2018). Details on measuring methods for specific effects and cytotoxicity can be found in König et al., 2017 and Escher et al., 2019, respectively. The measured EC_{10} were converted to EU_{bio} (Eq. 2.5) and the corresponding cytotoxicity IC_{10} were converted to TU_{bio} (Eq. 2.6). The mean values of TU_{bio} of the four bioassays were used for modeling because previous work has shown that cytotoxicity is typically very similar for different cell lines (Escher et al., 2020; Lee et al., 2021) since the cell death is triggered by many underlying processes and not directly by the mechanism investigated by the reporter gene activation.

2.3.3 Parameter estimation

The parameters of the model were estimated in two steps. In the first step, the nonlinear least-squares solver was used to estimate transport parameters from ECd data and the first order reaction rate constants for the effect of individual micropollutants. Bayesian inference was then used to estimate reaction rate constant for the overall mixture effects.

Deterministic parameter estimation

The nonlinear least-squares solver was used in estimating the mean travel time Δt_{ECd}, the lumped dispersion coefficient D (Eq. 2.9), and the first-order reaction rate constant of the detected individual compound's effect (Eq. 2.18). An optimized single value for each parameter will be found by the search algorithm.

The MultiStart algorithm (trust-region-reflective searching method (Liu et al., 2020)) was used to evaluate the outcome of the objective function (Eq. A.14). The global solution was found from the results of local solvers with multiple (500 - 1500) starting points. Normalized root mean square error (NRMSE) was computed for each compound to evaluate the goodness of the model fit (thus the model errors). NRMSE is defined as the root mean square error divided by the difference between the maximum ($y_{\mathrm{obs,max}}$) and minimum values ($y_{\mathrm{obs,min}}$) in the observations (Eq. A.15).

Bayesian inference parameter estimation

Bayesian calibration was used to estimate the first order reaction constant in modeling the total effects and toxic units EU_{bio} and TU_{bio}. Bayes rule states that given the data $\boldsymbol{y}$, the posterior probability density of parameter $\boldsymbol{\theta}$, $P(\boldsymbol{\theta}|\boldsymbol{y})$, is proportional to the product of the likelihood of the data $P(\boldsymbol{y}|\boldsymbol{\theta})$ and the prior parameter probability density $P(\boldsymbol{\theta})$:

$$P(\boldsymbol{\theta}|\boldsymbol{y}) \propto P(\boldsymbol{y}|\boldsymbol{\theta}) \cdot P(\boldsymbol{\theta}) \tag{2.21}$$

Likelihood function. If $\boldsymbol{\theta} = [\lambda_j, \sigma_{\epsilon,j}]$ is the parameter vector, $\boldsymbol{y}_{\mathrm{obs}} = [y_{\mathrm{obs},1}, ..., y_{\mathrm{obs},n}]$ is the observation vector, then the likelihood function is defined as:

$$\mathcal{L}(\boldsymbol{\theta}|\boldsymbol{y}_{\mathrm{obs}}) = \prod_{i=1}^{n} \frac{1}{\sqrt{2\pi\sigma_\epsilon^2}} \exp\left(-\frac{1}{2}\frac{[y_{\mathrm{model},i}(\lambda) - y_{\mathrm{obs},i}]^2}{\sigma_\epsilon^2}\right) \tag{2.22}$$

where i [-] is the observation index, n [-] the total number of the observations. Apart from the first-order reaction rate constant λ, the standard deviation σ_ϵ in the likelihood function was also estimated.

Prior parameter distribution. A prior distribution represents the belief about the existing information before any observations are provided (van Ravenzwaaij et al., 2018). It can be derived based on existing theories, past experiments or constraints due to logical reasons. To derive the prior distribution, we firstly assumed that the prior distribution of the first-order reaction rate constants of EU_{bio} and mean TU_{bio} is informative and normal. A normal distribution was fitted to the deterministically calibrated first-order reaction rate constants of all the detected organic micropollutants (Section 2.3.3), and their corresponding reaction rate constants derived from the literature half-lives (predicted biodegradation half-life values from quantitative structure–activity/property relationship (QSAR) model (Mansouri et al., 2018) (https://comptox.epa.gov/dashboard) using Eq. A.16).

The prior distribution of $\sigma_{\epsilon,j}$ (Eq. 2.22) was assumed to be a bounded uniform distribution ($\sigma_{\epsilon,j} \sim \mathcal{U}(0, 5s)$). Here, s is the maximum value of the reported standard errors of the measured values of the grab samples collected at the WWTP effluent and 20% of the measurements' values. This was done in an effort to cover as many reasonable values as possible. Thus, by rearranging Eq. 2.22, Eq. A.16 and Eq. A.17, the posterior distribution is expressed as:

$$P_{\text{posterior}}(\boldsymbol{\theta}|\boldsymbol{y}_{\text{obs}}) = \prod_{i=1}^{n} \left(\frac{1}{\sqrt{2\pi\sigma_\epsilon^2}} \exp\left[-\frac{1}{2} \frac{(y_{\text{model},i}(\lambda) - y_{\text{obs},i})^2}{\sigma_\epsilon^2} \right] \right) \left(\frac{1}{\sigma_\lambda \sqrt{2\pi}} \exp\left(-\frac{1}{2} \left[\frac{\lambda - \mu_\lambda}{\sigma_\lambda} \right] \right)^2 \right) \frac{1}{5s} \tag{2.23}$$

Posterior sampling. The Metropolis–Hastings Markov chain Monte Carlo (MH-MCMC) algorithm was used to obtain samples of the posterior parameter distribution. The MH-MCMC was applied to data from four cell lines: AhR-CALUX, PPARγ-GeneBLAzer, ERα-GeneBLAzer and AREc32. Five Markov chains ran sequentially. Iterations needed for the five chains to converge differ among cell lines (10000 to 50000 iterations each chain), depending on uncertainties in the data from different cell lines. After the burn-in period (the first 50% iterations), chains' convergence was checked using the Gelman-Rubin diagnostic with the potential scale reduction factor $\hat{R} < 1.1$ (Brooks and Gelman, 1998; Gelman and Rubin, 1992). To avoid bias in the target distribution, the starting points of chains are randomized values (Gelman and Rubin, 1992) (randomization details in Appendix A.9).

2.4 Results & Discussion

2.4.1 ECd signals and unsteady flow

The measured ECd signals at all measuring stations (MS) (sampling map: Figure A.1) not only characterized the one dimensional in-stream transport phenomenon, but also conveyed information regarding the background river water quality, exhibiting a clear temporal pattern contrast between upstream and downstream locations from the WWTP effluent. There were no rain events recorded in 2020 between 20:00, August 19 (AS1 started sampling) and 17:15, August 21 (AS3 stopped sampling), apart from the two low precipitations of 0.22 mm and 0.1 mm at 21:00, August 18 and 06:00, August 20, respectively (https://www.wetter-bw.de). During this period, the mean effluent discharge from the WWTP (0.12 $m^3\ s^{-1}$, $\pm$ 0.27 $m^3\ s^{-1}$) contributed $\sim$ 47% of the mean discharge in the main channel (0.26 $m^3\ s^{-1}$, $\pm$ 0.13 $m^3\ s^{-1}$). A distinct ambient in-stream ECd diurnal cycle was observed at the measuring station upstream (MS Up) from the WWTP, where the dynamics of ECd corresponded to the water temperature temporal pattern (Figure A.6). The ECd values at the MSs in the main channel downstream from the WWTP were approximately 1.5 times higher than that at MS Up during the sampling period, demonstrating the contribution from the WWTP release. The calibrated hydrological transport parameters based on the ECd time series were used in the unsteady discharge calculation (Figure A.7; NRMSE of 0.0093 and 0.0084 (Table A.10) for calibration results at MS2 and MS3 respectively). Figure 2.1 illustrates the modeled discharge in the studied river stretch. The WWTP effluent discharge was dynamic after AS1 started sampling, and its contribution to the main river flow was high. The WWTP effluent prompted the formation of a discharge wave (increase from 0.12 $m^3\ s^{-1}$ to the peak of 0.64 $m^3\ s^{-1}$ in Figure 2.1B) that traveled downstream in the main channel, causing flow in the main channel to become unsteady (Figure 2.1C – E). Overlays of discharge at all MSs demonstrate how the wave propagated (Figure A.8). The highly dynamic WWTP effluent discharge was likely reflecting the fluctuations of the WWTP inlet. DOC (Figure A.9 A) was higher at day than at night and was also mainly

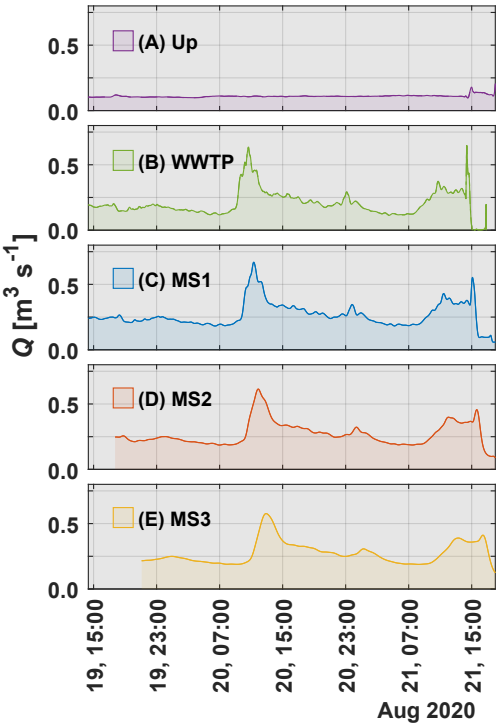

Figure 2.1: Computed unsteady flow during the sampling period: (A) Discharge at the location upstream from the wastewater treatment plant (Up); (B) Discharge at the wastewater treatment plant effluent (WWTP); (C) Discharge at measuring station one (MS1); (D) Discharge at measuring station two (MS2); (E) Discharge at measuring station three (MS3). Detailed sampling location information can be found in Figure A.1 .

influenced by the DOC of the WWTP. The pH followed the discharge and was at pH 8 at lower discharge but rose to over 9 at higher discharge (Figure A.9B).

2.4.2 In-stream concentration and effect dynamics

Detected chemicals' concentrations and mass fluxes. The in-stream dynamics of the concentrations of the detected micropollutants (Neale et al., 2015) were captured well by the Lagrangian sampling scheme (Figure A.10 – Figure A.19, Table A.4 – A.6). All analytical uncertainties are significantly smaller than the temporal variations observed in the data. Therefore, it can be concluded that the observed temporal variations reflected actual in-stream dynamics, not noise from measurement uncertainties. The modeled (model details in eq. A.8 – A.13) compounds' concentrations as well as their mass fluxes (Figure A.20 – Figure A.29) matched the observations well (NRMSE in Table A.10). Micropollutants mainly emitted via the WWTP showed better agreement between measured and modeled concentration time series than those that potentially originated from other sources. A more detailed discussion on the sources of the micropollutants follows in Section 2.4.3.

Individual bioactive chemicals' effects over time and space ($EU_{\mathrm{chem},i}$ and $TU_{\mathrm{chem},i}$). The dynamics of the detected micropollutants' specific effects expressed as $EU_{\mathrm{chem},i}$ and cytotoxicity, $TU_{\mathrm{chem},i}$, are closely related to their concentrations (Neale et al., 2015) (Eq. 2.1

– 2.2). Figure A.30 illustrates the measured $EU_{\text{chem},i}$ time series of compounds from MS2 and MS3 that were activating the AhR in AhR-CALUX assay. The pronounced $EU_{\text{chem},i}$ peaks recorded between 12:20 and 14:20 on August 20 were evidently caused by the earlier high release from the WWTP. The observed effect reduction from MS2 to MS3 (Figure 2.2A and B) was caused by the effective dissipation process (Eq. 2.18), since the main feeding tributary Ehrenbach had very low discharge (0.001 – 0.002 m^3s^{-1}). Linearly derived from the concentrations, the simulated time courses of $EU_{\text{chem},i}$ were able to reproduce the temporal variations of the measurements (e.g. the $EU_{\text{chem},i}$ peak for all compounds except 2-aminobenzothiazole and benzothiazole-2-sulfonic acid (B-2-SA)), and fell within the range of measurement uncertainties. Particularly in the cases of benzotriazole (Figure 2.2A), diuron and telmisartan (Figure A.30), the modeled $EU_{\text{chem},i}$ time courses were able to accurately capture the observed peaks, as well as the tailings (from 21:00 on August 20 to 10:00 on August 21) of the EU dynamics at both MS2 and MS3 (NRMSE (Eq. A.15)) of the nine compounds in Table A.10). B-2-SA displayed an entirely different temporal pattern from the rest of the eight compounds (Figure 2.2B). Instead of being elevated by the WWTP input, the $EU_{\text{chem},i}$ observations experienced a drop between 12:20 and 14:20, as well as observable fluctuations between 13:00 and 17:00 at both MSs on August 20. Afterwards, pronounced peaks were observed at later hours between 21:00 on August 20 and 05:00 on August 21. A previous study (Kloepfer et al., 2005) found that surface runoff also caused a substantial amount of B-2-SA into receiving waters and B-2-SA was the dominant compound among other benzothiazoles in the municipal wastewater. This conclusion might shed lights on the reason for different temporal pattern found in B-2-SA in our study. Still, the model was capable of reproducing most of the features in B-2-SA data. The modeled $EU_{\text{chem},i}$ time courses for individual compounds in PPARγ-GeneGLAzer and AREc32 can be found in Figure A.31 – Figure A.32, respectively. NRMSE for all detected compounds at MS2 and MS3 are shown in Table A.10.

Individual bioactive chemicals' effect unit fluxes. The high release from the WWTP not only functioned as a major contributor of effects in the Steinlach River, but also played a crucial role in characterizing the in-stream temporal patterns of $EU_{\text{chem},i}$ fluxes. The $EU_{\text{chem},i}$ fluxes of B-2-SA and benzotriazole in AhR-CALUX are shown in Figure 2.2C – D. The modeled discharge time series was plotted alongside the $EU_{\text{chem},i}$ fluxes (Figure 2.2E–F). The major temporal patterns of the $EU_{\text{chem},i}$ for AhR-CALUX (Figure A.30) were masked by the discharge features. The $EU_{\text{chem},i}$ fluxes were heavily shaped by the unsteady discharge. The discharge waves that were caused by the sudden WWTP release led to the $EU_{\text{chem},i}$ fluxes peaking at 12:00 at MS2 and 13:10 at MS3. The modeled $EU_{\text{chem},i}$ fluxes' were able to produce the peaks that propagated from MS2 to MS3 in the observations of 4&5 methyl-benzotriazole, benzotriazole, climbazole, diuron, isoproturon and telmisartan (although slight deviations from the data can be seen, e.g. in the last six hours of the sampling period for tramadol.). The $EU_{\text{chem},i}$ flux of B-2-SA, similar to its $EU_{\text{chem},i}$, exhibited a different temporal pattern from the rest of the compounds that were activating the AhR at both MSs. In particular, the $EU_{\text{chem},i}$ flux of B-2-SA clearly peaked twice during our sampling period, and the modeled results at MS3 showed the largest deviation from the data in comparison to all other compounds approximately at midnight of August 21. Nevertheless, the modeled $EU_{\text{chem},i}$ fluxes were able to reproduce the key features in the observations for the detected compounds in AhR-CALUX, PPARγ-GeneBLAzer and AREc32 (Figure A.33 – Figure A.35). The model also performed well when applied to the cytotoxicity data. As

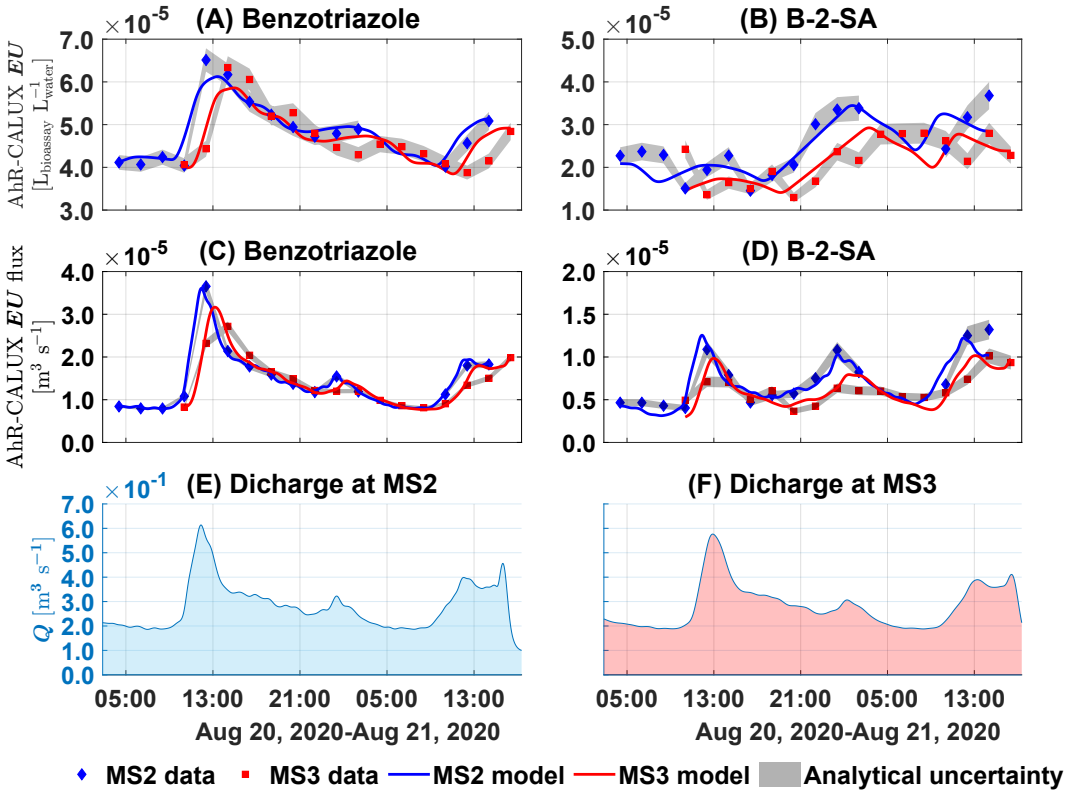

Figure 2.2: $EU_{\text{chem},i}$ (A) – (B) and $EU_{\text{chem},i}$ fluxes (C) – (D) of the two detected chemicals that were activated in AhR-CALUX. Each dot represents the mean value of this two-hour interval for which eight sub-samples were mixed. Analytical uncertainties (one standard deviation) originating from the concentration measurements are illustrated by the grey area. Discharges at MS2 and MS3 are shown in light blue and red areas, respectively. Three missing data points at MS2 were due to the malfunction of auto-sampler 2 between 03:30 and 07:30 on August 21, 2020. Abbreviations: B-2-SA – Benzothiazole-2-sulfonic acid; MS – Measuring station.

the $EU_{\text{chem},i}$ and $TU_{\text{chem},i}$ only differed by a scaling factor, the modeled time course of the $TU_{\text{chem},i}$ in six cell lines (AhR-CALUX, PPARγ-GeneBLAzer, ERα-GeneBLAzer, AREc32, AR-GeneBLAzer and GR-GeneBLAzer in Figure A.36 – Figure A.41) again were able to reproduce the main features of the individual compound's cytotoxicity time series. Similar results can be seen in the case of cytotoxicity fluxes (Figure A.42 – Figure A.47 , Table A.10). By applying the convolution-based transport model with the first-order reaction kinetics to the individual effects data, we demonstrated that the model was able to quantitatively characterize in-stream mechanisms of the individual effects.

Predicted mixture effects of bioactive chemicals (EU_{chem} and TU_{chem}). The detected bioactive chemicals are expected to contribute to the mixture effects that were measured in a water sample. However, this contribution is often very small, even if hundreds of chemicals are included in an analytical method (Neale et al., 2020), which means that the analysed chemicals are often not mixture effect drivers. Therefore we go stepwise from individual chemicals $EU_{\text{chem},i}$ to the mixture of detected chemicals EU_{chem} and address the experimental mixture effects EU_{bio} only in the next section. Regardless the goodness of the fit for the individual compounds, their contributions to the total effects EU_{bio} differ. Fig-

ure 2.3A – C display the percentages of the mean $EU_{\text{chem},i}$ of the individual micropollutants from MS1 over the whole sampling period.

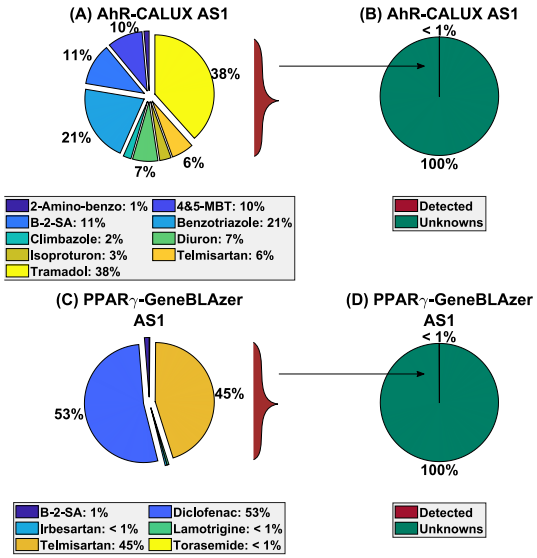

Figure 2.3: Contribution (%) of the mean effect units over the sampling period from individual micropollutants to the whole mixture at auto-sampler 1 for the bioassay AhR and PPARγ. (A) and (C): Contribution of individual micropollutants effects to EU_{chem}; (B) and (D): Contribution of all detected micropollutants to EU_{bio}; Abbreviations: 2-Amino-benzo – 2-Aminobenzothiazole; 4&5-MBT – 4&5 Methyl-benzotriazole; B-2-SA – Benzothiazole-2-sulfonic acid; Detected – Effect of all detected compounds; Unknowns – Effect of the non-detected compounds. Unit of EU: [$L_{\text{biosassy}} \cdot L_{\text{water}}^{-1}$]

Within the mixture effect EU_{chem} ($EU_{\text{chem}} = \sum_{i=1}^{n} EU_{\text{chem},i}$ (Eqs. 2.1 – 2.3)), the contributions from the individual compounds varied over different bioassays, but did not differ significantly between sampling locations. B-2-SA contributed a relatively large fraction of EU_{chem} in PPARγ-GeneBLAzer and AREc32, and tramadol in AhR-CALUX (full results can be found in Figure A.48 – Figure A.49.). In all three bioassays, the contribution of all detected and activated compounds (EU_{chem}) to the total effect (EU_{bio}) was less than 1% regardless of the locations (Figure 2.3B and D), indicating that the majority of the effects in EU_{bio} was contributed by the non-detected compounds. Neale et al., 2020 reported similar low fractions of explained effects in the same three bioassays in water samples from diverse rain events in rivers of similar size. They also mixed 17 chemicals that were deemed to be mixture effect drivers in 107 concentration ratios simulating the exact occurrence in the water samples and demonstrated an excellent agreement between the modeled EU_{chem} and the experiments with the designed mixtures $EU_{\text{bio,designed}}$ mixtures (Figure 5 in reference Neale et al., 2020). Hence, it is safe to assume that the EU_{chem} is indeed a good predictor of the true mixture effects of the quantified chemicals and the difference between EU_{bio} and EU_{chem} stems from unaccounted chemicals rather than non-additive and interactive mixture effects. The same holds for cytotoxicity, where the same mixtures tested as in Neale et al., 2020 also showed and excellent agreement between the modelled TU_{chem} and the experiments with the designed mixtures $TU_{\text{bio,designed}}$ mixtures (Escher et al., 2020).

In the case of cytotoxicity, no single compound showed the universal dominance at contributing individual effects ($TU_{\text{chem},i}$) to the mixture effects of the detected compounds (TU_{chem}) across all bioassays. The percentages of TU contributed by individual compounds

to TU_{chem} in AhR-CALUX, PPARγ-GeneBLAzer, ERα-GeneBLAzer, AREc32, AR-CALUX and GR-GeneBLAzer are shown in Figure A.50 – Figure A.52. Diclofenac, benzotriazole, sulpiride and terbutryn contributed the overall high percentages in PPARγ-GeneBLAzer, AR-CALUX, GR-GeneBLAzer and ERα-GeneBLAzer, respectively. In AhR-CALUX and AREc32, TU_{chem} was more evenly composed out of the effects of individual compounds. No significant spatial variations of the individual TU contributions were observed.

The time patterns of the mixture effects from all the detected and active compounds, EU_{chem} and TU_{chem} (Eqs. 2.3 – 2.4), were dominated by those compounds that contributed some of the largest shares of the effects in the mixture (Figure A.53 and Figure A.55). Similar to the individual effects, the dynamics of the fluxes (Figure A.54 and Figure A.56) were dominated by that of the discharge. Modeled flux results were able to reproduce the major features (e.g. the main peak caused by the WWTP's effluent sudden release) observed in the data from all three bioassays.

The total mixture effects (EU_{bio} and TU_{bio}) and fluxes. The measured time series and modeled time series ensemble of EU_{bio} in AhR-CALUX, PPARγ-GeneBLAzer, ERα-GeneBLAzer and AREc32 at MS2 and MS3 are shown in Figure A.57 – Figure A.58, respectively. The EU_{bio}, representing the total specific burden that resulted from all of the organic micropollutants in the water sample, displayed relatively high variations at certain time points, and unclear transport patterns along the river course (Figure 2.4). This is presumably because the discharge was not stable during the sampling period (Figure 2.1) and therefore the composition of the components triggering the mixture effect were highly variable. Similar to the $EU_{\text{chem},i}$ fluxes of the detected compounds, as well as the results from Müller et al., 2021 in storm events, in this study the observed fluxes of EU_{bio} were mainly dominated by the temporal patterns of the unsteady discharge (Figure 2.4). In all four bioassays, pronounced flux peaks were seen at around 12:00 on August 20. However, the individual temporal pattern in each bioassay could also be differentiated. In both PPARγ-GeneBLAzer and ERα-GeneBLAzer (Figure 2.4B – C), a pronounced drop of EU_{bio} flux could be observed at around 15:00. At the same time, the mean TU_{bio} flux also experienced the drop (Figure A.62), indicating that the observation could not have been caused by masking effect of the cytotoxicity. Furthermore, in comparison with the other three bioassays, the measured EU_{bio} fluxes in AREc32 (Figure 2.4D) could clearly be seen experiencing smaller temporal oscillations. Through MH-MCMC sampling, the convolution-based reactive transport model yielded the EU_{bio} fluxes ensemble after all chains converged, and the statistics of the modeled effect fluxes ensemble were computed. The means and three posterior intervals (PI) (68.27% PI = mean $\pm\,\sigma$; 95.45% PI = mean $\pm\,2\sigma$; 99.73% PI = mean $\pm\,3\sigma$) of the modeled EU_{bio} fluxes ensemble were depicted in Figure 2.4. The model ensemble was capable of capturing the main features of the flux dynamics mainly characterized by the transport (e.g., Figure 2.4A). ERα-GeneBLAzer and AREc32 (Figure 2.4C – D) showed relatively large outliers at certain time points. The input uncertainties that influence the characterizations of the dynamics were not included, which could explain the different dynamics for PPARγ-GeneBLAzer and AREc32 (Figure 2.4B and D). The poorest model fit was in the case of PPARγ-GeneBLAzer (Figure 2.4B). The observations in PPARγ-GeneBLAzer had the largest measurement standard errors. This resulted in limited learning from the data as seen from the similar prior and posterior distributions of the reaction rate constant (Figure A.65). The ensembles of EU_{bio} fluxes in the four bioassays at MS3 are displayed in Figure A.59.

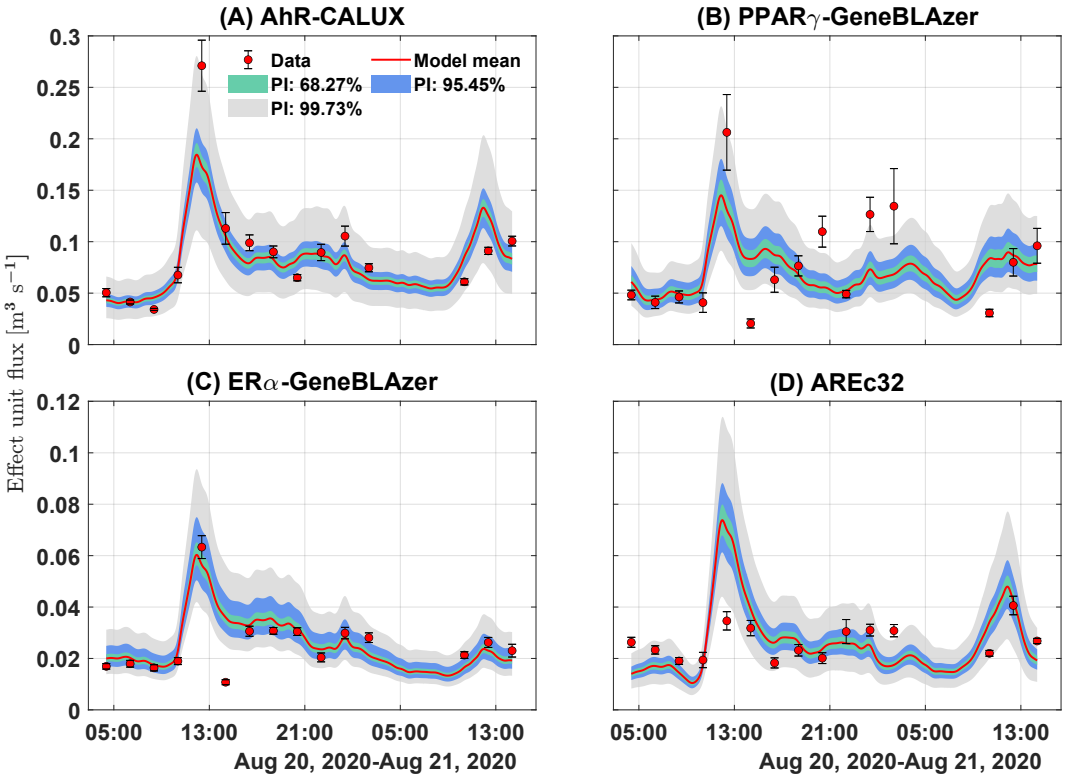

Figure 2.4: EU_{bio} fluxes ensemble of four cell lines at MS2. Ensemble was obtained through the posterior distributions of reaction rate constants sampled by Metropolis–Hastings Markov chain Monte Carlo (MH-MCMC) (Figure S64). Mean and three ranges of posterior intervals (PI) of the ensemble were computed (68.27% PI = mean ± σ; 95.45% PI = mean ± 2σ; 99.73% PI = mean ± 3σ). Analytical uncertainties (one standard error) are shown by error bars in red. Three missing data points at MS2 were due to the malfunction of auto-sampler 2 between 03:30 and 07:30 on August 21, 2020.

In the case of the toxic unit of the whole bioactive mixture (TU_{bio}), the measured TU_{bio} values in different bioassays should be relatively similar, since TUs are quantified based on the same endpoint, even in different bioassays. The model with Bayesian calibration was applied to the mean TU_{bio} (Section 2.2) measured in AhR-CALUX, PPARγ-GeneBLAzer, ERα-GeneBLAzer and AREc32. The modeled time course ensembles of TU_{bio} at MS2 and MS3 are plotted in Figure A.60 and Figure A.61, respectively, and show similar performance in terms of coverage as for EU, e.g., 11 out of the 15 observations at MS2 (Figure A.60) and 12 out of the 16 observations at MS3 (Figure A.61), considering the measurement errors, were in the 95.45% posterior interval of the model ensemble. Figure A.62 and Figure A.63 depict the modeled TU_{bio} flux ensembles. Similar to EU_{bio} flux, the modeled TU_{bio} flux ensembles were able to reproduce the flux peak in the data at both MS2 and MS3. The number of iterations the MH-MCMC took to converge for each bioassay data set are given in Figure A.64 - Figure A.71.

2.4.3 Sources of micropollutants

Effects comparison: upstream and downstream of the WWTP. The model performances vary for micropollutants that mainly stem from the WWTP and other potential

non-point sources. Thus, it is essential to characterize the sources for the micropollutant mixtures. The concentrations of all compounds in grab samples are given in Table A.3 and illustrated in Figure A.74. As expected the typical WWTP effluent substances were not detected at MS Up and MS Ehr, but could be found at MS Muehl and MS1. Still, atrazine-2-hydroxy, mecoprop, terbuthylazine-2-hydroxy and carbendazim were found at MS Up and MS Ehr. Additionally, atrazine, atrazine-desethyl, nicosulfuron, terbuthylazine and tebuconazole were also detected at MS Ehr (Table A.3). All of these compounds are either herbicides, herbicide metabolites or fungicides (Table A.1) that could come from other sources, e.g. agricultural fields during and after their application periods (Wittmer et al., 2010).

Figure 2.5 depicts the grab samples' EU of detected individual compounds (EU_{chem_i}), the mixture of all detected compounds (EU_{chem}) and the total mixture (EU_{bio}) quantified in PPARγ-GeneBLAzer. Results from AhR-CALUX and AREc32 are shown in Figure A.75

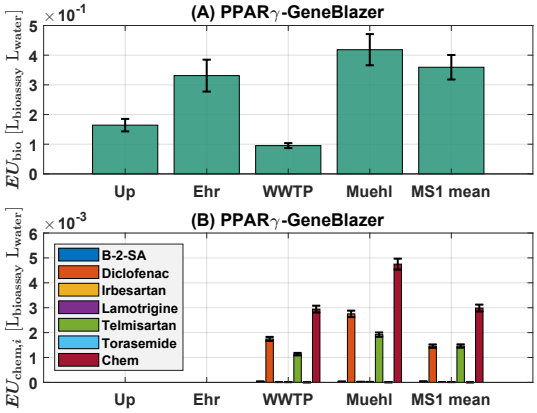

Figure 2.5: The effect units (EU) of grab samples: (A) Total mixture effect (EU_{bio}); (B) Individual effects $EU_{\text{chem},i}$; No grab samples were taken at MS2 and MS3. Measurement uncertainties (standard deviation) are shown by the error bars. Abbreviations: Ehr – Ehrenbach; Muehl – Mühlbach; B-2-SA – Benzothiazole-2-sulfonic acid; Chem – Effect units of the sum of detected bioactive compounds (Eq. 2.3).

Evidently there is a large difference in scale between EU_{bio} and EU_{chem} as shown in Figure 2.3 and discussed in this section. The non-detects in EU_{chem} at sites Up and Ehr while EU_{bio} were similar as for other sites are likely to be explained by chemicals causing the effect that were not included in the chemical analysis. EC_{10} values of individual compounds are in Table A.7 – A.8. At all sampling locations, 15 out of the 42 contaminants found in the grab samples showed at least one specific effect. Diuron, isoproturon, and tramadol were active in two of the three bioassays. 2-aminobenzothiazole and B-2-SA triggered specific effects in all three bioassays. At MS Up and MS Ehr, none of the detected compounds displayed any specific effects, indicating that at those two locations, the detected chemicals made no contributions to the EU_{bio}, in terms of triggering the modes of action quantified by AhR-CALUX, PPARγ-GeneBLAzer and AREc32. None of the target analytes activated ERα. EU_{bio} of grab samples in ERα-GeneBLAzer is shown in Figure A.76. At the same locations (MS Up and MS Ehr), the EU_{bio} from grab samples were also less than 0.01 (inverse of 100 REF) in AhR-CALUX, ERα-GeneBLAzer and AREc32, but activated effects in PPARγ-GeneBLAzer. Similar results can be found when looking at cytotoxicity. TU_{bio} of grab samples were quantified and above the limit of detection in AhR-CALUX,

PPARγ-GeneBLAzer, ERα-GeneBLAzer and AREc32 (Figure A.77 – Figure A.79). The total bioactive mixture from MS Up and MS Ehr showed cytotoxicity in all four bioassays.

EU_{bio} and TU_{bio} were measured at unexpectedly high values at locations upstream from the WWTP, indicating other non-point sources that contribute to the total mixture effects. PPARγ-GeneBLAzer, EU_{bio} from MS Up and MS Ehr were both higher than that from the WWTP effluent. However, considering the low discharge in Ehrenbach (0.001 – 0.002 m^3 s^{-1}) and Mühlbach (0.04 – 0.056 m^3 s^{-1}), the load of the chemicals and effects from the two tributaries are relatively low. In AhR-CALUX and PPARγ-GeneBLAzer, TU_{bio} from MS UP and MS Ehr were both higher than that in samples from WWTP effluent (Figure A.77). Oddly, in AREc32 and ERα-GeneBLAzer, the TU_{bio} of the WWTP effluent was less than 0.01. Still, in AREc32 and ERα-GeneBLAzer, TU_{bio} of MS Up and MS Ehr were measured at the same order of magnitude to that of measuring station Mühlbach (MS Muehl) and MS1.

The results suggest that micropollutants from MS Up and MS Ehr cannot activate the modes of action of aryl hydrocarbon receptor induction, estrogenicity and oxidative stress response. But even without the input from the WWTP, there are unknown chemicals in the river that are potent enough to activate the peroxisome proliferator–activated receptor activity, as well as cytotoxicity in AhR-CALUX, PPARγ-GeneBLAzer, ERα-GeneBLAzer and AREc32. The presence of unknown compounds triggering specific effects in PPARγ-GeneBLAzer as well as showing strong cytotoxicity in all four bioassays might be attributed to undetected biocide or pesticide diffusion. Previous studies (Wittmer et al., 2010; Munz et al., 2016; Chow et al., 2020) pointed out that biocides and pesticides from mixed lands and urban areas can enter rivers via pathways caused by rain events (e.g. dispersive losses and combined sewer overflows). Existing natural compounds in rivers may also activate effects in bioassays. Salam et al., 2008 and Rau et al., 2006 confirmed that strong PPARγ agonists can be from plants and herbs (e.g., psi-baptigenin and hesperidin), which were not on our list of target analytes (Table A.1). Further discussion on $TU_{\text{chem},i}$ of grab samples can be found in Appendix A.25).

From individual micropollutants to the total mixture: prior and posterior distribution of the reaction rate constants. The $EU_{\text{chem},i}$ observations from the individual micropollutants were illustrated together with EU_{bio} across all MSs in the main channel in Figure S80. Echoing grab samples shown in Figure 2.5, $EU_{\text{chem},i}$ at all three MSs were out-weighted by EU_{bio}. Corroboratory results were reported from numerous previous studies. (Escher et al., 2015; König et al., 2017; Neale et al., 2015, 2017, 2020) The potentially large number of none-detected micropollutants in the mixture were considered the main contributors to the total specific mixture effects.

Only a limited numbers of micropollutants in the mixture could be identified, for which the reaction rate constants could be quantified. Within Bayesian inference, the reaction rate constants of the effects of the total mixture (EU_{bio} and TU_{bio}) were treated as random variables. The posterior distributions of the random variables were quantified (1) based on previous knowledge of individual micropollutants that were possibly in the mixture (the prior), and (2) conditioning on the data (the likelihood). Prior and posterior distributions of reaction rate constants for EU_{bio} and mean TU_{bio} are given in Figure A.64 – Figure A.73.

2.5 Implications

There is a lack of mechanistic models applied to study the process of the micropollutant mixture effects in rivers. We extended the 1D advection-dispersion-reaction equation from single micropollutants to the measured mixture effects, quantitatively studying the in-stream processes of the mixture effects. We demonstrated that the computationally cheap convolution-based reactive transport model can be applied not only to simulate the effects of a large number of individual compounds detected in the mixture, but also to be coupled with stochastic methods to provide quantitative insights of the fate of the overall mixture effects.

Different transfer functions can be tested so that more insights about the process of the mixture effects in different systems (e.g., on suspended particles) can be provided. Time dependent parameters can also be included, for instance, when modeling transient source(s) from tributaries during rain events, even in the stochastic processes (e.g. with hierarchical modeling). A next step should be to test if this approach can also be applied to the micro-pollutant mixture effects during storm events, including the micropollutant effects associated with river sediments.

Chapter 3

Modeling the processes and dynamics of the mixture effects of organic micropollutants in a small river during a storm event

Abstract

The threat to river water quality posed by the cumulative mixture effects from micropollutant mixtures is potentially elevated by rain events, which supply various routes for micropollutants to enter rivers. The in-stream processes of the mixture effects during rain events are not fully understood. In the present study, the mixture effects in the solid-phase extraction extracts from water collected during a storm were quantified in *in vitro* bioassays, and were expressed as effect units (EU) for activation of the arylhydrocarbon receptor (AhR-CALUX) or oxidative stress response (AREc32) and toxic units (TU) for cytotoxicity in both cell lines. We sought to quantitatively understand the in-stream processes of the mixture effects in rain events and addressed the following challenges. The measured EU/TU time-series signals exhibit complex temporal patterns. During the storm, point sources (e.g., wastewater treatment plants) and inputs from the transient lateral influxes were included. The discharge in the river channel becomes highly transient, causing the reactive transport process parameters of the solute to be time-dependent. Hypothesizing the transient discharge plays the role of the source term for the mixture effects, we simulated the discharge during a storm separately from the mixture effects using a flood routing (diffusive wave) model. Hypothesizing the in-stream processes for EU/TU are transient advection and dispersion, local equilibrium sorption and the source term that is proportional to the transient discharge, a one-dimensional transient reactive transport model was applied to simulate the in-stream dynamics of mixture effects data (AhR-CALUX and AREc32). We addressed the uncertainty in the temporal patterns of the mixture effects stochastically, e.g., treating model boundary and initial conditions as random variables. Gaussian process regression (GPR) and its conditional realizations were used to mimic all plausible temporal patterns of the model inflow boundary conditions. In this way, we could efficiently compute ensemble time-series output of mixture effects using a relatively computationally heavy transient model with deterministically calibrated pa-

rameters. The modeled ensemble output effectively reproduced the complex dynamics of the measured EU/TU and their fluxes. The results in return verified our parameterization for the transient in-stream processes influenced by the diffusive wave transient discharge. GPR proved to be a robust non-parametric approach to approximate the temporal dynamics of the mixture effects, as well as to construct the mixture model's inflow boundary conditions. Our results showed that the storm-caused transient discharge played a vital role in characterizing the advective and dispersive transport processes for the mixture effects by directly influencing the velocity with which the mixture effects travel in the river. Besides the WWTP as a point source, the storm introduced the lateral inflow into the river that functioned as a lateral inflow-proportioned source for the mixture effects along the river course. The mass conservation nature of the mixture effects in a transient system demonstrated the prospect of using the mixture effects as the state variable suitable for parameterizing more complex process-based models, e.g., coupling transport processes in rivers with hyporheic exchange.

3.1 Introduction

Rain events play a unique role at introducing anthropogenic organic micropollutants into rivers. The classic point-sources, e.g., wastewater treatment plants (WWTPs) are no longer the only major entry points for micropollutants to enter the water body (Spahr et al., 2020). Lateral influxes from, e.g., surfaces runoff (urban (Dittmer et al., 2020) and farmlands (Neumann et al., 2002)), and combined sewage overflow (Launay et al., 2016), provide an equally significant and dispersive entry route that is often spatially distributed along river channels. The highly dynamic nature of rain events leads the overall input of micropollutants into rivers, as well as their in-stream reactive transport processes to be transient.

Investigating the mixture effects of micropollutants, particularly quantifying the specific mixture effects and cytotoxicity using *in vitro* bioassay, complementary to chemical analysis (König et al., 2017; Lee et al., 2022), offers a new perspective of studying river water quality (Escher et al., 2021). The mixture effects, such as effect unit (EU), EU_{bio}, and toxic unit (TU), TU_{bio}, are quantified as concentration equivalent (Escher et al., 2018, 2021). To quantitatively describe the in-stream processes of the mixture effects from a mass-balance point of view, we extended the advection-dispersion-reaction equation (ADR) from a single micropollutant to the mixture effects, applying a one-dimensional reactive transport model in the convolution form to EU_{bio} and TU_{bio} data that was collected during unsteady flow conditions (Wei et al., 2022). The results confirmed the ADR was valid for characterizing the in-stream processes of the mixture effects under unsteady flow conditions.

The convolution-based reactive transport model could hold in the transient state only if certain conditions (e.g., small time scale of flow velocity) are met (Boudreau, 1997; Cirpka et al., 2007). During heavy rain events, the velocity with which the solutes travel becomes highly transient as a result of the changing discharge and the cross-sectional areas of the river channel over time. The transient velocity also affects the dispersion process, of which the longitudinal dispersion coefficient is linearly scaled to the velocity (Mellage et al., 2022; Störiko et al., 2022; Wang et al., 2022). To parameterize the transient lateral influxes into such complex system, the partial differential equation (PDE)-based transient models, although suffering from relatively higher (than the convolution-based model) computational costs, have the advantage of explicitly expressing the complex processes. The rates defined inside the PDE-based models have physical meanings and could be easily coupled with

time-dependent parameters, which could be determined by fitting the model results to the observations and evaluating the goodness of the fit when they are difficult to measure directly.

In the current study, we faced certain challenges when applying the PDE-based transient models to mixture effects. Informative data acquisition is limited by logistic capacities in the field during rain events. The highly transient features of the system we are trying to highlight could happen in short period which requires high frequency sampling at each location. In practise considering the coarse temporal resolution of the sampling scheme and the measurement errors, a single interpolated result from the time-series observations of the mixture effects could not robustly approximate the real-world temporal patterns of the signal. When using such interpolated result as either model input or observations for parameter estimates, it produces unsatisfying modeled results and misleads the understanding of the internal processes.

We sought to understand the dynamics of the mixture effects during rain events from three quantitative perspectives: 1) explicitly expressing the transient in-stream processes that govern the dynamics of the mixture effects during rain events; 2) robustly characterizing the mixture effects time-series signals; 3) efficiently computing the ensemble output from the transient model to reproduce the complex dynamics in the measurements. We applied the transient models to the mixture effects data from the river water samples collected during a storm event using Lagrangian sampling scheme (Schwientek et al., 2016; Guillet et al., 2019) (sampling details in Glaser et al., 2020). The potential sources of the individual micropollutants and the mixture effects, their complex portion of contributions to the system during this storm event, as well as the impact of different endpoints of mixture effects with respects to river water quality were discussed provided by Müller and colleagues (Müller et al., 2021) (providing data for current study), thus they are not part of the discussion in the current study. We simulated the transient discharge using the general Hayami flood routing model (Moussa, 1996) including a uniformly distributed lateral inflow over the domain. The lateral inflow was computed via convolution of effective precipitation and the transfer function with gamma distribution shape. Taking the simulated transient discharge in computing the flow velocity, we implemented a deterministic one-dimensional PDE-based transient reactive transport model for the mixture effects dynamics, for which the reaction terms we considered a transient first-order source term and local equilibrium for the sorption process. To approximate the temporal patterns of mixture effects as robustly as possible, we introduced stochastic elements into the model by treating the time-series input as random variables. We used the Gaussian process regression (GPR) (Schulz et al., 2018) to compute the posterior of the random variable input. The conditioned realizations from the posterior were used as the mixture model input enabled PDE model to generate ensemble output. We simulated the spatial and temporal dynamics of the EU, the EU flux, the TU and the TU flux. The EU and TU were quantified in two *in vitro* bioassays (AhR-CALUX (Brennan et al., 2015) and AREc32 (Wang et al., 2006)). Our combined approach presented a robust characterization of the mixture effects time-series, offering an efficient way to compute ensemble results through deterministic parameter values while explicitly expressing the transient physical processes for the mixture effects.

3.2 Methods & Theory

3.2.1 Underlying data acquisition

In current study, all time values are expressed as durations in hours. Exceptions are the ones explicitly written as clock time in ISO 8601 format. All clock time was in CEST.

Field campaign. The underlying sampling campaign took place in July 2019 in the Ammer River, Baden-Württemberg, Germany. The study segment is approximately 8 km long, starting at 4 km downstream of Herrenberg, ending in Pfäffingen. Two autosamplers (AS) were installed at the beginning (MS1) and the end (MS2) of the segment to collect composite time-series samples (30-minute temporal resolution). Figure B.1 shows the sampling map. AS 1 sampled from 2019-07-27 19:09 to 2019-07-28 09:00. AS 2 sampled from 2019-07-27 20:03 to 2019-07-28 10:00. One conductivity-temperature-depth diver (CTD) was installed at each MS. CTD 1 (at MS1) recorded from 2019-07-27 00:00 to 2019-07-28 09:00. CTD 2 (at MS2) started at the same time as CTD 1 and stopped at 2019-07-28 11:00. All time was in central European summer time (CEST). The CTD measurement temporal resolution was 15 minutes. Measured water depth was converted to discharge using a rating curve (Eq. B.1). Precipitation data (1-hour resolution) was obtained from three weather stations in Herrenberg (https://opendata.dwd.de/climate_environment/CDC/observations_germany/), Unterjesingen and Bondorf (https://www.wetter-bw.de/Internet/AM/NotesBwAM.nsf/). The mean precipitation of the three stations was used to compute lateral inflow (Eq. 3.5). The detailed sampling procedure can be found in Glaser et al., 2020. Figure 3.1A shows the inflow signal and lateral influxes entering the domain during the storm. The river channel geometry is shown in Figure 3.1B.

Laboratory work. The dissolved phase enriched extracts were obtained by solid phase extraction and were analysed with two *in vitro* bioassays named AhR-CALUX for aryl hydrocarbon receptor induction (Brennan et al., 2015) and AREc32 for oxidative stress (Escher et al., 2013). Detailed description of chemical analysis of the micropollutants and mixture effects measurements can be found in the work done by Müller et al..

Effect unit and toxic unit. The specific effects (e.g., activation of the AhR, triggered by binding of chemicals to the arylhydrocarbon receptor (Escher et al., 2021).) and cytotoxicity in the river water, stemming from the micropollutants contributed mainly by WWTPs, were quantified in *in vitro* bioassays and expressed as effect unit (EU) (Müller et al., 2018) for specific effects and toxic unit (TU) (Müller et al., 2018) for cytotoxicity. Both EU and TU can be used to characterize the experimentally determined mixture effects (EU_{bio} and TU_{bio}).

The EU and TU describing the mixture effects of the whole water sample, EU_{bio_j} [$L_{\text{bioassay}} \cdot L_{\text{water}}^{-1}$] and TU_{bio_j} [$L_{\text{bioassay}} \cdot L_{\text{water}}^{-1}$], are defined in Eqs. 3.1 – 3.2,

$$EU_{\text{bio}_j} = \frac{1}{EC_{k,\text{assay}_j}} \tag{3.1}$$

$$TU_{\text{bio}_j} = \frac{1}{IC_{k,\text{assay}_j}} \tag{3.2}$$

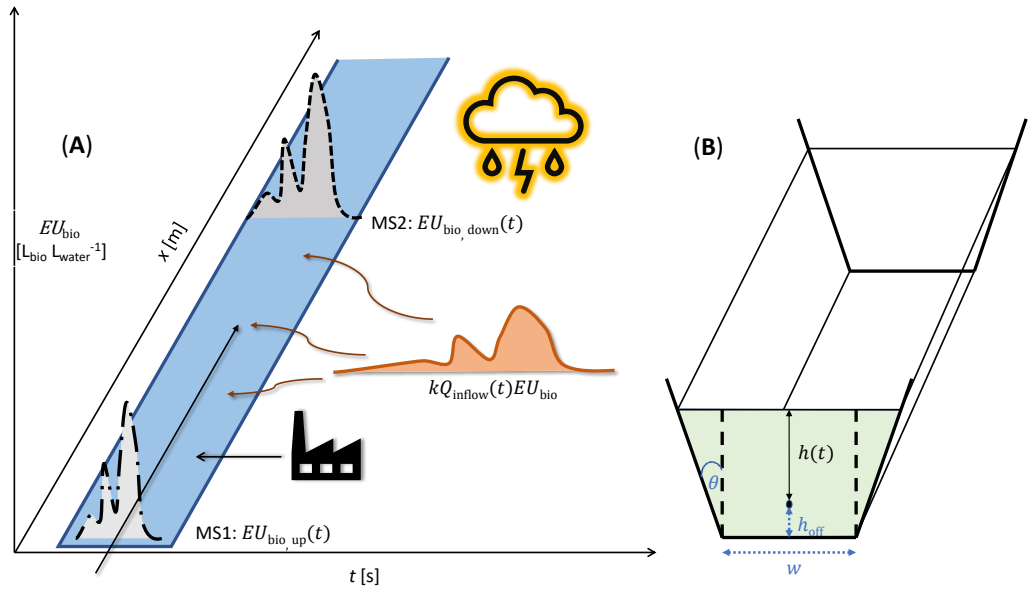

Figure 3.1: Schematic of the study setup. (A): The EU_{bio} time-series signal traveled from MS1 to MS2. The orange transient influxes were caused by the storm. We assumed the influxes to be uniformly distributed along the river. (B): River channel geometry. The cross-sectional area of the channel was assumed to be isosceles trapezoidal. Variables in blue were estimated. Abbreviation: MS-measuring station.

where EC_{k,assay_j} and IC_{k,assay_j} are the effect concentration (EC) (Müller et al., 2018) and and inhibition concentration (IC) (Müller et al., 2018) of the whole water sample that trigger k effects (typically k is 10% of the maximum effect (Escher et al., 2015; Jia et al., 2015) or the induction ratio of 1.5 (Müller et al., 2018; Escher and Neale, 2021) and cytotoxicity, respectively in assay j. The units of EC and IC are relative enrichment factor (REF [$L_{water} \cdot L_{bioassay}^{-1}$]) (Escher et al., 2021; König et al., 2017). For TU of the whole bioactive mixture (TU_{bio}), the measured TU_{bio} values in different bioassays are relatively similar (Wei et al., 2022), since TUs are quantified based on the same endpoint (cell viability (Escher et al., 2021). Therefore, we used the mean TU_{bio} values for modeling.

Effect unit and toxic unit fluxes. The fluxes $F_k(t)$ of the EU ($k = EU_{bio\,j}$) and the TU ($k = TU_{bio\,j}$) are defined by the products of the effect units and toxic units, respectively, with the corresponding discharge (Q in [m^3 s^{-1}]) at time t (Eq. 3.3. EU is replaced by TU when computing the cytotoxicity flux).

$$F_k(t) = EU_k(t) \cdot Q(t) \tag{3.3}$$

3.2.2 Discharge model

During the storm, a discharge wave was formed in the river channel and propagated downstream in the study segment. For the natural channel flood routing modeling, the full one-dimensional Saint-Venant equations (Beg et al., 2022) can be simplified in the momentum equation in practice, leaving the system to be characterized by a diffusive wave (Fan and Li, 2006). The high precipitation also created transient lateral inflow into the river channel (Sun et al., 2023). Assuming the lateral inflow is uniformly distributed along the river

course, we implemented the model proposed by Hayami 1951 and Moussa 1996 to simulate the discharge under such conditions (Eq. 3.4),

$$Q_{\text{down}}(t) = Q_{\text{up}}(0) + Q_{\text{inflow}}(0) + \frac{C}{L}\int_0^t [Q_{\text{inflow}}(\lambda) - Q_{\text{inflow}}(0)]\, d\lambda + \frac{L}{2\pi D^{1/2}} \exp\left(\frac{CL}{2D}\right) \int_0^t \left[Q_{\text{up}}(t-\tau) - Q_{\text{up}}(0) - \frac{C}{L}\int_0^{t-\tau} [Q_{\text{inflow}}(\lambda) - Q_{\text{inflow}}(0)]\, d\lambda\right] \cdot \frac{\exp\left[-\frac{CL}{4D}\left(\frac{L}{C\tau} + \frac{C\tau}{L}\right)\right]}{\tau^{3/2}} d\tau \tag{3.4}$$

where Q_{down} [$m^3\ s^{-1}$] and Q_{up} [$m^3\ s^{-1}$] are the discharge at the upstream and downstream locations in the river channel, respectively. Q_{inflow} [$m^3\ s^{-1}$] is the lateral inflow caused by the high precipitation. C [$m\ s^{-1}$] is the celerity. D [$m^2\ s^{-1}$] is the longitudinal dispersion coefficient. L [m] is the length of the study river segment. t [s] is the sampling time point. A rating curve (Eq. B.1) was used to convert measured water depth [m] to discharge, which was used as model input and data for calibration.

The lateral inflow was approximated via convolution of effective precipitation and transfer functions. We implemented the convolution model suggested by (Aron and Borrelli, 1973), which predicts stream base flow by convoluting the effective rain fall $I(t)$ [$m^3\ s^{-1}$] (Eq. 3.5). Effective rain fall I is the precipitation [$mm\ h^{-1}$] (data source in Section 3.2.1) multiplied by the catchment area [km^2] (134 km^2 (Glaser et al., 2020)). k [-] ($k \in [0, 1]$) is the coefficient describing the fraction of lateral inflow that goes into the study river segment.

$$Q_{\text{inflow}}(t) = k \int_0^t I(t-\tau) q(\tau) d\tau \tag{3.5}$$

We tested two transfer functions suggested by Aron and Borrelli, 1973 for $q(t)$ to compare the modeled $Q_{\text{down}}(t)$. The first transfer function is a gamma distribution (Eq. 3.6),

$$q(t) = \frac{1}{\Gamma(\beta)\alpha^\beta} t^{\beta-1} \exp\left(-\frac{t}{\alpha}\right) \tag{3.6}$$

where α [s] and β [-] are the rate and shape parameter, respectively. The second transfer function (Eq. B.2) contains only one lumped parameter R [$s^{-1/2}$]. Eq. 3.6 was chosen because it yielded better results when coupled with Eqs. 3.4 – 3.5, and the original expression of R in Eq. B.2 includes field parameters such as soil transmissivity and specific yield (Naney et al., 1978) that are cumbersome to obtain. Modeled discharge results from the two transfer functions are in Section 3.3.1 and Appendix B.3. D, C, k, α, and β are parameters to be estimated (Section 3.2.6).

3.2.3 Transport model: turbidity

The turbidity was used as conservative tracer to estimate hydrological parameters in the study domain. N is turbidity [NTU]. We considered the in-stream transport of the turbidity was governed by the one-dimensional transient advective-dispersive transport model (Eq. 3.7),

$$\frac{\partial N}{\partial t} = -v(t)\frac{\partial N}{\partial x} + D(t)\frac{\partial^2 N}{\partial x^2} + k_{\text{turb}} \cdot Q_{\text{inflow}}(t) \cdot N \tag{3.7}$$

where $k_{\text{turb}} \cdot Q_{\text{inflow}}(t) \cdot N$ is the transient source term that represents the turbidity brought into the domain by the uniform lateral inflow. k_{turb} is the first-order increase constant [m^{-3}]. $Q_{\text{inflow}}(t)$ is the lateral inflow (Eq. 3.5) [$m^3\ s^{-1}$].

The transient velocity $v(t)$ was computed by dividing $Q(t)$ (Eq. 3.4) by the cross-sectional area $A(t)$, which we considered a isosceles trapezoidal shape that was defined by Eq. 3.8,

$$A(t) = \frac{2[h(t) + h_{\text{off}}] \cdot \tan(\theta) + w}{2} \cdot [h(t) + h_{\text{off}}] \tag{3.8}$$

where $h(t)$ [m] is the measured water level (15-minute temporal resolution) at time t, h_{off} [m] the water level offset, w [m] channel bottom width and θ the bank slope in degrees. The hydrodynamic dispersion coefficient D [$m^2\ s^{-1}$] is linearly scaled to v in Eq. 3.9 (Wang and Cirpka, 2021; Störiko et al., 2022; Wang et al., 2022),

$$D(t) = \alpha_{\text{L}} \cdot v(t) \tag{3.9}$$

where α_{L} is the longitudinal dispersivity [m]. α_{L}, w, h_{off}, θ and k_{turb} were hydrological parameters to be estimated (Section 3.2.6), which are later used in the reactive transport model for the mixture effects (details in Section 3.2.4).

3.2.4 Reactive transport model: mixture effects (EU_{bio})

We applied the one-dimensional transient reactive transport model to the effect unit in dissolved phase (EU_{bio}). To represent the lateral inflow process under uniform but transient flow, the first-order transient source term was added. To account for sorption, we assumed the local equilibrium (Liu et al., 2021). The governing equation of EU_{bio} is expressed by Eq. 3.10 (EU was replaced by TU when modeling the cytotoxicity),

$$R \cdot \frac{\partial EU_{\text{bio}}}{\partial t} = -v(t)\frac{\partial EU_{\text{bio}}}{\partial x} + [D(t) + D_{\text{spec}}] \cdot \frac{\partial^2 EU_{\text{bio}}}{\partial x^2} + k_{\text{source}} \cdot Q(t) \cdot EU_{\text{bio}} \tag{3.10}$$

where D_{spec} [$m^2\ s^{-1}$] the EU_{bio} specific dispersion coefficient, k_{source} [m^{-3}] the increasing coefficient, and R [-] the retardation factor. k_{source} and R are assay specific parameters to be estimated (Section 3.2.6). Eq. 3.7 and Eq. 3.10 were spatially discretized using finite difference method (Noye and Tan, 1989) and solved using *ode15s* (Shampine and Reichelt, 1997) in MATLAB.

3.2.5 Model input characterization

Inflow input characterization: Gaussian process regression. The measured time-series signals at measuring station 1 (MS1) were used as model inflow input. In reality, the measurements often contain missing sample points. The sampling temporal resolution (30-minute) is relatively coarse over the sampling period (3.5-hour). The uncertainties in the measurements affect our understanding of the true dynamics of the signal. Considering those factors, a single interpolated time-series from the measurements is not a robust characterization of the real-world temporal patterns, let along being used as inflow boundary conditions (Dirichlet boundary conditions). The Gaussian process regression (GPR) (Schulz et al., 2018), which includes measurement errors into its covariance matrix, was applied to compute the posterior distribution of the time-series signals, e.g. EU_{bio}, that

are functions of time $\boldsymbol{t}$. All the 'possible' functions form a multivariate normal distribution with mean $\mu(\boldsymbol{t})$ and covariance matrix Σ (Eqs. 3.11 – 3.12).

$$\boldsymbol{EU}_{\text{bio, MS1}} = f(\boldsymbol{t}) \sim \mathcal{N}(\mu(\boldsymbol{t}), \Sigma) \tag{3.11}$$

$$\Sigma = \begin{bmatrix} \boldsymbol{k}_{11} & \boldsymbol{k}_{12} \\ \boldsymbol{k}_{21} & \boldsymbol{k}_{22} \end{bmatrix} \tag{3.12}$$

$\boldsymbol{t}_1$ is the time points of the observations, the measurement errors ($\boldsymbol{\sigma}_\epsilon$) are passed into the training process by Eq. 3.13,

$$k_{11} = \text{cov}(\boldsymbol{t}_1, \boldsymbol{t}_1) + \boldsymbol{\sigma}_\epsilon^2 \boldsymbol{I} \tag{3.13}$$

where $\boldsymbol{I}$ is an identity matrix. The covariance $\boldsymbol{k}$ is computed by the squared exponential kernel function (RBF kernel) (Eleftheriadis et al., 2017), of which the hyperparameters were optimized by *fitrgp* (Khuwaileh and Metwally, 2020; Rasmussen and Williams, 2006) in MATLAB. The n [-] number of realizations of the ensemble were used as model inflow input (Eq. 3.14).

$$\boldsymbol{EU}_{\text{bio, MS1}} \approx \{\boldsymbol{EU}^1{}_{\text{bio, MS1}}, \boldsymbol{EU}^2{}_{\text{bio, MS1}}, \dots, \boldsymbol{EU}^{\text{n}}{}_{\text{bio, MS1}}\} \tag{3.14}$$

Initial conditions characterization. With n [-] number of realizations used as the inflow boundary conditions (Eq. 3.14), the equal n [-] number of the initial conditions, $\boldsymbol{EU}_{\text{bio, initial}} \approx \{\boldsymbol{EU}^1{}_{\text{bio, initial}}, \boldsymbol{EU}^2{}_{\text{bio, initial}}, \dots, \boldsymbol{EU}^{\text{n}}{}_{\text{bio, initial}}\}$, were needed at each spatially discretized node. $\boldsymbol{EU}_{\text{bio, initial}}$ was treated as a random variable characterized by an estimated mean value ($\overline{EU}_{\text{bio, initial}}$) (Section 3.2.6) and the error term (Eq. 3.15).

$$\boldsymbol{EU}_{\text{bio, initial}} = \overline{EU}_{\text{bio, initial}} + \mathcal{N}(0, 0.04 \cdot \overline{EU}^2_{\text{bio, initial}}) \tag{3.15}$$

The error term was characterized by a normal distribution centered at 0 with a standard deviation of 20% of $\overline{EU}_{\text{bio, initial}}$.

3.2.6 Parameters estimation: Deterministic method

The discharge, turbidity and mixture effects models (Eqs. 3.4 – 3.10 and 3.15) were calibrated using a nonlinear least-squares solver, for which the objective function is defined in Eq. 3.16,

$$\arg\min_{\boldsymbol{\theta} \in R} F(\boldsymbol{\theta}) = \sum_{i=1}^{n} \left[f_i(\boldsymbol{\theta}, x) - y_{\text{obs},i}(x) \right]^2 \tag{3.16}$$

where $\boldsymbol{\theta}$ is the parameter vector; $y_{\text{obs,i}}$ the ith observations; f_i the modeled result cooresponding to $y_{\text{obs,i}}$; x the spatial coordinate. *lsqnonlin* algorithm (trust-region-reflective searching method (Liu et al., 2020) in MATLAB was used to find the optimal parameter values. The mean Normalized root-mean-square error (NRMSE) was computed for each compound to evaluate the goodness of the ensemble model fit (Eqs. 3.17 – 3.18),

$$\overline{\text{s}_i} = \frac{\sum_{j=1}^{m} (y_{\text{model},i,\,j} - y_{\text{obs},i,\,j})^2}{m} \tag{3.17}$$

$$\text{NRMSE} = \frac{\sqrt{\sum_{i=1}^{n} (\overline{\text{s}_i})/n}}{y_{\text{obs,max}} - y_{\text{obs,min}}} \tag{3.18}$$

where m and n are the number of realizations and observations, respectively; i and j the realization and observation indices, respectively.

3.3 Results & Discussion

3.3.1 The discharge

A nine-hour long rain event was first recorded on 2019-07-26 at approximately 20:00 by the Bondorf weather station (peaked at 6.5 mm h^{-1}) and 21:00 by the Unterjesingen weather station (peaked at 8.9 mm h^{-1}). Afterwards the rain winded down for about nine hours. A sudden high precipitation was recorded at 20.4 mm h^{-1} on 2019-07-26 at 20:00 by the Herrenberg station. The two rain events caused the formation of a discharge peak in the study river segment by introducing storm water and lateral inflow into the system. The lateral inflow contains contributions from dispersive paths (the uniform lateral inflow in Eq. 3.4), e.g., groundwater, soil water, surface run-off and tributaries (Kazezyilmaz-Alhan et al., 2007; Sun et al., 2023) input after the raining period, all of which acted as the transient source to the discharge in the study segment. The modeled lumped lateral inflow using the transfer function Eq. 3.6, and downstream (MS2) discharge are in Figure 3.2A. The modeled lateral inflow (Eq. 3.5) showed a smooth and matching peak

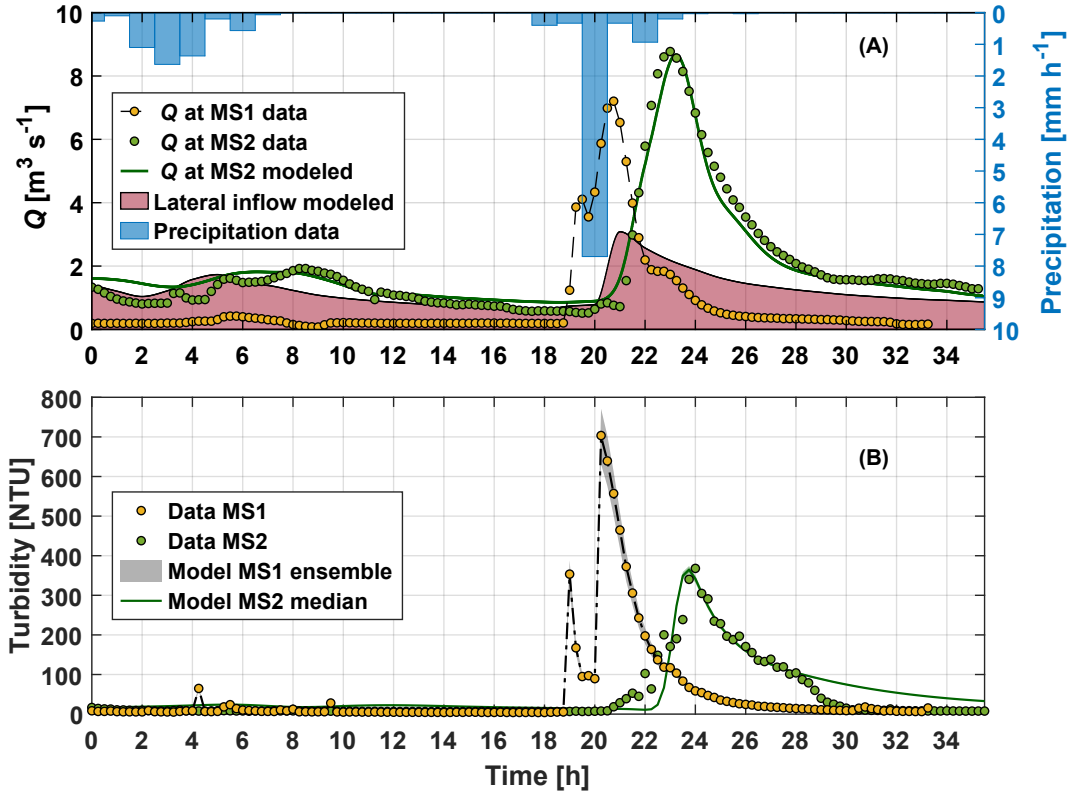

Figure 3.2: Discharge and turbidity dynamics. (A): The modeled discharge at MS2 shown in green. The early peaks of the modeled lateral inflow (red area) were contributed by base flow from the groundwater and surface runoff from the tributaries. Precipitation is shown in blue in bars. (B): The modeled turbidity at MS2 shown as a green curve. Abbreviation: MS-measuring station. The experimental data was reprinted from Glaser et al..

response to the precipitation, whereas using Eq. B.2, the modeled lateral inflow showed unrealistically oscillating temporal patterns without a peak in Figure B.3, although the peak existed in the input precipitation. As a result, the modeled MS2 discharge showed a

very good fit to the observations by matching the travel time of the peak, and catching the tail of the data (NRMSE = 0.043). The increase of the discharge at MS2 was also captured by the zeroth-order transient source term in the model. The modeled peak of the lateral inflow at around 20.5th hour was earlier than the discharge peak (22nd hour) at MS2. This can be explained by the existence of multiple tributaries between the two MSs, of which the input would cause the earlier peak in the lateral inflow. We also tested using Eq. B.2 in the model. Although Aron and Borrelli, 1973 concluded that Eq. B.2 worked better at predicting run-offs caused by precipitations, in our case the results were less satisfactory (Figure B.3). This is potentially due to the lack of direct measurement of the field specific parameters for the lumped parameter R in Eq. B.2.

3.3.2 The turbidity

The turbidity time-series signals were assumed to serve as a conservative tracer, from the hydrological parameters were estimated. The model (Eq. 3.7) considering the processes of the transient advection, dispersion and the lateral inflow source term was able to capture the dynamics of the observations well. Figure 3.2B illustrates the modeled turbidity time-series. The earlier and smaller curve at MS1 was smoothed out at MS2 due to the transient advection and dispersion. The model was able to sufficiently reproduce the downstream turbidity dynamics by matching the peak of the curve at 24-hour, as well as the initial tailing of the curve after the peak ($\overline{NRMSE}$ = 0.088). The calibrated parameter values are summarized in Table 3.1. We used the turbidity signal to estimate the hydrological parameters because the turbidity signal was only introduced into the system during the storm, functioning as the injection of a tracer. Thus, the time-series signal at MS1 could be used to formulate the model boundary condition. The electrical conductivity (ECd) also has been used as a conservative tracer (Cirpka et al., 2007; Glaser et al., 2020; Guillet et al., 2019) in practice. However, in our study site (Figure B.1), there were two WWTPs and multiple tributaries in between the two measuring stations and no time-series measurements were conducted at those sites. Figure B.2B shows that the ECd at MS2 was uniformly higher than that at MS1 through the whole sampling period, as well as a disrupted transport pattern (delayed arrival time of the peak), indicating the constantly high impact from WWTPs. During the storm period, the transient lateral influxes from non-point sources also played a role in shaping the ECd signal. Additional (however hidden) processes needed to be parameterized into the model (Eq. 3.7) to describe such a complex system. The informative boundary condition for the ECd required mixing signals from MS1 and WWTPs. No time-series sampling was conducted at those sites. Without observations, especially at the two WWTP outlets where the ECd was highly impacted by their release, it is difficult to construct informative boundary conditions for the model. Thus, the turbidity signal was deemed to be more representative to characterize the hydrological patterns of the conservative solutes and to estimate the transport parameters.

Although ECd in our study was not an ideal conservative tracer, we still applied a conservative transient transport model. Details are in Appendix B.5. Modeled ECd results are in Figure B.6. The GPR was applied to the turbidity time-series data at MS1 (yellow dots in Figure 3.2B) to compute the posterior (grey area in Figure 3.2B). The individual realization was sampled from the posterior and used as the model input (Section 3.3.3). Time-series observations of turbidity, electrical conductivity and discharge are shown in Figure B.2 (reprinted from Glaser et al..).

3.3.3 Ensemble model input

Time-series signals & Ensemble inflow boundary conditions. The measured EU_{bio} at MS1 was deemed to be the input (inflow boundary condition) for the transient reactive transport model (Eq. 3.10). The dynamics of the inflow signal strongly influence that of the model output. A single interpolated time-series signal, without including the uncertainties (i.e., the measurement errors) is not able to represent the underlying dynamics as robustly as possible. By treating the time-series as random variables, we introduce a stochastic perspective in constructing the model boundary conditions. The signal's dynamics were presented by the ensemble (the posterior distribution) obtained through the Gaussian process regression (GPR). Figure 3.3 illustrates the EU_{bio} ensemble in water phase from AhR-CALUX (Figure 3.3A) and AREc32 (Figure 3.3B) at MS1. The mean and 95% pos-

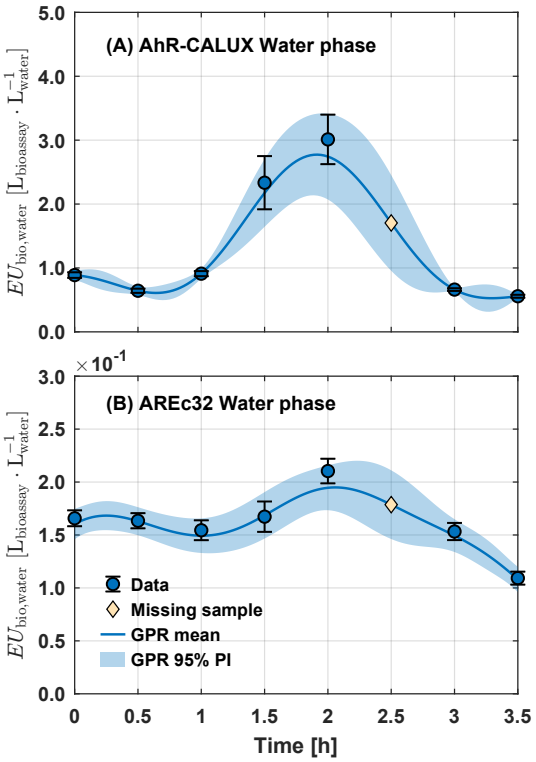

Figure 3.3: Time-series signal of EU_{bio} in the water phase (A) $EU_{bio,\,AhR}$ [$L_{bioassay} \cdot L_{water}^{-1}$], (B) $EU_{bio,\,AREc32}$ [$L_{bioassay} \cdot L_{water}^{-1}$] at MS1. Signal ensemble (characterized by mean and PI) was obtained through the posterior distribution computed by GPR. The realizations of the posterior were used as model input. Error bars represent the measurement errors. Abbreviation: GPR–Gaussian process regression; PI–posterior interval.

terior interval were used to represent the posterior distribution, of which the realizations were used as model input. Figure B.7 shows 100 realizations. In this way, in contrast to fully believing in a single time-series, the dynamics of the signal were characterized in a more robust way by including the measurement errors into the covariance matrix of GPR for uncertainty quantification, and presenting the possible outcomes according to the respective probabilities. By using an ensemble time-series input, the model also generates an ensemble time-series output.

Characterization of the initial mixture effects. To solve the PDE, initial conditions, the state variable values at the initial time ($t = 0$), are required. In several previous studies applying one-dimensional reactive transport models in rivers and flow-through column experiments (Liu, 2018; Liu et al., 2019; Strobel et al., 2023), the initial conditions were treated as a constant value (typically zero) in the spatial domain. This can be interpreted that the studied domain is clear (low background signal (Kunkel and Radke, 2011)) of the signals that are under investigation until the inflow boundary conditions start to enter the studied domain. In the current study, the initial conditions are the mixture effects, e.g., EU_{bio}, at 0-hour in each of the discretized node along the river course. Figure 3.3 shows the initial condition distributions of EU_{bio} determined with the AhR-CALUX along the study domain. Since we applied the ensemble inflow boundary condition, the number of

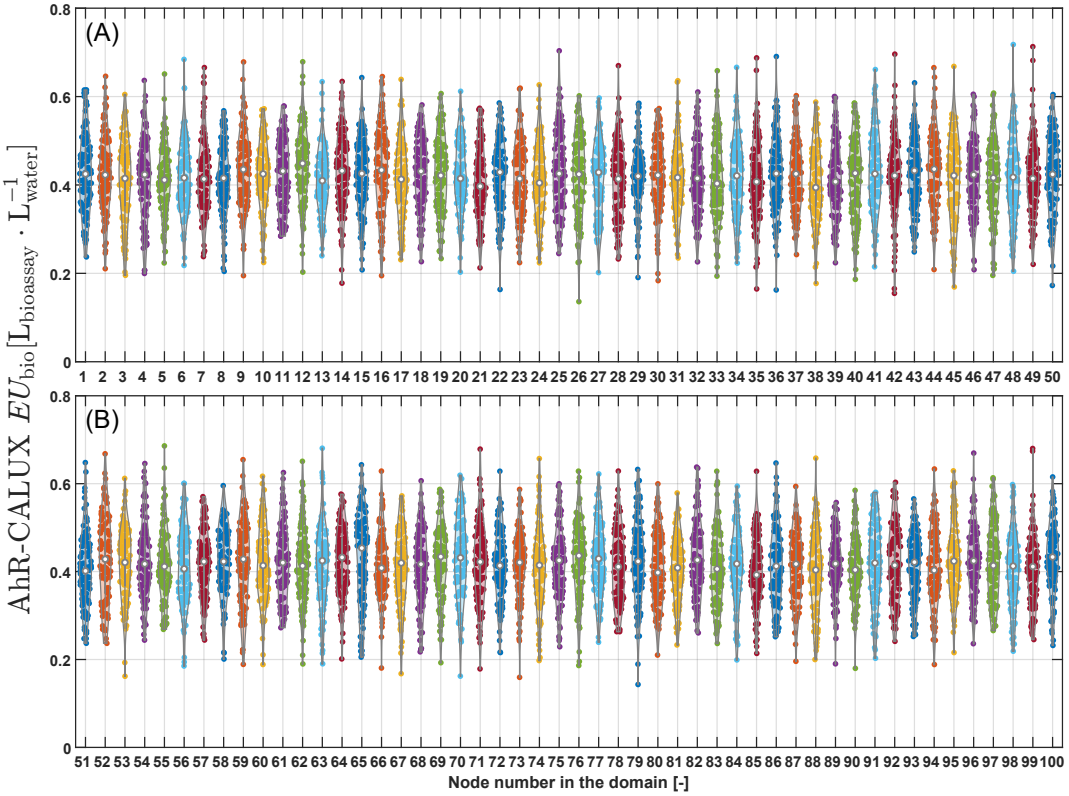

Figure 3.4: Initial condition distributions of EU_{bio} in AhR-CALUX in water phase. The study domain of the river was spatially discretized into 100 nodes in the model. (A): the first half of the domain. (B): the second half of the domain. The initial condition of EU_{bio} at each node was assumed following a Gaussian distribution, which was formed by an optimized mean value and a standard deviation of 20% of the mean. The stochastic perspective was introduced into the initial conditions.

initial conditions at each node needs to match that of the realizations from the ensemble inflow boundary condition. At each node, the initial conditions are samples drawn from a Gaussian distribution (Eq. 3.15) of which the parameters are estimated values. In such way, the mixture effects at 0-hour were presented through a random process that is more robust than a fixed constant value. In the Lagrangian sampling scheme that was used to collect time-series water samples, the estimated mean travel time of the water parcels will affect the early stage of the temporal patterns of the collected time-series signals, of which at the

downstream locations (of the upstream observation point) are also influenced by the initial conditions. The estimated mean travel time under transient flow conditions is much less accurate than that under baseflow conditions. Therefore, without a well understanding of the initial condition in current study, fitting the modeled results against the data including the ones from the early period would mislead the parameter estimates. It was logistically impossible to obtain all EU_{bio} observations along the domain at 0-hour, and unrealistic if a constant value was assumed, particularly when we used the ensemble inflow boundary conditions. We interpreted the initial EU_{bio} from a stochastic perspective by treating the initial EU_{bio} at every node of the domain a random variable that was characterized by a Gaussian distribution, of which the mean represents the background EU_{bio} in the river. The mean of the Gaussian distribution was computed based on the optimized value (Parameters estimation and Table 3.1). Constructing distributions is the most representative way to mimic all the EU_{bio} at 0-hour, from where the realizations were used in parallel with that from GPR (Ensemble model input).

3.3.4 In-stream dynamics of mixture effect units and their fluxes

Total mixture effect units (EU_{bio}) The mixture effects time-series signals displayed clear in-stream dynamics that were the results of advection, dispersion, and additional lateral input. The 100 realizations from the GPR input computed 100 time-series for EU_{bio} at downstream locations. The modeled ensemble time-series results quantitatively expressed different levels of the uncertainty of the modeled dynamics. Figure 3.5 depicts the ensemble inflow signals at MS1, and the 50th percentile, 60th (20 percentile – 80th percentile) and 90th (5th percentile – 95th percentile) interpercentile for the modeled EU_{bio} ensemble at MS2. Both of the measured $EU_{\text{bio, AhR}}$ in AhR-CALUX (Figure 3.5A) and $EU_{\text{bio, AREc32}}$ in AREc32 (Figure 3.5B) at MS2 showed peaks of the signals at 4.5-hour that clearly traveled from the peaks at 1.5-hour at MS1. The one-dimensional transient reactive model (Eq. 3.10) produced the ensemble time-series that mimic the dynamics of the data reasonably well ($\overline{NRMSE} = 0.159$ for AhR-CALUX; $\overline{NRMSE} = 0.259$ for AREc32). The transient velocity computed from the parameters estimated based on turbidity (Table 3.1) led to an accurate arrival time of the modeled EU_{bio} peaks at MS2. The spreading of the signals at MS2 between 3-hour and 6-hour, and the smoothness of the modeled ensemble time-series, which was also observed in the matching data, showed the effect from the transient dispersion processes (Eqs. 3.8 –3.9). With regards to the lateral influxes, EU_{bio} in AREc32 showed higher increase than EU_{bio} in AhR-CALUX during the storm period. The transient first-order source term in the model represented the spatially uniform lateral influxes along the study domain and was able to capture such increase for EU in both bioassays. The transient dispersion also led to the smooth increase of the EU_{bio} signal at MS2. Without considering the dispersion, the modeled ensemble time-series would have shown oscillating increasing patterns due to the different travel time (velocity) for each sample at MS1 to arrive at MS2. The modeled results showed inferior fit to data at earlier hours (from 0-hour to 3.5-hour) at MS2. The results did not necessarily indicate a poor overall model performance or incorrect parameterization, since for the model to produce better a fit during this time frame, additional signals at earlier hour (earlier than 0-hour) at MS1 were required.

In-stream dynamics of total mixture effect unit fluxes. The EU_{bio} fluxes dynamics were heavily influenced by that of the highly transient discharge. Similar results were found in

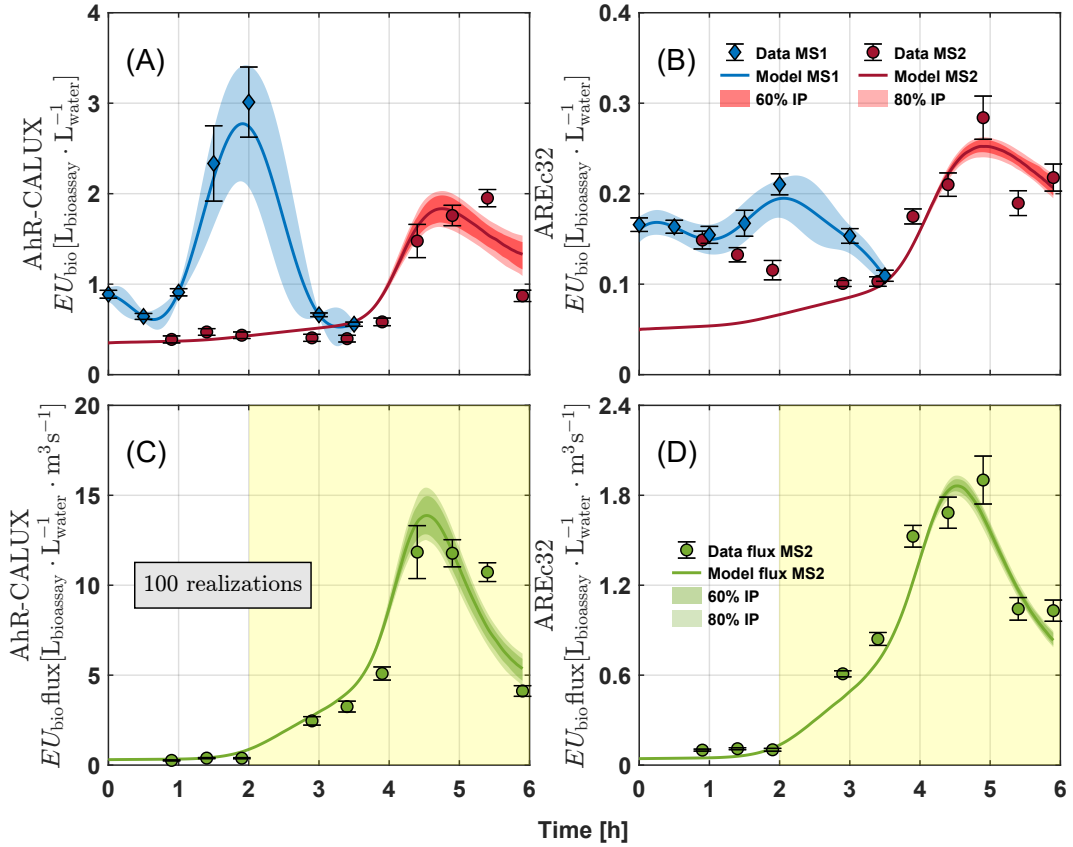

Figure 3.5: Modeled (A) $EU_{\text{bio, AhR}}$ [$L_{\text{bioassay}} \cdot L_{\text{water}}^{-1}$], (B) $EU_{\text{bio, AREc32}}$ [$L_{\text{bioassay}} \cdot L_{\text{water}}^{-1}$], (C) $EU_{\text{bio, AhR}}$ fluxes [$L_{\text{bioassay}} \cdot L_{\text{water}}^{-1} \cdot m^3 s^{-1}$], and (D) $EU_{\text{bio, AREc32}}$ fluxes [$L_{\text{bioassay}} \cdot L_{\text{water}}^{-1} \cdot m^3 s^{-1}$]. The ensemble from GPR was shown for EU_{bio} in blue (A, B), from where 100 realizations were generated as model input. The modeled EU_{bio} ensembles at MS2 are in red and were approximated by 100 realizations. The EU_{bio} fluxes are shown in green (C, D). The modeled EU_{bio} fluxes ensembles at MS2 were approximated by 100 realizations. The light yellow (C, D) represents the period when fluxes arrived at MS2 during the storm. Abbreviation: MS-measuring station; IP-interpercentile.

Wei et al., 2022. Figure 3.5C and Figure 3.5D show the EU_{bio} fluxes at MS2 in AhR-CALUX and AREc32, respectively. The discharge wave started to arrive at MS2 at approximately 2-hour. The EU_{bio} fluxes at MS2 started to increase at the matching time and peaked approximately at 4.7-hour. The modeled ensemble fluxes could reproduce the dynamics in the data ($\overline{NRMSE}$ = 0.184 for AhR-CALUX; $\overline{NRMSE}$ = 0.095 for AREc32), particularly the rising period and the peaks of the fluxes. The EU_{bio} fluxes started to drop after 4.5-hour. At the same time, TU_{bio} flux (Figure 3.6B) also appeared to drop, suggesting that there was no masking effect from the cytotoxicity.

Total mixture cytotoxicity (TU_{bio}) and flux Like EU_{bio}, the cytotoxicity of the total mixture effect was quantified as TU_{bio} (Escher et al., 2021). The same transient model (Eq. 3.10) was applied to the mean TU_{bio} of AhR-CALUX and AREc32. The modeled dynamics of TU_{bio} are shown in Figure 3.6A. The modeled TU_{bio} ensemble showed inferior fit at the beginning hours, but very well cover of the data after approximately 3.5-hour. Considering the relatively large measurement uncertainty (error bars in Figure 3.6A) and some missing

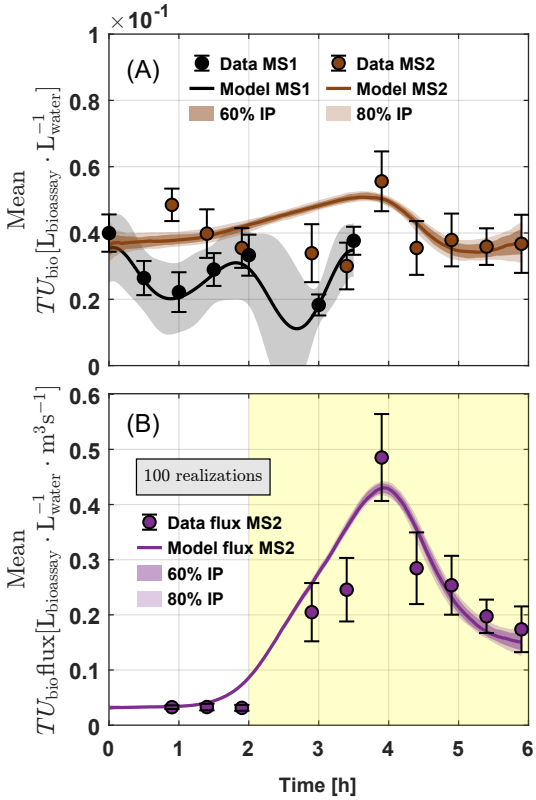

Figure 3.6: Modeled mean TU_{bio} and TU_{bio} flux. The ensemble from GPR was shown for TU_{bio} in grey (A), from where 100 realizations were generated as model input. The modeled TU_{bio} ensembles at MS2 are in brown and are approximated by 100 realizations. The TU_{bio} fluxes are shown in purple (B). The modeled TU_{bio} fluxes ensembles at MS2 are approximated by 100 realizations. The light yellow (B) represents the period when fluxes arrived at MS2 during the storm. Abbreviation: MS-measuring station; IP-interpercentile.

data at MS1 to constrain the construction of the ensemble model input using GPR, thus the overall goodness of fit for TU_{bio} was worse ($\overline{NRMSE}$ = 0.372). In comparison with EU_{bio} (especially EU_{bio} in AhR-CALUX), TU_{bio} showed relatively high increase at MS2, suggesting the large input from the lateral influx. TU_{bio} flux at MS2 is shown in Figure 3.6B. The modeled ensemble fluxes reproduced the main feature of the data well ($\overline{NRMSE}$=0.1175). The modeled fluxes fitted the data particularly well at the rising and lowering period. The arrival time of the peak of the flux was also captured by the model.

3.3.5 In-stream processes understandings.

The modeled ensemble EU_{bio} and TU_{bio} were able to capture the major temporal features of the measurements, thus supporting our parameterizations of the bulk controlling processes for the mixture effects in rivers. Whilst the transport processes that determine the arrival of the peak EU_{bio} and its spreading over time were largely influenced by the transient velocity, and the source-term characterized the input of from the lateral inflow caused by the storm, in our parameterization, both transport processes and the source-term were ultimately directly influenced by the transient discharge. Figure B.4 shows the simulated flow velocity with which the mixture effects were traveling, peaked at 1.11 [m s^{-1}], re-

lated by the discharge and cross-sectional area (Eq. 3.4 and Eq. 3.8). The previous study (Glaser et al., 2020) showed that the estimated mean flow velocity in the same segment of the Ammer River during the baseflow conditions was approximately 0.39 [ms^{-1}]. Prior to the storm-caused water entering (20-hour in Figure B.4) the studied domain, our results showed a mean flow velocity of 0.31 [$m\ s^{-1}$], thus verifying our estimated cross-sectional area parameters in Table 3.1.

The source term was parameterized as linearly scaled to the uniformly distributed (over the space) later inflow that was caused by the storm, therefore the rate of increase of the EU_{bio} and TU_{bio} was proportional to the contribution of the mixture effects coming from the dispersive non-point source. The estimated source term coefficients for EU_{bio} in AhR-CALUX and AREc32 and TU_{bio} showed minor differences (2.00×10^{-5} [m^{-1}], 2.78×10^{-5} [m^{-1}], and 1.48×10^{-5} [m^{-1}], respectively in Table 3.1), indicating the contributions from the lateral inflow are similar for all mixture effects. In comparison with EU_{bio} in AREc32 (Figure 3.5B) and TU_{bio} (Figure 3.6A), EU_{bio} in AhR-CALUX (Figure 3.5A) shows relatively smaller increase from the lateral inflow, which is counter-intuitive since lateral inflow-scaled source term coefficients for all three mixture effects are nearly indistinguishable from one another. EU_{bio} in AhR-CALUX was also one order of magnitude higher than EU_{bio} in AREc32 and TU_{bio}, establishing a higher rate of increase for EU_{bio} in AhR-CALUX than for EU_{bio} in AREc32 and TU_{bio}. This can be explained by the large dispersive fluxes EU_{bio} in AhR-CALUX introduced by the inflow boundary conditions (MS1). Although longitudinal dispersivity (α_L) and transient velocity were identical for all mixture effects, the time-series signal of EU_{bio} in AhR-CALUX at MS1 showed strong oscillations, particularly between 0.5-hour and 2-hour, causing the steep gradient when the EU_{bio} front was moving through the studied domain. The strong dispersive fluxes therefore smoothed out the transient increase of EU_{bio} from the lateral inflow. The time-series signals of EU_{bio} in AREc32 (Figure 3.5B) and TU_{bio} (Figure 3.6A) at MS1 showed relatively smoother patterns, thus the dispersive effects on the downstream signals were less prominent, leading to a relatively large increase from the lateral inflow. The transport processes, therefore, played a critical role at characterizing the mixture effects in-stream signal patterns in the transient flow conditions.

3.4 Implications

Modeling the fate of the mixture effects in river water during rain events faces challenges, e.g., relatively complex parameterizations are needed; Processes in the standard reactive transport model become transient; Certain parameter values, e.g., dispersivity, river channel cross-sectional area, could not be measured directly in the field, however played an important role in characterizing the in-stream processes. Representative observations are difficult to obtain during the rain due to the highly transient nature of the system in a short period. The observed mixture effects show complex in-stream dynamics. By introducing stochastic input into the PDE-based transient reactive transport model, we can construct the mixture model input in a robust way, efficiently compute the ensemble model output, as well as explicitly express the known in-stream processes. Process-based models' performances are limited due to the relatively simplified parameterization compared to real-world complexity, particularly when data used for constructing model input or evaluating the model parameterization contains many unknown elements or provides limited information. To improve the partial/ordinary differential equation (PDE/ODE) model per-

Table 3.1: Estimated model parameters

	Parameters	Symbol	Unit	Values
Discharge (Eqs. 3.4 – 3.6)	Longitudinal dispersion coefficient	D	$m^2 s^{-1}$	1.05×10^2
	Celerity	C	$m\ s^{-1}$	8.56×10^{-1}
	Rate	α	-	3.28×10^5
	Shape	β	-	5.00×10^{-1}
	Fraction	k	-	9.99×10^{-1}
Turbidity (Eqs. 3.7 – 3.9)	Offset height	h_{off}	m	8.02×10^{-1}
	Channel bottom width	w	m	3.0
	Longitudinal dispersivity	α_{L}	m	2.50×10^2
	Channel angle	θ	-	3.00×10^1
	Mean turbidity initial condition	N_{IC}	NTU	1.60×10^1
	1st-order transient source term coefficient	k_{turb}	m^{-3}	1.80×10^{-5}
$EU_{\text{bio,ahr}}$ (Eq. 3.10)	Specific diffusion coefficient	$D_{\text{spec,ahr}}$	$m^2 s^{-1}$	1.01×10^1
	1st-order transient source term coefficient	$k_{\text{source,ahr}}$	m^{-3}	2.00×10^{-5}
	Mean initial condition	$EU_{\text{bio,ahr,initial}}$	$L_{\text{bioassay}}\ L_{\text{water}}^{-1}$	3.53×10^{-1}
	Retardation factor	$R_{\text{bio,ahr}}$	-	1.108
$EU_{\text{bio,are}}$ (Eq. 3.10)	Specific diffusion coefficient	$D_{\text{spec,are}}$	$m^2 s^{-1}$	1.00×10^1
	1st-order transient source term coefficient	$k_{\text{source,are}}$	m^{-3}	2.78×10^{-5}
	Mean initial condition	$EU_{\text{bio,are,initial}}$	$L_{\text{bioassay}}\ L_{\text{water}}^{-1}$	5.00×10^{-2}
	Retardation factor	$R_{\text{bio,are}}$	-	1.097
$\overline{TU}_{\text{bio}}$ (Eq. 3.10)	Specific diffusion coefficient	$D_{\text{spec,TU}}$	$m^2 s^{-1}$	9.587
	1st-order transient source term coefficient	$k_{\text{source,TU}}$	m^{-3}	1.48×10^{-5}
	Mean initial condition	$TU_{\text{bio,initial}}$	$L_{\text{bioassay}}\ L_{\text{water}}^{-1}$	3.70×10^{-2}
	Retardation factor	$R_{\text{bio,TU}}$	-	1.112

formance on mixture effects, deep learning methods, especially neural networks, could be used to train certain rates that cannot be observed inside the PDE/ODE, making the mixture effects model a neural PDE/ODE, thus providing processes that have physical meanings, as well as good simulation performance. Combining with Bayesian inference, the hybrid model can also be used to identify the unknown physical processes.

Chapter 4

Application of neural network aided reactive transport models to field data: in-stream dynamics of the mixture effects of organic micropollutants

Abstract

The mixture effects of organic micropollutants in rivers, quantified in *in vitro* bioassays, show complex in-stream dynamics. The advection-dispersion-reaction (ADR) equation based numerical models, coupled with ensemble input, show a promising capability to reproduce the observed complex in-stream dynamics. Such setup is computationally expensive, hindering the formation of parameter posterior distributions within traditional Bayesian inference. To avoid the high computational costs while applying Bayesian inference, we applied the computationally cheaper simulation-based inference (SBI) method to a one-dimensional numerical reactive transport model, approximating the posterior through a trained deep learning neural network. We also aimed to improve the model accuracy for the mixture effects. We applied the physics-informed neural network (PINN) to solve the same ADR, comparing the solutions, estimated parameter values and the computational efforts with that of the numerical model. The models and the training methods are tested on observations that are mixture effects with three end points from a 7.7-km-long segment of the Ammer River in southwest Germany under baseflow conditions. SBI shows high efficiency converging to the posterior, yielding physically meaningful parameter values and their uncertainties. However, the modeled ensemble breakthrough curves show an inferior fit to the observed mixture effects than PINN. PINN yields improved accuracy, particularly at locations where a relatively large number of observations exist. The overall space-time accuracy still suffers from the sparse availability of real-world mixture effects data. Both methods show strengths in varying aspects, suggesting a choice between the two is highly dependent on the specific modeling goal. We show the potential of using deep neural networks to aid the reactive transport model in real-world problem applications.

4.1 Introduction

The mixture effects of organic micropollutants in rivers, quantified in *in vitro* bioassays, have been used as a novel and reliable state variable to evaluate river water quality (Escher et al., 2021). The mixture effect represents an overall burden from all micropollutants in the samples, reflecting their environmental impacts through specific endpoints. Studying the dynamics of the mixture effects in rivers provides knowledge of the bulk in-stream processes that the micropollutant mixtures undergo. The in-stream processes are assumed being characterized by the advection-dispersion-reaction (ADR) equations (Wei et al., 2022). Typically, time-series signals from the Lagrangian sampling scheme are used to study the reactive transport processes and dynamics of the solutes (Liu et al., 2020; Guillet et al., 2019). However, observed time-series signals of the mixture effects show complex dynamics in previous studies (Wei et al., 2022; Müller et al., 2020, 2021), and often an ensemble model result is required to effectively reproduce the complex in-stream dynamics while maintaining the ADR parameterizations. Therefore, uncertainty (distribution) of the model parameters and the input need to be quantitatively addressed. Numerical reactive transport models coupled with ensemble inflow boundary conditions characterised by Gaussian process regression (GPR) (Schulz et al., 2018) show promising results (Chapter 3). Such a setup is computationally expensive. Implementing Bayesian methods (e.g., Markov Chain Monte-Carlo (MCMC)) under such a setup to obtain the parameter posterior distributions is further constrained by the large number of model runs needed (obstacle one). Uncertainty originating from the model parameterization - a simplified version of the real-world processes in rivers - and numerical methods that discretize the space-time domain into discontinuous "dots (or boxes)" challenges the aim of reproducing the observed in-stream dynamics of the mixture effects as close as possible under the constraints of the defined physical rates (obstacle two). While the process-based models aim to achieve solutions that are as close as possible to the meaningful and complex information from the measurements under the known and parameterized controlling physical processes, even the most detailedly described model still produces inconsistencies with the data due to the unknown environmental processes that influence data behaviors, which are not included in the conceptualization, thus are not present in the model. The recent rapidly advanced deep learning methods showed the potential to overcome this challenge when embedding with the existing knowledge regarding the processes in the environment. Artificial Neural Networks, a deep learning method under the category of machine learning, have been used in a wide range of real-word applications, e.g., natural language processing, medical image diagnosis and autonomous driving (Cuomo et al., 2022; Lecun et al., 2015; Shinde and Shah, 2018; Fujiyoshi et al., 2019). Through the training process using back propagation (Wright et al., 2022), the weights and bias of the neurons in each layer are updated. Adding the non-linear activation function (Ramachandran et al., 2018) to each neuron, the highly adaptive structure gives ANN the ability to efficiently learn features from complex data over time. Well trained NNs demonstrate promising performances in terms of prediction accuracy. Recent development of machine learning frameworks, e.g., *PyTorch* and *TensorFlow* (Abadi et al., 2016), makes the implementation of ANN rather straightforward.

To address the parameter uncertainty through Bayesian inference, presenting the posterior distributions of the parameters, and to avoid high computational costs (obstacle one), we applied the simulation-based inference (SBI) method. SBI was developed based on the idea of "emulator" to tackle the "intractable likelihood" issue (Greenberg et al., 2019; Gut-

mann and Corander, 2016; Lueckmann et al., 2018; Cranmer et al., 2020). Recent advances in deep neural networks framework enable the fusion of Bayesian philosophy with the power of deep learning. The *sbi* toolbox (Tejero-Cantero et al., 2020; Gonçalves et al., 2020) is built on top of the widely used machine learning framework *PyTorch* (Paszke et al., 2019). The toolbox allows the approximation of posterior distributions through a trained neural network, which quantitatively establishes a relationship between the forward model run results (prior runs) and the corresponding parameters sampled from the prior distribution. The prior runs could be executed in parallel so that the computational costs are drastically reduced, demonstrating a clear advantage over the iterative Markov process in MCMC.

ANN is a pure data-driven approach. It does not provide any physically interpretable information of the underlying system that connects the model input and output. In the field of process-based modeling, the attempt to merge the high prediction accuracy of ANN with the constraints set by physical laws (obstacle two) prompts what is known as physics-informed neural network (PINN) (Raissi et al., 2019). The governing equations of process-based models commonly are partial differential equations that often need numerical discretization, typically in space (e.g., when the transport processes are involved) before the integration over time. Spatial discretizations introduce uncertainties, or sometimes numerical instability. Certain high-order discretization schemes are complicated to implement (Du and Ekaterinaris, 2022). The discretized systems can be computationally expensive, particularly if two-dimensional or three-dimensional transport is modeled. PINN has the advantage of not requiring any spatial discretizations (Cuomo et al., 2023). Instead, it computes the gradients of the ANN using the highly efficient auto-differentiation module (Pang et al., 2020) that is also used in back propagation. The sum of computed gradients are equal to the governing partial differential equations, thus forming the physics-informed part of the ANN. In return, the physics-informed constraints enable the training of ANNs on a relatively small amount of data (Tartakovsky et al., 2020), whereas standard ANNs need a large amount of data for training, which is often logistically challenging to obtain when studying real-world environmental systems (Karniadakis et al., 2021). PINN has been applied in various process-based modeling studies on real-world problems, e.g., the advection-dispersion equation for solute transport coupled with Darcy flow equation (He and Tartakovsky, 2021), the groundwater flow equation (Cuomo et al., 2023), gas transport (Strelow et al., 2023) and COVID-19 dynamics (Berkhahn and Ehrhardt, 2022). Tartakovsky et al., 2020 shows the learnability of physical parameters by applying PINN to a groundwater flow problem. A broader perspective of PINN is also intensively studied by others. Shen et al., 2023 highlights the advantage and applicability of merging machine learning with process-based models in various fields of Geoscience. Karniadakis et al., 2021 explains the fundamental theory behind PINN in details. Cuomo et al., 2022 outlines the pipelines of PINN from different NN architectures, types of loss functions, to learning methods. PINN shows high accuracy in terms of matching the analytical and numerical model results. However, there is a lack of studies using real-world observations to train PINN. The majority of the real-world problem application of PINN use only the solutions from either analytical or numerical models as training sets. Berkhahn and Ehrhardt, 2022 uses real-world observations for training when modeling the COVID-19 dynamics, however the underlying dynamics of COVID-19 is described a systems of ordinary differential equations. The advantage of auto-differentiation with respect to space and time is not fully explored.

We applied PINN to compute the solution of a one-dimensional reactive transport

problem on mixture effects. We trained the PINN model on time-series data collected from a Lagrangian sampling campaign in two segments (3.6 km and 4.1 km, respectively) of Ammer River in the southwest of Germany (see Glaser et al., 2020 for the sampling details). The water samples are tested on *in vitro* bioassays named AhR-CALUX for aryl hydrocarbon receptor induction, PPARγ-GeneBLAzer for peroxisome proliferator-activated receptor activity, AREc32 for oxidative stress response, and ERα-GeneBLAzer for estrogenicity (see Müller et al., 2020 for the bioassay analysis details). The training method is adaptive moment estimation (*Adam*) (Kingma and Ba, 2015). The three physical parameters, retardation factor, dispersivity, and first-order reaction constant in each segment, together with the weights and bias in the PINN model, are estimated by *Adam*. Other hyperparameters. e.g., learning rate, weights decay, weights in the loss functions, are set manually (see Table C.2). We compared the modeled results, the estimated parameter values and the computationally expense of SBI and PINN.

The present study aimed to overcome obstacle one and two, demonstrating the strengths of deep learning methods for the parameter estimating and approximating the solutions of the process-based models, as well as the limitations when applying to real-word environmental data. SBI yields physically meaningful parameter values from the neural posterior objects, and requires relatively similar computational time. The modeled ensemble breakthrough curves could capture the major features in the observation dynamics, but the prediction accuracy is inferior to that from PINN. PINN shows improved prediction accuracy, however mainly at locations of the space-time domain where the weights are high in the loss functions and relatively large number of observations exist. The overall space-time domain prediction suffers from the scarcity of data. The modeled results are highly sensitive to the hyperparameter values, which up to now lacks of a computationally cheap method to either define before training or estimate during the training. The auto-differentiation is computationally cheap and straightforward to implement. But the training process is still time-consuming. Retraining the NN is required when transferring to another modeling scenario, e.g., new boundary conditions or new parameter sets, for scenario analysis. PINN shows promising potential for improving the prediction accuracy of reactive transport models. But the limitations become obvious when applied to field data. The trade-off between model accuracy and constraining model structure to physical laws still remains a challenge to be tackled.

4.2 Methods & Theory

4.2.1 Mixture effects field data acquisition

Field campaign. The underlying sampling campaign took place from 2018-06-19 to 2018-06-20 in the Ammer River, Baden-Württemberg, Germany. The studied river site is approximately 7.7 km long. Three measuring stations divided the studied river site into two segments by with the length of 3.6 km and 4.1 km each, starting at 4 km downstream of the city of Herrenberg, ending in the city of Pfäffingen (Figure C.1). Three auto-samplers (AS) were installed at upstream, midstream and downstream measuring station, respectively, collecting composite time series samples (1-hour temporal resolution; mixed by four sub-samples collected every 15 minutes) over 24 hours at each MS. The detailed sampling procedure can be found in Glaser et al., 2020.

***In vitro* bioassays.** The collected water samples were tested on four *in vitro* bioassays, AhR-CALUX, AREc32, PPARγ-GeneBlAzer and ER-GeneBlAzer for the four endpoints of aryl hydrocarbon receptor induction, peroxisome proliferator–activated receptor activity respectively, oxidative stress response and estrogenicity, respectively. Detailed information regarding the the measurement of the effect concentration and inhibitory concentration can be found in Müller et al., 2020. We applied the model to the mixture data from AhR-CALUX, PPARγ-GeneBlAzer and ER-GeneBlAzer. We left AREc32 out due to the scarce number of data points.

4.2.2 The governing equation

Reactive transport. We previously demonstrated that the mixture effects such as EU_{bio} can be used as an intensive state variable, of which the rate of change is governed by the mass conservation law. To quantitatively describe the fate of the mixture effects in the studied segment of the Ammer river, we consider the in-stream processes including advection, dispersion, first-order kinetic dissipation and equilibrium sorption. We set up the one-dimensional reactive transport model for the mixture effect as in Eq. 4.1,

$$R_i \cdot \frac{\partial EU_{\text{bio}}}{\partial t} = -v_i \cdot \frac{\partial EU_{\text{bio}}}{\partial x} + v_i \cdot \alpha_i \cdot \frac{\partial^2 EU_{\text{bio}}}{\partial x^2} - k_i \cdot EU_{\text{bio}} \tag{4.1}$$

where R [-] is the retardation factor; v [$\text{m} \cdot \text{s}^{-1}$] the velocity; α [m] the dispersivity; k [s^{-1}] the first-order dissipation constant. The studied river course is divided into two segments. Processes in each segment are differentiated by its own parameters indexed by i ($i \in \{1, 2\}$).

Boundary conditions. The studied river site was divided into two segments. The sampling site map is shown in Figure C.1. We hypothesized that the processes in the two river segments are independent. We simulated the in-stream dynamics in the two segments separately, e.g., when SBI (see SBI) was used, the time-series signals measured at measuring station (MS) upstream (MS upstream) and midstream (MS midstream) were used as the inflow boundary conditions (Dirichlet boundary conditions) to simulate time-series signals at MS midstream and downstream (MS downstream), respectively. In this way, the possible correlations between parameters of the two segments can be avoided.

The time-series signals of the mixture measured at MS upstream and MS midstream along the river course were used as model inflow boundary condition. Similar to the method used in Section 3.2.5 of Chapter 3, to include the measurement uncertainties and address the uncertainties from interpolation that was used to characterize the dynamics of the signal, we applied the Gaussian Process Regression (GPR) to compute the posterior, from which the individual conditional realizations was used as ensemble model input.

4.2.3 Solutions of the reactive transport models for the mixture effects

To numerically solve the model that involves transport processes (Eq. 4.1), one common approach is to firstly discretize the right-hand side of the partial differential equation (PDE) using e.g., finite difference method (FDM), transforming a partial differential equation into a series of ordinary differential equations (ODE). Afterwards numerical ODE solvers could be applied for the integration over time (Shampine and Reichelt, 1997). In order to overcome the numerical instability (oscillations in the solutions), often cases flux limiters (Dubey, 2013) are used in the spatial discretization scheme. Modern numerical ODE

solvers are able to automatically adjust the step size during the time integration, further reducing the numerical errors. Nevertheless, this approach is relatively complex to implement and computationally expensive, particularly when transport processes are two or three-dimensional, or the system is nonlinear and the manually defined Jacobian matrix is required to reduce the computational cost.

As a comparison, we also applied the physical-informed neural network (PINN) (Raissi et al., 2019; Karniadakis et al., 2021) for computing the solution of Eq. 4.1 and estimating the physical parameter values (see Parameter estimates and forward runs for the numerical approach).

Numerical approach: the spatial discretization and integration over time. We applied the upwind FDM to discreitize the transport processes at right-hand side of the Eq. 4.1 (similar to Eq. 1.14 and Eq. 1.15 in Chapter 1). The advective transport is discretized as in Eq. 4.2,

$$\left.\frac{\partial EU_{\text{bio}}}{\partial x}\right|_i = \frac{EU_{\text{bio}i} - EU_{\text{bio}i-1}}{\Delta x} \tag{4.2}$$

where i is the spatial index for the nodes in the discretized domain. The dispersive transport is discretized as in Eq. 4.3,

$$\left.\frac{\partial^2 EU_{\text{bio}}}{\partial x^2}\right|_i = \frac{EU_{\text{bio}i+1} - EU_{\text{bio}i} + EU_{\text{bio}i-1}}{\Delta x^2} \tag{4.3}$$

where i denotes the nodes in the spatial domain. The discretized system was implemented in the open-source programming language Python, and solved using the ODE solver *solve_ivp* (explicit Runge-Kutta method of order 5(4) (Dormand and Prince, 1986)) from the *SciPy* library (Virtanen et al., 2020).

Physics-informed neural network. Under the deep learning framework *PyTorch* (Paszke et al., 2019), we applied the physics-informed neural network (PINN) to solve the partial differential equation Eq. 4.1, and compared the modeled results and the estimated parameter values. The key idea of the PINN is to firstly construct the neural network that takes the space and time coordinates, x [m] and t [s], as the input, and computes the states, in our case the mixture effects, e.g., EU_{bio}, as the output. The EU_{bio} is expressed as a function of x and t in Eq. 4.4,

$$EU_{\text{bio}}(x,t) = \mathcal{N}_{\text{neural}}(x,t) \cdot k_{\text{normal}}(x) \tag{4.4}$$

where $\mathcal{N}_{\text{neural}}$ is the neural network. $\mathcal{N}_{\text{neural}}$ consists of nine hidden layers with 50 neurons in each layer, using linear and hyperbolic tangent activation functions (Han et al., 2018) in tandem for the forward passing. $k_{\text{normal}}(x,t)$ is a space-dependent normalization factor (details in later context).

Then we computed the gradient of the state with respect to x and t. The automatic differentiation feature in *PyTorch* used by the back propagation (Wright et al., 2022) during the training of the neural network is computationally efficient and easy to implement for the gradient calculation. We substituted Eq. 4.4 into Eq. 4.1, reformulating the new function named f_{neural} using Euler' notation in Eq. 4.5,

$$f_{\text{neural}} \,:\, R_i \cdot \partial_t \mathcal{N}_{\text{neural}} + v_i \cdot \partial_x \mathcal{N}_{\text{neural}} - v_i \cdot \alpha_i \cdot \partial_{xx} \mathcal{N}_{\text{neural}} + k_i \cdot \mathcal{N}_{\text{neural}} \stackrel{!}{=} 0 \tag{4.5}$$

where the right-hand side is set to be zero. Eq. 4.4 and Eq. 4.5 are the backbone of the PINN. The former represents the neural network part of the PINN. The latter supplies the physics information and constraint. The general code implementation in *PyTorch* is shown in Algorithm 1.

Algorithm 1 Defining the physics-informed-neural network in *PyTorch*

```
def N_neural (x, t):                          ▷ define the neural network (Eq. 4.4)
    EU = neural_network.forward (x, t)
    return EU

def f_neural (x, t):                          ▷ compute the gradient (Eq. 4.5)
    EU_t = torch.autograd.grad (EU, t)
    EU_x = torch.autograd.grad (EU, x)
    EU_xx = torch.autograd.grad (EU_x, x)
    f_neural = R * EU_t + v * EU_x - alpha * v * EU_xx + k * EU
    return f_neural
```

To train the PINN and estimate the physical parameters, we parameterized three loss functions that take into account the constraints from the $\mathcal{N}_{\text{neural}}$ (downstream data), f_{neural} (the physical governing equation), and the inflow boundary condition. The three loss functions compute the mean square error (MSE) (Raissi et al., 2019). The optimal parameters were estimated by minimizing the MSE. The loss function of $\mathcal{N}_{\text{neural}}$ is expressed in Eq. 4.6,

$$\mathcal{L}_{\mathcal{N}_{\text{neural}}}(\mathbf{w}, \boldsymbol{\sigma}) = \frac{1}{n}\sum_{i=1}^{n}\left[\mathcal{N}_{\text{neural}}(\mathbf{x}_{\text{data}}, t_i, \mathbf{w}, \boldsymbol{\sigma}) - y_{\text{data}}(t_i)/y_{\text{max,data}}\right]^2 \tag{4.6}$$

where $\mathbf{x}_{\text{data}}$ is the spatial coordinates that observations ($\mathbf{y}_{\text{data}}$) are present; n is the number of y_{data}. $\mathbf{w}$ and $\boldsymbol{\sigma}$ are the weights and bias of the neural network, respectively. The loss function of f_{neural} is expressed in Eq. 4.7,

$$\mathcal{L}_{f_{\text{neural}}}(\boldsymbol{\theta}) = \frac{1}{n}\sum_{i=1}^{n}\left[f_{\text{neural}}(\mathbf{x}_{\text{all}}, t_i, \boldsymbol{\theta}) - 0\right]^2 \tag{4.7}$$

where $\mathbf{x}_{\text{all}}$ is the spatial coordinates of the whole domain. $\boldsymbol{\theta}$ represents the physical parameters. The loss function of the inflow boundary is expressed in Eq. 4.8,

$$\mathcal{L}_{\text{boundary}} = \frac{1}{n}\sum_{i=1}^{n}\left[\mathcal{N}_{\text{neural}}(\mathbf{x}_{\text{boundary}}, t_i) - y_{\text{boundary}}(t_i)/y_{\text{max,boundary}}\right]^2 \tag{4.8}$$

where $\mathbf{x}_{\text{boundary}}$ is the spatial coordinates that the inflow boundary ($\mathbf{y}_{\text{boundary}}$) is present. n is the number of $\mathbf{y}_{\text{boundary}}$. The total loss is the weighted summation of the three loss functions expressed in Eq. 4.9,

$$\mathcal{L}_{\text{total}} = w_1 \cdot \mathcal{L}_{\mathcal{N}_{\text{neural}}} + w_2 \cdot \mathcal{L}_{f_{\text{neural}}} + w_3 \cdot \mathcal{L}_{\text{boundary}} \tag{4.9}$$

where w_i is the weight [-] for each loss. w_i is used to adjust the sensitivity of the three losses (Strelow et al., 2023). We apply the adaptive moment estimation (*Adam*) optimizer (Kingma and Ba, 2015) to minimize Eq. 4.9 through a iterative process, of which the number (3000 – 5000 epochs in the present study) is called epoch when the whole dataset was used

during the training, and obtain the estimated physical parameter values and the optimized PINN output. The learning rate (e.g., 1e-2) is automatically decaying after several (100 - 200) iterations. We also include the weight decay (L2 regularization) (Kingma and Ba, 2015) to prevent over-fitting.

To further improve the training, we applied the space-dependent normalization terms (similar to the time-dependent normalization in Zong et al., 2023) in the loss function of $\mathcal{L}_{\mathcal{N}_{\text{neural}}}$ (Eq. 4.6) and $\mathcal{L}_{\text{boundary}}$ (Eq. 4.8), where the normalization terms ($y_{\text{max,data}}$ and $y_{\text{max,boundary}}$) are the maximum values of the $\mathbf{y}_{\text{data}}$ and $\mathbf{y}_{\text{boundary}}$, respectively. k_{normal} consists of the linearly interpolated values between $\mathbf{y}_{\text{max,data}}$ and $\mathbf{y}_{\text{max,boundary}}$.

4.2.4 Parameter estimates and forward runs for the numerical approach

The mean travel time (thus the mean velocity v) of the solute in the two river segments were estimated in previous work (Glaser et al., 2020). We used the literature v for Eq. 4.1. To estimate the rest of the model parameters ($[\alpha_i, k_i, R_i]$) and their uncertainties for each mixture effect, we applied Bayesian optimization methods to obtain the posterior distribution of each parameter. As we previously mentioned, Bayes rule states that given the data $\boldsymbol{y}$, the posterior probability density of parameter $\boldsymbol{\theta}$, $P(\boldsymbol{\theta}|\boldsymbol{y})$, is proportional to the product of the likelihood of the data $P(\boldsymbol{y}|\boldsymbol{\theta})$ and the prior parameter probability density $P(\boldsymbol{\theta})$:

$$P(\boldsymbol{\theta}|\boldsymbol{y}) \propto P(\boldsymbol{y}|\boldsymbol{\theta}) \cdot P(\boldsymbol{\theta}) \tag{4.10}$$

To sample the posterior, we applied the simulation-based inference (SBI).

Simulation-based inference. A closed-form of the likelihood function is required when Markov Chain Monte Carlo (MCMC) is applied to sample the posterior. One of the most common assumptions is that the likelihood has a Gaussian shape (Eq. 1.19). In reality, the shape of the likelihood function could be any other shapes. Vrugt 2016 presented various forms of likelihood functions that MCMC users can choose. The simulation-based inference (SBI) (Tejero-Cantero et al., 2020; Gutmann and Corander, 2016) allows a "likelihood-free" Bayesian inference (Cranmer et al., 2020). The workflow of SBI follows:

1) draws parameter samples from prior distributions.

2) initiates model forward runs using these parameter samples.

3) trains a deep neural networks that establish the quantitative relationship between the model forward run results (input of the trained neural network) and the parameters (output of the trained neural network) from the prior. The training (inferring) process was accomplished by the Sequential Neural Posterior Estimation (SNPE) – C (Greenberg et al., 2019; Allgeier and Cirpka, 2023) method.

4) imports the observations into the trained neural network, which maps the posterior distribution directly.

Figure 4.1 illustrates the SBI procedures in numerical order. We applied the *PyTorch* based toolkit, *sbi* (Tejero-Cantero et al., 2020), to achieve the Neural Posterior Estimation (NPE) (Greenberg et al., 2019).

To include the measurement errors when sampling from the neural posterior, we treat the input of the trained neural network object (P_{NE}) as a random variable, of which the samples are drawn from either a multivariate Gaussian ($\mathcal{N}$) or multivariate lognormal (if there is a negative value) distribution that is parameterized by the measurements ($\mathbf{y}_{\text{data}}$) and measurement errors (σ_{data}). Algorithm 2 illustrates the sampling workflow. At each

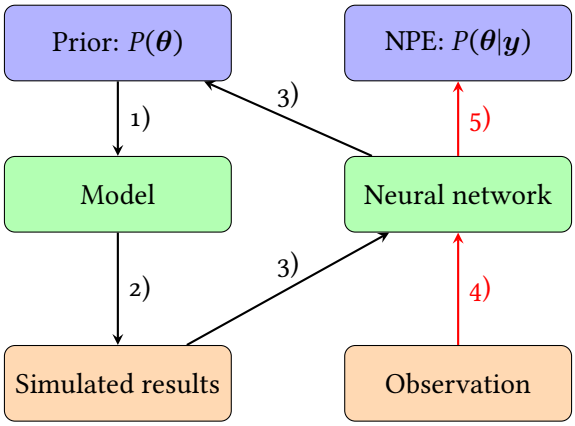

Figure 4.1: SBI flow chart: no likelihood function is required. 1) draw parameter samples from the prior; 2) forward model runs; 3) establish and train the neural network using SNPE – C; 4) import observations as the input of the trained neural network; 5) map the posterior from the neural network. NPE–Neural posterior estimation. SPNE – Sequential Neural Posterior Estimation

iteration, a vector of data sample ($\mathbf{y}_i$) is draw from $\mathcal{N}$ (or lognormal). The a corresponding vector of model parameters $\mathbf{p}_i$ then computed through the P_{NE}. After all iterations, the individual $\mathbf{p}_i$ can be assembled to the parameter matrix ($\mathbf{P}$) that is used for computing the ensemble model results.

Algorithm 2 Sampling from the neural posterior.

Require: Neural posterior object: P_{NE}
Require: number of samples to be drawn: N_{samples}
Require: measurements and measurement errors for parameter estimates: $\mathbf{y}_{\text{data}}$, σ_{data}
  for i = 1 to N_{samples} **do**
    $\mathbf{y}_i \sim \mathcal{N}(\mathbf{y}_{\text{data}}, \sigma_{\text{data}}, 1)$ ▷ draw data from a multivariate Gaussian distribution
    if $y_i < 0, \forall y_i \in \mathbf{y}_i$ **then**,
      $\mathbf{y}_i \sim Lognormal(log(\mathbf{y}_{\text{data}}), \sigma_{\text{data}}, 1)$ ▷ draw data from a multivariate lognormal distribution
    end if
    $\mathbf{p}_i \sim P_{\text{NE}}(1, , \mathbf{y}_i)$ ▷ sampling the individual parameter vector
    $\mathbf{P}[:, i] = \mathbf{p}_i$ ▷ assembling the parameter matrix
  end for

Prior distribution for SBI. The prior distributions for the model parameters $[\alpha_i, k_i, R_i]$ are uniform distributions, of which the ranges are defined as wide as possible to cover all the potential values. We use parameter values from Table 3.1 in Chapter 3 as base values and setup the lower boundary of e.g., [5e-3, 8e-6, 1.0] and upper boundary of [500.0, 1e-4, 50.0] for $[\alpha_i, k_i, R_i]$. The units are [m], [s^{-1}] and [-] for α_i, k_i and R_i, respectively for EU_{bio} in PPARγ-GeneBLAzer.

Forward runs with ensemble input. Similar to the approach in Section 3.2.5 in Chapter 3, we use the ensemble input from GPR as the inflow boundary condition for the model

forward run. For every GPR sample that is used as the model input $\mathbf{x}_i$, a vector of parameters $\mathbf{p}_i$ is drawn from the parameter matrix $\mathbf{P}$ previously assembled (from Algorithm 2). Algorithm 3 shows the model forward run coupled with ensemble model input and parameter sets from the neural posterior.

Algorithm 3 Forward run with ensemble input from Gaussian Process Regression.

Require: model: $\mathcal{M}$
Require: posterior sample matrix: $\mathbf{P}$ (from Algorithm 2)
Require: number of samples to be drawn: N_{samples}
Require: measurements and measurement errors for model input: $\mathbf{x}_{\text{input}}$, σ_{input}
  for i = 1 to N_{samples} **do**
    $\mathbf{x}_i \sim \mathcal{GP}(\mathbf{x}_{\text{input}}, \sigma_{\text{input}}, 1)$ ▷ draw input samples from Gaussian Process Regression
    $\mathbf{p}_i \sim \mathbf{P}[:, i]$ ▷ draw parameter samples from the posterior sample matrix
    $\hat{\mathbf{y}}_i = \mathcal{M}(\mathbf{p}_i, \mathbf{x}_i)$ ▷ forward run (solving Eq. 4.1)
    $\hat{\mathbf{Y}}[:, i] = \hat{\mathbf{y}}_i$ ▷ store the ensemble model output
  end for

4.3 Results & Discussion

4.3.1 Simulation-based inference & Gaussian process aided reactive transport

Simulation-based inference (SBI) provides uncertainty analysis of the estimated model parameters by approximating the posterior distributions through a trained neural network, from which the optimized parameter samples can be drawn for computing the ensemble model results.

Neural posterior estimation. The neural posterior distributions of the parameters obtained through the simulation-based inference are approximated by a neural network (ANN) of which the input is the observations. The ANN is trained using the prior distribution samples (input of the ANN) and the corresponding simulation results (training set for the ANN). The likelihood function in the Bayesian rule (Eq. 4.10) is not needed.

We hypothesize that the processes in the two river segments are independent, that is, the parameters in segment 1 are not correlated to the ones in segments 2 due to the different environmental conditions, e.g., shading and macrophyte abundance, in the two segments (Glaser et al., 2020), therefore the parameters for the mixture effects in PPARγ–GeneBLAzer at MS mid and MS down are estimated separately. Figure 4.2A–B illustrate the prior and posterior distributions of ($[\alpha_i, k_i, R_i], i \in \{1, 2\}$) from SBI for EU_{bio} in PPARγ–GeneBLAzer in segment 1 and 2, respectively. The main diagonals show the prior and posterior distributions for the three parameters that are in kernel density estimation (KDE) from 1000 samples. The upper corner plots show individual samples (1000 samples) of the joint prior and posterior distributions. The joint KDEs are shown in the lower corner plots. In both segments, the prior and posterior distributions for all parameters show various levels of differences. The posterior distributions of the estimated parameters ($[\alpha_i, k_i, R_i], i \in \{1, 2\}$) approach Gaussian distributions, showing much narrower ranges than the priors, particularly for k and R, indicating the sorption and dissipation mechanisms are highly constrained by the observed mixture effect. The mixture effect in seg-

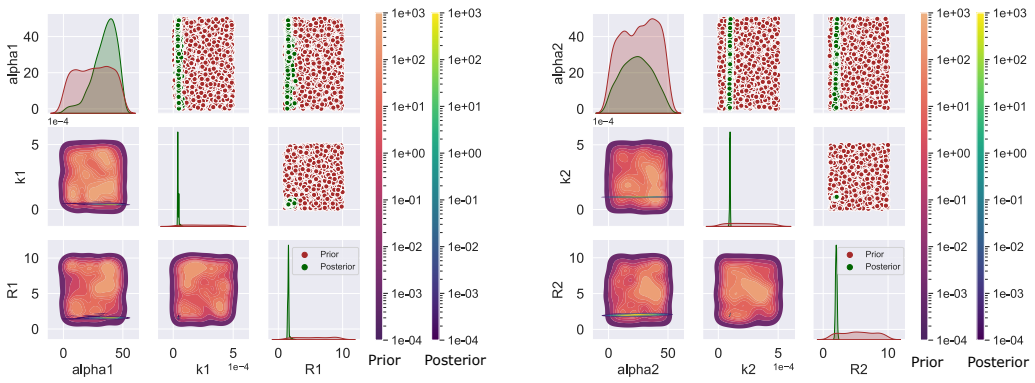

(A) Segment 1 **(B)** Segment 2

Figure 4.2: Prior and posterior of EU_{bio} in PPARγ–GeneBLAzer in segment 1 (A) and segment 2 (B) from SBI. The light red and green probability density functions in the main diagonals are the prior and posterior distributions, respectively. The upper corners show the individual 1000 samples for the three parameters. The lower corners show the kernel density estimate of the 1000 samples for the three parameters. α_i [m] is the dispersivity; k_i [s $^{-1}$] the first-order dissipation constant; R_i [-] the retardation factor ($i \in \{1, 2\}$.)

ment 2 shows stronger retardation (mean = 2.00 [-]) and dissipating reactions (mean = 9.66×10^{-5} [s^{-1}]) than that in segment 1 (mean = 1.57 [-] and mean = 4.10×10^{-5} [s^{-1}], respectively). The dispersivity α in both segments shows less distinct difference (less sensitive to the observed mixture effects), particularly in segment 2 (Figure 4.2B), indicating less dependence of dispersion on the observed mixture effect. The parameters estimate for AhR-CALUX and ERα-GenenBLAzer in Figure C.2 – Figure C.3 show consistent results, where the clearer difference between the prior and posterior distributions are seen in k and R. Such finding is not surprising since the transport mechanism (advection and dispersion) of the solute is mainly dependent on that of the fluid, except the solute specific pore-diffusion, e.g., Eq. 1.11, which would be orders of magnitude smaller than the velocity dependent hydrodynamic dispersion (Khakimov et al., 2017), therefore it should be consistent for all solutes. One of the advantages that SBI offers is the low computational cost. The only time-consuming process is the forward model runs (step 2 in Figure 4.1) after the parameter samples are drawn from the prior distributions. The forward run using parameter from prior is "embarrassingly parallel". Python library *joblib* (Faouzi and Janati, 2020) is integrated inside *sbi* toolbox, providing efficient parallel computing power. The whole inferencing took approximately two hours for 20000 forward runs on a AMD Ryzen 7 4700U (2.00 GHz) CPU.

In-stream dynamics. The parameter samples were drawn (Algorithm 2) from the trained neural posterior from SBI (Figure 4.2). Combining with the ensemble input from the Gaussian Process Regression (GPR), the ensemble temporal dynamics of the mixture effects were computed from 500 realizations ($N_{\text{sample}} = 500$ in algorithm Algorithm 3). Figure 4.3 illustrates the modeled EU_{bio} in PPARγ–GeneBLAzer time-series signals. The mean of the ensemble output and the 95% confidence interval (CI) of the ensemble output were computed. Overall, the modeled time-series could reproduce the major features in the temporal dynamics of the measurements. The majority of the measurements at both sites

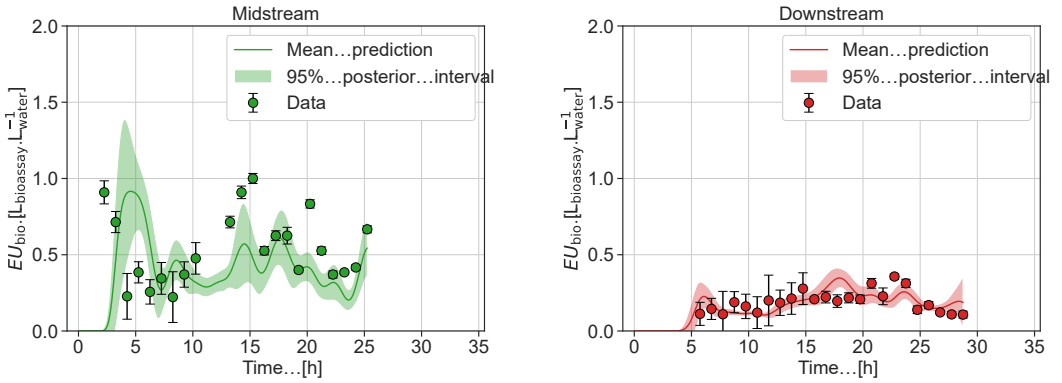

(A) EU_{bio} in PPARγ–GeneBLAzer at midstream site

(B) EU_{bio} in PPARγ–GeneBLAzer at downstream site

Figure 4.3: Modeled ensemble time-series for EU_{bio} in PPARγ–GeneBLAzer at the midstream (A) and downstream site (B). The light green and red areas represent the 95% confidence interval of the modeled ensemble from 500 realizations ($N_{sample} = 500$ in Algorithm 3). Analytical uncertainties (one standard error) from the measurement are shown by the error bars.

fall withing the 95% confidence interval (CI) of the modeled ensemble. Still, the model performances vary when comparing the modeled results at the midstream and the downstream site. At the midstream site (Figure 4.3A), the modeled ensemble misses the initial large drop (2.5th – 5th hour) in the measured EU_{bio} by being delayed for approximately two hours. During the periods between 10th – 15th hour and 20th – 23th hour, the modeled results are lower than the measured EU_{bio}. At a few time points (at approximately 14th, 16th, 21st and 22nd hour), even the upper 95% CI of the modeled ensemble could not capture the lower error bar of the measurement. But throughout the whole period, the modeled ensemble could reproduce the overall temporal patterns in the measured EU_{bio}, particularly by capturing the initial drop after approximately 7th hour, as well as the strong oscillations spanning over 16-hour long period (9th hour – 25th hour) which peak at 14th, 17th and 25th hour. At the downstream site (Figure 4.3B), our approach yields better model performance. The measured EU_{bio} shows relatively constant temporal dynamics comparing to that at the midstream. The mean of the modeled ensemble effectively captures the overall temporal patterns of the measured EU_{bio}. The relatively large deviation happened only at one short period (17th – 19th hour) where the modeled ensemble show a small peak and the temporal pattern of the measured EU_{bio} is almost constant. The 95% CI of the modeled ensemble covers 22 out of the 24 measured EU_{bio} over the 24-hour sampling period considering the measurement errors. The only two exceptions are at approximately 17th and 23rd hour where measurements considering the measurement errors fall outside of the 95% CI of the modeled ensemble. Modeled mixture effects ensemble at the midstream and downstream sites in AhR–CALUX and ERα–GeneBLAzer are in Figure C.4 and Figure C.5, respectively. Our approach that integrates the stochastic input from GPR and parameters from the neural posterior yields overall good fit of the modeled ensemble to the measured EU_{bio} at both midstream and downstream site, which in return supports validity of the processes that we parameterized. The computed mean root mean square error ($\overline{\text{RMSE}}$, Eq. C.1) and mean normalized root mean square error ($\overline{\text{NRMSE}}$, Eq. C.2) for all three bioassay in the two segments are in Table C.1.

4.3.2 Physics-informed neural network

Space-time distribution and in-stream dynamics. The space and time coordinates are the input of the neural network in PINN, allowing the model to compute the space-time distribution of EU_{bio}. Figure 4.4A shows the modeled space-time distribution of EU_{bio} in PPARγ–GeneBLAzer in segment 2 (between midstream and downstream site). Unlike

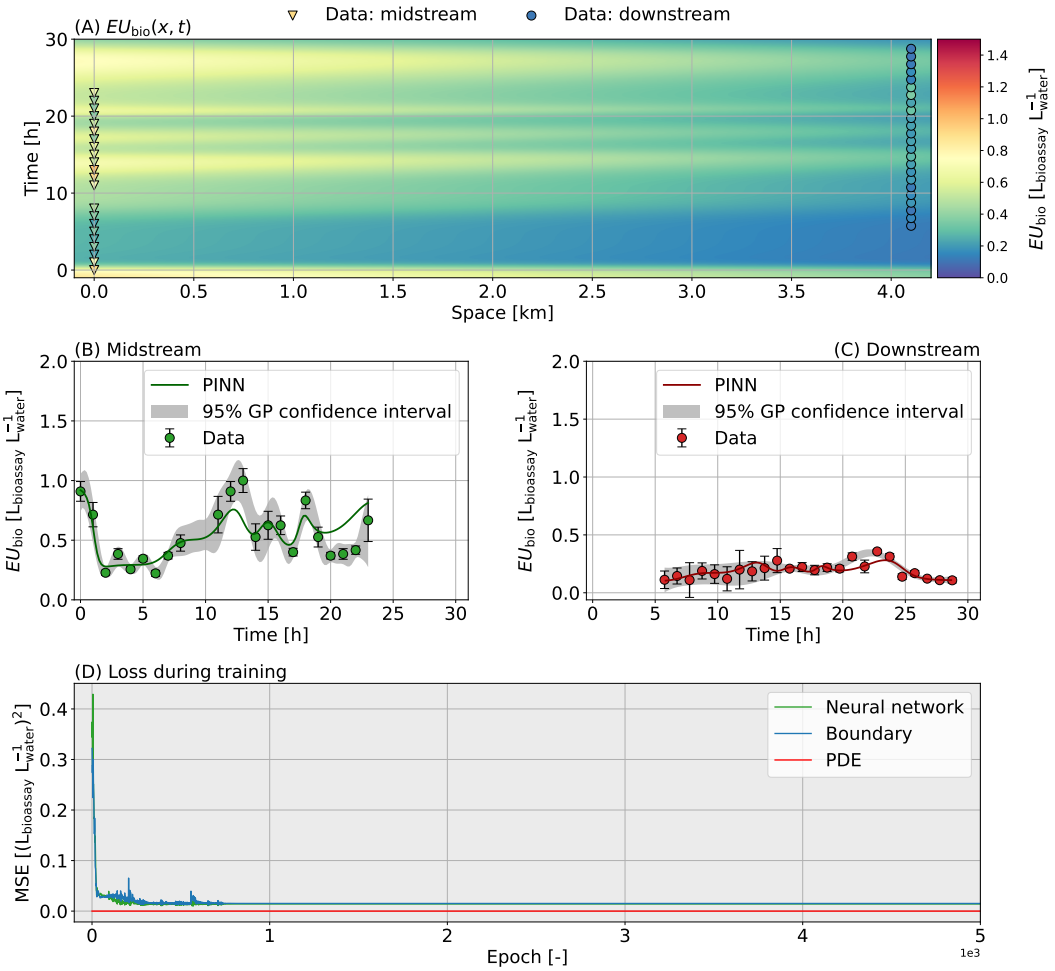

Figure 4.4: EU_{bio} in PPARγ–GeneBLAzer in segment 2 bounded by the midstream and downstream sites. (A) shows the distribution of EU_{bio} in the whole space-time domain. (B) and (C) show EU_{bio} at midstream and downstream sites, respectively. The light grey areas represent the 95% confidence interval of the Gaussian process regression on data. The training processes of the three loss functions (Eqs. 4.6, 4.7, and 4.8) are shown in (D). Epoch: the number of iterative training process when the whole dataset is used during the training (Section 4.2.3).

the standard numerical or analytical reactive transport models, to train the solution at the whole space-time domain, PINN requires observations collected across the domain. In practice when time-series samples in rivers are collected, it is logistically challenging to sample over a period of days with a high spatial resolution along a river course that is kilometers long. In the current study, the data from upstream, midstream and downstream sites provides constraints for PINN to train the boundaries of the domain (Eq. 4.6 and 4.8). To effectively show the measured EU_{bio} at a finer temporal resolution (one minute), instead

of using interpolated EU_{bio} values, we compute the 95% confidence interval (CI) from the Gaussian Process Regression (GPR) (methods in Section 3.2.5 of Chapter 3) on the measurements and show them in the grey areas in Figure 4.4B – C. The 95% CI of GPR, considering the measurement errors, not only realistically represents the temporal dynamics of EU_{bio} between the measurement points, but also helps to robustly illustrate the temporal dynamics of the EU_{bio} measurements at the time points where the measurements are missing. Figure 4.4B – C show the modeled time-series of EU_{bio} in PPARγ–GeneBLAzer at midstream and downstream sites, respectively. For both sites, PINN demonstrates the superior capability at capturing the temporal patterns of the measured EU_{bio} in PPARγ–GeneBLAzer. Three metrics, root mean square error (RMSE Eq. C.3), normalized root mean square error (NRMSE Eq. C.4), and MSE (Eq. 4.6), are computed for evaluating the performance and are shown in Table C.2. During the first 15 hours at midstream site (Figure 4.4B), the measured EU_{bio} experiences a sharp decrease in the first two hours, then gradually increases over a ten-hour period before experiencing oscillations during the next ten hours. The only relatively large deviation of the PINN results from the measurements appears in the last four hours of the sampling period. This is due to the sharp gradient presented (between 17th and 20th hour) that PINN is known to have difficulties to capture (more discussions in Section 4.3.3). At the downstream site (Figure 4.4C), the measured EU_{bio} shows rather different temporal patterns from that at the midstream site. The overall measured EU_{bio} is lower than that at the midstream site. A smooth temporal pattern of EU_{bio} is observed during the whole sampling period and the sharp drop observed at the beginning of the midstream disappears at the downstream site. The simulated results from PINN could accurately reproduce (MSE = 1.40×10^{-2} in Table C.2) the temporal dynamics of the measurements at the downstream site. All modeled results fall within the analytical uncertainty (one standard error) of the measurement except the two points between 20th and 25th-hour. For both sites, the results from PINN fall within the 95% CI of GPR at the time points where there are no measurements. Essentially by taking the space and time coordinates, PINN is able to reproduce the dynamics at both locations simultaneously, between which exists a rather drastic transition of EU_{bio} measurements. PINN shows the advantage over the numerical model (Eq. 4.1) that requires complex parameterization to achieve the similar performance, especially when the data used for constructing the input and the output shows such different temporal patterns. We train the PINN model on the same CPU used to train the neural network in SBI. The training takes 21.17 minutes to complete 5000 epochs. Figure 4.4D shows the three losses from the neural network, PDE, and the inflow boundary over the training process (Eq. 4.6, Eq. 4.7, and Eq. 4.8, respectively). All three losses become relatively constant after 1000 epochs. The simulated mixture effects from PINN for AhR–CALUX and ERα–GeneBLAzer in the two segments are in Figure C.6 – Figure C.7 and Figure C.9 – Figure C.10, respectively.

4.3.3 Methods selection: an objective-oriented choice

Performance limitations of PINN when applied to field data. Comparing the overall temporal dynamics at the midstream and the downstream site in Figure 4.4B – C, EU_{bio} at the midstream site shows much stronger oscillations (particularly the 12th – 22th hour) than EU_{bio} at the downstream site. Various literature (Fuks and Tchelepi, 2020; Mishra and Molinaro, 2022; Arora, 2023) report that PINN has difficulty converging to the correct solution when a sharp gradient is present in the data used for training. Arora et al., 2022 shows that PINN suffers from poor accuracy in the solution or convergence issue when a

second-order spatial derivative of the governing PDE (Eq. 4.5) is computed. These inherent limitations of PINN lead to the deviation of the modeled results from the measurements at the last five hours of the sampling period at midstream. For the downstream where EU_{bio} shows a relatively constant temporal pattern, PINN shows better performance.

Another inherent limitation requiring attention is that since there is no measurement obtained at the locations between the three measuring stations (upstream, midstream and downs sites) due to logistic reasons, the model is trained only on the EU_{bio} measurement collected at the three sampling sites, meaning the modeled EU_{bio} at any locations between these three sites could not be quantitatively evaluated during the training process. Also, without training data in between the midstream and downstream site, the space-depended normalization factor $k_{\text{normal}}(x)$ can only be linearly interpolated between $y_{\text{max,data}}$ (Eq. 4.6) and $y_{\text{max,boundary}}$ (Eq. 4.8). This approach leads the modeled EU_{bio} to experience a linear decay, instead of the exponential decay between the two sampling sites, which is not coherent to the physical law imposed in Eq. 4.5. Figure 4.5A–B illustrate the three-dimensional field of space-time distribution of EU_{bio} in PPARγ–GeneBLAzer in segment 2. To compare the space-time distribution of the EU_{bio} from the one-dimensional reactive transport model coupled with SBI and GPR (SBI & GPR aided reactive transport) and PINN, the EU_{bio} ensemble mean from SBI & GPR aided reactive transport model is shown in Figure 4.5A, where an exponential decay could be observed for EU_{bio}. Figure 4.5B shows the three-dimensional field of EU_{bio} from PINN, in which although PINN yields excellent fit at the boundaries (midstream and downstream site) of the domain, the computed EU_{bio} space-time distribution shows a linear decay over time. However, this particular limitation can be overcome if more spatially distributed training data is provided by setting up more sampling sites along the river course (if logistically applicable).

Comparison of methods. Both SBI & GPR aided reactive transport and PINN approximate the solution of the governing equation (Eq. 4.1) that describes the in-stream processes of the mixture effect EU_{bio}. The former integrates the stochastic input from GPR and the parameter samples from a neural posterior into the numerical model, where the physical processes are explicitly expressed and the ensemble EU_{bio} are computed. The latter computes the deterministic results of EU_{bio} through a trained neural network using the spatial and temporal coordinates as the input. The gradient of the solution with respect to space and time plays the critical role of physics-informing. The performance of the two approaches varies. Both methods have its own strengths and limitations. PINN shows clear advantages over the SBI & GPR aided reactive transport model in terms of prediction accuracy (comparing Figure 4.3A–B and Figure 4.4A–B). Even with an ensemble output, the latter could not guarantee the full capture of the temporal patterns of the measured EU_{bio}, outperformed by the deterministic result from PINN. On the other hand, SBI & GPR aided reactive transport model is able to compute a realistic EU_{bio} distribution across the whole space-time domain, whereas PINN, even with the imposed physical law constraints (Eq. 4.5), still needs more data (more spatially distributed data in our case) for training before achieving the similar computing accuracy for the whole space-time domain. Figure 4.5C–D shows the modeled space-time distribution of EU_{bio} in PPARγ–GeneBLAzer in segment 2 in the two-dimensional field. SBI & GPR aided reactive transport model (Figure 4.5C) is able to compute the correct characteristics (Shang et al., 2004), where colors are the EU_{bio} ensemble mean. The cotangent of the angle (θ) of the tilted characteristics mathematically represents the effective velocity ($\cot(\theta) = dx/dt = v/R$, Eq. 4.1) with which

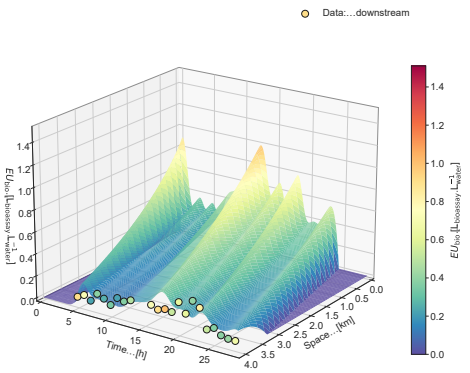

(A) SBI: mean EU_{bio} in the three-dimensional field

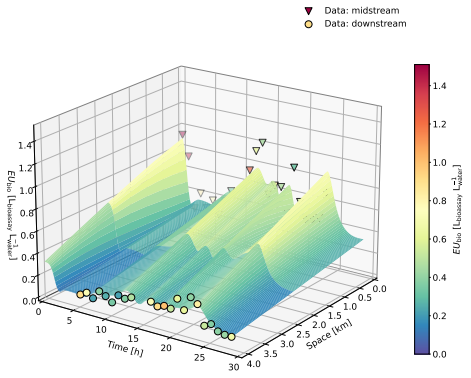

(B) PINN: EU_{bio} in the three-dimensional field

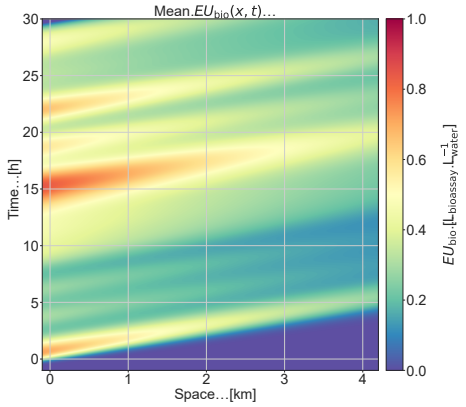

(C) SBI: mean EU_{bio} in the two-dimensional field

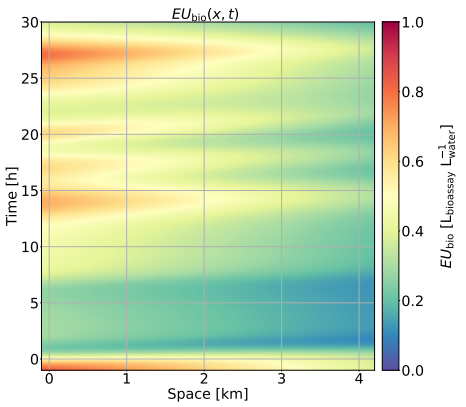

(D) PINN: EU_{bio} in the two-dimensional field

Figure 4.5: Modeled space-time distributions of EU_{bio} in PPARγ in segment 2. Results from SBI & GPR aided reactive transport are in (A) and (C); Results from PINN are in (B) and (D). In (C), the tilted characteristics mathematically represents the effective velocity ($\cot(\theta) = dx/dt = v/R$, Eq. 4.1) with which the state variable (EU_{bio}) travels through the system.

the state variable (EU_{bio}) travels through the system. PINN, although accurately computing the temporal patterns, could not reproduce the correct characteristics at the locations where there are no training data (Figure 4.5D). The computed three-dimensional field for EU_{bio} in AhR–CALUX and ERα–GeneBLAzer in the two segments are in Figure C.8A-B and Figure C.11A–B, respectively.

Method per choice. The preference for one method over the other depends on the objective of the modeling and setup of the experiments or field campaigns that provide the measurements. SBI & GPR aided reactive transport yields inferior prediction accuracy than PINN. But the former shows the advantages when the main objective of modeling is, e.g., to estimate the model parameter values that have physical meanings but could not be measured directly in the field or laboratories. SBI yields high sampling efficiency when combined with models that explicitly express (parameterize) the physical processes, meanwhile presenting meaningful parameter values and their uncertainty through poste-

rior distributions. Once the model parameterization is settled, scenarios analysis could be conducted by testing various parameter values, of which the results provide quantitative information regarding the optimal setup for the future field campaigns and experiment. To improve the prediction accuracy, a more complex parameterization is required, which in return would potentially hinder the parameter estimate performance.

On the other hand, PINN yields high prediction accuracy, demonstrating the merits when the main objective of the modeling is to 1) accurately reproduce the spatial and temporal patterns of the observations and 2) compute reliable predictions at future time and additional space points. Once the neural network is trained, the extrapolation of the results using the future space-time coordinates could be easily achieved since the forward runs of PINN is computationally cheap. However, training PINN to compute the accurate space-time distribution of state variables demands high spatial–temporal resolution data collected across the entire domain, which is challenging during large-scale field campaigns. Although the forward run of PINN is computationally cheap, the training process suffers from its time-consuming nature. Since the input of PINN is only the space-time coordinates, conducting scenario analysis to optimize the setups for the future field campaign is not possible.

4.4 Implications

To gain quantitative understanding of the in-stream processes of micropollutant mixture effects, yield accurate model prediction, and estimate model parameter values, balancing the levels of the model details and the computational costs is essential. We compared the results from SBI & GPR aided reactive transport and PINN, demonstrating the advantage of combining numerical and deep learning methods in process-based models when applying the model to the field data of the mixture effects. We also outlined the limitations of the two methods in real-world data applications, highlighting the trade-offs with respect to the purposes of the modeling.

Both methods require more data and less uncertainty in the data for training (calibration) and for verifying more realistic parameterization. For the future studies regarding mixture effects data acquisition, the mixture effects as a new state variable could be used to conduct laboratory flow-through column tests (Sorwat et al., 2021; Strobel et al., 2023), from where the data is produced in a more controlled environment. The factors that influence the reactive transport processes, e.g., flow rate, cross-sectional area and inflow concentration (mixture effect), can be fixed at constant values. The mixture data can also be collected at finer spatial and temporal resolution in laboratories due to less logistic constraints. The spatial and temporal behavior of concentration signals in porous media in laboratory conditions are well studied (Liu et al., 2021, 2022), which can be extrapolated to the mixture effects. Therefore, the measured mixture effects data can provide more informative and quantitative information for better parameterizing the model to understand the reactive transport processes of the mixture effects.

To further quantify the uncertainty from the description of the reactive transport processes of the mixture effects, a new perspective that maintains the differential equation structure while complemented by the deep learning method is need. The hybrid model (Rackauckas et al., 2020, 2021; Faizan Bangi and Kwon, 2022) consists of the parameterized known processes in differential equation forms and unknown processes quantified by a deep neural network. Recent advances in the programming language *Julia* (Bezanson

et al., 2012) and its library *DiffEqFlux.jl* (Rackauckas et al., 2019) enable implementing and solving such hybrid systems without modifying the physical model structure. Applying such hybrid models to the mixture effects field data has the potential to 1) provide insights into interpretable physical processes and 2) improve prediction accuracy, as well as 3) identify unknown physical processes for the mixture effects by combining with Bayesian inference (Dandekar et al., 2020). The rapid development of those tools opens the new doors of scientific machine learning for quantitative studies of the mixture effects.

Chapter 5

Summary

5.1 Key Findings

The main goal of the thesis is to address the in-stream processes of the organic micropollutants mixture effects quantified in *in vitro* bioassays from a quantitative point of view, providing complementary knowledge to the understandings of the single compounds in rivers (Liu et al., 2020). In pursuit of this goal, I firstly hypothesized that the fate of the mixture effects in rivers is characterized by the reactive transport processes that follow the mass conservation law. Secondly, I tested my hypothesis by integrating process-based models with mixture effect field data collected under different flow conditions, from where I interpreted the physical meanings of the estimated parameters and quantified their uncertainty from the stochastic perspective. Lastly, I explored deep learning methods to efficiently achieve more accurate (than numerical methods) solution for the previously used reactive transport models and the parameter posterior, while maintaining the parameterizations that represent physical laws for the mixture effects. In the following context, I highlight the key findings and their connections to the objectives outlined in Section 1.2.

1. Can the advection-dispersion-reaction (ADR) equation describe the in-stream processes of the mixture effects?

In Chapter 2, I formulated the solution of the one-dimensional process-based model involving advection, dispersion and first-order dissipation reaction processes into the convolution form, which facilitates the quantification of model parameter values and uncertainty using the Metropolis-Hasting Markov Chain Monte-Carlo. The model was applied to mixture effects data collected using the Lagrangian sampling scheme under unsteady flow conditions in the Steinlach river. Using the parameters from the posterior distribution, the model was able to compute the ensemble results that effectively reproduce the spatial and temporal dynamics of the measured mixture effects with various endpoints. We show that the mixture effects of the organic micropollutants can be treated as intensive state variables, of which the rates of change in rivers can be viewed as bulk processes that are quantitatively expressed by the advection-dispersion-reaction equation derived from the mass conservation law. Similar to the solute reactive transport, the transport processes of the mixture effects are controlled by that of the flow, thus the parameters can be determined by conservative tracers, whereas the reactive processes are

effects-specific. As a result, further more complex parameterizations could be developed for studying the processes of the mixture effects under transient flow conditions.

2. Can the ADR based-transient model be used to characterize the in-stream processes of the mixture effects under transient flow conditions?

In Chapter 3, I parameterized the one-dimensional partial differential equation-based reactive transport model with transient terms for the mixture effects. The model was conditioned on mixture effects data collected in the Ammer river during a storm event, during which the discharge wave formed by the transient flow was characterized by a diffusive wave model. To balance the need of presenting ensemble results and the computational costs of running the transient numerical model, I characterized the model inflow boundary conditions using the conditional realizations from the Gaussian Process Regression (GPR), with which the efficiently computed ensemble results could effectively reproduce the dynamics of the mixture effects measurements, supporting the validity of the model parameterization. We show that the storm-caused transient discharge played a crucial role in 1) delineating the advective and dispersive transport processes for the mixture effects, for the velocity with which the mixture effects travel in the river was directly impacted by the transient discharge; 2) introducing the lateral inflow into the river, functioning as a lateral inflow-proportioned source for the mixture effects along the river course, alongside the WWTP as a point source. The mixture effects in-stream signal patterns in the transient flow conditions were largely characterized by the transport processes.

3. How can the combination of numerical and deep learning methods be used to solve the ADR, estimate parameter values, and improve the model performance for the mixture effects?

In Chapter 4, I applied the rapidly developing deep learning tools to improve the performance (prediction accuracy and parameter estimates efficiency) of the one-dimensional reactive transport model conditioned on the real-world mixture effects data. I implemented the simulation-based inference (SBI) to efficiently approximate the posterior distribution. Coupled with ensemble input from the GPR, the model computed the ensemble mixture effects that could mimic the main features of the measured mixture effects dynamics. I also applied the physics-informed neural network (PINN) on the mixture effect data, which yielded superior prediction accuracy. However, through the comparison of the two approaches in terms of the model training efforts, the amount of data needed for training, especially when the models are conditioned on real-world field data, I demonstrated that the preference of one approach over the other is heavily dependent on the goal of the modeling. PINN is a powerful tool when the prediction accuracy is the focus. When parameter estimates is the primary modeling task, SBI coupled with the numerical model is the more suitable approach.

Overall, I conclude that the bulk reactive transport processes of the mixture effects, effect unit and toxic unit, under both baseflow and transient flow conditions in rivers, can be quantitatively described by the advection-dispersion-reaction equation. With informative field measurements, the estimated dissipation reactive constants provide quantitative information regarding bulk kinetic reactions of the organic micropollutant mixture. Since

there are no documented laboratory measurements about the bulk reactive constants for the mixture effects, our optimized results can be used not only to analyze the fate of the mixture in different environments but also as an indicator for possible biological accumulation. From the qualitative perspective, the bulk kinetic reaction constants provides information for developing environmental remediation strategy and regulations with regards the mixture effects limits. With our modeling approach, further more detailed parameterizations can be developed for the processes of the mixture in more complex environment, e.g., multi-compartment. Our time-series characterization methods and deep learning fused angle provides the option for efficient parameter posterior estimates and ensemble results computing for complex reactive transport models to capture the intricate dynamics of the mixture field data.

· § ·

One of the main obstacles I encountered during my doctoral research was to reproduce the complex in-stream dynamics observed in the measured mixture effects while parameterizing explainable physical processes. I tackled the obstacle by utilizing a combination of tools from various modeling perspectives: numerical modeling, convolution, Gaussian Process Regression, Bayesian optimization, deterministic global optimization, and deep learning methods including simulation-based inference and physics-informed neural network. This experience taught me that a real-world environmental system can rarely be well understood using a single method. The complex nature of the real-world problems we are facing frequently requires various angles of approach and strong collaboration of multiple disciplines in order to achieve the solution that is as fruitful as possible.

5.2 Outlook

Experimental settings for mixture effects for future quantitative study

One of the main hypotheses of the thesis is that the mixture effect is concentration equivalent. Through Chapter 2, Chapter 3, and Chapter 4, I demonstrated that the mixture effect, of which the rate of change follows the mass conservation law, is an invaluable intensive state variable for quantitative studies of river water quality. As I previously mentioned in Section 4.4, the mixture effects can be futher used for studying the transport and reactive processes of mixture effects of organic micropollutants in more complex environment, e.g., porous media. However, to minimize the uncertainty originating from the conceptualization stage, the experiments should be conducted in a more controlled environment, e.g., flow-through column experiments in laboratories, where certain parameters of the investigating processes can be fixed at constant values, and the mixture effects can be measured at finer spatial and temporal resolutions. Also under such conditions, the spatial and temporal behavior of the concentration signal (therefore can be extrapolated to the mixture effects) is very well studied. All of these can provide more insightful data for setting up more comprehensively parameterized models for the mixture effects.

Regarding studying the mixture effects in rivers, one of the potential new angles is to couple the reactive transport processes in the moving water phase with the hyporheic zone to study, e.g., the turnover of the mixture of legacy compounds (Liu et al., 2020). The information from the laboratory experiments, as well as the models built on top of that can then be used for improving the field sampling schemes in rivers. Similar to the laboratory

experiments, if the logistic constraints could be overcome, a sampling scheme with finer spatial and resolutions in both water phase and hyporheic zone would provide invaluable information for parameterizing more detailed river models for the mixture effects.

Deep learning aiding process-based models, not the other way around.

As I previously mentioned in Section 1.1, process-based modeling operates on the inevitable "conundrum" that the conceptual uncertainty in the efforts of describing the investigating environmental system is tremendous to begin with. Since not all uncertainty introduced by the observed processes affect the overall system behavior, a typical yet effective way to conduct modeling is to identify and concentrate on the controlling factors of the system.

Conditioned on data, process-based models are used to obtain parameter values of the real-world system, particularly those parameters that are difficult to measure directly. Uncertainty originates from the fact that models are the simplification of the real-world system, and data is scarce and contains measurement errors. Adding complex processes in the model imposes constraints on the computational efforts, hindering the application of Bayesian inference when (quite often) ensemble results are needed. The balance between model complexity and its practicality has been a long debate.

In an effort to overcome these obstacles, the environmental modeling field is advancing towards the joint force of numerical tools and deep learning techniques. This is largely due to the fact that over the recent years, the neural network-based deep learning methods already show superior performance in terms prediction accuracy (Shinde and Shah, 2018; Fujiyoshi et al., 2019; Wright et al., 2022; Cuomo et al., 2022) and become easy to implement thanks to the growth in computing hardware development and maturation of deep learning frameworks, e.g., *PyTorch* and *TensorFlow*.

Therefore in my view, the balance between uncertainty quantification and model complexity will not need to be a compromised scenario, if we take the advantage of the new tools from the rapidly developing new scientific computing programming languages and their libraries. As I mentioned in Section 4.4, a hybrid system that inserts a neural network inside the traditional numerical reactive transport model implemented in *Julia* has various advantages over the traditional process-based models. *Julia*, as a high-level scientific computing language, stands out for maintaining the speed of low-level programming language. It provides various efficient numerical tools, e.g., a comprehensive and high-performance ODE solver suite that can solve the hybrid system, from its rapidly developing libraries *(DifferentialEquations.jl, Flux.jl, DiffEqFlux.jl, Turing.jl)*, all of which can be used in the hybrid models. Moreover, the core of the hybrid models is to prioritize the known physical processes that are well studied. The neural network added alongside these physical processes plays aiding roles, e.g., to help the model capture the intricate patterns in data and nonlinear relationships of unknown processes. In this way, the merits of the physical models, e.g., interpretablilty, consistency, overpower the drawback of neural networks, e.g., being sensitive to the variations in data, tendency to overfit training data. Comparing with other ways of fusing the deep learning and numerical tools where the role of latter often is out weighted by the former, in my opinion, the philosophy behind the hybrid model makes it a more suitable way for the future development of process-based models. Combining with Bayesian inference, the hybrid model presents a suite of powerful tools that are able to interpret the known processes, improve the prediction accuracy, estimate the parameters of the system, as well as identify the hidden physical processes.

Bibliography

Abadi, M., Barham, P., Chen, J., Chen, Z., Davis, A., Dean, J., Devin, M., Ghemawat, S., Irving, G., Isard, M., Kudlur, M., Levenberg, J., Monga, R., Moore, S., Murray, D. G., Steiner, B., Tucker, P., Vasudevan, V., Warden, P., Wicke, M., Yu, Y., and Zheng, X. TensorFlow: A system for large-scale machine learning. *Proc. 12th USENIX Symp. Oper. Syst. Des. Implementation, OSDI 2016*, (June 2021):265–283, 2016.

Adams, W., Garman, E., Van Genderen, E., Gorsuch, J., and Dwyer, R. Modeling and interpreting biological effects of mixtures in the environment: Introduction to the metal mixture modeling evaluation project. *Environ. Toxicol. Chem.*, 34(4):721–725, 2015. doi:10.1002/etc.2750.

Allgeier, J. and Cirpka, O. A. Surrogate-Model Assisted Plausibility-Check, Calibration, and Posterior-Distribution Evaluation of Subsurface-Flow Models. *Water Resour. Res.*, pages 1–28, 2023. ISSN 0043-1397. doi:10.1029/2023wr034453.

Antweiler, R. C., Writer, J. H., and Murphy, S. F. Evaluation of wastewater contaminant transport in surface waters using verified Lagrangian sampling. *Sci. Total Environ.*, 470-471:551–558, 2014. ISSN 18791026. doi:10.1016/j.scitotenv.2013.09.079.

Aron, G. and Borrelli, J. Stream baseflow prediction by convolution of antecedent rainfall effects. *J. Am. Water Resour. Assoc.*, 9(2):360–365, 1973. ISSN 17521688. doi:10.1111/j.1752-1688.1973.tb01743.x.

Arora, R. A Deep Learning Framework for Solving Hyperbolic Partial Differential Equations: Part I. pages 1–20, 2023. doi:https://doi.org/10.48550/arXiv.2307.04121.

Arora, R., Kakkar, P., Dey, B., and Chakraborty, A. Physics-informed neural networks for modeling rate- and temperature-dependent plasticity. 2022. doi:https://doi.org/10.48550/arXiv.2201.08363.

Barber, L. B., Keefe, S. H., Brown, G. K., Furlong, E. T., Gray, J. L., Kolpin, D. W., Meyer, M. T., Sandstrom, M. W., and Zaugg, S. D. Persistence and potential effects of complex organic contaminant mixtures in wastewater-impacted streams. *Environ. Sci. Technol.*, 47(5): 2177–2188, 2013. ISSN 0013936X. doi:10.1021/es303720g.

Beg, M. N. A., Meselhe, E. A., Kim, D. H., Halgren, J., Wlostowski, A., Ogden, F. L., and Flowers, T. Diffusive Wave Models for Operational Forecasting of Channel Routing at Continental Scale. *JAWRA J. Am. Water Resour. Assoc.*, (October):1–24, 2022. doi:10.1111/1752-1688.13080.

Berkhahn, S. and Ehrhardt, M. *A physics-informed neural network to model COVID-19 infection and hospitalization scenarios*, volume 2022. 2022. ISBN 4920243952. doi:10.1186/s13662-022-03733-5.

Bezanson, J., Karpinski, S., Shah, V. B., and Edelman, A. Julia: A Fast Dynamic Language for Technical Computing. pages 1–27, 2012.

Boudreau, B. P. *Diagenetic models and their implementation: modelling transport and reactions in aquatic sediments.* Number 505. Springer Berlin Heidelberg, Berlin, first edition, 1997. ISBN 13:97S-3-642-64399-6. doi:Io.Ioo7/97S-3-642-60421-S.

Brennan, J. C., He, G., Tsutsumi, T., Zhao, J., Wirth, E., Fulton, M. H., and Denison, M. S. Development of Species-Specific Ah Receptor-Responsive Third Generation CALUX Cell Lines with Enhanced Responsiveness and Improved Detection Limits. *Environ. Sci. Technol.*, 49(19):11903–11912, 2015. ISSN 15205851. doi:10.1021/acs.est.5b02906.

Brooks, S. P. and Gelman, A. General methods for monitoring convergence of iterative simulations. *J. Comput. Graph. Stat.*, 7(4):434–455, 1998. ISSN 15372715. doi:10.1080/10618600.1998.10474787.

Carrera, J., Saaltink, M. W., Soler-Sagarra, J., Jingjing, W., and Valhondo, C. Reactive Transport: A Review of Basic Concepts with Emphasis on Biochemical Processes. *Energies*, 15(3), 2022. ISSN 19961073. doi:10.3390/en15030925.

Cedergreen, N. Quantifying synergy: A systematic review of mixture toxicity studies within environmental toxicology. *PLoS One*, 9(5), 2014. ISSN 19326203. doi:10.1371/journal.pone.0096580.

Chavez Rodriguez, L., Ingalls, B., Schwarz, E., Streck, T., Uksa, M., and Pagel, H. Gene-Centric Model Approaches for Accurate Prediction of Pesticide Biodegradation in Soils. *Environ. Sci. Technol.*, 54(21):13638–13650, 2020. ISSN 15205851. doi:10.1021/acs.est.0c03315.

Chow, R., Scheidegger, R., Doppler, T., Dietzel, A., Fenicia, F., and Stamm, C. A review of long-term pesticide monitoring studies to assess surface water quality trends. *Water Res. X.*, 9(August):100064, 2020. ISSN 2589-9147. doi:10.1016/j.wroa.2020.100064.

Cirpka, O. A. and Valocchi, A. J. Two-dimensional concentration distribution for mixing-controlled bioreactive transport in steady state. *Adv. Water Resour.*, 30(6-7):1668–1679, 2007. ISSN 03091708. doi:10.1016/j.advwatres.2006.05.022.

Cirpka, O. A., Fienen, M. N., Hofer, M., Hoehn, E., Tessarini, A., Kipfer, R., and Kitanidis, P. K. Analyzing bank filtration by deconvoluting time series of electric conductivity. *Ground Water*, 45(3):318–328, 2007. ISSN 0017467X. doi:10.1111/j.1745-6584.2006.00293.x.

Clement, C. F. Solutions of the continuity equation. *Proc. R. Soc. London. A. Math. Phys. Sci.*, 364(1716):107–119, 1978. ISSN 0080-4630. doi:10.1098/rspa.1978.0190.

Costanzo, S. D., Murby, J., and Bates, J. Ecosystem response to antibiotics entering the aquatic environment. *Mar. Pollut. Bull.*, 51(1-4):218–223, 2005. ISSN 0025326X. doi:10.1016/j.marpolbul.2004.10.038.

Cranmer, K., Brehmer, J., and Louppe, G. The frontier of simulation-based inference. *Proc. Natl. Acad. Sci. U. S. A.*, 117(48):30055–30062, 2020. ISSN 10916490. doi:10.1073/pnas.1912789117.

Cuomo, S., Di Cola, V. S., Giampaolo, F., Rozza, G., Raissi, M., and Piccialli, F. Scientific Machine Learning Through Physics–Informed Neural Networks: Where we are and What's Next. *J. Sci. Comput.*, 92(3):1–62, 2022. ISSN 15737691. doi:10.1007/s10915-022-01939-z.

Cuomo, S., De Rosa, M., Giampaolo, F., Izzo, S., and Schiano Di Cola, V. Solving groundwater flow equation using physics-informed neural networks. *Comput. Math. with Appl.*, 145:106–123, 2023. ISSN 08981221. doi:10.1016/j.camwa.2023.05.036.

Dandekar, R., Chung, K., Dixit, V., Tarek, M., Garcia-Valadez, A., Vemula, K. V., and Rackauckas, C. Bayesian Neural Ordinary Differential Equations. pages 1–20, 2020.

Desiante, W. L., Minas, N. S., and Fenner, K. Micropollutant biotransformation and bioaccumulation in natural stream biofilms. *Water Res.*, 193, 2021. ISSN 18792448. doi:10.1016/j.watres.2021.116846.

Dittmer, U., Bachmann-Machnik, A., and Launay, M. A. Impact of combined sewer systems on the quality of urban streams: Frequency and duration of elevated micropollutant concentrations. *Water*, 12(3), 2020. ISSN 20734441. doi:10.3390/w12030850.

Dormand, J. R. and Prince, P. J. A reconsideration of some embedded Runge-Kutta formulae. *J. Comput. Appl. Math.*, 15(2):203–211, 1986. ISSN 03770427. doi:10.1016/0377-0427(86)90027-0.

Du, Y. and Ekaterinaris, J. A. Time-marching schemes for spatially high order accurate discretizations of the Euler and Navier–Stokes equations. *Prog. Aerosp. Sci.*, 130(January): 100795, 2022. ISSN 03760421. doi:10.1016/j.paerosci.2021.100795.

Dubey, R. K. Flux limited schemes: Their classification and accuracy based on total variation stability regions. *Appl. Math. Comput.*, 224:325–336, 2013. ISSN 00963003. doi:10.1016/j.amc.2013.08.027.

Eleftheriadis, S., Nicholson, T. F., Deisenroth, M. P., and Hensman, J. Identification of Gaussian process state space models. In *Adv. Neural Inf. Process. Syst.*, volume 2017-Decem, pages 5310–5320, 2017.

Escher, B. I., Neale, P. A., and Leusch, F. D. *Bioanalytical Tools in Water Quality Assessment*. IWA Publishing, London, second edition, 2021. ISBN 9781789061987. doi:10.2166/9781843393689.

Escher, B. I., Henneberger, L., König, M., Schlichting, R., and Fischer, F. C. Cytotoxicity burst? Differentiating specific from nonspecific effects in tox21 in vitro reporter gene assays. *Environ. Health Perspect.*, 128(7):1–10, 2020. ISSN 15529924. doi:10.1289/EHP6664.

Escher, B. I., Neale, P. A., and Villeneuve, D. L. The advantages of linear concentration–response curves for in vitro bioassays with environmental samples. *Environ. Toxicol. Chem.*, 37(9):2273–2280, 2018. ISSN 15528618. doi:10.1002/etc.4178.

Escher, B. I., Braun, G., and Zarfl, C. Exploring the concepts of concentration addition and independent action using a linear low-effect mixture model. *Environ. Toxicol. Chem.*, 39 (12):2552–2559, 2020. ISSN 15528618. doi:10.1002/etc.4868.

Escher, B. I. and Neale, P. A. Effect-based trigger values for mixtures of chemicals in surface water detected with in vitro bioassays. *Environ. Toxicol. Chem.*, 40(2):487–499, 2021. ISSN 15528618. doi:10.1002/etc.4944.

Escher, B. I., Glauch, L., Mayer, P., Schlichting, R., König, M., Mayer, P., and Schlichting, R. Baseline toxicity and volatility cutoff in reporter gene assays used for high-throughput Screening. *Chem. Res. Toxicol.*, 32(8):1646–1655, 2019. ISSN 15205010. doi:10.1021/acs.chemrestox.9b00182.

Escher, B. I., Neale, P. A., and Leusch, F. D. L. Effect-based trigger values for in vitro bioassays: Reading across from existing water quality guideline values. *Water Res.*, 81: 137–148, 2015. ISSN 18792448. doi:10.1016/j.watres.2015.05.049.

Escher, B. I., Van Daele, C., Dutt, M., Tang, J. Y. M., and Altenburger, R. Most oxidative stress response in water samples comes from unknown chemicals: The need for effect-based water quality trigger values. *Environ. Sci. Technol.*, 47(13):7002–7011, 2013. ISSN 0013936X. doi:10.1021/es304793h.

Faizan Bangi, M. S. and Kwon, J. S. I. Universal hybrid modeling of batch kinetics of aerobic carotenoid production using Saccharomyces Cerevisiae. *Proc. Am. Control Conf.*, 2022-June:3716–3721, 2022. ISSN 07431619. doi:10.23919/ACC53348.2022.9867779.

Fan, P. and Li, J. C. Diffusive wave solutions for open channel flows with uniform and concentrated lateral inflow. *Adv. Water Resour.*, 29(7):1000–1019, 2006. ISSN 03091708. doi:10.1016/j.advwatres.2005.08.008.

Faouzi, J. and Janati, H. Pyts: A python package for time series classification. *J. Mach. Learn. Res.*, 21:1–6, 2020. ISSN 15337928.

Fent, K., Weston, A. A., and Caminada, D. Ecotoxicology of human pharmaceuticals. *Aquat. Toxicol.*, 76(2):122–159, 2006. ISSN 0166445X. doi:10.1016/j.aquatox.2005.09.009.

Fujiyoshi, H., Hirakawa, T., and Yamashita, T. Deep learning-based image recognition for autonomous driving. *IATSS Res.*, 43(4):244–252, 2019. ISSN 03861112. doi:10.1016/j.iatssr.2019.11.008.

Fuks, O. and Tchelepi, H. A. LIMITATIONS OF PHYSICS INFORMED MACHINE LEARNING FOR NONLINEAR TWO-PHASE TRANSPORT IN POROUS MEDIA. *J. Mach. Learn. Model. Comput.*, 1(1):19–37, 2020. ISSN 2689-3967. doi:10.1615/jmachlearnmodelcomput.2020033905.

Gasperi, J., Sebastian, C., Ruban, V., Delamain, M., Percot, S., Wiest, L., Mirande, C., Caupos, E., Demare, D., Kessoo, M. D. K., Saad, M., Schwartz, J. J., Dubois, P., Fratta, C., Wolff, H., Moilleron, R., Chebbo, G., Cren, C., Millet, M., Barraud, S., and Gromaire, M. C. Micropollutants in urban stormwater: Occurrence, concentrations, and atmospheric contributions for a wide range of contaminants in three French catchments. *Environ. Sci. Pollut. Res.*, 21(8):5267–5281, 2014. ISSN 16147499. doi:10.1007/s11356-013-2396-0.

Gelman, A. and Rubin, D. B. Inference from iterative simulation using multiple sequences. *Stat. Sci.*, 7(4):457–472, 1992. ISSN 08834237. doi:10.1214/ss/1177011136.

Glaser, C., Zarfl, C., Werneburg, M., Böckmann, M., Zwiener, C., and Schwientek, M. Temporal and spatial variable in-stream attenuation of selected pharmaceuticals. *Sci. Total Environ.*, 741:1–11, 2020. ISSN 18791026. doi:10.1016/j.scitotenv.2020.139514.

Glaser, C., Zarfl, C., Rügner, H., Lewis, A., and Schwientek, M. Analyzing particle-associated pollutant transport to identify in-stream sediment processes during a high flow event. *Water*, 12(6):1794, 2020. ISSN 20734441. doi:10.3390/w12061794.

Glaser, C., Schwientek, M., Junginger, T., Gilfedder, B. S., Frei, S., Werneburg, M., Zwiener, C., and Zarfl, C. Comparison of environmental tracers including organic micropollutants as groundwater exfiltration indicators into a small river of a karstic catchment. *Hydrol. Process.*, 34(24):4712–4726, 2020. ISSN 10991085. doi:10.1002/hyp.13909.

Gonçalves, P. J., Lueckmann, J. M., Deistler, M., Nonnenmacher, M., Öcal, K., Bassetto, G., Chintaluri, C., Podlaski, W. F., Haddad, S. A., Vogels, T. P., Greenberg, D. S., and Macke, J. H. Training deep neural density estimators to identify mechanistic models of neural dynamics. *Elife*, 9:1–46, 2020. ISSN 2050084X. doi:10.7554/ELIFE.56261.

Greenberg, D. S., Nonnenmacher, M., and Macke, J. H. Automatic posterior transformation for likelihood-free inference. *36th Int. Conf. Mach. Learn. ICML 2019*, 2019-June:4288–4304, 2019.

Guillet, G., Knapp, J. L. A., Merel, S., Cirpka, O. A., Grathwohl, P., Zwiener, C., and Schwientek, M. Fate of wastewater contaminants in rivers: Using conservative-tracer based transfer functions to assess reactive transport. *Sci. Total Environ.*, 656:1250–1260, 2019. ISSN 18791026. doi:10.1016/j.scitotenv.2018.11.379.

Guillossou, R., Le Roux, J., Mailler, R., Vulliet, E., Morlay, C., Nauleau, F., Gasperi, J., and Rocher, V. Organic micropollutants in a large wastewater treatment plant: What are the benefits of an advanced treatment by activated carbon adsorption in comparison to conventional treatment? *Chemosphere*, 218:1050–1060, 2019. ISSN 18791298. doi:10.1016/j.chemosphere.2018.11.182.

Gutmann, M. U. and Corander, J. Bayesian Optimization for Likelihood-Free Inference of Simulator-Based Statistical Models. *J. Mach. Learn. Res.*, 17:1–47, 2016.

Han, S.-H., Kim, K. W., Kim, S., and Youn, Y. C. Artificial Neural Network: Understanding the Basic Concepts without Mathematics. *Dement. Neurocognitive Disord.*, 17(3):83, 2018. ISSN 1738-1495. doi:10.12779/dnd.2018.17.3.83.

Hanamoto, S., Nakada, N., Yamashita, N., and Tanaka, H. Modeling the photochemical attenuation of down-the-drain chemicals during river transport by stochastic methods and field measurements of pharmaceuticals and personal care products. *Environ. Sci. Technol.*, 47(23):13571–13577, 2013. ISSN 0013936X. doi:10.1021/es4035478.

Hayami, S. On the propagation of flood waves. *Bull. - Disaster Previs. Res. Institute, Kyoto Univ.*, 1:1–16, 1951.

He, Q. Z. and Tartakovsky, A. M. Physics-Informed Neural Network Method for Forward and Backward Advection-Dispersion Equations. *Water Resour. Res.*, 57(7):1–20, 2021. ISSN 19447973. doi:10.1029/2020WR029479.

Höge, M., Guthke, A., and Nowak, W. The hydrologist's guide to Bayesian model selection, averaging and combination. *J. Hydrol.*, 572(February):96–107, 2019. ISSN 00221694. doi:10.1016/j.jhydrol.2019.01.072.

Jaeger, A., Posselt, M., Betterle, A., Schaper, J., Mechelke, J., Coll, C., and Lewandowski, J. Spatial and temporal variability in attenuation of polar organic micropollutants in an urban lowland stream. *Environ. Sci. Technol.*, 53:2383–2395, 2018. ISSN 0013-936X. doi:10.1021/acs.est.8b05488.

Jia, A., Escher, B. I., Leusch, F. D., Tang, J. Y., Prochazka, E., Dong, B., Snyder, E. M., and Snyder, S. A. In vitro bioassays to evaluate complex chemical mixtures in recycled water. *Water Res.*, 80:1–11, 2015. ISSN 18792448. doi:10.1016/j.watres.2015.05.020.

John, V., Linke, A., Merdon, C., Neilan, M., and Rebholz, L. G. On the divergence constraint in mixed finite element methods for incompressible flows. *SIAM Rev.*, 59(3):492–544, 2017. ISSN 00361445. doi:10.1137/15M1047696.

Karniadakis, G. E., Kevrekidis, I. G., Lu, L., Perdikaris, P., Wang, S., and Yang, L. Physics-informed machine learning. *Nat. Rev. Phys.*, 3(6):422–440, 2021. ISSN 25225820. doi:10.1038/s42254-021-00314-5.

Kazezyilmaz-Alhan, C. M., Medina, M. A., and Richardson, C. J. A wetland hydrology and water quality model incorporating surface water/groundwater interactions. *Water Resour. Res.*, 43(4):1–16, 2007. ISSN 00431397. doi:10.1029/2006WR005003.

Khakimov, E., Chung, S. Y., Senapathi, V., Elzain, H. E., and Son, J. The Characteristics of Hydrogeological Parameters of Unconsolidated Sediments in the Nakdong River Delta of Busan City, Korea. *J. Soil Groundw. Environ.*, 22(3):27–41, 2017. ISSN 1598-6438. doi:10.7857/jsge.2017.22.3.027.

Khuwaileh, B. A. and Metwally, W. A. Gaussian process approach for dose mapping in radiation fields. *Nucl. Eng. Technol.*, 52(8):1807–1816, 2020. ISSN 2234358X. doi:10.1016/j.net.2020.01.013.

Kim, M.-K. and Zoh, K.-D. Occurrence and removals of micropollutants in water environment. *Environ. Eng. Res.*, 21(4):319–332, 2016. doi:10.4491/eer.2016.115.

Kingma, D. P. and Ba, J. L. Adam: A method for stochastic optimization. *3rd Int. Conf. Learn. Represent. ICLR 2015 - Conf. Track Proc.*, pages 1–15, 2015.

Klöckner, P., Seiwert, B., Eisentraut, P., Braun, U., Reemtsma, T., and Wagner, S. Characterization of tire and road wear particles from road runoff indicates highly dynamic particle properties. *Water Res.*, 185, 2020. ISSN 18792448. doi:10.1016/j.watres.2020.116262.

Kloepfer, A., Jekel, M., and Reemtsma, T. Occurrence, sources, and fate of benzothiazoles in municipal wastewater treatment plants. *Environ. Sci. Technol.*, 39(10):3792–3798, 2005. ISSN 0013936X. doi:10.1021/es048141e.

König, M., Escher, B. I., Neale, P. A., Krauss, M., Hilscherová, K., Novák, J., Teodorović, I., Schulze, T., Seidensticker, S., Kamal Hashmi, M. A., Ahlheim, J., and Brack, W. Impact of untreated wastewater on a major European river evaluated with a combination of in vitro bioassays and chemical analysis. *Environ. Pollut.*, 220:1220–1230, 2017. ISSN 18736424. doi:10.1016/j.envpol.2016.11.011.

Kunkel, U. and Radke, M. Fate of pharmaceuticals in rivers: Deriving a benchmark dataset at favorable attenuation conditions. *Water Res.*, 46(17):5551–5565, 2012. ISSN 18792448. doi:10.1016/j.watres.2012.07.033.

Kunkel, U. and Radke, M. Reactive tracer test to evaluate the fate of pharmaceuticals in rivers. *Environ. Sci. Technol.*, 45(15):6296–6302, 2011. ISSN 0013936X. doi:10.1021/es104320n.

Launay, M. A., Dittmer, U., and Steinmetz, H. Organic micropollutants discharged by combined sewer overflows – Characterisation of pollutant sources and stormwater-related processes. *Water Res.*, 104:82–92, 2016. ISSN 18792448. doi:10.1016/j.watres.2016.07.068.

Lecun, Y., Bengio, Y., and Hinton, G. Deep learning. *Nature*, 521(7553):436–444, 2015. ISSN 14764687. doi:10.1038/nature14539.

Lee, J., Schlichting, R., König, M., Scholz, S., Krauss, M., and Escher, B. I. Monitoring Mixture Effects of Neurotoxicants in Surface Water and Wastewater Treatment Plant Effluents with Neurite Outgrowth Inhibition in SH-SY5Y Cells. *ACS Environ. Au*, 2(6): 523–535, 2022. ISSN 26942518. doi:10.1021/acsenvironau.2c00026.

Lee, J., Braun, G., Henneberger, L., König, M., Schlichting, R., Scholz, S., and Escher, B. I. Critical Membrane Concentration and Mass-Balance Model to Identify Baseline Cytotoxicity of Hydrophobic and Ionizable Organic Chemicals in Mammalian Cell Lines. *Chem. Res. Toxicol.*, 34(9):2100–2109, 2021. ISSN 15205010. doi:10.1021/acs.chemrestox.1c00182.

Levenberg, K. A method for the solution of certain non-linear problems in least squares. *Q. Appl. Math.*, 2(2):164–168, 1944. ISSN 0033-569X. doi:10.1090/qam/10666.

Li, Z., Sobek, A., and Radke, M. Fate of pharmaceuticals and their transformation products in four small European rivers receiving treated wastewater. *Environ. Sci. Technol.*, 50 (11):5614–5621, 2016. ISSN 15205851. doi:10.1021/acs.est.5b06327.

Liu, Y., Zarfl, C., Basu, N. B., and Cirpka, O. A. Turnover and legacy of sediment-associated PAH in a baseflow-dominated river. *Sci. Total Environ.*, 671:754–764, 2019. ISSN 18791026. doi:10.1016/j.scitotenv.2019.03.236.

Liu, H., Maghoul, P., Shalaby, A., Bahari, A., and Moradi, F. Integrated approach for the MASW dispersion analysis using the spectral element technique and trust region reflective method. *Comput. Geotech.*, 125(June):103689, 2020. ISSN 18737633. doi:10.1016/j.compgeo.2020.103689.

Liu, Y., Zarfl, C., Basu, N. B., Schwientek, M., and Cirpka, O. A. Contributions of catchment and in-stream processes to suspended sediment transport in a dominantly groundwater-fed catchment. *Hydrol. Earth Syst. Sci.*, 22(7):3903–3921, 2018. ISSN 16077938. doi:10.5194/hess-22-3903-2018.

Liu, Y., Zarfl, C., Basu, N. B., and Cirpka, O. A. Modeling the fate of pharmaceuticals in a fourth-order river under competing assumptions of transient storage. *Water Resour. Res.*, 56(3):e2019WR026100, 2020. ISSN 19447973. doi:10.1029/2019WR026100.

Liu, B., Finkel, M., and Grathwohl, P. Mass transfer principles in column percolation tests: Initial conditions and tailing in heterogeneous materials. *Materials (Basel).*, 14(16), 2021. ISSN 19961944. doi:10.3390/ma14164708.

Liu, Y. Modelling the Fate of Sediments and Micropollutants in Rivers. 2018.

Liu, B., Finkel, M., and Grathwohl, P. First order approximation for coupled film and intraparticle pore diffusion to model sorption/desorption batch experiments. *J. Hazard. Mater.*, 429(January):128314, 2022. ISSN 18733336. doi:10.1016/j.jhazmat.2022.128314.

Loos, R., Carvalho, R., António, D. C., Comero, S., Locoro, G., Tavazzi, S., Paracchini, B., Ghiani, M., Lettieri, T., Blaha, L., Jarosova, B., Voorspoels, S., Servaes, K., Haglund, P., Fick, J., Lindberg, R. H., Schwesig, D., and Gawlik, B. M. EU-wide monitoring survey on emerging polar organic contaminants in wastewater treatment plant effluents. *Water Res.*, 47(17):6475–6487, 2013. ISSN 18792448. doi:10.1016/j.watres.2013.08.024.

Lueckmann, J. M., Bassetto, G., Karaletsos, T., and Macke, J. H. Likelihood-free inference with emulator networks. *Proc. Mach. Learn. Res.*, 96:32–53, 2018. ISSN 26403498.

Luo, Y., Guo, W., Ngo, H. H., Nghiem, L. D., Hai, F. I., Zhang, J., Liang, S., and Wang, X. C. A review on the occurrence of micropollutants in the aquatic environment and their fate and removal during wastewater treatment. *Sci. Total Environ.*, 473-474:619–641, 2014. ISSN 18791026. doi:10.1016/j.scitotenv.2013.12.065.

Maloszewski, P. and Zuber, A. Principles and practice of calibration and validation of mathematical models for the interpretation of environmental tracer data in aquifers. *Adv. Water Resour.*, 16(3):173–190, 1993. ISSN 03091708. doi:10.1016/0309-1708(93)90036-F.

Małoszewski, P. and Zuber, A. Determining the turnover time of groundwater systems with the aid of environmental tracers. 1. Models and their applicability. *J. Hydrol.*, 57 (3-4):207–231, 1982. ISSN 00221694. doi:10.1016/0022-1694(82)90147-0.

Mandaric, L., Mor, J. R., Sabater, S., and Petrovic, M. Impact of urban chemical pollution on water quality in small, rural and effluent-dominated Mediterranean streams and rivers. *Sci. Total Environ.*, 613-614:763–772, 2018. ISSN 18791026. doi:10.1016/j.scitotenv.2017.09.128.

Mansouri, K., Grulke, C. M., Judson, R. S., and Williams, A. J. OPERA models for predicting physicochemical properties and environmental fate endpoints. *J. Cheminformatics.*, 10 (1):1–19, 2018. ISSN 17582946. doi:10.1186/s13321-018-0263-1.

Marquardt, D. W. An Algorithm for Least-Squares Estimation of Nonlinear Parameters. *J. Soc. Ind. Appl. Math.*, 11(2):431–441, 1963. ISSN 0368-4245. doi:10.1137/0111030.

Marx, C., Mühlbauer, V., Krebs, P., and Kuehn, V. Environmental risk assessment of antibiotics including synergistic and antagonistic combination effects. *Sci. Total Environ.*, 524-525:269–279, 2015. ISSN 18791026. doi:10.1016/j.scitotenv.2015.04.051.

Mellage, A., Zakai, G., Efrati, B., Pagel, H., and Schwartz, N. Paraquat sorption- and organic matter-induced modifications of soil spectral induced polarization (SIP) signals. *Geophys. J. Int.*, 229(2):1422–1433, 2022. ISSN 0956-540X. doi:10.1093/gji/ggab531.

Mishra, S. and Molinaro, R. Estimates on the generalization error of physics-informed neural networks for approximating a class of inverse problems for PDEs. *IMA J. Numer. Anal.*, 42(2):981–1022, 2022. ISSN 14643642. doi:10.1093/imanum/drab032.

Morales Oreamuno, M. F., Oladyshkin, S., and Nowak, W. Information-Theoretic Scores for Bayesian Model Selection and Similarity Analysis: Concept and Application to a Groundwater Problem. *Water Resour. Res.*, 59(7):1–25, 2023. ISSN 19447973. doi:10.1029/2022WR033711.

Moschet, C., Vermeirssen, E. L., Singer, H., Stamm, C., and Hollender, J. Evaluation of in-situ calibration of chemcatcher passive samplers for 322 micropollutants in agricultural and urban affected rivers. *Water Res.*, 71:306–317, 2015. ISSN 18792448. doi:10.1016/j.watres.2014.12.043.

Moussa, R. Analytical Hayami solution for the diffusive wave flood routing problem with lateral inflow. *Hydrol. Process.*, 10(9):1209–1227, 1996. ISSN 08856087. doi:10.1002/(SICI)1099-1085(199609)10:9<1209::AID-HYP380>3.0.CO;2-2.

Müller, A., Österlund, H., Nordqvist, K., Marsalek, J., and Viklander, M. Building surface materials as sources of micropollutants in building runoff: A pilot study. *Sci. Total Environ.*, 680:190–197, 2019. ISSN 18791026. doi:10.1016/j.scitotenv.2019.05.088.

Müller, M. E., Escher, B. I., Schwientek, M., Werneburg, M., Zarfl, C., and Zwiener, C. Combining in vitro reporter gene bioassays with chemical analysis to assess changes in the water quality along the Ammer River, Southwestern Germany. *Environ. Sci. Eur.*, 30(1): 5–8, 2018. ISSN 21904715. doi:10.1186/s12302-018-0148-y.

Müller, M. E., Werneburg, M., Glaser, C., Schwientek, M., Zarfl, C., Escher, B. I., and Zwiener, C. Influence of emission sources and tributaries on the spatial and temporal patterns of micropollutant mixtures and associated effects in a small river. *Environ. Toxicol. Chem.*, 39(7):1382–1391, 2020. ISSN 15528618. doi:10.1002/etc.4726.

Müller, M. E., Zwiener, C., and Escher, B. I. Storm event–driven occurrence and transport of dissolved and sorbed organic micropollutants and associated effects in the Ammer River, southwestern Germany. *Environ. Toxicol. Chem.*, 40(1):88–99, 2021. ISSN 15528618. doi:10.1002/etc.4910.

Munz, N. A., Burdon, F. J., Zwart, D.de, Junghans, M., Melo, L., Reyes, M., Schönenberger, U., Singer, H. P., Hollender, J., Spycher, B., and Stamm, C. Pesticides drive risk of micropollutants in wastewater-impacted streams during low flow conditions. *Water Res.*, 110:366–377, 2016. ISSN 00431354. doi:10.1016/j.watres.2016.11.001.

Naney, J. W., DeCousey, D. G., Barnes, B. B., and Gander, G. A. Predicting Base Flow Using Hydrogeologic Parameters. *JAWRA J. Am. Water Resour. Assoc.*, 14(3):640–650, 1978. ISSN 17521688. doi:10.1111/j.1752-1688.1978.tb02213.x.

Nash, J. P., Kime, D. E., Van der Ven, L. T., Wester, P. W., Brion, F., Maack, G., Stahlschmidt-Allner, P., and Tyler, C. R. Long-term exposure to environmental concentrations of the pharmaceutical ethynylestradiol causes reproductive failure in fish. *Environ. Health Perspect.*, 112(17):1725–1733, 2004. ISSN 00916765. doi:10.1289/ehp.7209.

Neale, P. A., Munz, N. A., Aït-Aïssa, S., Altenburger, R., Brion, F., Busch, W., Escher, B. I., Hilscherová, K., Kienle, C., Novák, J., Seiler, T. B., Shao, Y., Stamm, C., and Hollender, J. Integrating chemical analysis and bioanalysis to evaluate the contribution of wastewater effluent on the micropollutant burden in small streams. *Sci. Total Environ.*, 576:785–795, 2017. ISSN 18791026. doi:10.1016/j.scitotenv.2016.10.141.

Neale, P. A., Altenburger, R., Aït-Aïssa, S., Brion, F., Busch, W., de Aragão Umbuzeiro, G., Denison, M. S., Du Pasquier, D., Hilscherová, K., Hollert, H., Morales, D. A., Novák, J., Schlichting, R., Seiler, T. B., Serra, H., Shao, Y., Tindall, A. J., Tollefsen, K. E., Williams, T. D., and Escher, B. I. Development of a bioanalytical test battery for water quality monitoring: Fingerprinting identified micropollutants and their contribution to effects in surface water. *Water Res.*, 123:734–750, 2017. ISSN 18792448. doi:10.1016/j.watres.2017.07.016.

Neale, P. A., Aït-Aïssa, S., Brack, W., Creusot, N., Denison, M. S., Deutschmann, B., Hilscherová, K., Hollert, H., Krauss, M., Novák, J., Schulze, T., Seiler, T. B., Serra, H., Shao, Y., and Escher, B. I. Linking in vitro effects and detected organic micropollutants in surface water using mixture-toxicity modeling. *Environ. Sci. Technol.*, 49(24):14614–14624, 2015. ISSN 15205851. doi:10.1021/acs.est.5b04083.

Neale, P. A., Braun, G., Brack, W., Carmona, E., Gunold, R., König, M., Krauss, M., Liebmann, L., Liess, M., Link, M., Schäfer, R. B., Schlichting, R., Schreiner, V. C., Schulze, T., Vormeier, P., Weisner, O., and Escher, B. I. Assessing the mixture effects in in vitro bioassays of chemicals occurring in small agricultural streams during rain events. *Environ. Sci. Technol.*, 54(13):8280–8290, 2020. ISSN 15205851. doi:10.1021/acs.est.0c02235.

Neumann, M., Schulz, R., Schäfer, K., Müller, W., Mannheller, W., and Liess, M. The significance of entry routes as point and non-point sources of pesticides in small streams. *Water Res.*, 36(4):835–842, 2002. ISSN 00431354. doi:10.1016/S0043-1354(01)00310-4.

Noye, B. J. and Tan, H. H. Finite difference methods for solving the two-dimensional advection–diffusion equation. *Int. J. Numer. Methods Fluids*, 9(1):75–98, 1989. ISSN 10970363. doi:10.1002/fld.1650090107.

Ojoghoro, J. O., Scrimshaw, M. D., and Sumpter, J. P. Steroid hormones in the aquatic environment. *Sci. Total Environ.*, 792:148306, 2021. ISSN 18791026. doi:10.1016/j.scitotenv.2021.148306.

Ort, C. and Siegrist, H. Assessing wastewater dilution in small rivers with high resolution conductivity probes. *Water Sci. Technol.*, 59(8):1593–1601, 2009. ISSN 02731223. doi:10.2166/wst.2009.174.

Pang, B., Nijkamp, E., and Wu, Y. N. Deep Learning With TensorFlow: A Review. *J. Educ. Behav. Stat.*, 45(2):227–248, 2020. ISSN 19351054. doi:10.3102/1076998619872761.

Paszke, A., Gross, S., Massa, F., Lerer, A., Bradbury, J., Chanan, G., Killeen, T., Lin, Z., Gimelshein, N., Antiga, L., Desmaison, A., Köpf, A., Yang, E., DeVito, Z., Raison, M., Tejani, A., Chilamkurthy, S., Steiner, B., Fang, L., Bai, J., and Chintala, S. PyTorch: An imperative style, high-performance deep learning library. *Adv. Neural Inf. Process. Syst.*, 32(NeurIPS):8024–8035, 2019. ISSN 10495258.

Petrovic, M., De Alda, M. J. L., Diaz-Cruz, S., Postigo, C., Radjenovic, J., Gros, M., and Barcelo, D. Fate and removal of pharmaceuticals and illicit drugs in conventional and membrane bioreactor wastewater treatment plants and by riverbank filtration. *Philos. Trans. R. Soc. A Math. Phys. Eng. Sci.*, 367(1904):3979–4003, 2009. ISSN 1364503X. doi:10.1098/rsta.2009.0105.

Rackauckas, C., Ma, Y., Martensen, J., Warner, C., Zubov, K., Supekar, R., Skinner, D., Ramadhan, A., and Edelman, A. Universal Differential Equations for Scientific Machine Learning. pages 1–55, 2020.

Rackauckas, C., Sharma, R., and Lie, B. Hybrid Mechanistic + Neural Model of Laboratory Helicopter. *Proc. 61st SIMS Conf. Simul. Model. SIMS 2020, Sept. 22-24, Virtual Conf. Finl.*, 176(September):264–271, 2021. doi:10.3384/ecp20176264.

Rackauckas, C., Innes, M., Ma, Y., Bettencourt, J., White, L., and Dixit, V. DiffEqFlux.jl - A Julia Library for Neural Differential Equations. pages 1–17, 2019.

Radjenović, J., Petrović, M., and Barceló, D. Fate and distribution of pharmaceuticals in wastewater and sewage sludge of the conventional activated sludge (CAS) and advanced membrane bioreactor (MBR) treatment. *Water Res.*, 43(3):831–841, 2009. ISSN 00431354. doi:10.1016/j.watres.2008.11.043.

Raissi, M., Perdikaris, P., and Karniadakis, G. E. Physics-informed neural networks: A deep learning framework for solving forward and inverse problems involving nonlinear partial differential equations. *J. Comput. Phys.*, 378:686–707, 2019. ISSN 10902716. doi:10.1016/j.jcp.2018.10.045.

Ramachandran, P., Zoph, B., and Le, Q. V. Searching for activation functions. *6th Int. Conf. Learn. Represent. ICLR 2018 - Work. Track Proc.*, pages 1–13, 2018.

Rasmussen, E. C. and Williams, C. K. *Gaussian Processes for Machine Learning*, volume 38. MIT Press, Cambridge, MA, USA, 2006. ISBN 026218253X.

Rau, O., Wurglics, M., Dingermann, T., Abdel-Tawab, M., and Schubert-Zsilavecz, M. Screening of herbal extracts for activation of the human peroxisome proliferator-activated receptor. *Pharmazie*, 61(11):952–956, 2006. ISSN 00317144.

Ravenzwaaij, D.van, Cassey, P., and Brown, S. D. A simple introduction to Markov Chain Monte–Carlo sampling. *Psychon. B. Rev.*, 25(1):143–154, 2018. ISSN 15315320. doi:10.3758/s13423-016-1015-8.

Reemtsma, T., Berger, U., Arp, H. P. H., Gallard, H., Knepper, T. P., Neumann, M., Quintana, J. B., and Voogt, P. D. Mind the Gap: Persistent and Mobile Organic Compounds - Water Contaminants That Slip Through. *Environ. Sci. Technol.*, 50(19):10308–10315, 2016. ISSN 15205851. doi:10.1021/acs.est.6b03338.

Riml, J., Wörman, A., Kunkel, U., and Radke, M. Evaluating the fate of six common pharmaceuticals using a reactive transport model: Insights from a stream tracer test. *Sci. Total Environ.*, 458-460:344–354, 2013. ISSN 00489697. doi:10.1016/j.scitotenv.2013.03.077.

Rodríguez-Molina, D., Mang, P., Schmitt, H., Chifiriuc, M. C., Radon, K., and Wengenroth, L. Do wastewater treatment plants increase antibiotic resistant bacteria or genes in the environment? Protocol for a systematic review. *Syst. Rev.*, 8(1):1–8, 2019. ISSN 20464053. doi:10.1186/s13643-019-1236-9.

Salam, N. K., Huang, T. H., Kota, B. P., Kim, M. S., Li, Y., and Hibbs, D. E. Novel PPAR-gamma agonists identified from a natural product library: A virtual screening, induced-fit docking and biological assay study. *Chem. Biol. Drug Des.*, 71(1):57–70, 2008. ISSN 17470277. doi:10.1111/j.1747-0285.2007.00606.x.

Schaper, J. L., Posselt, M., Bouchez, C., Jaeger, A., Nuetzmann, G., Putschew, A., Singer, G., and Lewandowski, J. Fate of trace organic compounds in the hyporheic zone: influence of retardation, the benthic biolayer, and organic carbon. *Environ. Sci. Technol.*, 53(8): 4224–4234, 2019. ISSN 15205851. doi:10.1021/acs.est.8b06231.

Schmitt, M., Wack, K., Glaser, C., Wei, R., and Zwiener, C. Separation of photochemical and non-photochemical diurnal in-stream attenuation of micropollutants. *Environ. Sci. Technol.*, 55(13):8908–8917, 2021. ISSN 0013-936X. doi:10.1021/acs.est.1c02116.

Schulz, E., Speekenbrink, M., and Krause, A. A tutorial on Gaussian process regression: Modelling, exploring, and exploiting functions. *J. Math. Psychol.*, 85:1–16, 2018. ISSN 10960880. doi:10.1016/j.jmp.2018.03.001.

Schwarz, E., Khurana, S., Chakrawal, A., Chavez Rodriguez, L., Wirsching, J., Streck, T., Manzoni, S., Thullner, M., and Pagel, H. Spatial Control of Microbial Pesticide Degradation in Soil: A Model-Based Scenario Analysis. *Environ. Sci. Technol.*, 56(20):14427–14438, 2022. ISSN 15205851. doi:10.1021/acs.est.2c03397.

Schwientek, M., Rügner, H., Beckingham, B., Kuch, B., and Grathwohl, P. Integrated monitoring of particle associated transport of PAHs in contrasting catchments. *Environ. Pollut.*, 172:155–162, 2013. ISSN 02697491. doi:10.1016/j.envpol.2012.09.004.

Schwientek, M., Guillet, G., Rügner, H., Kuch, B., and Grathwohl, P. A high-precision sampling scheme to assess persistence and transport characteristics of micropollutants in rivers. *Sci. Total Environ.*, 540:444–454, 2016. ISSN 18791026. doi:10.1016/j.scitotenv.2015.07.135.

Schwindt, S., Callau Medrano, S., Mouris, K., Beckers, F., Haun, S., Nowak, W., Wieprecht, S., and Oladyshkin, S. Bayesian Calibration Points to Misconceptions in Three-Dimensional Hydrodynamic Reservoir Modeling. *Water Resour. Res.*, 59(3), 2023. ISSN 19447973. doi:10.1029/2022WR033660.

Shampine, L. F. and Reichelt, M. W. The MATLAB ODE suite. *Soc. Ind. Appl. Math.*, 18(1): 1–22, 1997. doi:https://doi.org/10.1137/S1064827594276424.

Shang, H., Forbes, J. F., and Guay, M. Model Predictive Control for Quasilinear Hyperbolic Distributed Parameter Systems. *Ind. Eng. Chem. Res.*, 43(9):2140–2149, 2004. ISSN 08885885. doi:10.1021/ie030653z.

Shen, C., Appling, A. P., Gentine, P., Bandai, T., Gupta, H., Tartakovsky, A., Baity-Jesi, M., Fenicia, F., Kifer, D., Li, L., Liu, X., Ren, W., Zheng, Y., Harman, C. J., Clark, M., Farthing, M., Feng, D., Kumar, P., Aboelyazeed, D., Rahmani, F., Beck, H. E., Bindas, T., Dwivedi, D., Fang, K., Höge, M., Rackauckas, C., Roy, T., Xu, C., and Lawson, K. Differentiable modeling to unify machine learning and physical models and advance Geosciences. 2023. ISSN 2662138X. doi:10.1038/s43017-023-00450-9.

Shinde, P. P. and Shah, S. A Review of Machine Learning and Deep Learning Applications. *Proc. - 2018 4th Int. Conf. Comput. Commun. Control Autom. ICCUBEA 2018*, pages 1–6, 2018. doi:10.1109/ICCUBEA.2018.8697857.

Sorwat, J., Mellage, A., Maisch, M., Kappler, A., Cirpka, O. A., and Byrne, J. M. Chromium (VI) removal kinetics by magnetite-coated sand: Small-scale flow-through column experiments. *J. Hazard. Mater.*, 415(February):125648, 2021. ISSN 18733336. doi:10.1016/j.jhazmat.2021.125648.

Spade, D. A. *Markov chain Monte Carlo methods: Theory and practice*, volume 43. Elsevier B.V., 1 edition, 2020. ISBN 9780444642110. doi:10.1016/bs.host.2019.06.001.

Spahr, S., Teixidó, M., Sedlak, D. L., and Luthy, R. G. Hydrophilic trace organic contaminants in urban stormwater: Occurrence, toxicological relevance, and the need to enhance green stormwater infrastructure. *Environ. Sci. Water Res. Technol.*, 6(1):15–44, 2020. ISSN 20531419. doi:10.1039/c9ew00674e.

Störiko, A., Pagel, H., Mellage, A., and Cirpka, O. A. Does It Pay Off to Explicitly Link Functional Gene Expression to Denitrification Rates in Reaction Models? *Front. Microbiol.*, 12(June):1–13, 2021. ISSN 1664302X. doi:10.3389/fmicb.2021.684146.

Störiko, A., Pagel, H., Mellage, A., Van Cappellen, P., and Cirpka, O. A. Denitrification-Driven Transcription and Enzyme Production at the River-Groundwater Interface: Insights From Reactive-Transport Modeling. *Earth Sp. Sci. Open Arch.*, 58:e2021WR031584, 2022. doi:10.1029/2021WR031584.

Strelow, E. L., Gerisch, A., Lang, J., and Pfetsch, M. E. Physics informed neural networks: A case study for gas transport problems. *J. Comput. Phys.*, 481:112041, 2023. ISSN 10902716. doi:10.1016/j.jcp.2023.112041.

Strobel, C., Abramov, S., Huisman, J. A., Cirpka, O. A., and Mellage, A. Spectral Induced Polarization (SIP) of Denitrification-Driven Microbial Activity in Column Experiments Packed With Calcareous Aquifer Sediments. *J. Geophys. Res. Biogeosciences*, 128(1):1–21, 2023. ISSN 21698961. doi:10.1029/2022JG007190.

Sun, Z., Cheng, K., Liu, J., Guo, W., and Guo, J. Simulation of Water Quality in a River Network with Time-Varying Lateral Inflows and Pollutants. *Water (Switzerland)*, 15(16), 2023. ISSN 20734441. doi:10.3390/w15162861.

Tartakovsky, A. M., Marrero, C. O., Perdikaris, P., Tartakovsky, G. D., and Barajas-Solano, D. Physics-Informed Deep Neural Networks for Learning Parameters and Constitutive Relationships in Subsurface Flow Problems. *Water Resour. Res.*, 56(5):1–16, 2020. ISSN 19447973. doi:10.1029/2019WR026731.

Tejero-Cantero, A., Boelts, J., Deistler, M., Lueckmann, J.-M., Durkan, C., Gonçalves, P., Greenberg, D., and Macke, J. sbi: A toolkit for simulation-based inference. *J. Open Source Softw.*, 5(52):2505, 2020. doi:10.21105/joss.02505.

Toride, N., Leij, F. J., and Genuchten, M. T.van. A comprehensive set of analytical solutions for nonequilibrium solute transport with first-order decay and zero-order production. *Water Resour. Res.*, 29(7):2167–2182, 1993. ISSN 19447973. doi:10.1029/93WR00496.

Varga, B., Somogyi, V., Meiczinger, M., Kováts, N., and Domokos, E. Enzymatic treatment and subsequent toxicity of organic micropollutants using oxidoreductases - A review. *J. Clean. Prod.*, 221:306–322, 2019. ISSN 09596526. doi:10.1016/j.jclepro.2019.02.135.

Virtanen, P., Gommers, R., Oliphant, T. E., Haberland, M., Reddy, T., Cournapeau, D., Burovski, E., Peterson, P., Weckesser, W., Bright, J., Walt, S. J.van der, Brett, M., Wilson, J., Millman, K. J., Mayorov, N., Nelson, A. R., Jones, E., Kern, R., Larson, E., Carey, C. J., Polat, I., Feng, Y., Moore, E. W., VanderPlas, J., Laxalde, D., Perktold, J., Cimrman, R., Henriksen, I., Quintero, E. A., Harris, C. R., Archibald, A. M., Ribeiro, A. H., Pedregosa, F., Mulbregt, P.van, and Contributors, S. . SciPy 1.0: fundamental algorithms for scientific computing in Python. *Nat. Methods*, 17(3):261–272, 2020. ISSN 15487105. doi:10.1038/s41592-019-0686-2.

Vogt, T., Hoehn, E., Schneider, P., Freund, A., Schirmer, M., and Cirpka, O. A. Fluctuations of electrical conductivity as a natural tracer for bank filtration in a losing stream. *Adv. Water Resour.*, 33(11):1296–1308, 2010. ISSN 03091708. doi:10.1016/j.advwatres.2010.02.007.

Vrugt, J. A. Markov chain Monte Carlo simulation using the DREAM software package: Theory, concepts, and MATLAB implementation. *Environ. Model. Softw.*, 75:273–316, 2016. ISSN 13648152. doi:10.1016/j.envsoft.2015.08.013.

Wang, J., Carrera, J., Saaltink, M. W., and Valhondo, C. A general and efficient numerical solution of reactive transport with multirate mass transfer. *Comput. Geosci.*, 158:104953, 2022. ISSN 00983004. doi:10.1016/j.cageo.2021.104953.

Wang, X. J., Hayes, J. D., and Wolf, C. R. Generation of a stable antioxidant response element-driven reporter gene cell line and its use to show redox-dependent activation of Nrf2 by cancer chemotherapeutic agents. *Cancer Res.*, 66(22):10983–10994, 2006. ISSN 00085472. doi:10.1158/0008-5472.CAN-06-2298.

Wang, P. and Cirpka, O. A. Surface Transient Storage Under Low-Flow Conditions in Streams With Rough Bathymetry. *Water Resour. Res.*, 57(12), 2021. ISSN 19447973. doi:10.1029/2021WR029899.

Wei, R., Escher, B. I., Glaser, C., König, M., Schlichting, R., Schmitt, M., Störiko, A., Viswanathan, M., and Zarfl, C. Modeling the Dynamics of Mixture Toxicity and Effects of Organic Micropollutants in a Small River under Unsteady Flow Conditions. *Environ. Sci. Technol.*, 56(20):14397–14408, 2022. ISSN 0013-936X. doi:10.1021/acs.est.2c02824.

Wicke, D., Matzinger, A., Sonnenberg, H., Caradot, N., Schubert, R. L., Dick, R., Heinzmann, B., Dünnbier, U., Seggern, D.von, and Rouault, P. Micropollutants in urban stormwater runoff of different land uses. *Water (Switzerland)*, 13(9), 2021. ISSN 20734441. doi:10.3390/w13091312.

Wittmer, I. K., Bader, H. P., Scheidegger, R., Singer, H., Lück, A., Hanke, I., Carlsson, C., and Stamm, C. Significance of urban and agricultural land use for biocide and pesticide dynamics in surface waters. *Water Res.*, 44(9):2850–2862, 2010. ISSN 00431354. doi:10.1016/j.watres.2010.01.030.

Wright, L. G., Onodera, T., Stein, M. M., Wang, T., Schachter, D. T., Hu, Z., and McMahon, P. L. Deep physical neural networks trained with backpropagation. *Nature*, 601 (7894):549–555, 2022. ISSN 14764687. doi:10.1038/s41586-021-04223-6.

Zhi, H., Kolpin, D. W., Klaper, R. D., Iwanowicz, L. R., Meppelink, S. M., and Lefevre, G. H. Occurrence and Spatiotemporal Dynamics of Pharmaceuticals in a Temperate-Region Wastewater Effluent-Dominated Stream: Variable Inputs and Differential Attenuation Yield Evolving Complex Exposure Mixtures. *Environ. Sci. Technol.*, 54(20):12967–12978, 2020. ISSN 15205851. doi:10.1021/acs.est.0c02328.

Zong, Y., He, Q., and Tartakovsky, A. M. Improved training of physics-informed neural networks for parabolic differential equations with sharply perturbed initial conditions. *Comput. Methods Appl. Mech. Eng.*, 414:116125, 2023. ISSN 00457825. doi:10.1016/j.cma.2023.116125.

Appendix A

Supplementary information for chapter 2

A.1 Upstream discharge estimation

In the investigated river stretch, discharge in the main channel could not be quantified accurately without considering the involvement of the discharge at the upstream (Q_{up}) from the wastewater treatment plant (WWTP), at the effluent of the WWTP (Q_{w}), in the Mühlbach ($Q_{\mathrm{Mühlbach}}$) and Ehrenbach ($Q_{\mathrm{Ehrenbach}}$). Q_{up} has been continuously monitored by a gauging station at upstream of the WWTP since 2013. Based on these long-term data, an empirical upstream rating curve describing the relationship between discharge and water depth has been established as in Eq. A.1,

$$Q_{\mathrm{up}} = 23.2863d^2 - 1.2969d + 0.1150 \tag{A.1}$$

where Q_{up} [$\mathrm{m^3 s^{-1}}$] is the discharge, and d [m] is the water depth. Since the gauging station stopped providing valid discharge data from 23:00 on June 30, 2020, the water depths time-series at measuring station (MS) Up were converted to the discharge values by applying Eq. A.1. Water depth was measured by the conductivity - temperature - depth (CTD) diver, referencing to the water depths from manual measurements and corrected by subtracting the corresponding atmospheric pressures during the sampling period. Assuming ECd 'mass' balance (Eq. A.3), combining the measured ECd and computed Q_{up} time-series, the two-component mixing method presented by Schwientek et al., 2016 and Ort and Siegrist, 2009 was modified to determine the discharge from the WWTP effluent and at MS Down. Eq. A.2 – A.6 outline the detailed relationships among the measured ECds and discharges at MS Up, WWTP and MS Down.

$$Q_{\mathrm{d}} = Q_{\mathrm{w}} + Q_{\mathrm{up}} \tag{A.2}$$

$$Q_{\mathrm{d}} EC_{\mathrm{d}} = Q_{\mathrm{up}} EC_{\mathrm{up}} + Q_{\mathrm{w}} EC_{\mathrm{w}} \tag{A.3}$$

This chapter is published as supplementary information for "Modeling the Dynamics of Mixture Toxicity and Effects of Organic Micropollutants in a Small River under Unsteady Flow Conditions" in *Environmental Science & Technology* doi: 10.1021/acs.est.2c02824.

$$Q_{\mathrm{d}} = Q_{\mathrm{up}} \frac{EC_{\mathrm{up}} - EC_{\mathrm{w}}}{EC_{\mathrm{d}} - EC_{\mathrm{w}}} \tag{A.4}$$

$$Q_{\mathrm{w}} = Q_{\mathrm{up}} \frac{EC_{\mathrm{d}} - EC_{\mathrm{up}}}{EC_{\mathrm{w}} - EC_{\mathrm{d}}} \tag{A.5}$$

$$Q_{\mathrm{MS1}} = Q_d - Q_{\mathrm{Mühlbach}} + Q_{\mathrm{Ehrenbach}} \tag{A.6}$$

$$\overline{Q_{\mathrm{MS1}}(t)} = \overline{Q_{\mathrm{MS2}}(t)} = \overline{Q_{\mathrm{MS3}}(t)} \tag{A.7}$$

Q_{up}, Q_{w}, Q_{d}, Q_{MS1}, Q_{MS2}, Q_{MS3}, $Q_{\mathrm{Mühlbach}}$ and $Q_{\mathrm{Ehrenbach}}$ [$\mathrm{m^3 s^{-1}}$] are the discharges at the WESS gauging station (upstream from the WWTP), the WWTP effluent, the downstream from the WWTP, MS1, MS2, MS3, Mühlbach and Ehrenbach, respectively. EC_{up}, EC_{w} and EC_{d} are ECd values [$\mathrm{mS\ cm^{-1}}$] measured at the WESS gauging station, WWTP effluent and the downstream of the WWTP, respectively. The discharge in the two main tributaries Ehrenbach and Mülbach was measured three times during the first sampling day using the acoustic digital current meter (ADC) (Ott C2, Kempten, Germany). The discharges in the tributaries were assumed to be constant throughout the selected river segment due to the lacking ground water infiltration and relatively small amount of inflow from the four small tributaries (Schwientek et al., 2016 estimated that less than 1‰ of the discharge in the Steinlach main channel is contributed by the four small tributaries combing.).

A.2 Model-aided field experimental design

A scenario analysis was carried out prior to the field campaign to determine the appropriate field instrumental set-up under different flow conditions. A 1-D reactive transport model assuming steady-state discharge was modified from the work of Liu et al., 2020. Available data from the study of Schwientek et al., 2016 and Guillet et al., 2019 in the same river was used as the model input as well as for parameter estimation. The purpose of conducting this analysis was to balance the aim of quantitatively characterizing the dynamics of the in-stream micropollutants, observing the spatial distinction of toxic effects along the river channel, especially the effects originating from chemicals undergoing pronounced reactive in-stream processes, with our field and laboratory logistics' capacities. Thus, the analysis leads to optimizing the temporal sampling resolutions and the number of auto-samplers (ASs) to be used in the field campaign. After selecting three conservative compounds (atrazine, candesartan and carbamazepine), three day-time reactive compounds (DEET, oxcarbazepine and TAED) and three night-time reactive compounds (bisoprolol, trimethoprim and valsartan) based on previous studies (Schwientek et al., 2016; Guillet et al., 2019), the simulations of the downstream concentration time courses during the day and night time were performed separately. The model ran under numerous scenarios: 1) at various discharge values (0.18, 0.3, 2 and 3 $\mathrm{m^3\ s^{-1}}$ used during the day-time simulation; 0.16, 0.3, 2 and 3 $\mathrm{m^3\ s^{-1}}$ the night-time), 2) at two different time resolutions (1 and 2-hour), 3) as well as with two and three ASs. The modeled downstream removals and the calibrated reaction coefficients from different scenarios were compared. At last, the three ASs scheme was chosen and the ASs' locations were settled.

A.3 Lagrangian sampling campaign

The details of the sampling campaign can be found in the work of Schmitt et al., 2021. In here we provided a brief description of the study sites and the mechanism of the Lagrangian sampling scheme.

Study sites. The Steinlach River is a 25.9 km long 4th order stream that sources from the valley of the Eckenbachgraben near the town of Mössingen, passing through the southern part of Tübingen city, draining into the Neckar River of the Rhine basin in the state of Baden-Württemberg, Germany. It flows through the catchment of 140 km^2 (Schwientek et al., 2016), of which the use is 49% agriculture, 39% forest and 12% urban (Schwientek et al., 2013; Guillet et al., 2019). The Steinlach River has the mean discharge (as of March 1, 2016) of 1.84 m^3s^{-1} (https://www.hvz.baden-wuerttemberg.de/). However the discharge varies seasonally that it can reach 15 m^3s^{-1} in December (Schwientek et al., 2013) and drop to 0.1 m^3s^{-1} - 0.2 m^3s^{-1} during the dry period (Liu et al., 2018). The river stretch we were focusing on was fed by one main tributary Ehrenbach and four small creeks. A constructed diversion (Mühlbach) takes the water out of the main channel at approximately 1 km downstream of the wastewater treatment plant (WWTP) and flows into the Neckar River without returning to the main channel (Figure A.1). Information regarding the fluvial geomorphology can be found in Schwientek et al., 2016.

The wastewater treatment plant (WWTP AZV Steinlach-Wiesaz), locating at approximately 4 km upstream from the mouth of the Steinlach River (N4.8°2.8′5.32″ E9°3′5.33″), has the physical capacity of 115000 population equivalent (p.e.). It is equipped with a secondary treatment facility and is capable of removing 69.6% and 90% of the annual incoming nitrogen and phosphorus respectively (https://uwwtd.eu/Germany/treatment-plant/detpbw4165100000064/2016). The mean effluent flow rate from the WWTP is 0.26 m^3s^{-1} Guillet et al. (2019), which makes up 14% of the mean discharge in the main channel of the Steinlach. However during the dry seasons, discharge from the WWTP effluent can account for as high as 50% of the discharge in the Steinlach main channel (Schwientek et al., 2016). The river stretch provides an ideal environment for investigating the fate (transport and degradation) of organic micropollutants and their mixture effects due to multiple factors such as relatively shallow (20 cm (Guillet et al., 2019)) and sparse vegetation.

Sampling. In 2020, the conductiviy (ECd) at the three measurement stations (MS1 - MS3 in Figure A.1) was measured three times using the conductivity-temperature-depth (CTD) divers (Schlumberger Water Sciences Technology, Canada) before the sampling. Two CTD divers were installed the first time at MS1 and MS2, respectively on June 26 and were retrieved on June 30. The second installation was on July 14 and three CTD divers were set at MS1, MS2 and MS3, respectively (Figure A.1) and they were retrieved on July 17. However, the WESS gauging station stopped working by that time and discharge values from the State Institute for the Environment Baden-Württemberg (https://www.hvz.baden-wuerttemberg.de/pegel.html?id=00089) were used as a reference. During this period two rain events took place that increased the discharge from 0.3 m^3s^{-1} to over 1 m^3s^{-1} in less than 24 hours. During the third measuring period on August 14, one CTD diver each was left at MS2 and MS3 and they were retrieved on August 16. In parallel, the discharge time-series at the upstream of the WWTP was recorded by the gauging

station (MS Up) from Water Earth System Science (WESS) program from the University of Tübingen.

The sampling campaign preparation started on August 18, 2020. The first measuring station (MS1) was set at 1.086 km downstream from the WWTP effluent, so that a complete lateral mixing of solutes in the stream at all MSs could be assumed. MS2 was set at 1.163 km downstream from the MS1); MS3 1.505 km downstream from the MS2. At each MS, an automated sampler (AS) (ISCO 3700, Teledyne Isco, Inc., USA) was deployed to sample the time-series of river water. AS1 started sampling at 20:00 on August 19 and stopped at 13:45 on August 21. AS2 started at 03:00 on August 20 and stopped at 15:15 on August 21 (AS2 stopped working from 03:30 to 07:30 on August 21). AS3 started at 09:30 on August 20 and stopped at 17:15 on August 21. Table S2 displays the detailed AS schedule, as well as the underlying mechanism of the Lagrangian point of view of tracking the same water parcels travel in rivers. Sampling temporal resolution was two hours. Each two-hour sample was mixed with eight sub-samples that were taken every 15 minutes. All recording times were Central European Summer Time (CEST). Grab samples were taken upstream of the WWTP (WESS station), at the WWTP effluent, in the streams Ehrenbach, Mühlbach and at MS1. Information regarding sample process is in Schmitt et al., 2021. In parallel, electrical conductivity (ECd) at MS Up, MS WWTP, MS down, MS1, MS2 and MS3 was measured continuously (two minutes temporal resolution) during the whole sampling period.

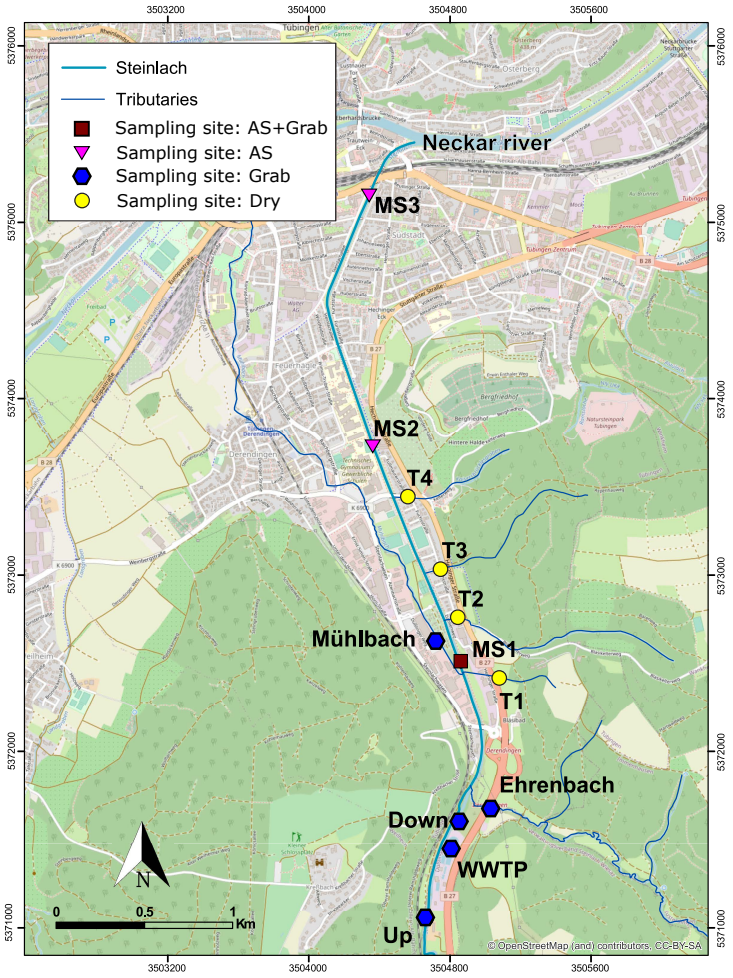

Figure A.1: Water flows from south to north in the main channel of the Steinlach river. Three grab samples were taken at MS1. No grab sample was taken at MS2 and MS3. One grab sample was taken at all of the rest of the MSs. T1-T4 represent the four small tributaries that flow into the main channel but were dry during the campaign. Abbreviation: AS – autosampler. Grab – grab sample. MS – measuring station. Map created by Victor Carvalho Cabral.

A.4 Electrical conductivity measurements correction

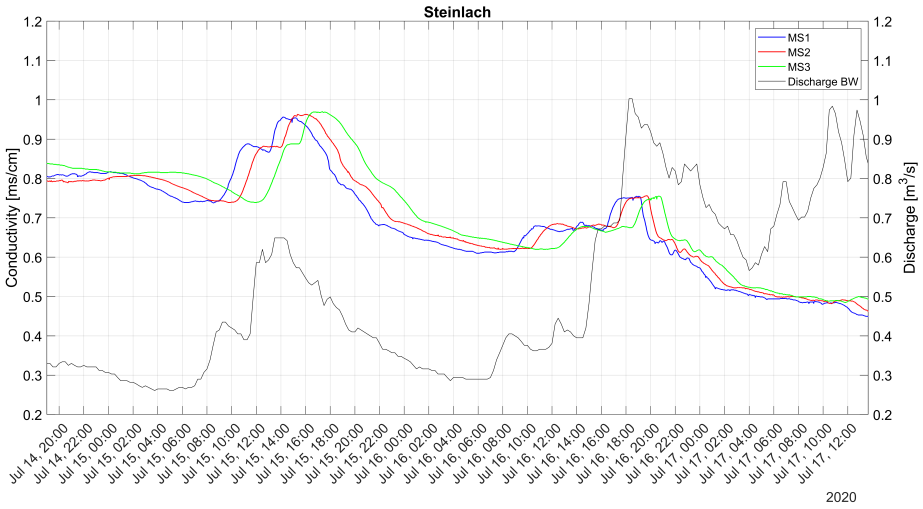

Figure A.2: ECd and discharge in Steinlach in July 2020. Discharge data is provided by State Institute for the Environment Baden-Württemberg (`https://www.hvz.baden-wuerttemberg.de/`)

Throughout the entire sampling period, the ECd measurements from the CTD probe at the WWTP effluent (Figure A.1) oscillated strongly (Figure A.4). On August 20, 2020, the CTD probe at the WWTP effluent experienced sudden drop of ECd signal. There were no rain events during the sampling campaign. Combined overflow sewage or separate sewer system will not be used under such condition. We can safely conclude that the CTD probe was pushed out of the water surface by the sudden high release from the WWTP approximately between 08:00 and 17:00, resulting the measured ECd dropped to unrealistically low values. Therefore, it was necessary to correct the signals in this time window and the following steps were used: 1) extracting the upper signal envelopes of the ECd values before and after the drop; 2) removing the polynomial trend in the disrupted part of the signal and generating random noise; 3) linearly interpolating the ECd values between the measurements before and after the drop ; 4) combining the random noise from 2) and linear interpolation results from 3) by addition; 5) smoothing the processed signals from 4) by moving mean; 6) Gaussian smoothing the reassembled signal vector: upper envelopes before the drop (from 1)), smoothed results from 5) and upper envelopes after the drop (from 1)). Figure A.3 displays scheme for the signal recovery and the corrected ECd results are shown in Figure A.5.

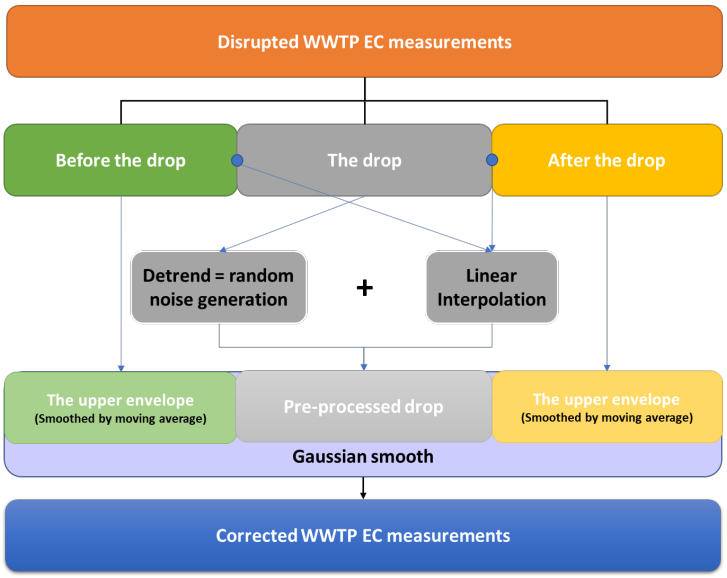

Figure A.3: Detailed procedures for correcting the measurements at the WWTP were disrupted due to the sudden high discharge from the WWTP.

Figure A.4: Measurements at the WWTP (illustrated in green color, showing strong oscillations.) were disrupted due to the sudden high discharge from the WWTP.

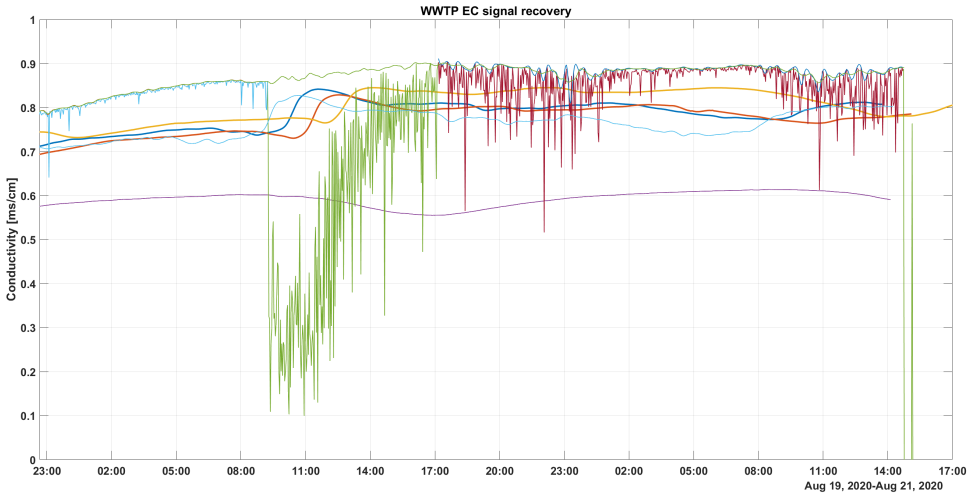

Figure A.5: The original WWTP EC signals before (plotted in light blue color) and after (plotted in dark pink color) the disrupt were separated. The corrected signals were plotted in between. The scheme of correction is in Figure A.3.

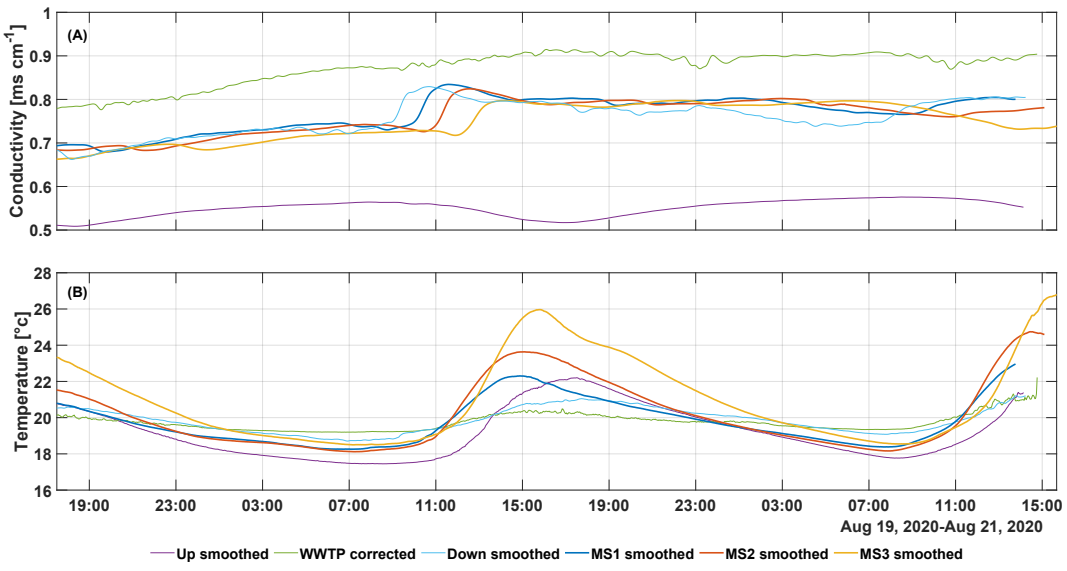

Figure A.6: Finally processed and temperature-compensated (A) ECd signals, and (B) water temperature measurements.

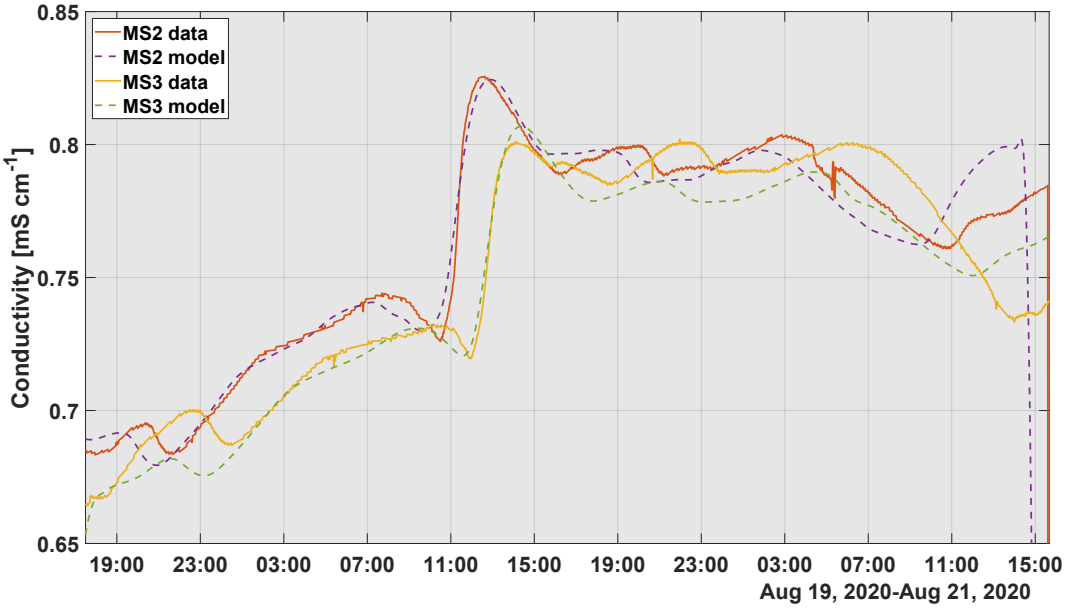

Figure A.7: Hydrological parameters (the dimensionless dispersion coefficient D and mean travel time Δt) were determined by fitting the modeled ECd to the measured results. The peak of the signal was the most important feature, of which the fit characterizes the hydrological parameters of the model.

A.5 Laboratory: chemical analysis

The collected water samples were stored in 1L brown glass bottles packed in iceboxes loaded with ice packs, and were transported to the laboratory as soon as possible during the campaign. A list of 80 organic micropollutants were selected as targeted compounds for our analysis, based on the information from the field campaigns in 2013 and 2015 (Guillet et al., 2019; Schwientek et al., 2016) at the similar sampling locations and sampling in 2017 in the Ammer River (Müller et al., 2018), into which the Steinlach drains. The concentrations of the micropollutants were quantified using a liquid chromatograph (1290 Infinity HPLC; Agilent Technologies; Waldbronn, Germany) coupled to tandem mass spectrometry (6470 Triple Quadrupole; Agilent Technologies, Santa Clara, USA). 46 out of the 80 targeted compounds were found in the water sample (the main categories of detected micropollutants were: pharmaceuticals, metabolites, fungicides, herbicides, surfactants and corrosion inhibitors). All sample preparation and full analytical work details can be found in the work of Schmitt et al., 2021.

A.6 Discharge time-series

Modeled discharge time-series showed that the sudden high release from the wastewater treatment plant caused the discharge in the river main channel to become unstable.

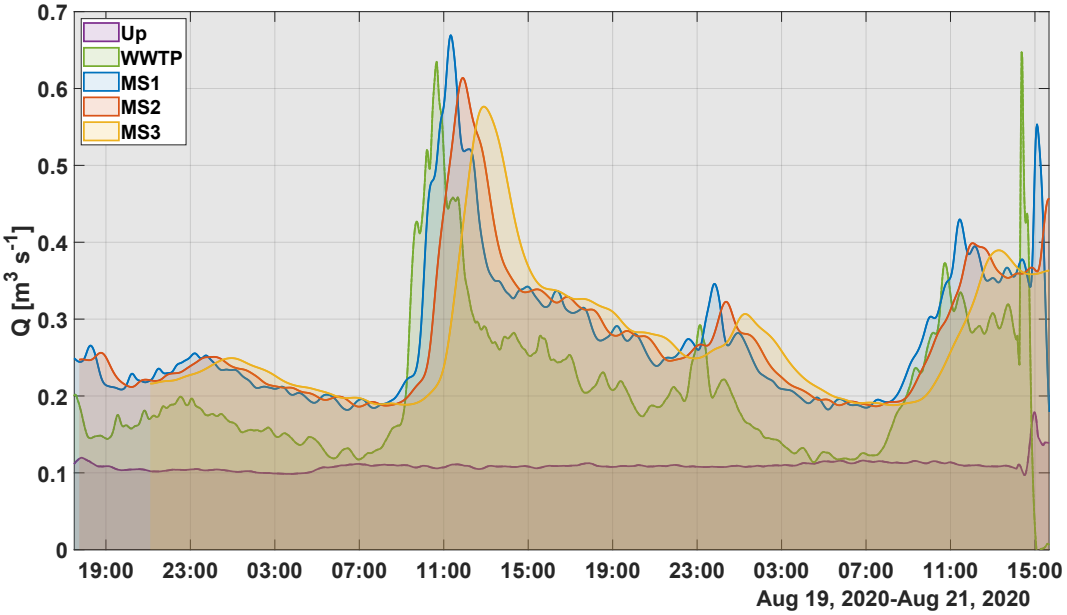

Figure A.8: Overlay of Figure 1A - E. The propagation of the wave in the river channel.

A.7 DOC and pH

Dissolved organic carbon (DOC) were measured from the grab samples during the day. From measuring station (MS) 1 to 3, additional night grab samples were also taken.

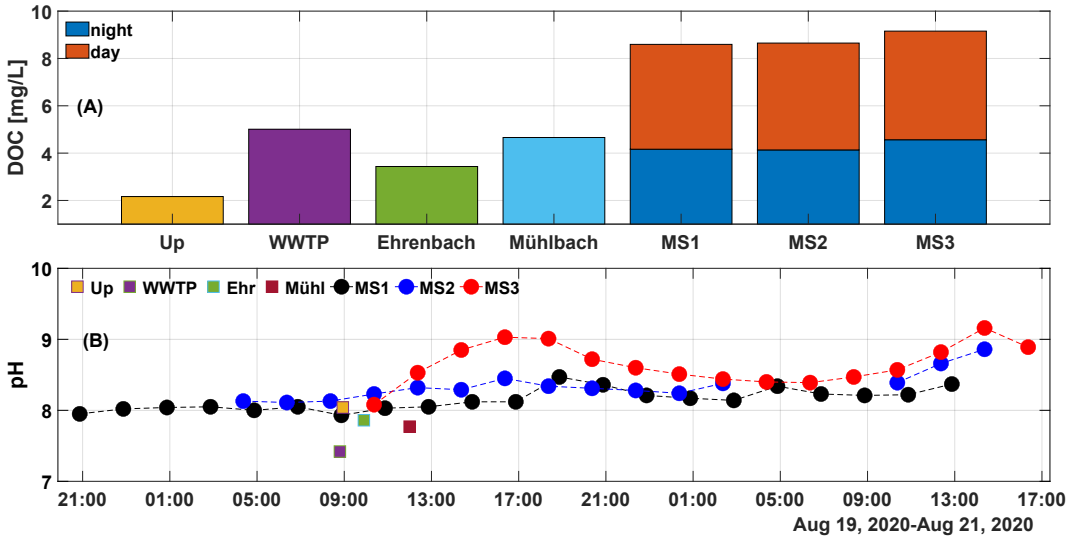

Figure A.9: (A) Grab samples of dissolved organic carbon during the night and day time. (B) Measured pH time-series.

A.8 Deterministic model: chemical concentration and mass flux

Reactive transport of individual compounds. The breakthrough curves of individual chemicals' concentration was modeled by the one-dimensional convolution-based reactive

transport model (Eq. A.8),

$$C_{i,\text{down}}(t) = \int_0^{t_{\max}} C_{i,\text{up}}(t-\tau) r_i(\tau) d\tau \tag{A.8}$$

where $C_{i,\text{up}}$ and $C_{i,\text{down}}$ are concentration [ng/L] of chemical i at upstream and downstream locations, respectively. i is the chemical index [-]. t is the sampling time point. $t_{\max}$ is the integral time interval. τ is the travel time of the individual water parcel. $r_i(\tau)$ is the reactive transfer function defined by Eq. A.9,

$$r_i(\tau) = g(\tau) \exp(-\lambda_i \cdot \tau) \tag{A.9}$$

where λ_i is the compound's specific first-order reaction constant [s^{-1}]. $g(\tau)$ is the conservative transfer function defined by Eq. A.10.

$$g(\tau) = \frac{1}{\tau \sqrt{\frac{4\pi D\tau}{\Delta t_{EC}}}} \exp\left[-\frac{(1-\frac{\tau}{\Delta t_{EC}})^2}{\frac{4D\tau}{\Delta t_{EC}}} \right] \tag{A.10}$$

The unsteady discharge is computed by using measured Q time-series at MS Up (WESS) as model input (Eq. A.11 – A.12).

$$Q_{\text{down}}(t) = \int_0^{t_{\max}} Q_{\text{up}}(t-\tau) q(\tau) d\tau \tag{A.11}$$

$$q(\tau) = \frac{1}{\tau \sqrt{\frac{20\pi D\tau}{3\Delta t_{\text{ECd}}}}} \exp\left[-\frac{(1-\frac{5\tau}{3\Delta t_{\text{ECd}}})^2}{\frac{20D\tau}{3\Delta t_{\text{ECd}}}} \right] \tag{A.12}$$

Details of Eq. A.9 – A.12 can be found in the Section 2 in the main text. The mass flux of individual compound is defined as the product of the concentration and the discharge (Eq. A.13).

$$F_i(t) = C_i(t) \cdot Q(t) \tag{A.13}$$

Objective function and the goodness of fit. We fitted the modeled downstream signals to the measured signal, deriving the transfer function's parameters, the mean travel time Δt_{ECd}, the lumped dispersion coefficient D and the first-order dissipation constants λ for the individual compounds. The deterministic calibration method requires objective function, which was defined as:

$$\min_{\theta}(f(\theta)) = \sum_{i=1}^{n} (f(\theta, x_i) - y_{\text{obs},i})^2 \tag{A.14}$$

where θ is the parameter to be found given the input (x_i) and observation ($y_{\text{obs},i}$). Normalized root-mean-square error (NRMSE) was computed for each compound to evaluate the goodness of the model fit.

$$\text{NRMSE} = \frac{\sqrt{\sum_{i=1}^{n} (y_{\text{model},i} - y_{\text{obs},i})^2 / n}}{y_{\text{obs,max}} - y_{\text{obs,min}}} \tag{A.15}$$

A.9 Stochastic model: randomizing the starting points for the Markov chains

Prior distribution To form the prior distribution, the detected organic micropollutants' reaction rate constants were derived from the literature half-lives (predicted biodegradation half-life values from quantitative structure–activity/property relationship (QSAR) model (Mansouri et al., 2018) (`https://comptox.epa.gov/dashboard`) using Eq. A.16,

$$\lambda = \frac{\ln(2)}{t_{1/2}} \tag{A.16}$$

where $t_{1/2,j}$ [time] is the literature half-life value, λ_j [time^{-1}] the first-order reaction rate constant. The prior probability density function (pdf) of the reaction constant $\lambda \sim \mathcal{N}(\mu_\lambda, \sigma_\lambda^2)$ is:

$$P_{\text{prior}}(\lambda) = \frac{1}{\sigma_\lambda \sqrt{2\pi}} \exp\left(-\frac{1}{2}\left[\frac{\lambda - \mu_\lambda}{\sigma_\lambda}\right]^2\right) \tag{A.17}$$

The starting point of the individual chain is a randomized value. For the first-order reaction rate constant λ, the starting points were drawn from a normal distribution centered at the deterministic calibration results, and with the variance derived empirically by computing the standard deviation of the 'predetermined' reaction rate constants time-series $\lambda(t)$ [s^{-1}]. By implementing the Lagrangian concept of tracking the same water packages (Jaeger et al., 2018; Glaser et al., 2020), the $\lambda(t)$ is defined as:

$$\lambda_{EU}(t) = \ln\left(\frac{EU_{\text{bio}_j,\text{down}}(t)}{EU_{\text{bio}_j,\text{up}}(t)}\right) / \Delta t_{\text{EC}} \tag{A.18}$$

$$\lambda_{TU}(t) = \ln\left(\frac{TU_{\text{bio}_j,\text{down}}(t)}{TU_{\text{bio}_j,\text{up}}(t)}\right) / \Delta t_{\text{EC}} \tag{A.19}$$

where t [time] is the sampling time point, Δt_{EC} [time] the mean travel time in the study reach. $EU_{\text{bio}_j,\text{up}}(t)$, $EU_{\text{bio}_j,\text{down}}(t)$, $TU_{\text{bio}_j,\text{up}}(t)$ and $TU_{\text{bio}_j,\text{down}}(t)$ are the assay-specific effect units and toxic units measured from the same water package passing the upstream and downstream sampling points, respectively. In the case of the standard deviation σ_ϵ in the likelihood function, a normal distribution from which the randomized starting points were drawn was parameterized using the reported measurement errors (Adams et al., 2015).

A.10 time-series of experimental and modeled concentration

The deterministic convolution-based model with first-order kinetics were able to reproduce the in-stream dynamics of the concentration of the individual micropollutants. Three missing data points at measuring station 2 were due to the malfunction of auto-sampler 2 between 03:30 and 07:30 on August 21, 2020.

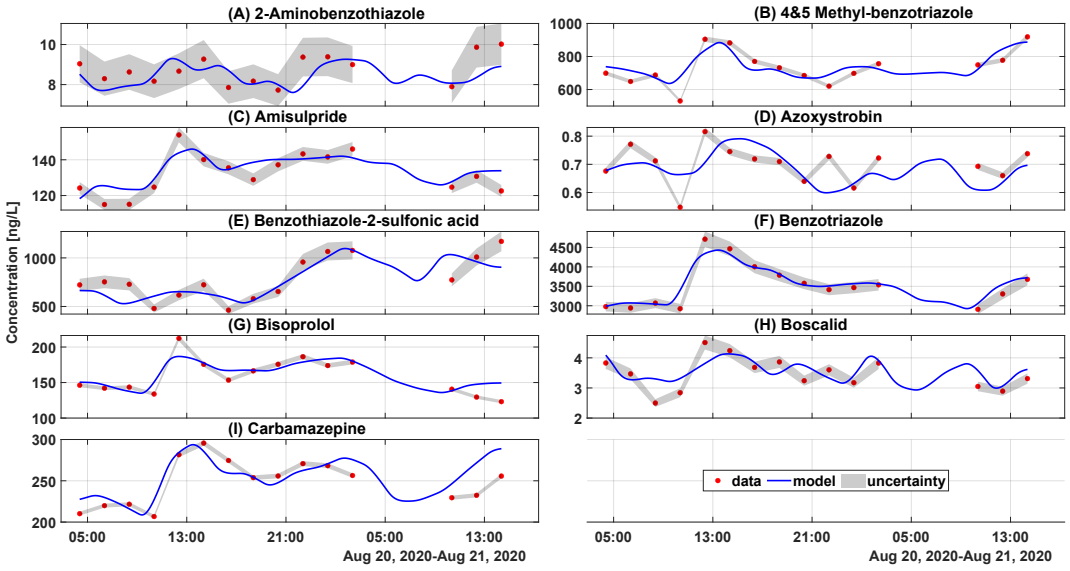

Figure A.10: The time course of measured concentration data and calibrated modeling results at MS2. Auto-sampler 2 stopped working from 03:30 to 07:30 on August 21, 2020. Completed measured concentration data can be found in Schmitt et al., 2021. Measured concentrations were reprinted (adapted) with permission from Schmitt et al., 2021. Copyright 2021 American Chemical Society.

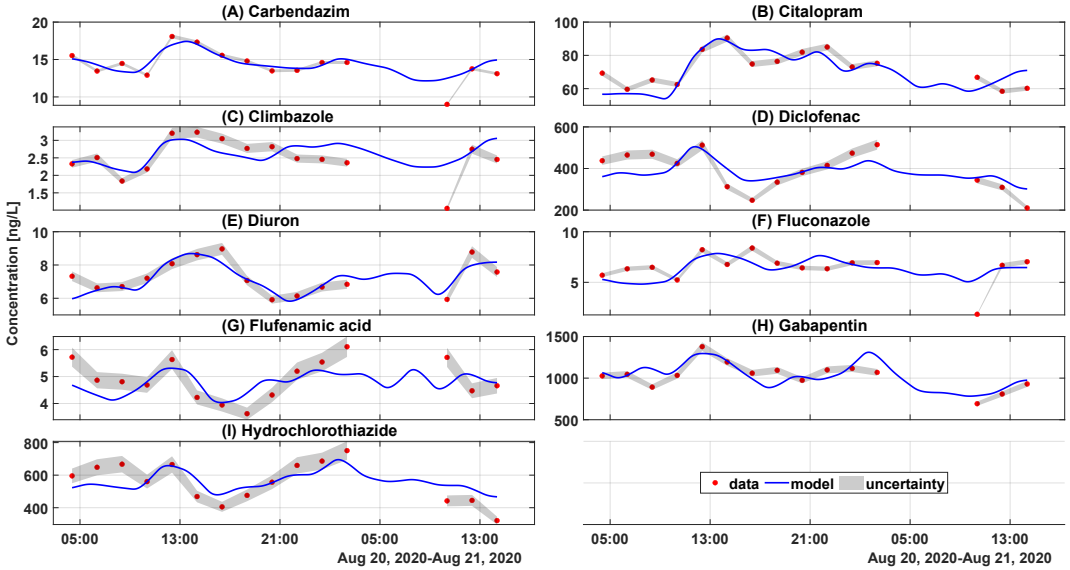

Figure A.11: The time course of measured concentration data and calibrated modeling results at MS2. Auto-sampler 2 stopped working from 03:30 to 07:30 on August 21, 2020. Completed measured concentration data can be found in Schmitt et al., 2021. Measured concentrations were reprinted (adapted) with permission from Schmitt et al., 2021. Copyright 2021 American Chemical Society.

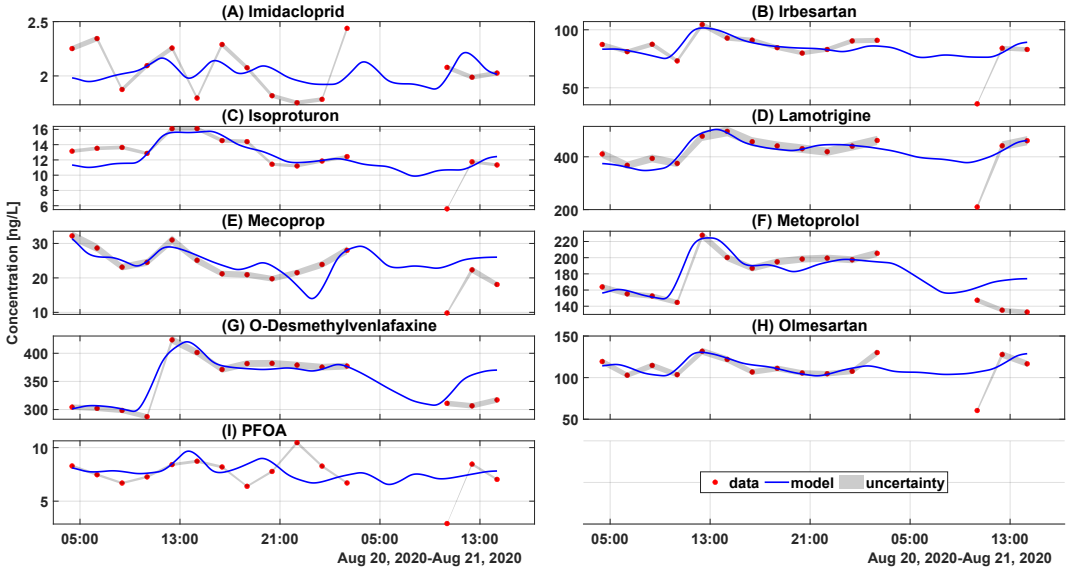

Figure A.12: The time course of measured concentration data and calibrated modeling results at MS2. Auto-sampler 2 stopped working from 03:30 to 07:30 on August 21, 2020. Completed measured concentration data can be found in Schmitt et al., 2021. Measured concentrations were reprinted (adapted) with permission from Schmitt et al., 2021. Copyright 2021 American Chemical Society. Abbreviation: PFOA – Pentadecafluorooctanoic acid.

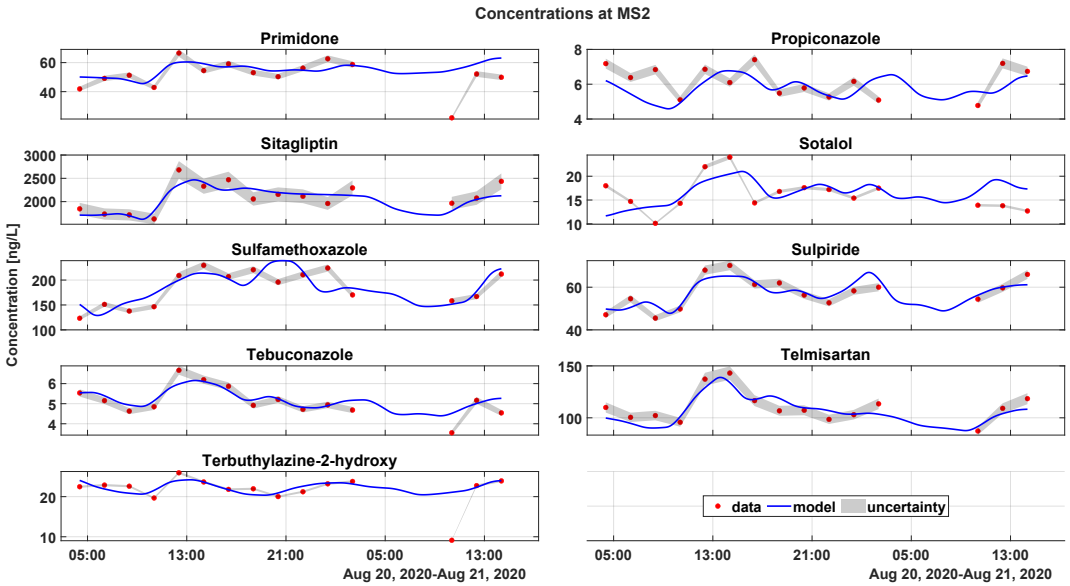

Figure A.13: The time course of measured concentration data and calibrated modeling results at MS2. Auto-sampler 2 stopped working from 03:30 to 07:30 on August 21, 2020. Completed measured concentration data can be found in Schmitt et al., 2021. Measured concentrations were reprinted (adapted) with permission from Schmitt et al., 2021. Copyright 2021 American Chemical Society.

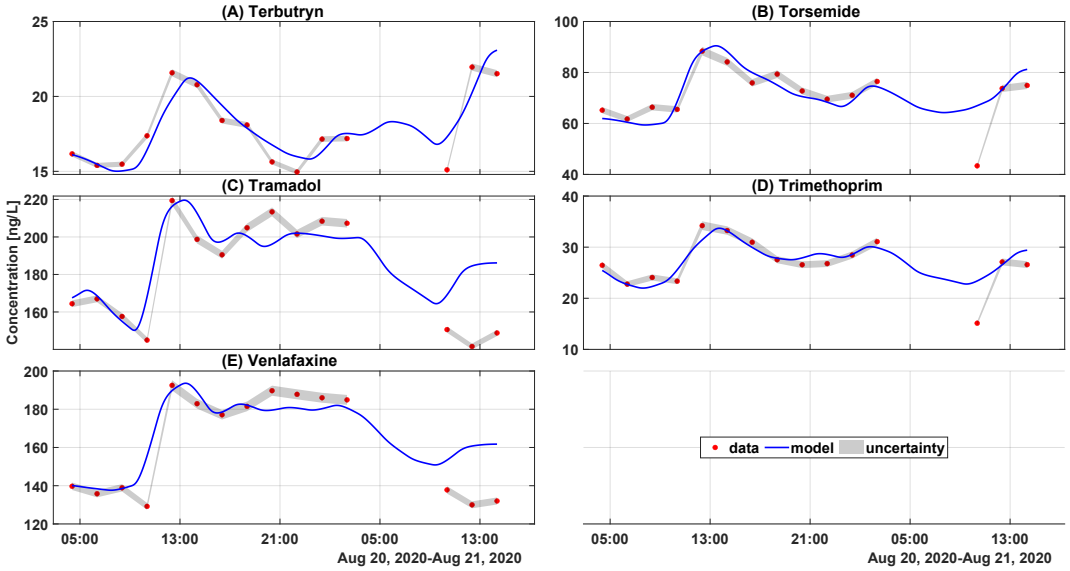

Figure A.14: The time course of measured concentration data and calibrated modeling results at MS2. Auto-sampler 2 stopped working from 03:30 to 07:30 on August 21, 2020. Completed measured concentration data can be found in Schmitt et al., 2021. Measured concentrations were reprinted (adapted) with permission from Schmitt et al., 2021. Copyright 2021 American Chemical Society.

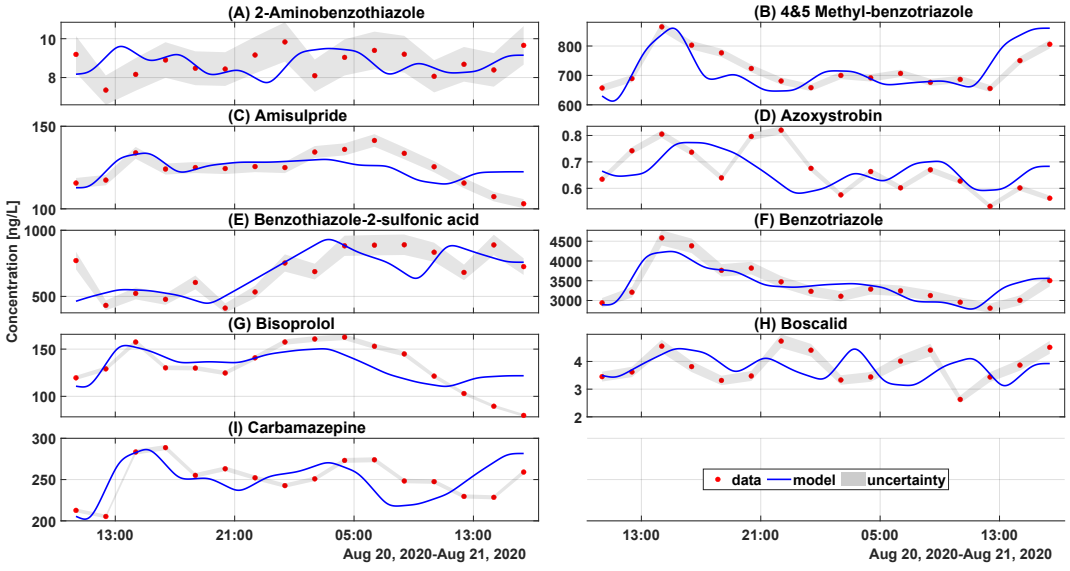

Figure A.15: The time course of measured concentration data and calibrated modeling results at MS3. Completed measured concentration data can be found in Schmitt et al., 2021. Measured concentrations were reprinted (adapted) with permission from Schmitt et al., 2021. Copyright 2021 American Chemical Society.

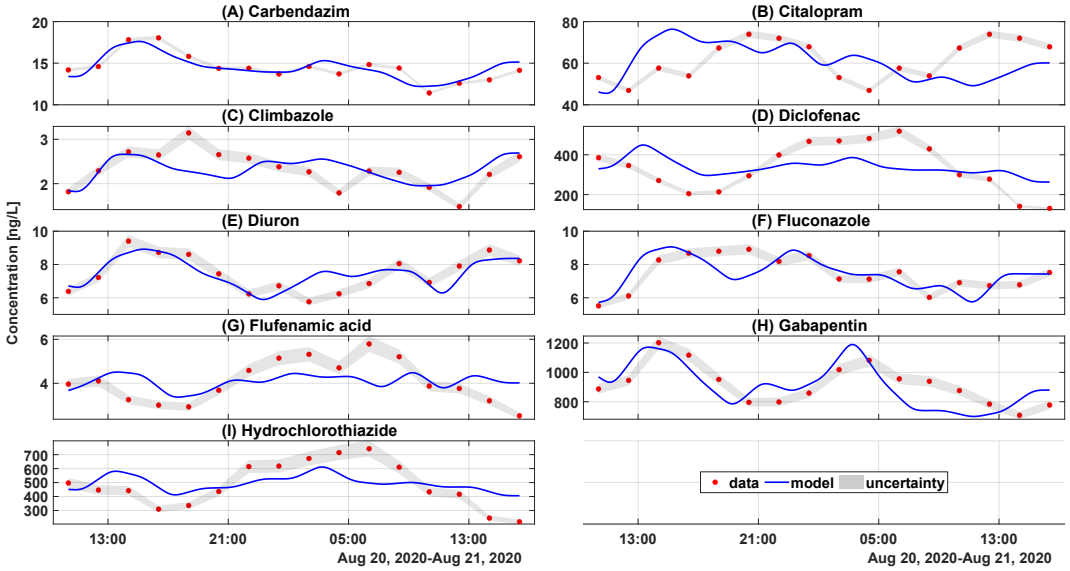

Figure A.16: The time course of measured concentration data and calibrated modeling results at MS3. Completed measured concentration data can be found in Schmitt et al., 2021. Measured concentrations were reprinted (adapted) with permission from Schmitt et al., 2021. Copyright 2021 American Chemical Society.

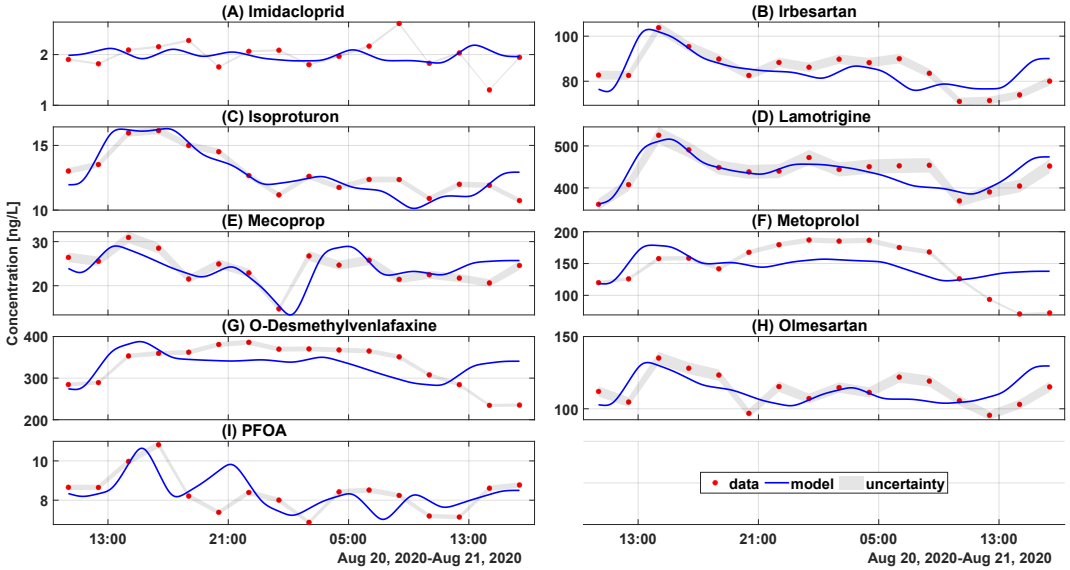

Figure A.17: The time course of measured concentration data and calibrated modeling results at MS3. Completed measured concentration data can be found in Schmitt et al., 2021. Measured concentrations were reprinted (adapted) with permission from Schmitt et al., 2021. Copyright 2021 American Chemical Society. Abbreviation: PFOA – Pentadecafluorooctanoic acid.

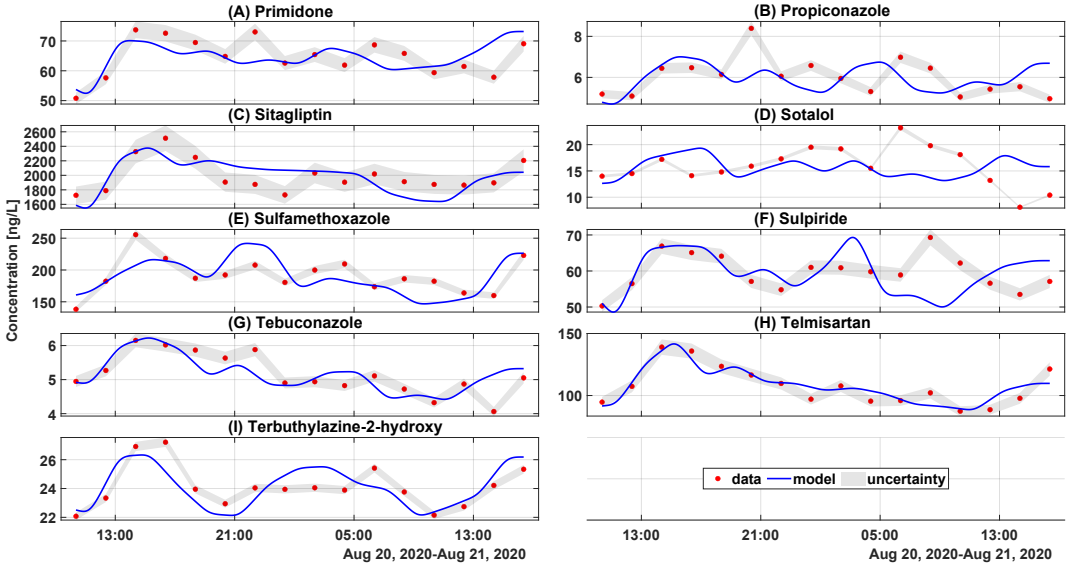

Figure A.18: The time course of measured concentration data and calibrated modeling results at MS3. Completed measured concentration data can be found in Schmitt et al., 2021. Measured concentrations were reprinted (adapted) with permission from Schmitt et al., 2021. Copyright 2021 American Chemical Society.

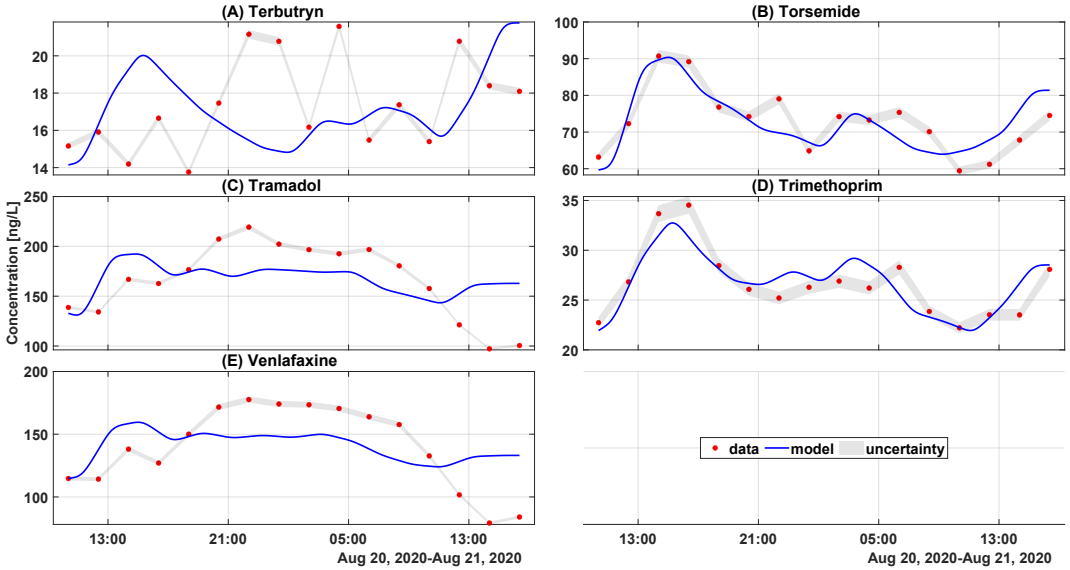

Figure A.19: The time course of measured concentration data and calibrated modeling results at MS3. Completed measured concentration data can be found in Schmitt et al., 2021. Measured concentrations were reprinted (adapted) with permission from Schmitt et al., 2021. Copyright 2021 American Chemical Society.

A.11 time-series of experimental and modeled mass flux

The deterministic convolution-based model with first-order kinetics were able to reproduce the in-stream dynamics of the mass flux of the individual micropollutants. Three

missing data points at measuring station 2 were due to the malfunction of auto-sampler 2 between 03:30 and 07:30 on August 21, 2020.

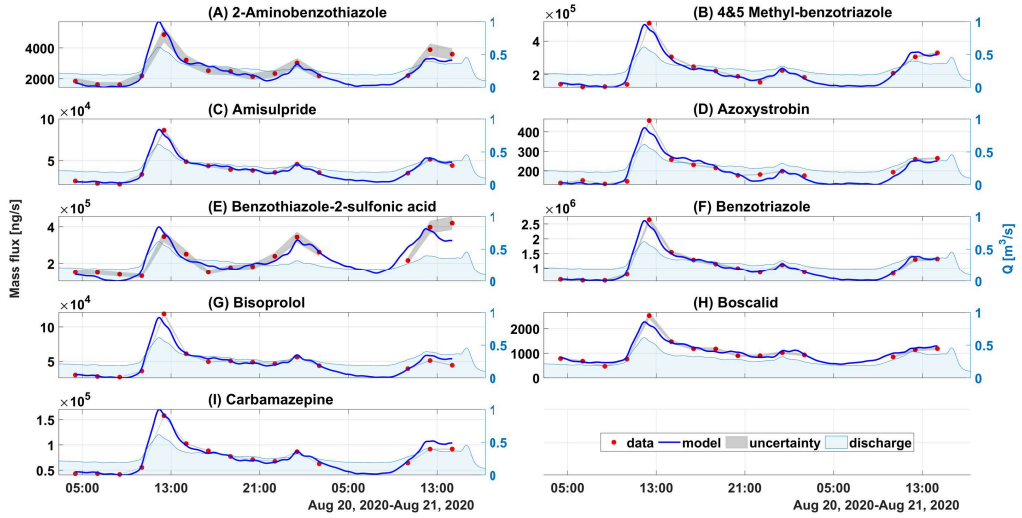

Figure A.20: The time course of mass flux data and calibrated modeling results at MS2. Auto-sampler 2 stopped working from 03:30 to 07:30 on August 21, 2020. Auto-sampler 2 stopped working from 03:30 to 07:30 on August 21, 2020.

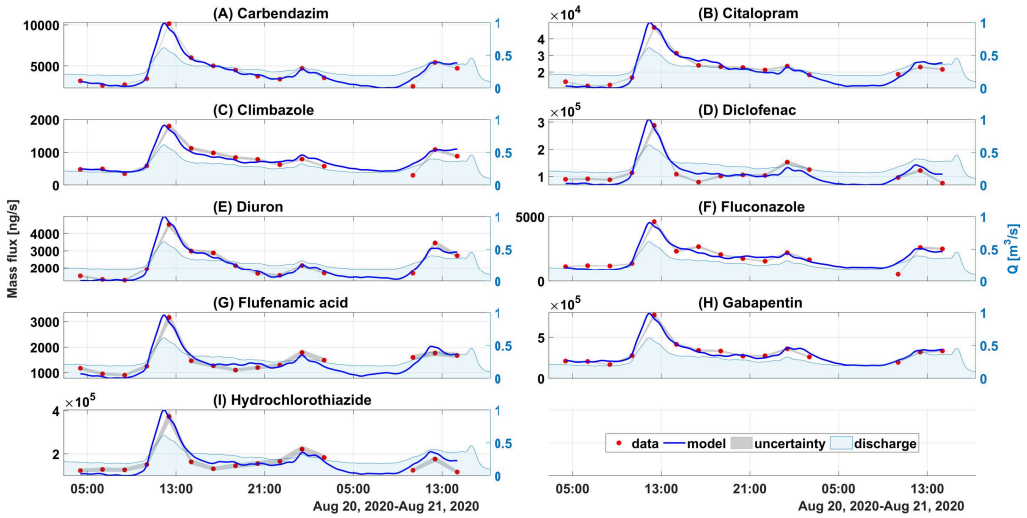

Figure A.21: The time course of mass flux data and calibrated modeling results at MS2. Auto-sampler 2 stopped working from 03:30 to 07:30 on August 21, 2020.

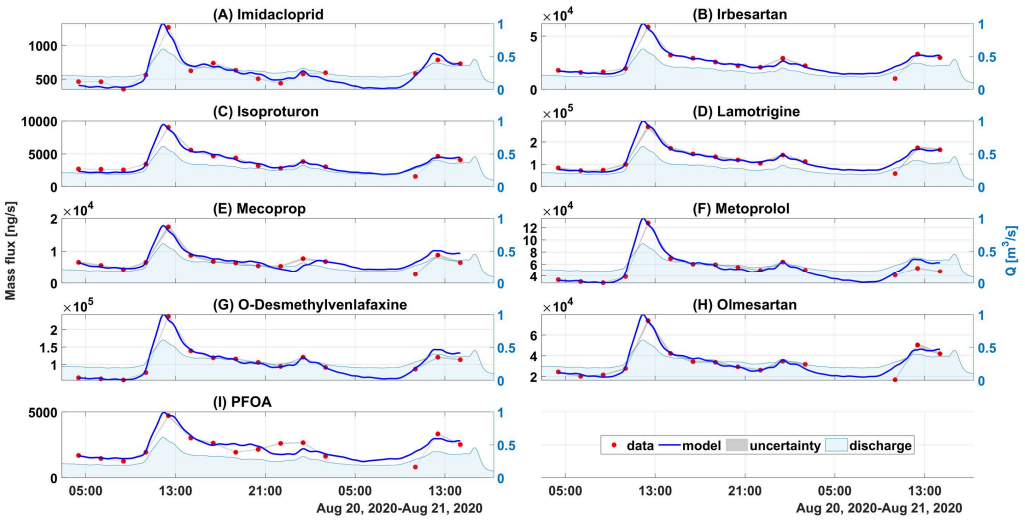

Figure A.22: The time course of mass flux data and calibrated modeling results at MS2. Autosampler 2 stopped working from 03:30 to 07:30 on August 21, 2020. Abbreviation: PFOA – Pentadecafluorooctanoic acid.

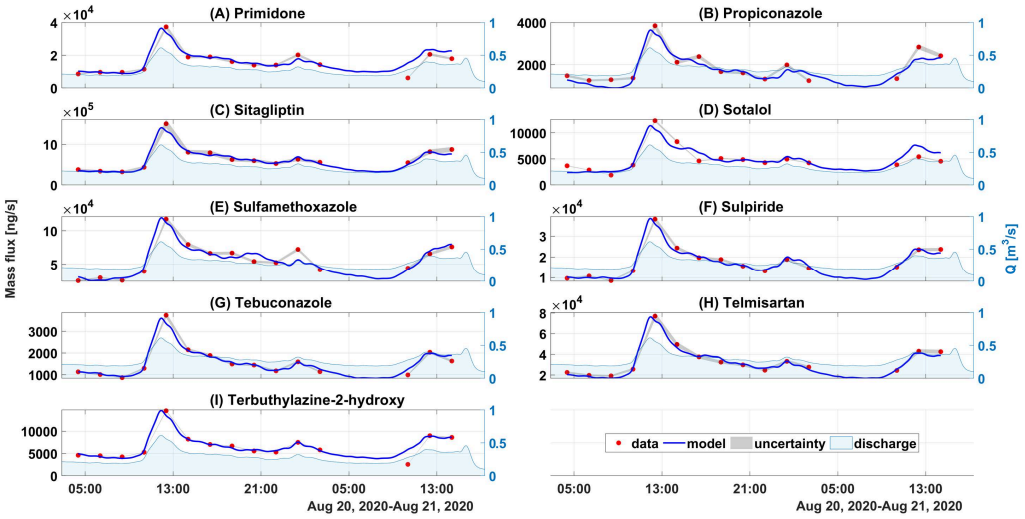

Figure A.23: The time course of mass flux data and calibrated modeling results at MS2. Autosampler 2 stopped working from 03:30 to 07:30 on August 21, 2020.

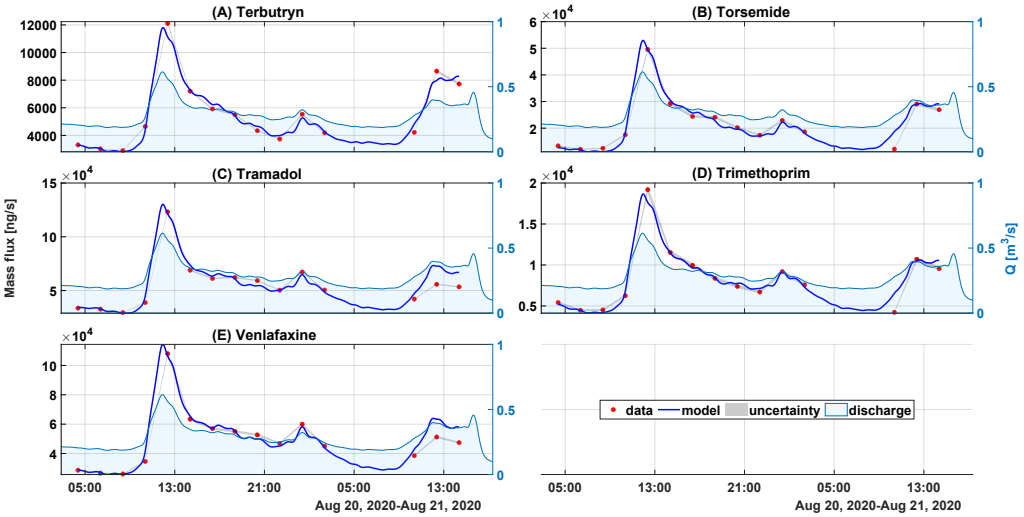

Figure A.24: The time course of mass flux data and calibrated modeling results at MS2. Autosampler 2 stopped working from 03:30 to 07:30 on August 21, 2020.

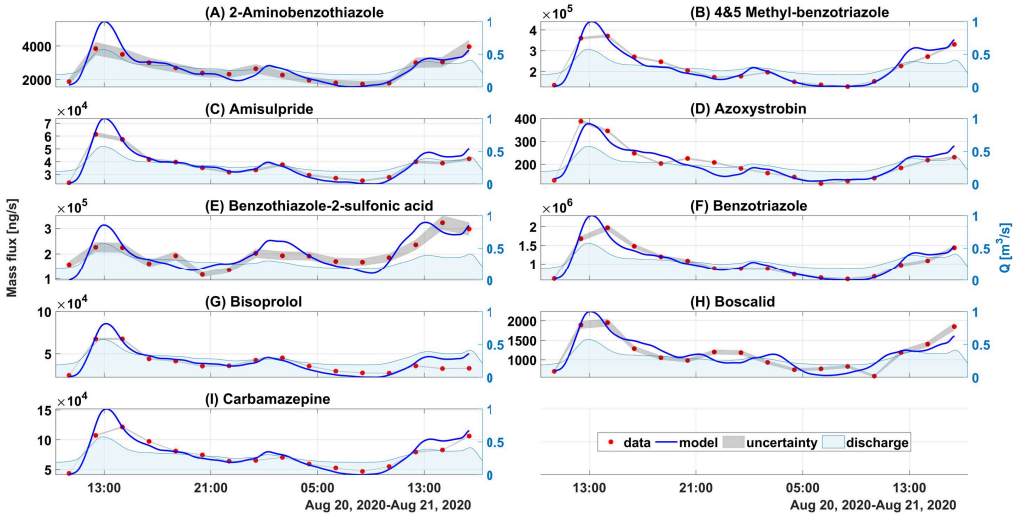

Figure A.25: The time course of mass flux data and calibrated modeling results at MS3.

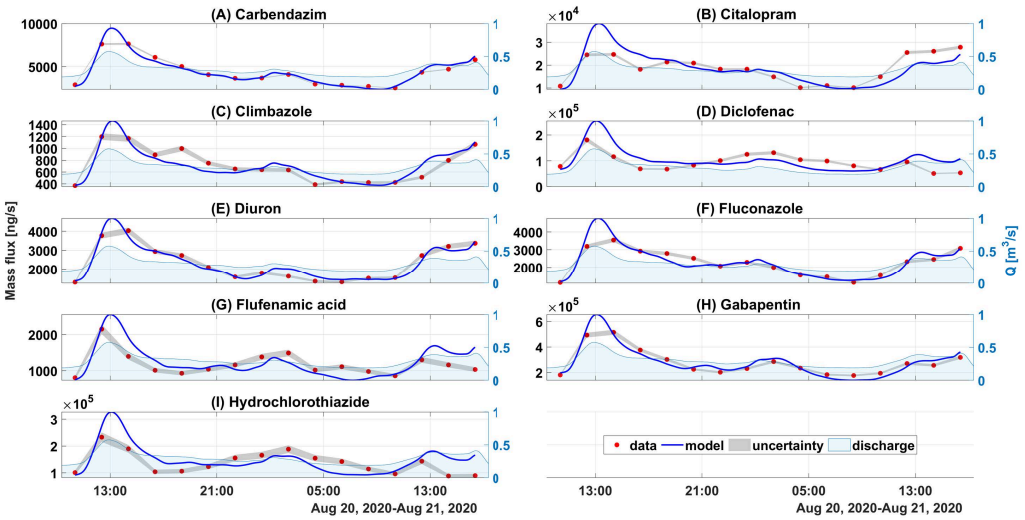

Figure A.26: The time course of mass flux data and calibrated modeling results at MS3.

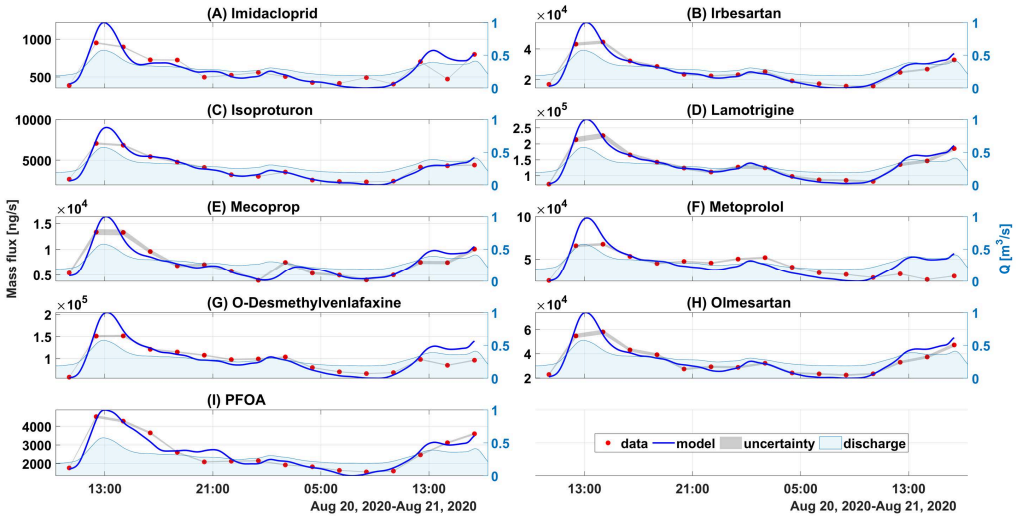

Figure A.27: The time course of mass flux data and calibrated modeling results at MS3. Abbreviation: PFOA – Pentadecafluorooctanoic acid.

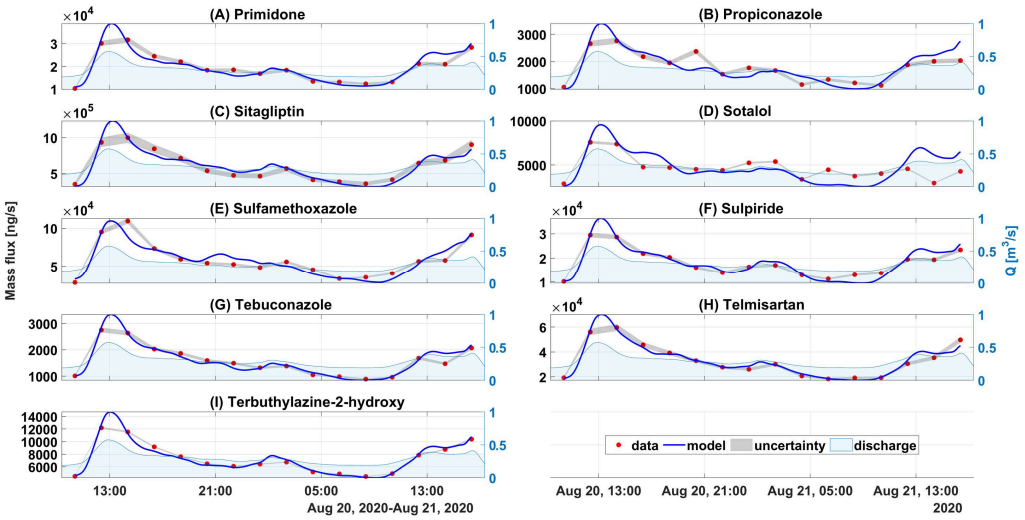

Figure A.28: The time course of mass flux data and calibrated modeling results at MS3.

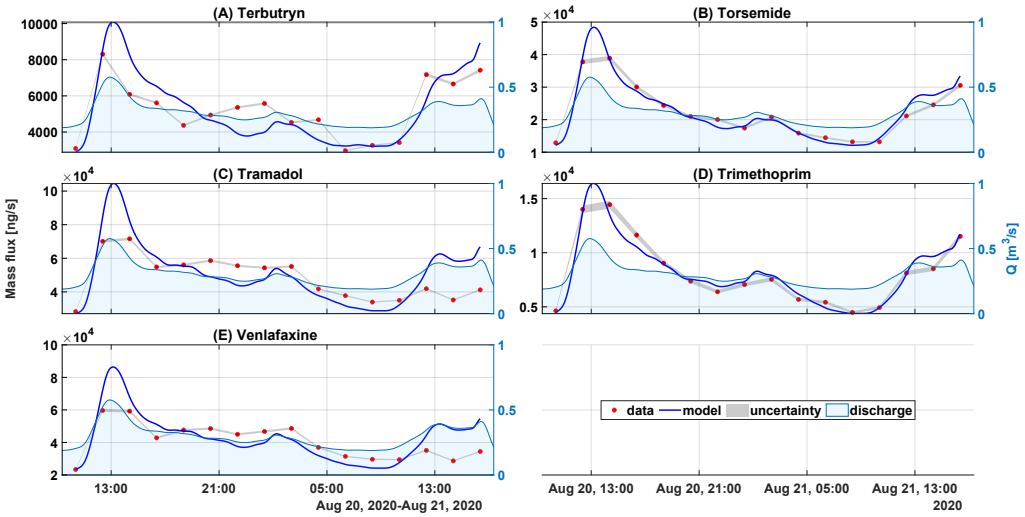

Figure A.29: The time course of mass flux data and calibrated modeling results at MS3.

A.12 Effect units of the individual detected compounds and their effect unit fluxes

Three missing data points at measuring station 2 were due to the malfunction of auto-sampler 2 between 03:30 and 07:30 on August 21, 2020.

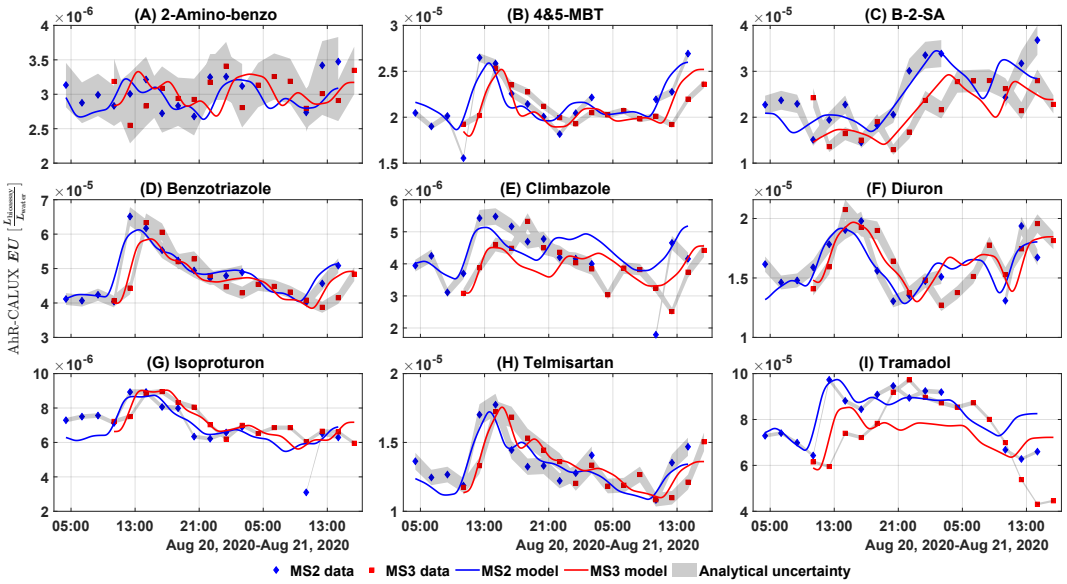

Figure A.30: Observed and modeled individual effect unit ($EU_{\text{chem},i}$) in AhR-CALUX at MS2 and MS3. 2-Amino-benzo – 2-Aminobenzothiazole; 4&5-MBT – 4&5 Methyl-benzotriazole; B-2-SA – Benzothiazole-2-sulfonic acid.

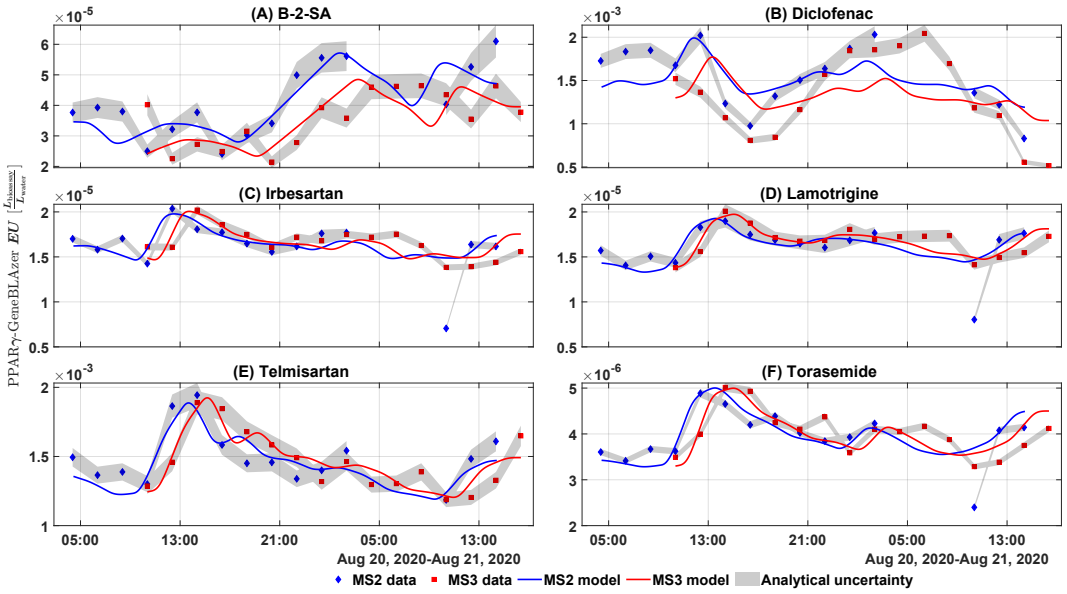

Figure A.31: Observed and modeled individual effect unit ($EU_{\text{chem},i}$) in PPARγ - GeneBLAzer at MS2 and MS3. B-2-SA – Benzothiazole-2-sulfonic acid.

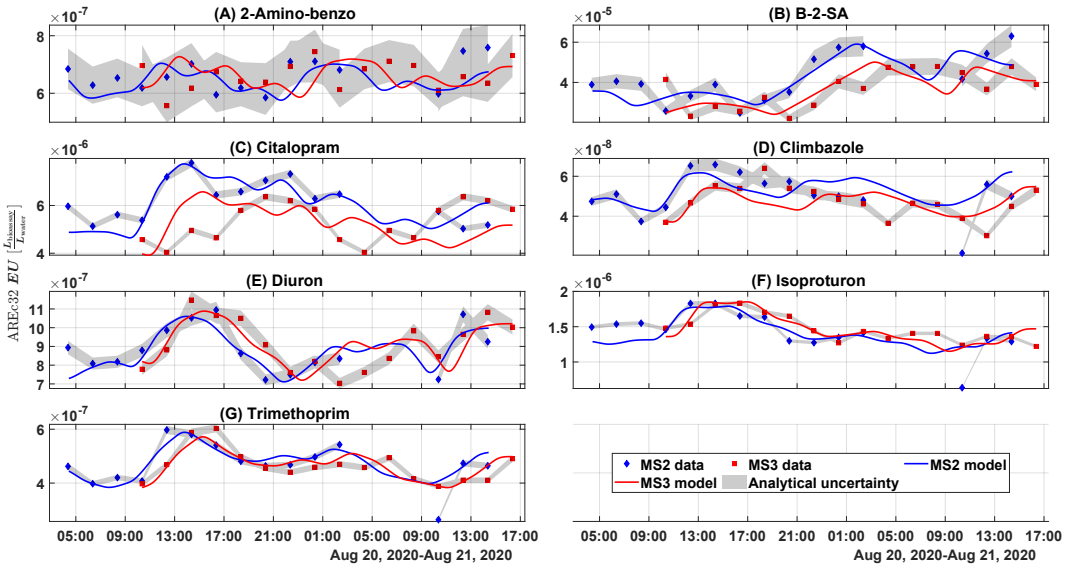

Figure A.32: Observed and modeled individual effect unit ($EU_{\mathrm{chem},i}$) in AREc32 at MS2 and MS3. 2-Amino-benzo – 2-Aminobenzothiazole; B-2-SA – Benzothiazole-2-sulfonic acid.

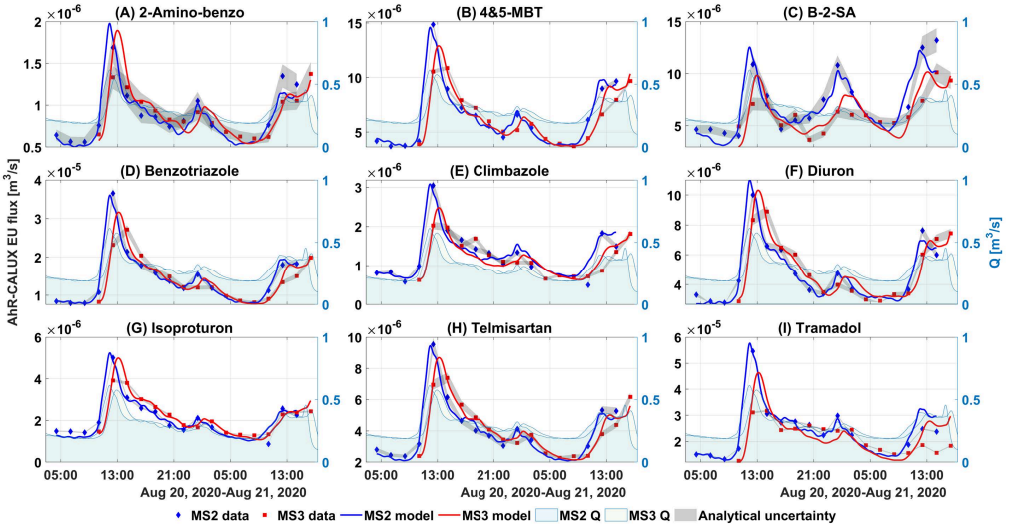

Figure A.33: Measured and modeled effect unit fluxes time-series of the detected chemicals that were activated in AhR-CALUX. Analytical uncertainties originating from the concentration measurements were illustrated in grey area. Discharges at the corresponding locations were shown in light blue and green areas. Abbreviations: 2-Amino-benzo – 2-Aminobenzothiazole; 4&5-MBT – 4&5 Methyl-benzotriazole; B-2-SA – Benzothiazole-2-sulfonic acid.

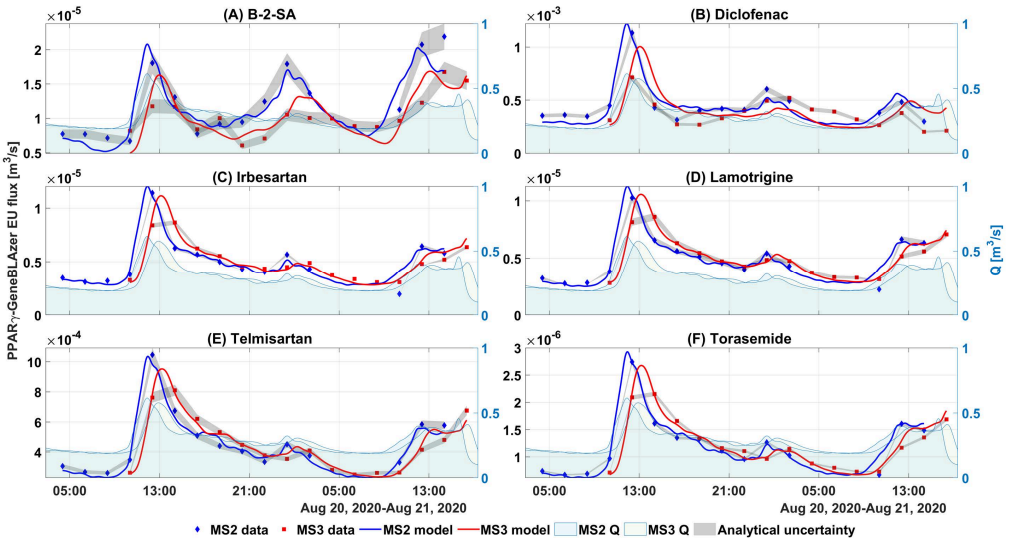

Figure A.34: Observed and modeled individual effect unit fluxes in PPARγ at MS2 and MS3. B-2-SA – Benzothiazole-2-sulfonic acid.

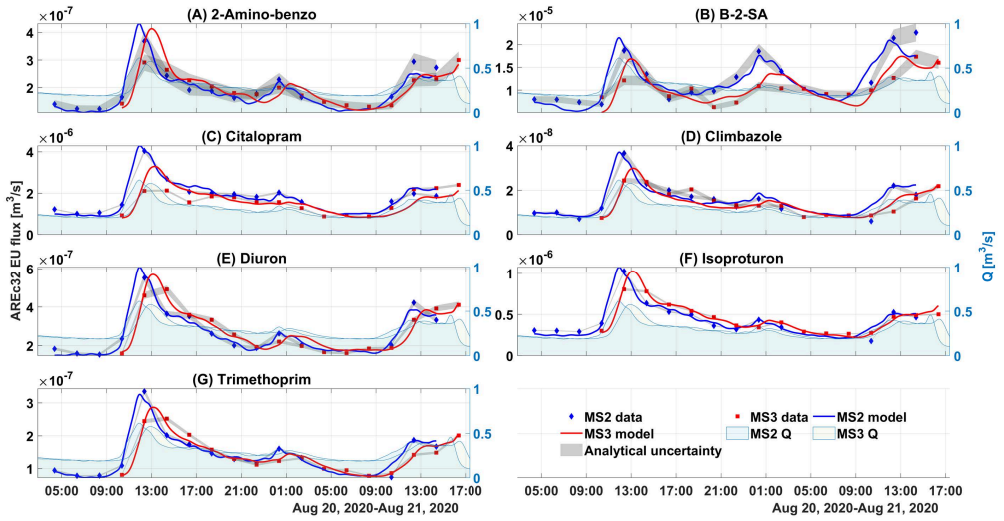

Figure A.35: Observed and modeled individual effect unit ($EU_{\mathrm{chem},i}$) flux in AREc32 at MS2 and MS3. 2-Amino-benzo – 2-Aminobenzothiazole; B-2-SA – Benzothiazole-2-sulfonic acid.

A.13 Toxic units of the individual detected compounds and their toxic unit fluxes

Three missing data points at measuring station 2 were due to the malfunction of auto-sampler 2 between 03:30 and 07:30 on August 21, 2020.

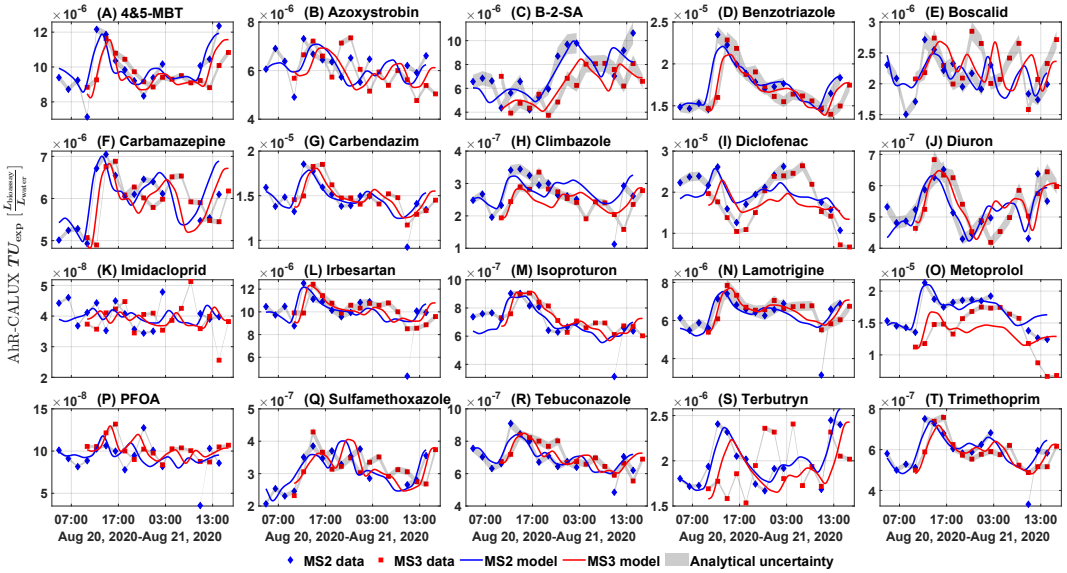

Figure A.36: Observed and modeled individual toxic unit ($TU_{\text{chem},i}$) in AhR-CALUX at MS2 and MS3. Abbreviations: 4&5-MBT – 4&5 Methyl-benzotriazole; B-2-SA – Benzothiazole-2-sulfonic acid; PFOA – Pentadecafluorooctanoic acid; SFOX – Sulfamethoxazole.

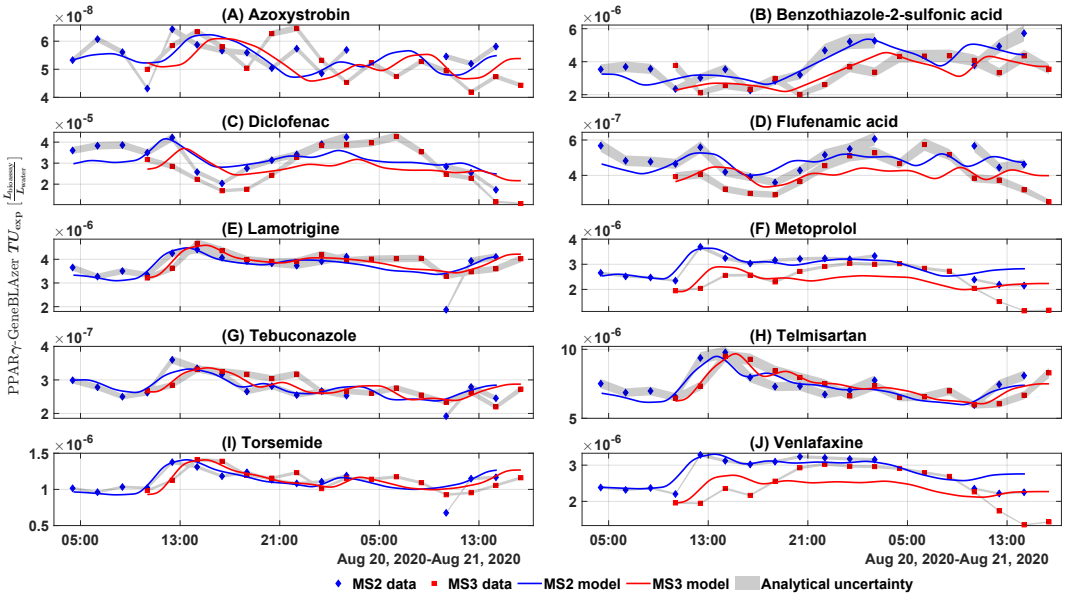

Figure A.37: Observed and modeled individual toxic unit ($TU_{\text{chem},i}$) in PPARγ - GeneBLAzer at MS2 and MS3.

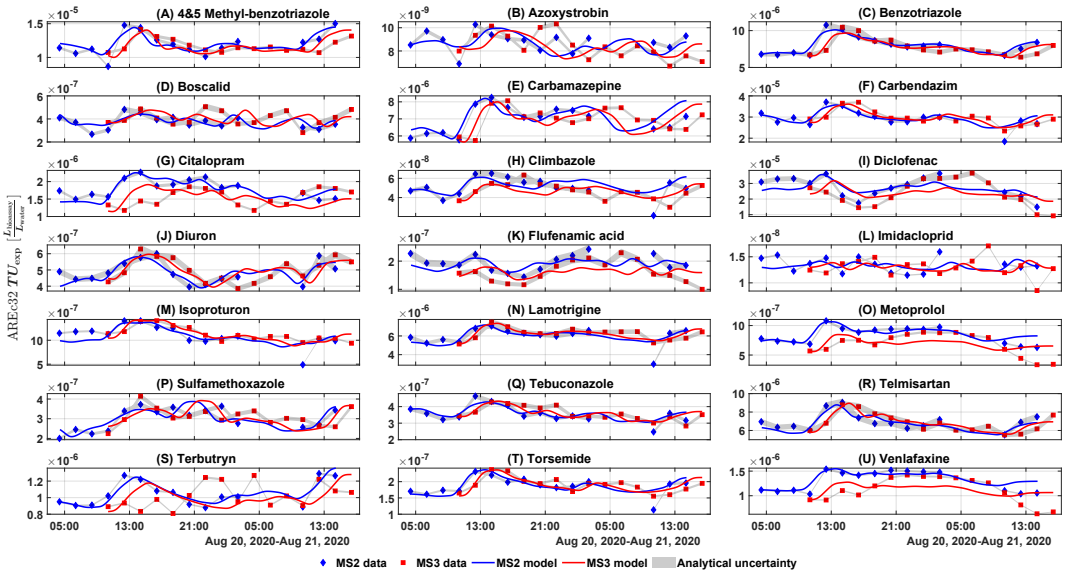

Figure A.38: Observed and modeled individual toxic unit ($TU_{\text{chem},i}$) in AREc32 at MS2 and MS3.

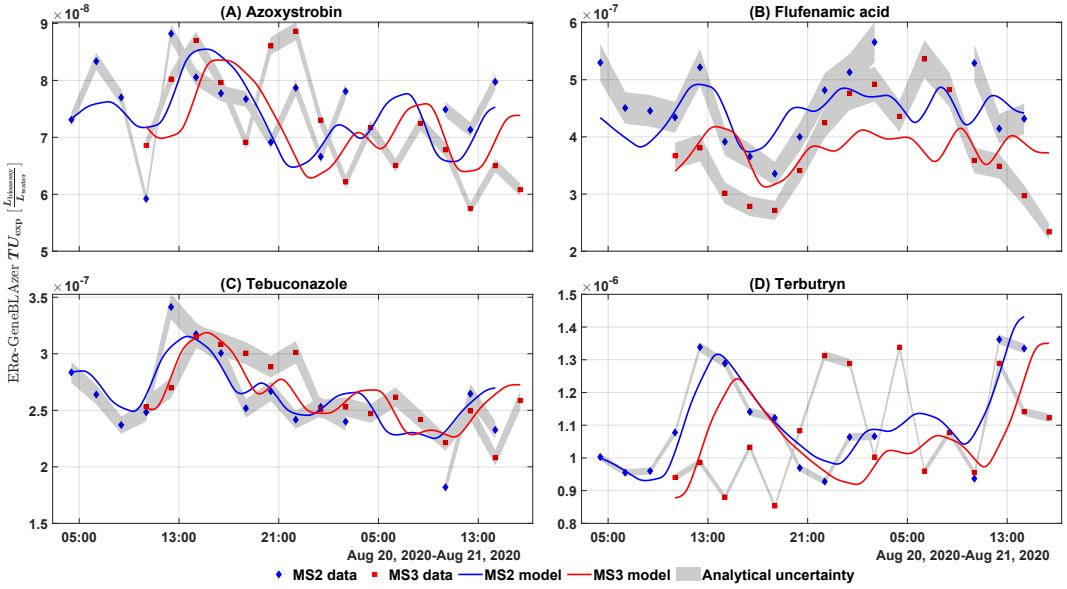

Figure A.39: Observed and modeled individual toxic unit ($TU_{\text{chem},i}$) at in ERα - GeneBLAzer MS2 and MS3.

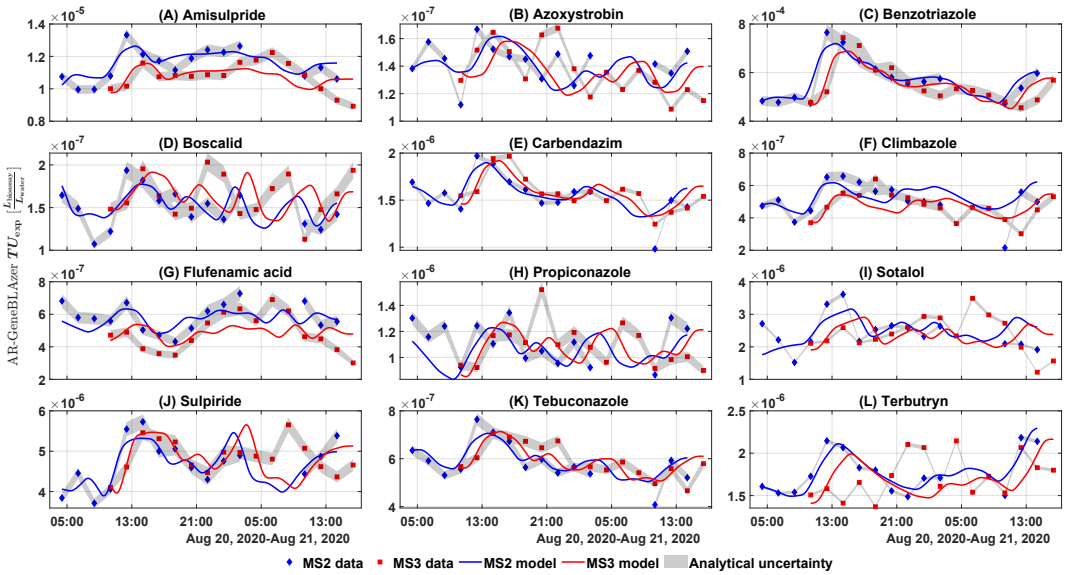

Figure A.40: Observed and modeled individual toxic unit ($TU_{\text{chem},i}$) in AR - GeneBLAzer at MS2 and MS3.

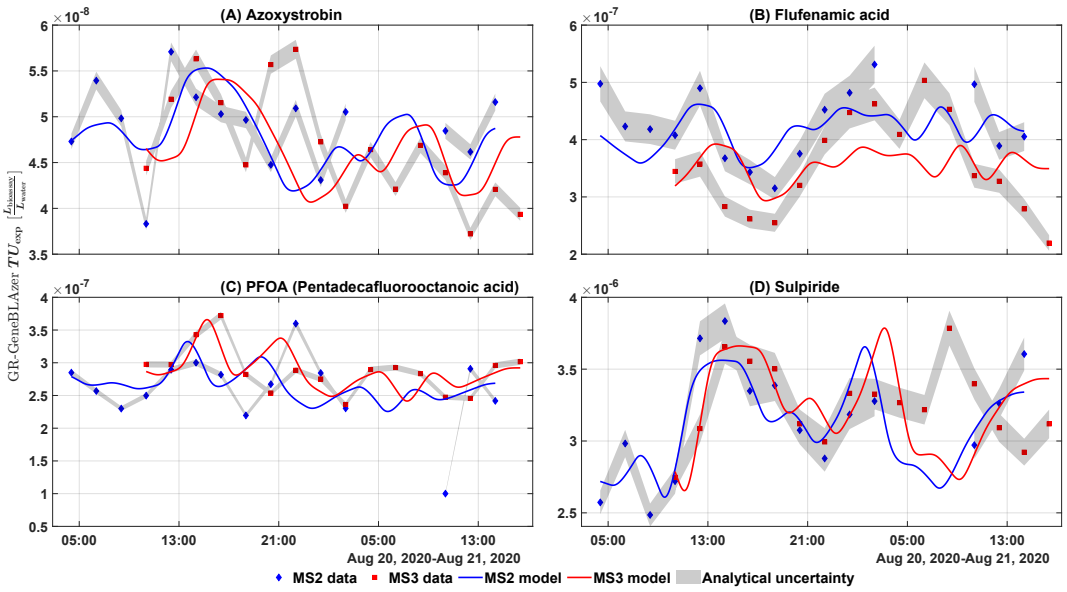

Figure A.41: Observed and modeled individual toxic unit ($TU_{\text{chem},i}$) in GR - GeneBLAzer at MS2 and MS3.

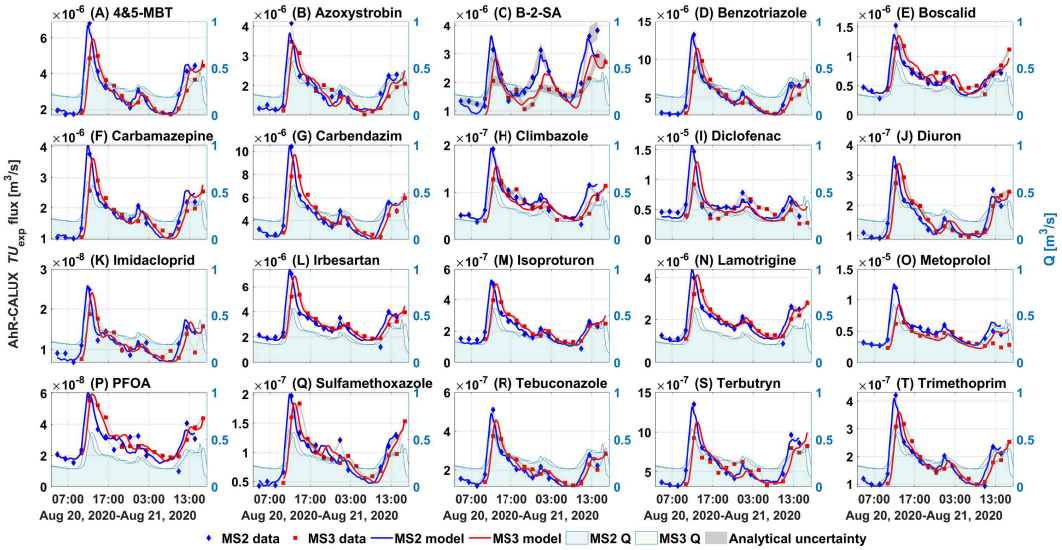

Figure A.42: Observed and modeled individual toxic unit ($TU_{\text{chem},i}$) flux. Abbreviation: 4&5-MBT – 4&5 Methyl-benzotriazole; B-2-SA – Benzothiazole-2-sulfonic acid; PFOA – Pentadecafluorooctanoic acid.

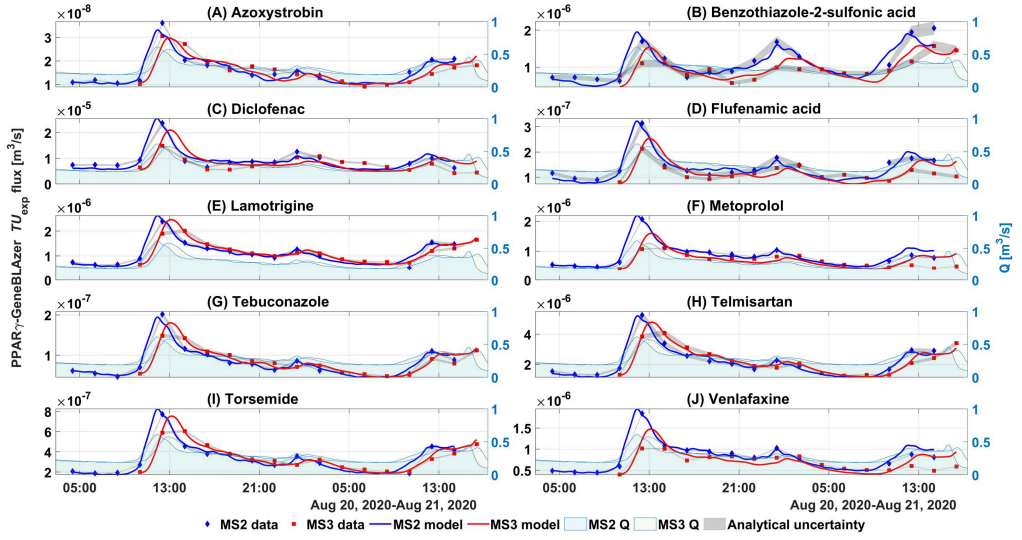

Figure A.43: Observed and modeled individual toxic unit ($TU_{\text{chem},i}$) flux in PPARγ - GeneBLAzer.

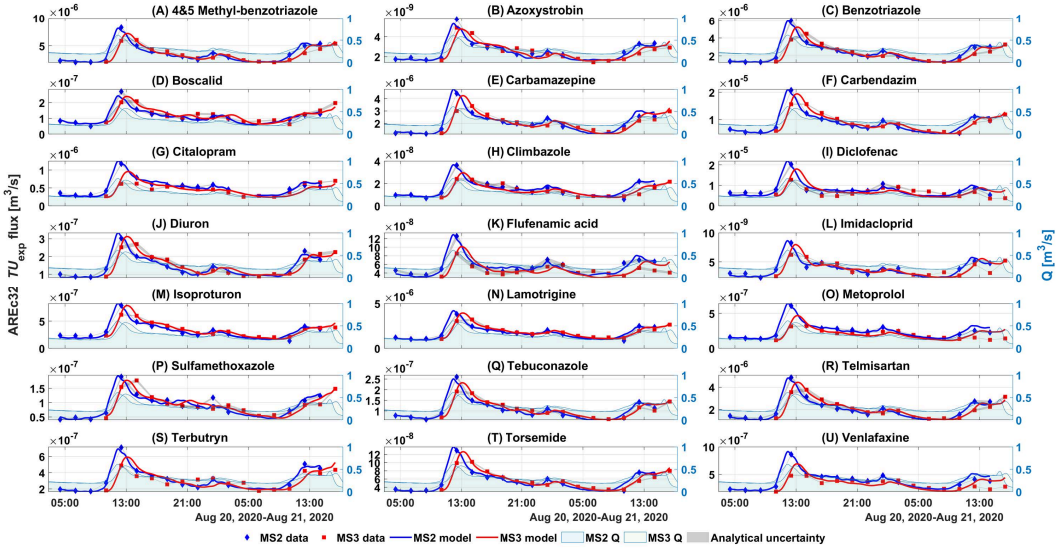

Figure A.44: Observed and modeled individual toxic unit ($TU_{\text{chem},i}$) flux in AREc32.

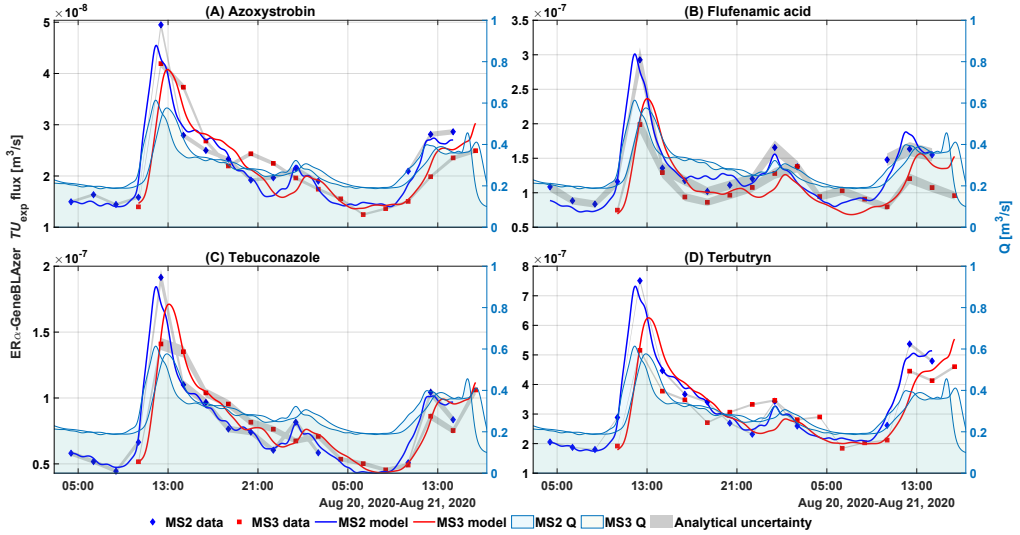

Figure A.45: Observed and modeled individual toxic unit ($TU_{\text{chem},i}$) flux in ERα - GeneBLAzer.

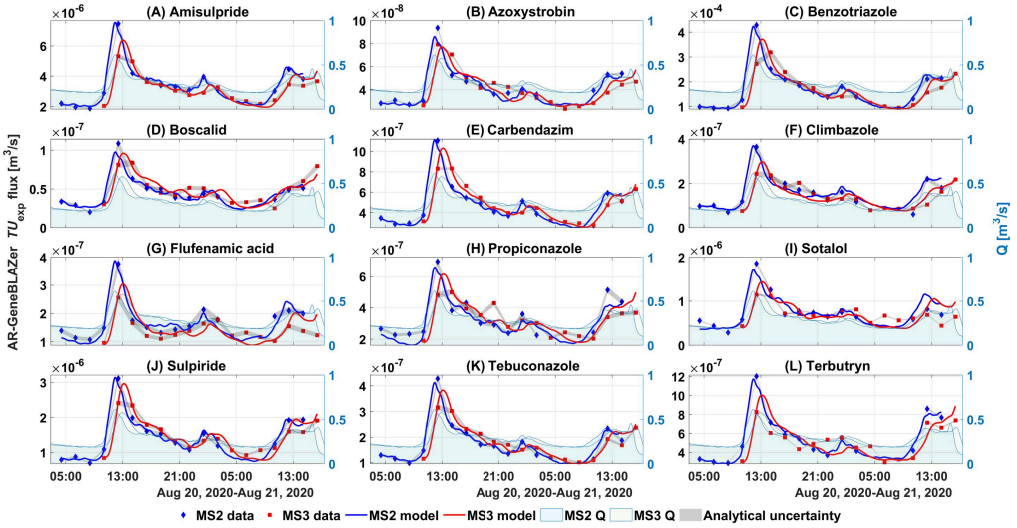

Figure A.46: Observed and modeled individual toxic unit ($TU_{\text{chem},i}$) flux in AR- GeneBLAzer.

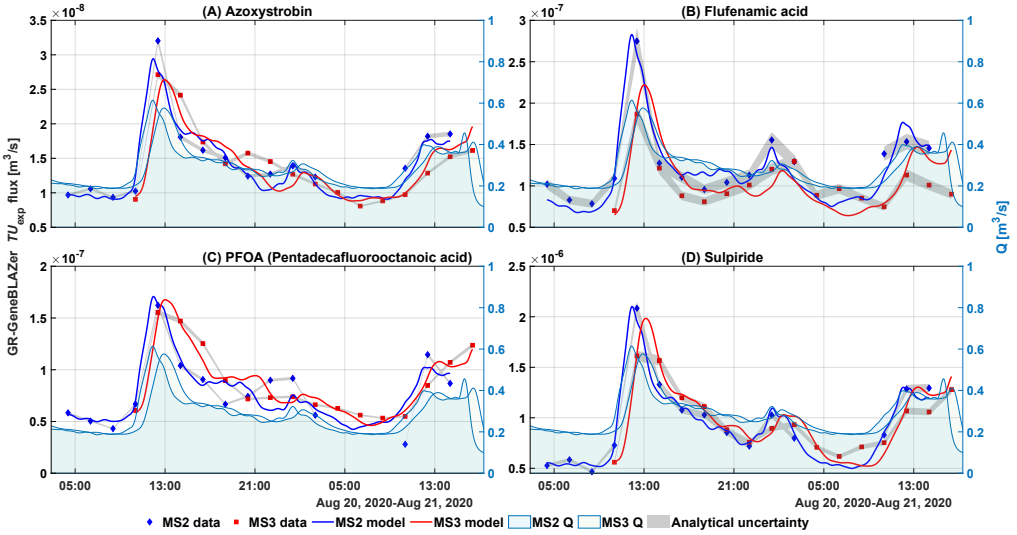

Figure A.47: Observed and modeled individual toxic unit ($TU_{\text{chem},i}$) flux in GR- GeneBLAzer.

A.14 Effect unit in the main channel: individual contributions to the mixture.

The individual compounds contributions to *EU*chem did not vary significantly over measuring stations (Figure A.48). Benzothiazole-2-sulfonic acid contributed the highest percent. Specifically 38%, 53% and 62% of the effect in AhR-CALUX , PPARγ-GeneBLAzer and AREc32, respectively from the samples taken by AS1, and 35%, 62% in AhR-CALUX and AREc32, respectively from the samples taken by AS3. Only in the case of PPARγ-GeneBLAzer, it contributed the second largest amount, overtaken by telmisartan (51%), in the samples taken by AS3. In comparison to EU_{bio} (Figure A.48), the individually detected compounds in total contributed less than 1% effects in all bioassays.

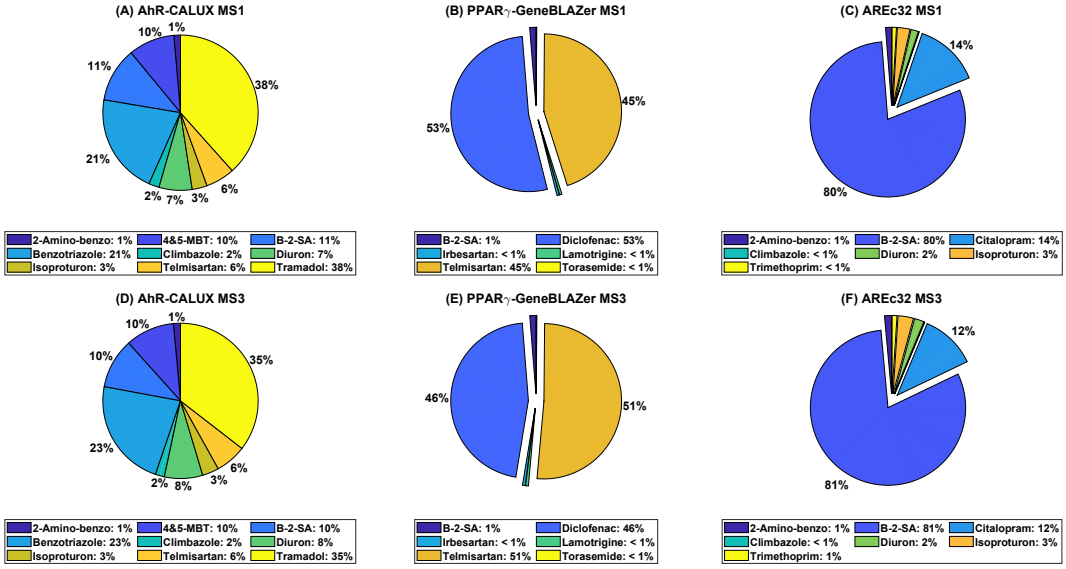

Figure A.48: The mean effect units over the sampling period from individual compounds: the individual percentage of the effect $EU_{\text{chem},i}$ contributed to EU_{chem} mixture. Abbreviations: 2-Amino-benzo – 2-Aminobenzothiazole; 4&5-MBT – 4&5 Methyl-benzotriazole; B-2-SA – Benzothiazole-2-sulfonic acid.

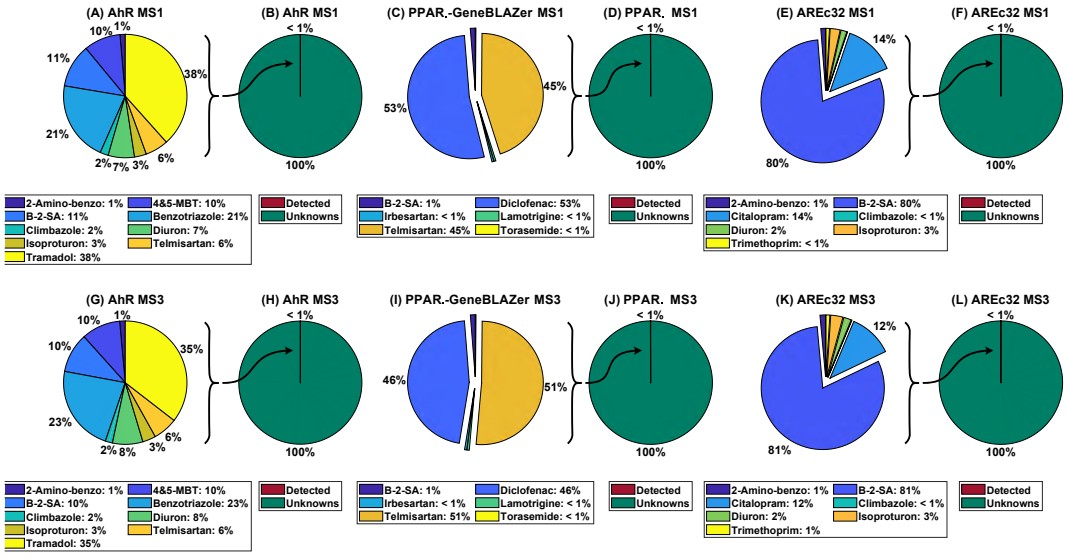

Figure A.49: The mean effect units over the sampling period from individual compounds: the individual percentage of the $EU_{\text{chem},i}$ contributed to EU_{chem} mixture in comparison with the share from the unknowns. Abbreviations: 2-Amino-benzo – 2-Aminobenzothiazole; 4&5-MBT – 4&5 Methyl-benzotriazole; B-2-SA – Benzothiazole-2-sulfonic acid.

A.15 Toxic units in the main channel: individual contributions to the mixture.

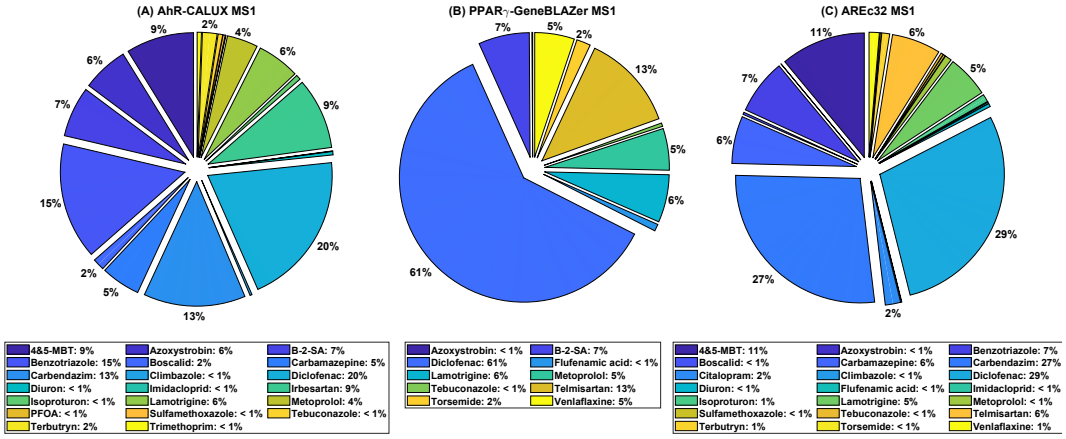

Figure A.50: The mean toxic units $TU_{\text{chem},i}$ over the sampling period from individual compounds to TU_{chem}. 2-Amino-benzo – 2-Aminobenzothiazole; 4&5-MBT – 4&5 Methyl-benzotriazole; B-2-SA – Benzothiazole-2-sulfonic acid; PFOA – Pentadecafluorooctanoic acid.

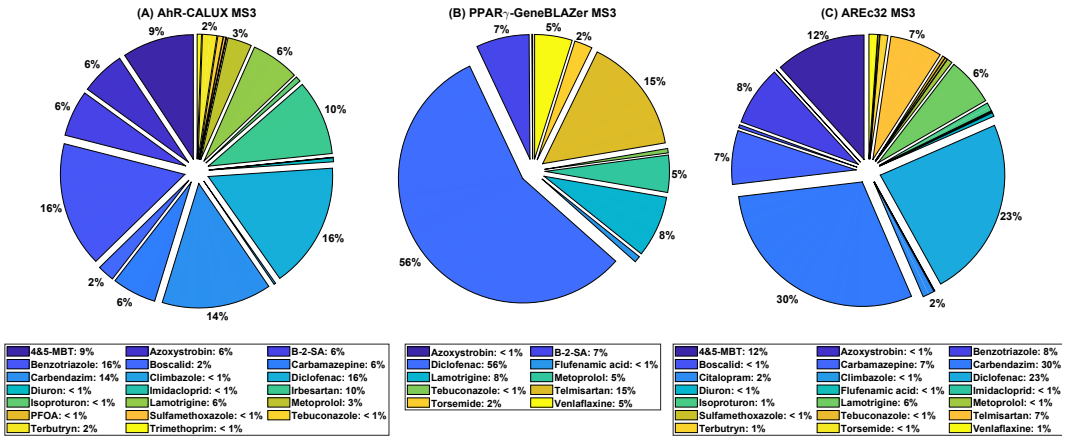

Figure A.51: The mean toxic units $TU_{\text{chem},i}$ over the sampling period from individual compounds to TU_{chem}. 2-Amino-benzo – 2-Aminobenzothiazole; 4&5-MBT – 4&5 Methyl-benzotriazole; B-2-SA – Benzothiazole-2-sulfonic acid; PFOA – Pentadecafluorooctanoic acid.

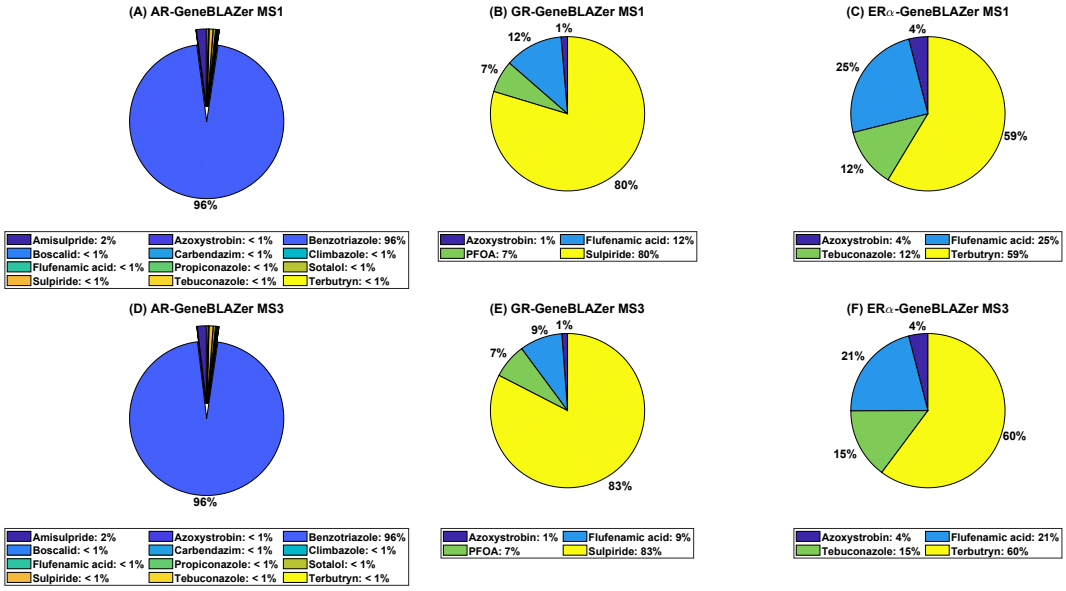

Figure A.52: The mean toxic units over the sampling period from individual compounds to TU_{chem}. PFOA – Pentadecafluorooctanoic acid.

A.16 Effect units of the detected compounds mixture and their fluxes

Three missing data points at measuring station 2 were due to the malfunction of autosampler 2 between 03:30 and 07:30 on August 21, 2020.

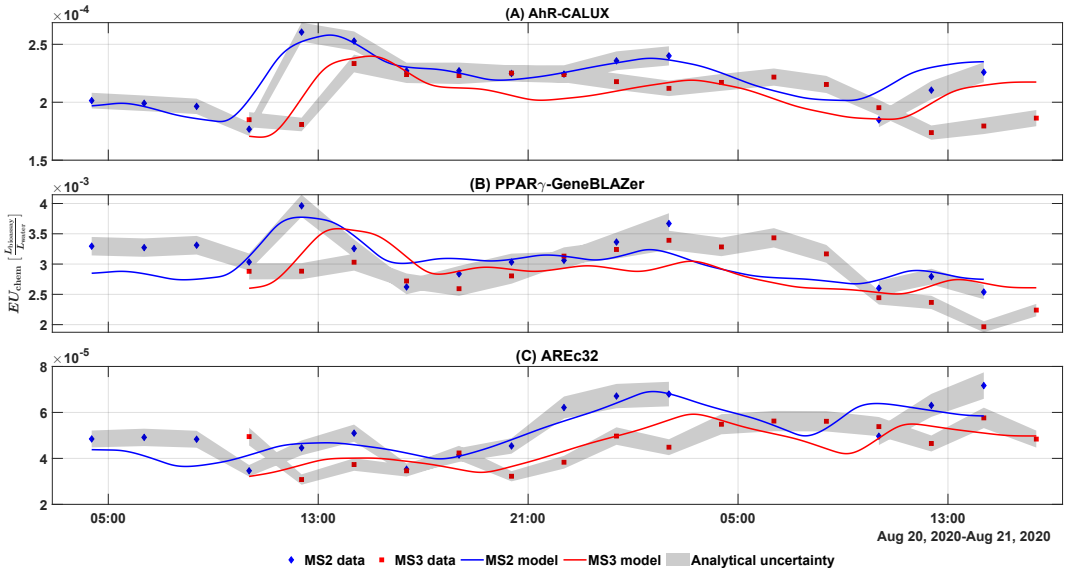

Figure A.53: Experimental and modeled EU_{chem} mixture at MS2 and MS3.

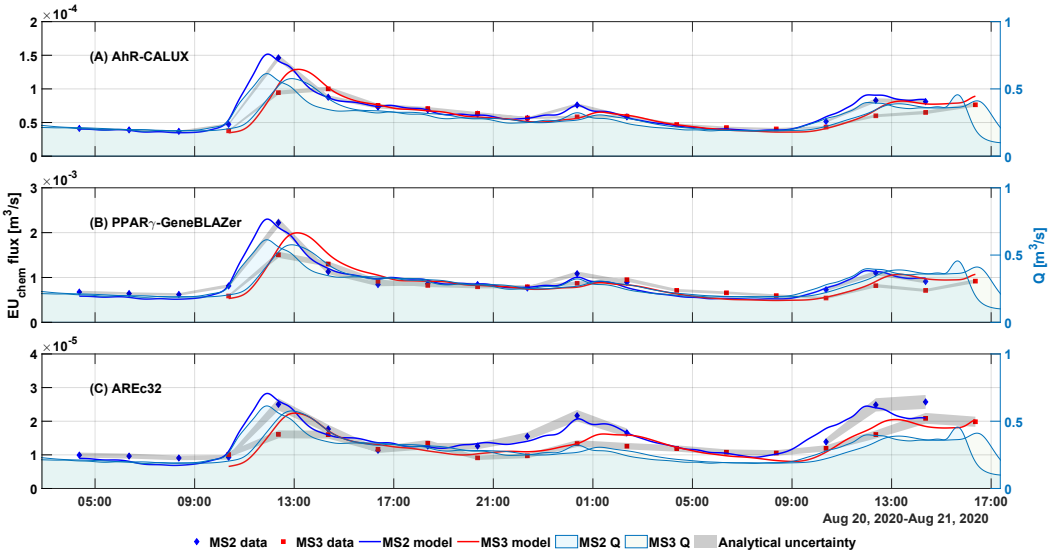

Figure A.54: Experimental and modeled EU_{chem} mixture flux at MS2 and MS3.

A.17 Toxic units of the detected compounds mixture and their fluxes

Three missing data points at measuring station 2 were due to the malfunction of autosampler 2 between 03:30 and 07:30 on August 21, 2020.

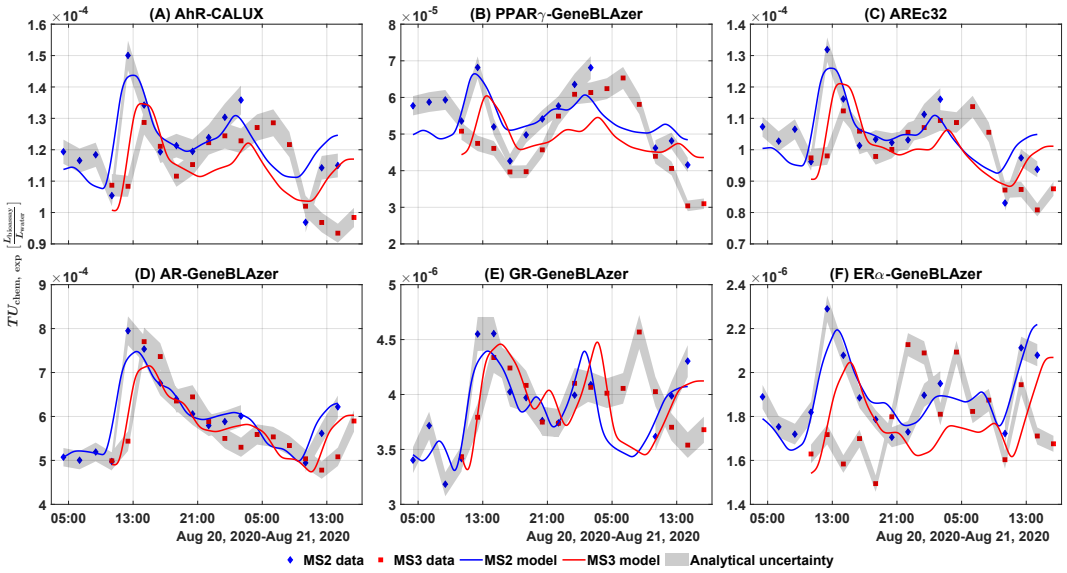

Figure A.55: Experimental and modeled TU_{chem} mixture at MS2 and MS3.

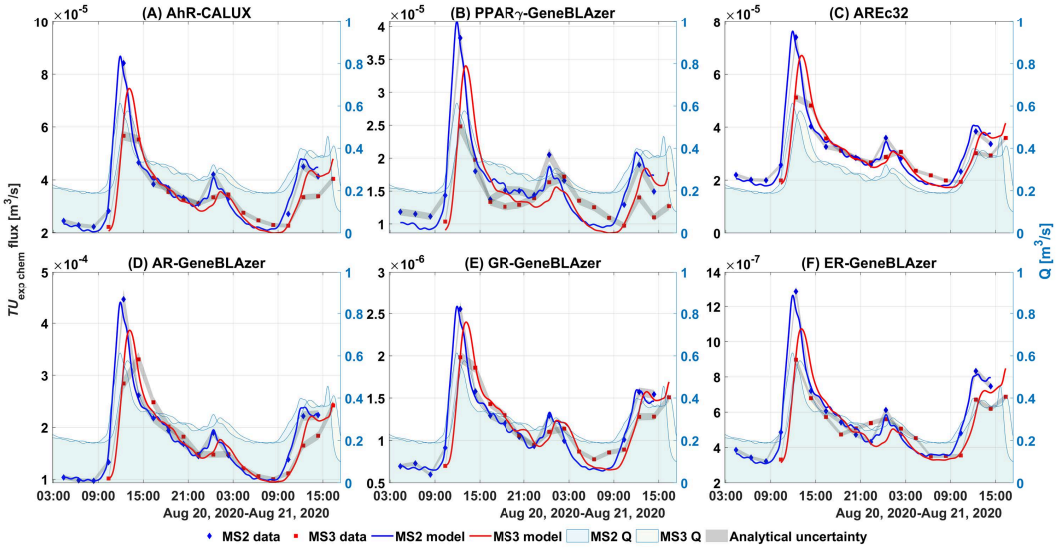

Figure A.56: Experimental and modeled TU_{chem} mixture flux at MS2 and MS3.

A.18 Effect units of the whole bioactive mixture

Three missing data points at measuring station 2 were due to the malfunction of autosampler 2 between 03:30 and 07:30 on August 21, 2020.

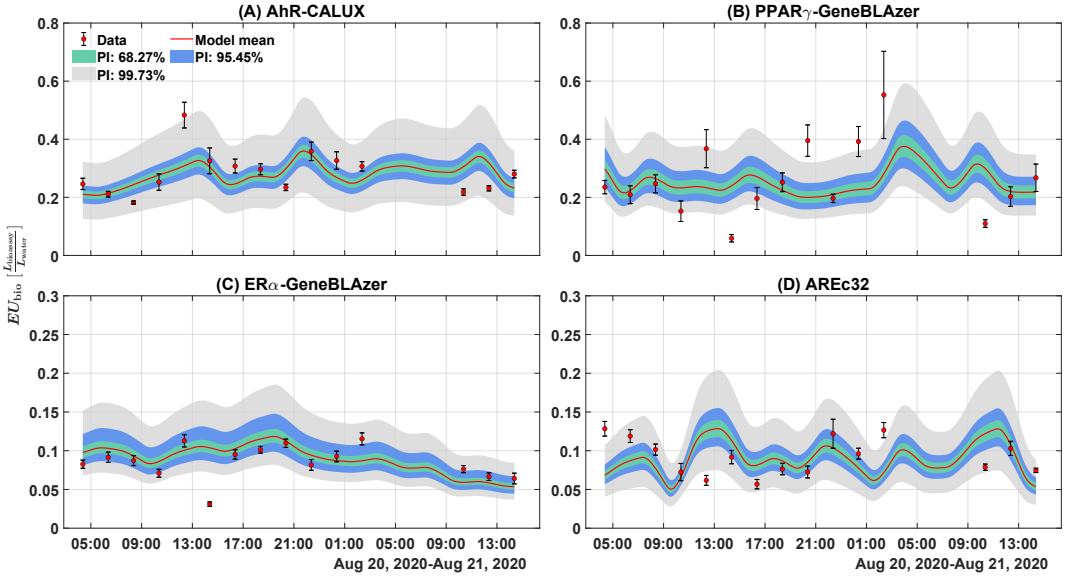

Figure A.57: Ensemble EU_{bio} at MS2. Posterior interval (PI).

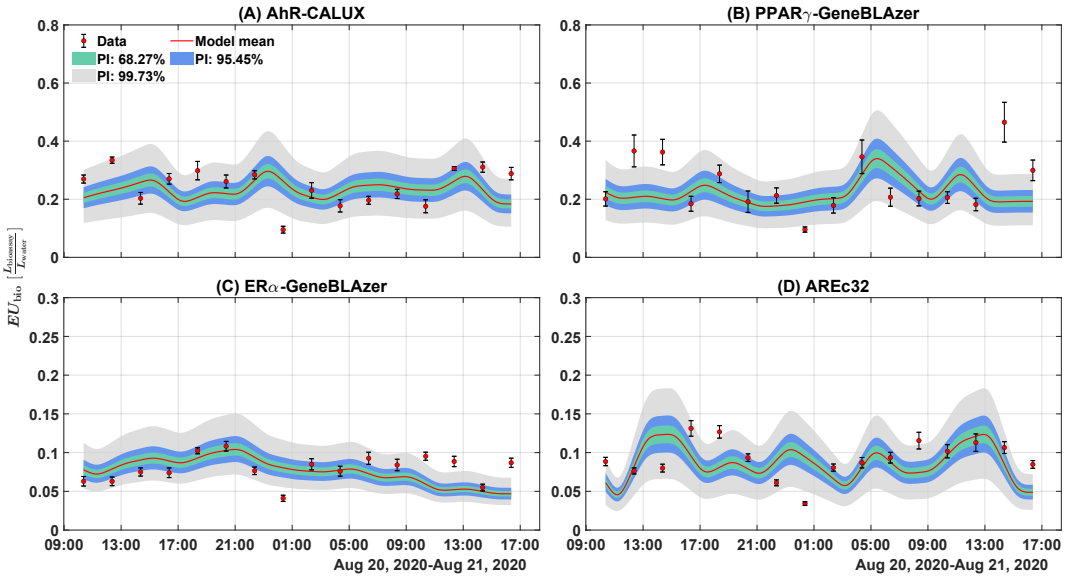

Figure A.58: Ensemble EU_{bio} at MS3. Posterior interval (PI).

A.19 Effect units fluxes of the whole bioactive mixture

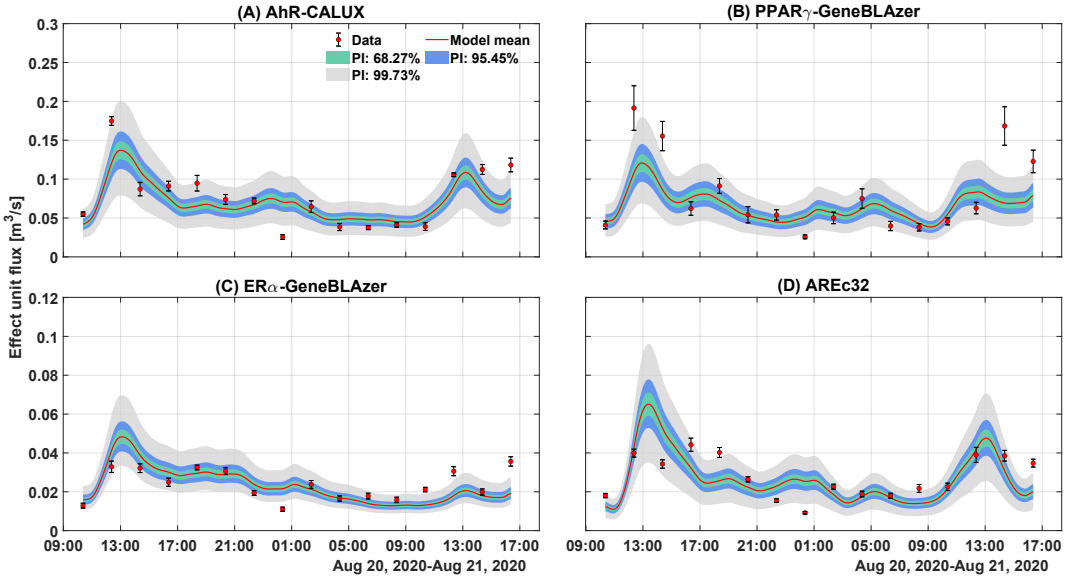

Figure A.59: Ensemble EU_{bio} at MS3. Posterior interval (PI).

A.20 Toxic units of the whole bioactive mixture

Toxic units of the whole bioactive mixture (TU_{bio}) were quantified on four *in vitro* bioassays named AhR-CALUX for aryl hydrocarbon receptor induction, PPARγ-GeneBLAzer for peroxisome proliferator-activated receptor activity, ERα-GeneBLAzer for estrogenicity and AREc32 for oxidative stress. Three missing data points at measuring station 2 were due to the malfunction of auto-sampler 2 between 03:30 and 07:30 on August 21,

2020. Mean TU_{bio} of the four bioassays were used for modeling, due to the same mode of actions.

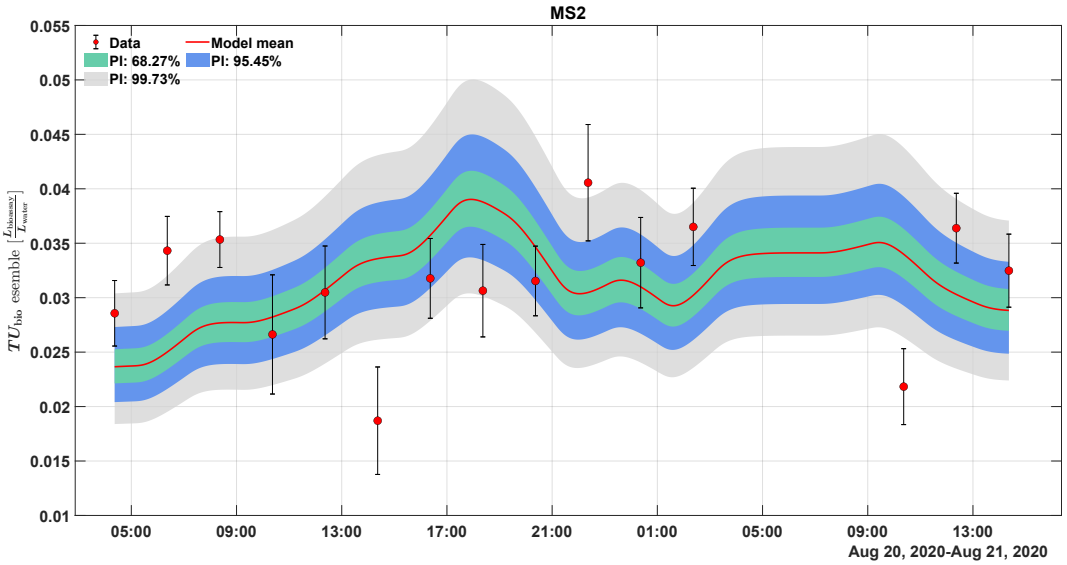

Figure A.60: Mean TU_{bio} ensemble at MS2. Posterior interval (PI).

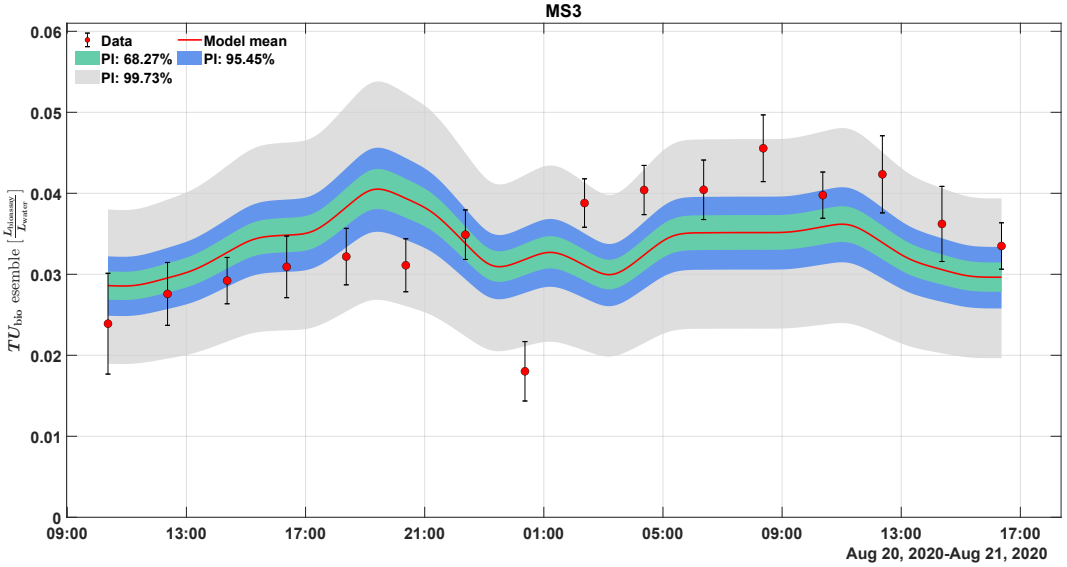

Figure A.61: Mean TU_{bio} ensemble at MS3. Posterior interval (PI).

A.21 Toxic units fluxes of the whole bioactive mixture

Three missing data points at measuring station 2 were due to the malfunction of auto-sampler 2 between 03:30 and 07:30 on August 21, 2020.

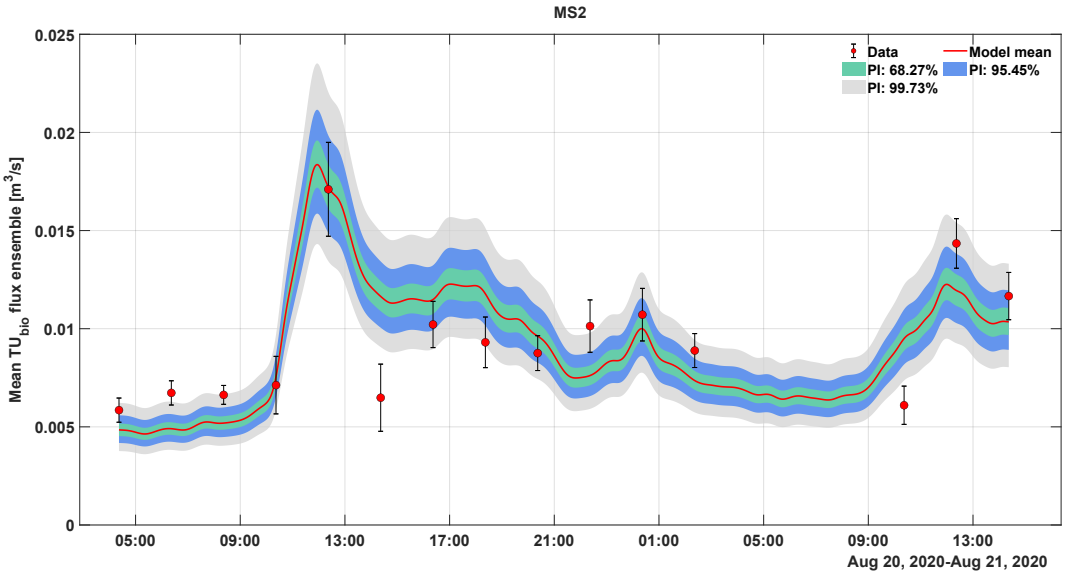

Figure A.62: Mean TU_{bio} ensemble at MS2. Posterior interval (PI).

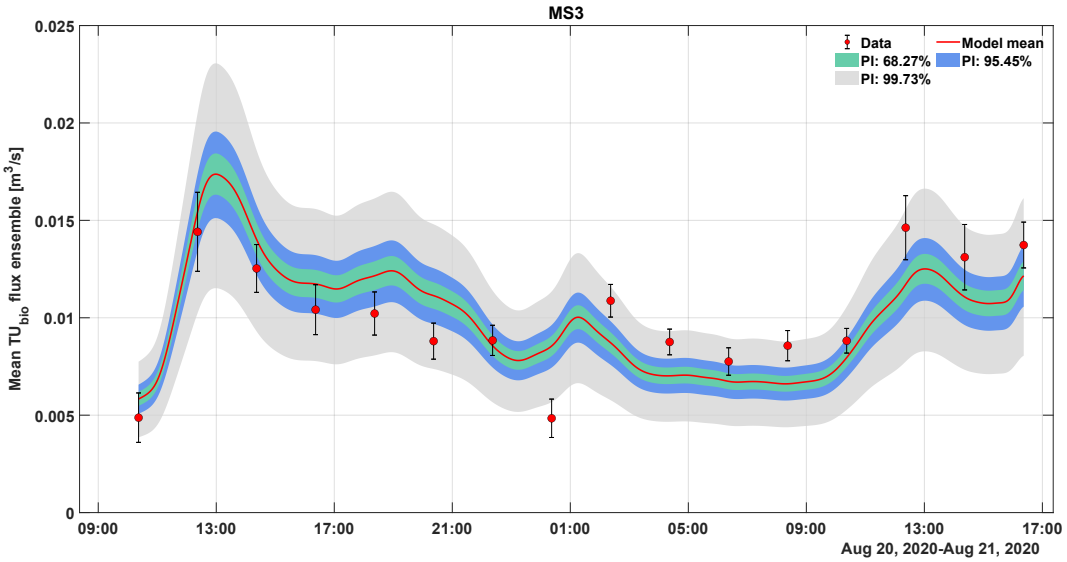

Figure A.63: Mean TU_{bio} ensemble at MS3. Posterior interval (PI).

A.22 Prior and posterior distributions: the reactive parameters of EU_{bio} and mean TU_{bio}

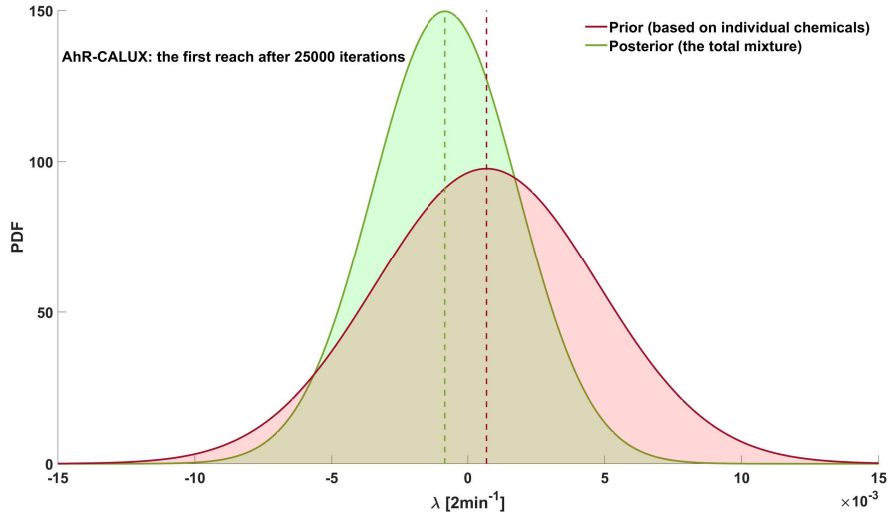

Figure A.64: Prior and posterior distribution of reaction constant of EU_{bio} in AhR - CALUX in the river segment between MS1 - MS2. Five Markov chains converged after 25000 iterations.

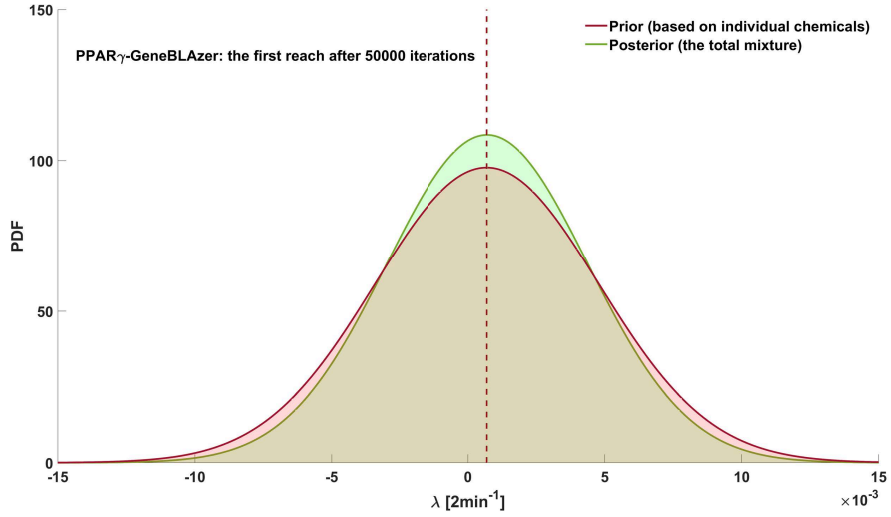

Figure A.65: Prior and posterior distribution of reaction constant of EU_{bio} in PPARγ - GeneBLAzer in the river segment between MS1 - MS2. Five Markov chains converged after 50000 iterations.

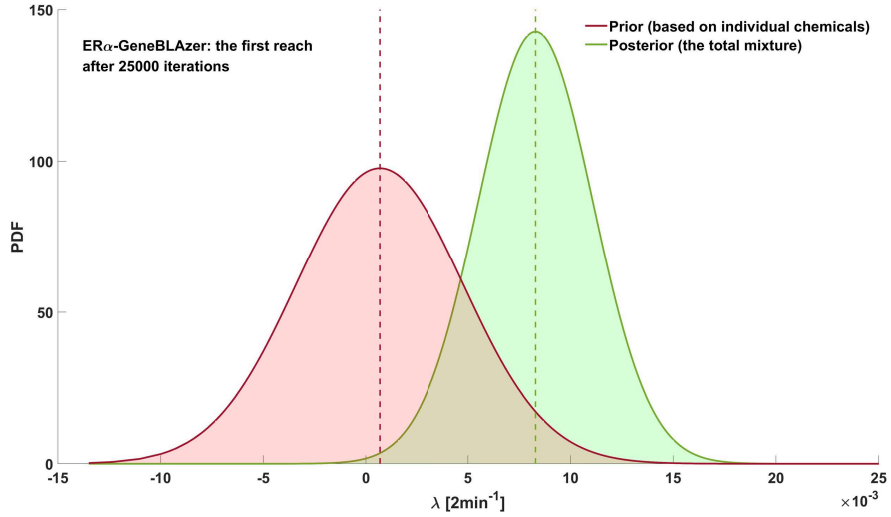

Figure A.66: Prior and posterior distribution of reaction constant of EU_{bio} in ERα - GeneBLAzer in the river segment between MS1 - MS2. Five Markov chains converged after 25000 iterations.

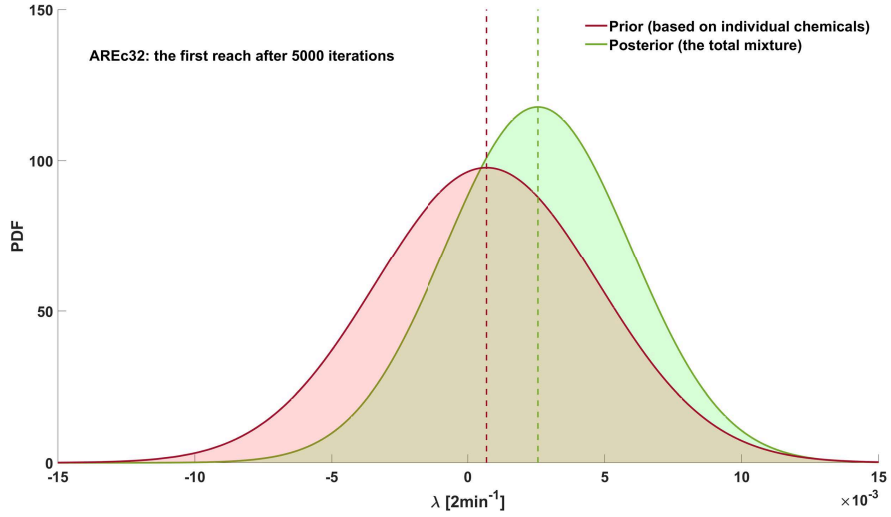

Figure A.67: Prior and posterior distribution of reaction constant of EU_{bio} in AREc32 in the river segment between MS1 - MS2. Five Markov chains converged after 5000 iterations.

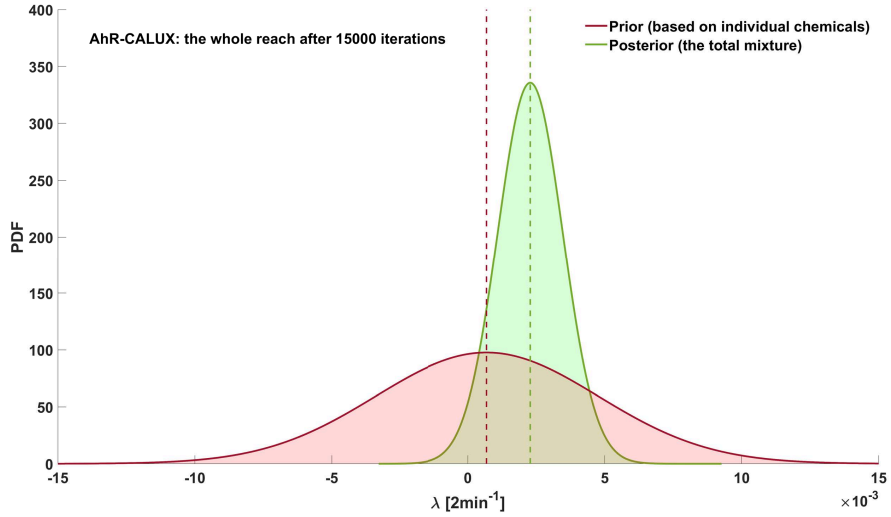

Figure A.68: Prior and posterior distribution of reaction constant of EU_{bio} in AhR - CALUX in the river segment between MS1 - MS3. Five Markov chains converged after 15000 iterations.

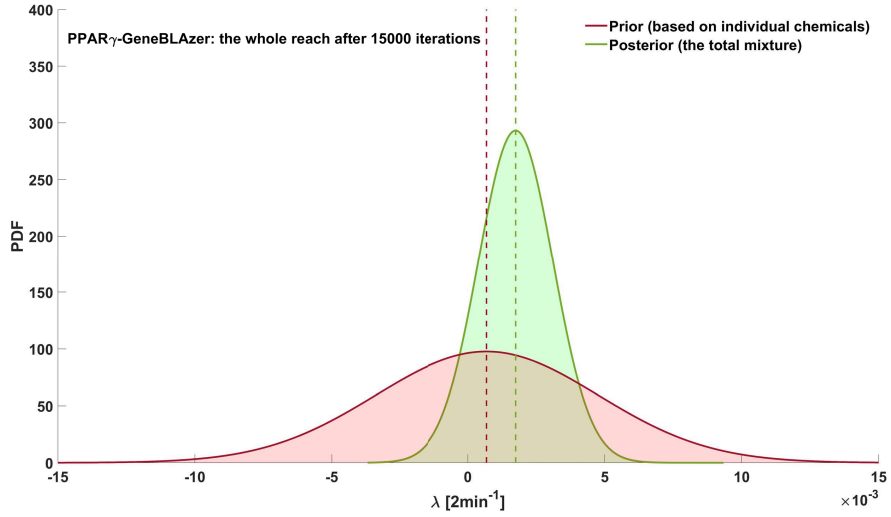

Figure A.69: Prior and posterior distribution of reaction constant of EU_{bio} in PPARγ - GeneBLAzer in the river segment between MS1 - MS3. Five Markov chains converged after 15000 iterations.

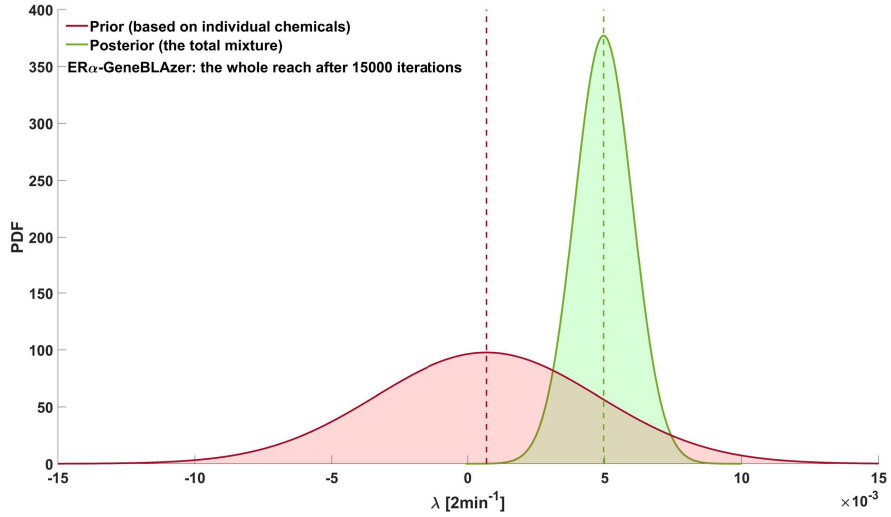

Figure A.70: Prior and posterior distribution of reaction constant of EU_{bio} in ERα - GeneBLAzer in the river segment between MS1 - MS3. Five Markov chains converged after 15000 iterations.

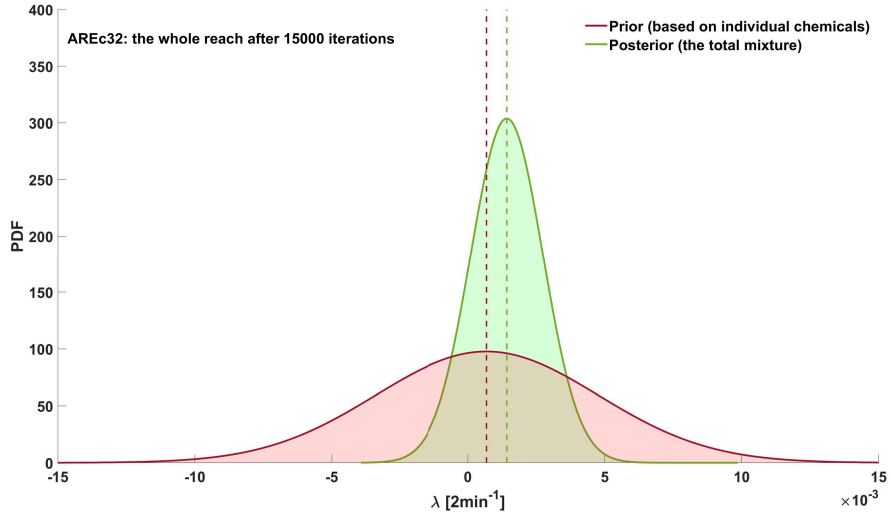

Figure A.71: Prior and posterior distribution of reaction constant of EU_{bio} in AREc32 in the river segment between MS1 - MS3. Five Markov chains converged after 15000 iterations.

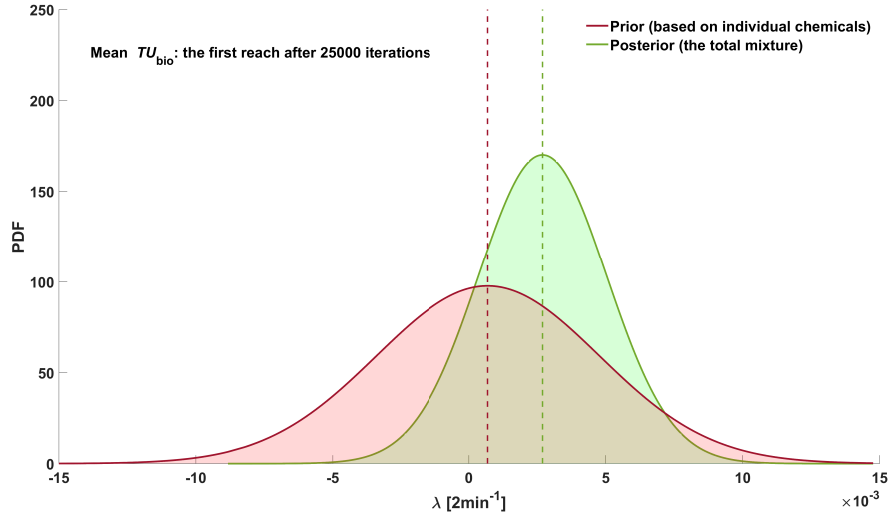

Figure A.72: Prior and posterior distribution of reaction constant of mean TU_{bio} in the river segment between MS1 - MS2. Five Markov chains converged after 25000 iterations.

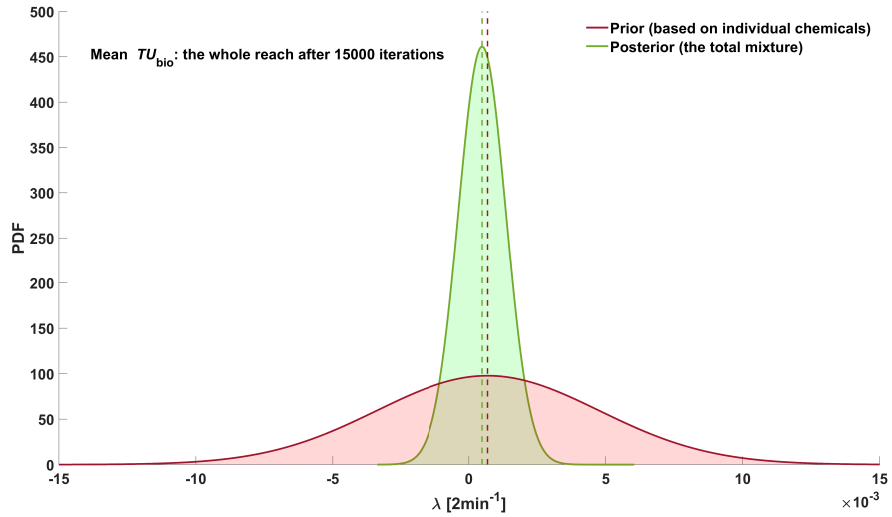

Figure A.73: Prior and posterior distribution of reaction constant of mean TU_{bio} in the river segment between MS1 - MS3. Five Markov chains converged after 15000 iterations.

A.23 Grab samples: concentration

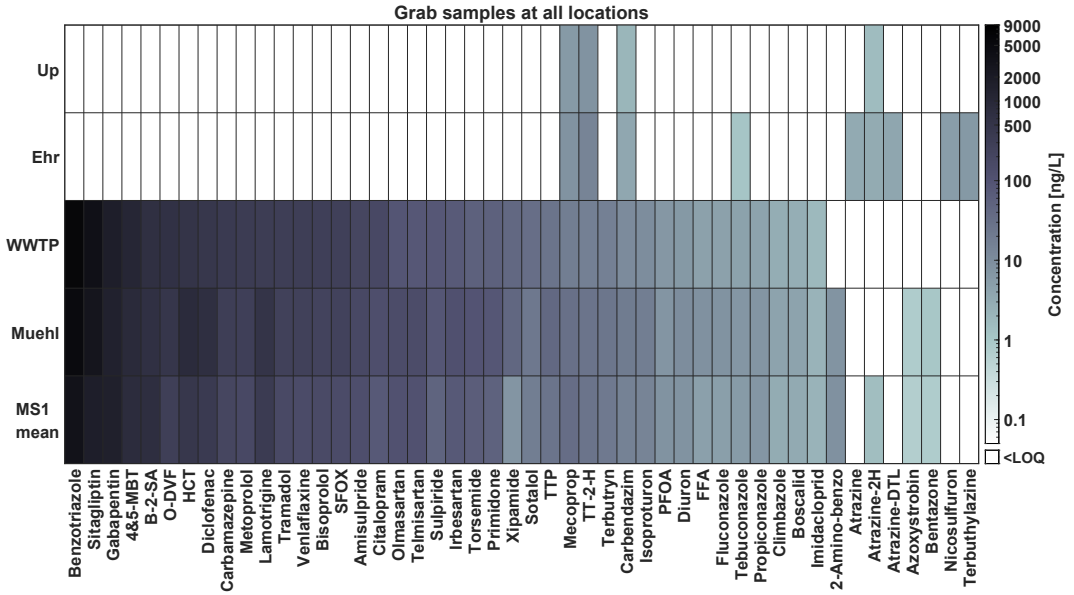

Figure A.74: Concentration of detected chemicals in the grab samples (no grab samples were taken at MS2 and MS3) show that multiple sources are responsible for the presence of micropollutants in the Steinlach River. Abbreviations: 2-Amino-benzo – 2-Aminobenzothiazole; 4&5-MBT – 4&5 Methyl-benzotriazole; B-2-SA – Benzothiazole-2-sulfonic acid; Flufenamic acid (FFA); Hydrochlorozhiazide (HCT); O-Desmethylvenlafaxine (O-DVF); Sulfamethoxazole (SFOX); Trimethoprim (TTP); Terbuthylazine-2-hydroxy (TT-2-H). Ehr – Ehrenbach; Muehl – Mühlbach; The time course of measured concentration data and calibrated modeling results at MS2. Auto-sampler 2 stopped working from 03:30 to 07:30 on August 21, 2020. Measured concentrations were reprinted (adapted) with permission from Schmitt et al., 2021. Copyright 2021 American Chemical Society).

A.24 Grab samples: effect unit

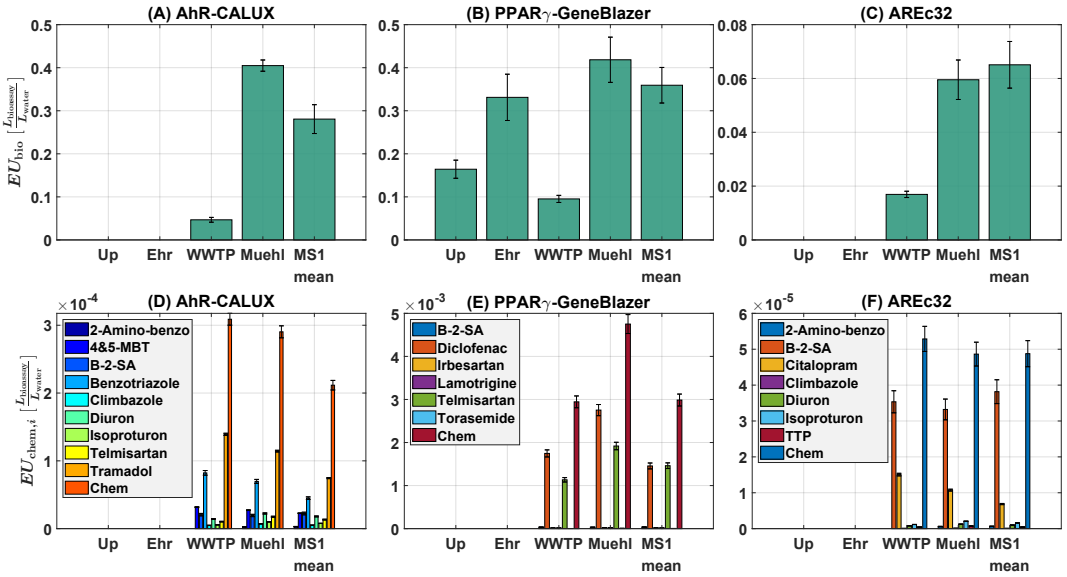

Figure A.75: The effect units of grab samples (no grab samples were taken at MS2 and MS3). EU_{bio} (A) – (C); Individual effects and mixture (D) – (F). $EU_{\text{chem}} = \sum_{i=1}^{n} EU_{\text{chem},i}$. Abbreviations: 2-Amino-benzo – 2-Aminobenzothiazole; 4&5-MBT – 4&5 Methyl-benzotriazole; B-2-SA – Benzothiazole-2-sulfonic acid; Trimethoprim (TTP); Specific effect of the whole bioactive mixture, EU_{bio}.

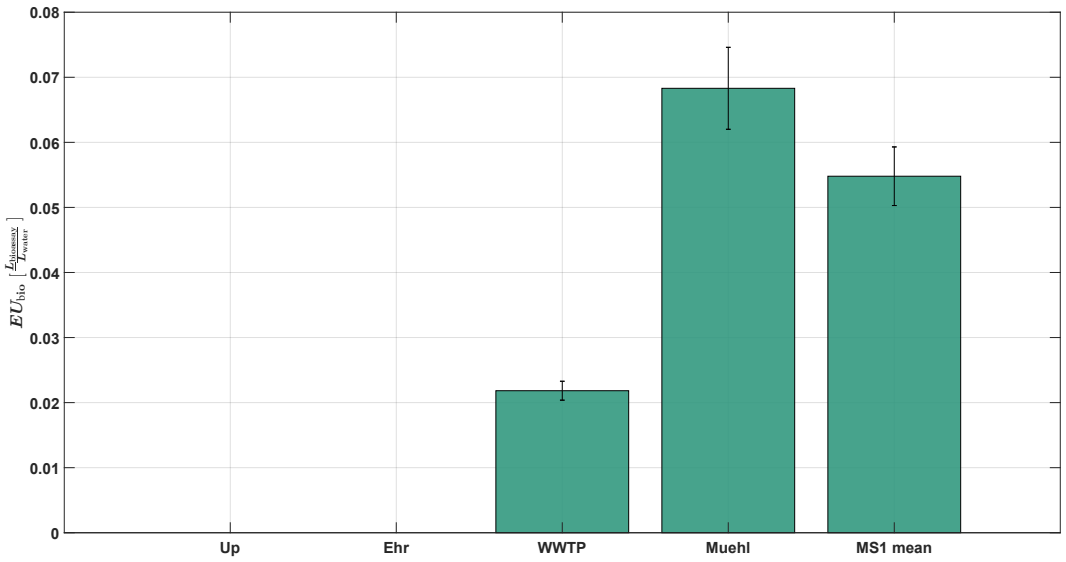

Figure A.76: The effect units of grab samples (no grab samples were taken at MS2 and MS3). Specific effect of the whole bioactive mixture, EU_{bio} in the ERα-GeneBLAzer assay.

A.25 Grab samples: toxic unit

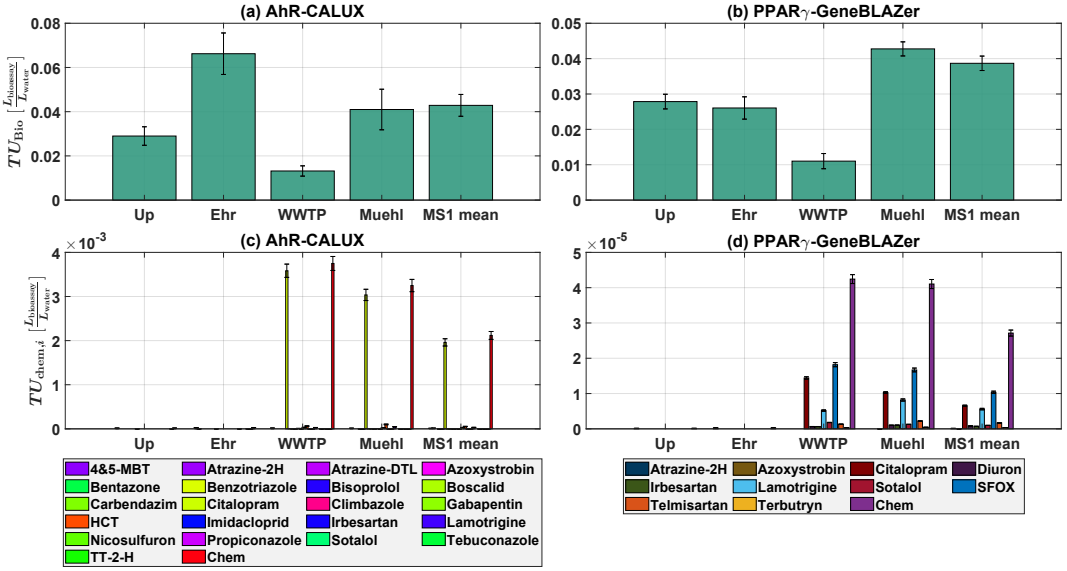

Figure A.77: The toxic units of grab samples taken at all locations. TU_{bio} (a) – (c); Individual effects and mixture (d) – (f). $TU_{\text{chem}} = \sum_{i=1}^{n} TU_{\text{chem},i}$. Abbreviations: 2-Aminobenzothiazole (2-Aminobenzo); 4&5 Methyl-benzotriazole (4&5-MBT); Atrazine-2-hydroxy (Atrazine-2H); Atrazine-desethyl (Atrazine-DTL); Benzothiazole-2-sulfonic acid (B-2-SA); Hydrochlorozhiazide (HCT); Sulfamethoxazole (SFOX); Trimethoprim (TTP); Terbuthylazine-2-hydroxy (TT-2-H); Toxic effect of the whole bioactive mixture TU_{bio}.

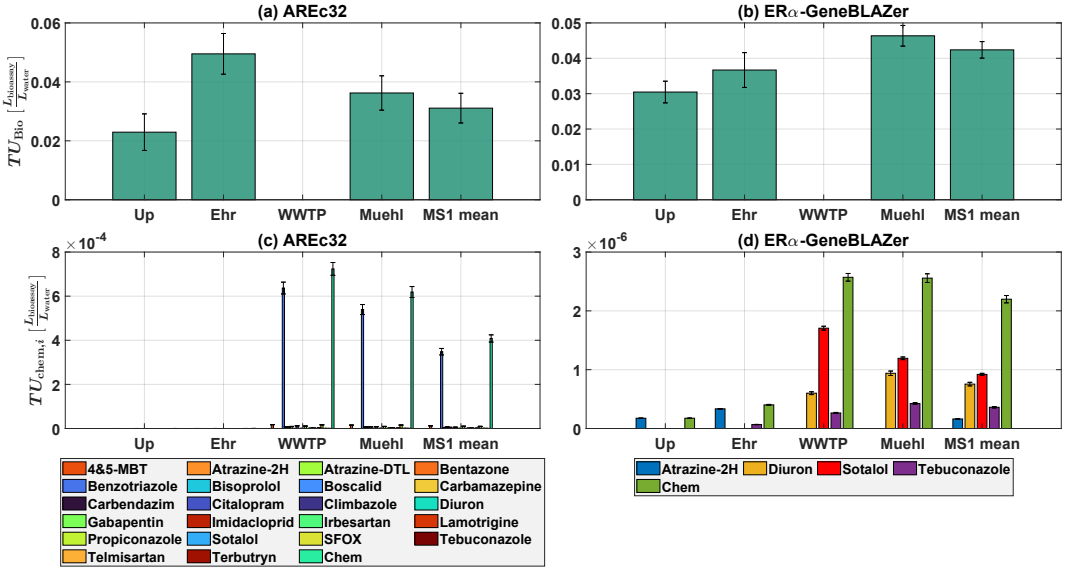

Figure A.78: The toxic units of grab samples (no grab samples were taken at MS2 and MS3). Mixture effects (a) – (b); Individual effects (c) – (d). $TU_{\text{chem}} = \sum_{i=1}^{n} TU_{\text{chem},i}$. Abbreviations: Atrazine-2-hydroxy (Atrazine-2H); 4&5 Methyl-benzotriazole (4&5-MBT); Atrazine-2-hydroxy (Atrazine-2H); Atrazine-desethyl (Atrazine-DTL); Benzothiazole-2-sulfonic acid (B-2-SA); Sulfamethoxazole (SFOX).

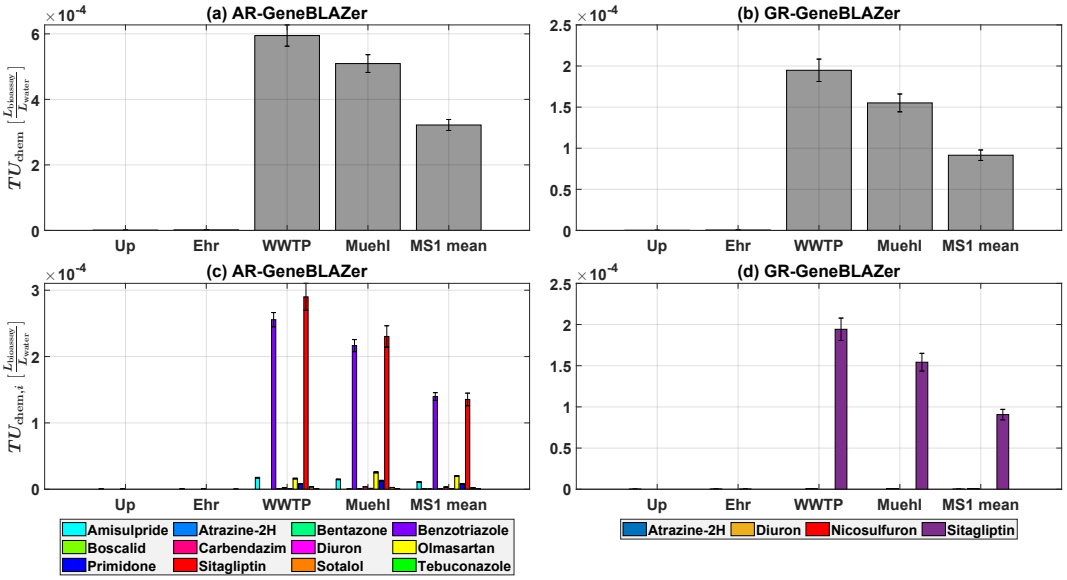

Figure A.79: The toxic units of grab samples taken at all locations. TU_{chem} (a) – (b); Individual effects (c) – (d). $TU_{\text{chem}} = \sum_{i=1}^{n} TU_{\text{chem},i}$. No TU_{bio} was tested on assay AR-GeneBLAzer and GR-GeneBLAzer. Abbreviations: 2-Aminobenzothiazole (2-Amino-benzo); 4&5 Methyl-benzotriazole (4&5-MBT); Atrazine-2-hydroxy (Atrazine-2H).

A.26 Spatial variation of effects

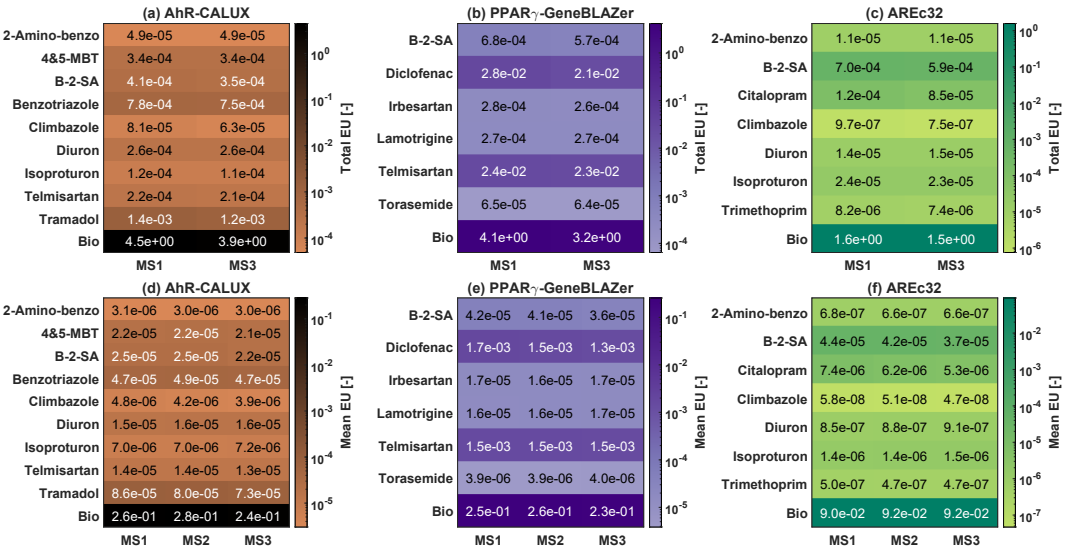

Figure A.80: Total (a) – (c) and mean (d) – (f) EU of detected compounds and the whole bioactive mixture. Total EU from MS2 were not included due to the fact that AS2 stopped sampling from 03:30 to 07:00 on August 21, 2020. Abbreviations: 2-Aminobenzothiazole (2-Amino-benzo); 4&5 Methyl-benzotriazole (4&5-MBT); Benzothiazole-2-sulfonic acid (B-2-SA). Total mixture effects (Bio)

A.27 Tables

Table A.1: The full list of targeted compounds. Detected compounds are highlighted in grey color.

Name	Category
2-Aminobenzothiazole	azo dye intermediate
4 & 5 Methyl-benzotriazole	corrosion inhibitor
Alachlor	herbicide
Amisulpride	pharmaceutical
Atrazine	herbicide
Atrazine-2-hydroxy	herbicide metabolite
Atrazine-desethyl	herbicide metabolite
Atrazine-desisopropyl	herbicide metabolite
Azoxystrobin	fungicide
Bentazone	herbicide
Benzothiazole-2-sulfonic acid	vulcanization accelerator
Benzotriazole	corrosion inhibitor
Bezafibrate	pharmaceutical
Bisoprolol	pharmaceutical
Bixafen	fungicide
Boscalid	fungicide
Carbamazepine	pharmaceutical
Carbendazim	fungicide
Chloridazon	herbicide
Chlorpyrifos	metabolite & insecticide
Citalopram	pharmaceutical
Climbazole	fungicide
Diazinon	insecticide
Diclofenac	pharmaceutical
Diflufenican	herbicide
Diuron	herbicide
Epoxiconazole	fungicide
Fenofibrate	pharmaceutical
Florasulam	herbicide
Fluconazole	pharmaceutical
Flufenacet	herbicide
Flufenamic acid	pharmaceutical
Fluxapyroxad	fungicide
Gabapentin	pharmaceutical
Hydrochlorozhiazide	pharmaceutical
Imidacloprid	insecticide
Indomethacin	pharmaceutical
Iodosulfuron-methyl	herbicide
Irbesartan	pharmaceutical
Isoproturon	herbicide
Lamotrigine	pharmaceutical

MCPA	herbicide
Mecoprop	herbicide
Mesosulfuron-methyl	herbicide
Metalaxyl	fungicide
Metamitron	herbicide
Methylprednisolone	pharmaceutical
Metolachlor	herbicide
Metoprolol	pharmaceutical
Metronidazole	pharmaceutical
Naproxen	pharmaceutical
Metsulfuron-methyl	herbicide
Nicosulfuron	herbicide
O-Desmethylvenlafaxine	pharmaceutical, metabolite
Olmesartan	pharmaceutical
PFOA (Pentadecafluorooctanoic acid)	surfactant
Pirimicarb	insecticide
Primidone	pharmaceutical
Propazine	fungicide
Propiconazole	fungicide
Prosulfuron	herbicide
Pyraclostrobin	fungicide
Simazine	herbicide
Sitagliptin	pharmaceutical
Sotalol	pharmaceutical
Sulfamethazine	pharmaceutical
Sulfamethoxazole	antibiotic
Sulpiride	pharmaceutical
Tebuconazole	fungicide
Telmisartan	pharmaceutical
Terbuthylazine	herbicide
Terbuthylazine-2-hydroxy	herbicide metabolite
Terbutryn	herbicide
Thiamethoxam	insecticide
Torsemide	pharmaceutical
Tramadol	pharmaceutical
Triclosan	biocide
Trimethoprim	pharmaceutical
Venlafaxine	pharmaceutical
Xipamide	pharmaceutical

Table A.2: time-series samples' collection order and time in August 2020. The same water packages tracked by the Lagrangian scheme are highlighted by the grey color. Red colors are the missing samples. Auto-sampler (AS)

AS1		**AS2**		**AS3**	
Order	Time	Order	Time	Order	Time
1	19.08.2020 20:00				
2	19.08.2020 22:00				
3	20.08.2020 00:00				
4	20.08.2020 02:00				
5	20.08.2020 04:00	1	20.08.2020 03:30		
6	20.08.2020 06:00	2	20.08.2020 05:30		
7	20.08.2020 08:00	3	20.08.2020 07:30		
8	20.08.2020 10:00	4	20.08.2020 09:30	1	20.08.2020 09:30
9	20.08.2020 12:00	5	20.08.2020 11:30	2	20.08.2020 11:30
10	20.08.2020 14:00	6	20.08.2020 13:30	3	20.08.2020 13:30
11	20.08.2020 16:00	7	20.08.2020 15:30	4	20.08.2020 15:30
12	20.08.2020 18:00	8	20.08.2020 17:30	5	20.08.2020 17:30
13	20.08.2020 20:00	9	20.08.2020 19:30	6	20.08.2020 19:30
14	20.08.2020 22:00	10	20.08.2020 21:30	7	20.08.2020 21:30
15	21.08.2020 00:00	11	20.08.2020 23:30	8	20.08.2020 23:30
16	21.08.2020 02:00	12	21.08.2020 01:30	9	21.08.2020 01:30
17	21.08.2020 04:00	13	21.08.2020 03:30	10	21.08.2020 03:30
18	21.08.2020 06:00	14	21.08.2020 05:30	11	21.08.2020 05:30
19	21.08.2020 08:00	15	21.08.2020 07:30	12	21.08.2020 07:30
20	21.08.2020 10:00	16	21.08.2020 09:30	13	21.08.2020 09:30
21	21.08.2020 12:00	17	21.08.2020 11:30	14	21.08.2020 11:30
Stop	21.08.2020 13:45	18	21.08.2020 13:30	15	21.08.2020 13:30
		Stop	21.08.2020 15:15	16	21.08.2020 15:30
				Stop	21.08.2020 17:15

Table A.3: Measured concentration (ng/L) of grab samples. Measured concentrations were reprinted (adapted) with permission from Markus Schmitt (Schmitt et al., 2021 Copyright 2021 American Chemical Society). Auto-sampler (AS); Limit of quantification (LOQ); Solid phase extraction (SPE); Upstream (up); Ehrenbach (Ehr); Measuring station 1 (MS1); Mühlbach (Muhl); Wastewater treatment plant (WWTP).

Concentration [ng/L]	SPE Blank 1	SPE Blank 2	SPE Blank 3	AS1 Blank	AS2 Blank	AS3 Blank	grab up	grab Ehr	grab MS1 1	grab MS1 2	grab MS1 3	grab Muhl	grab WWTP
2-Aminobenzothiazole	< LOQ	< LOQ	< LOQ	< LOQ	< LOQ	< LOQ	< LOQ	< LOQ	8,3	8,9	8,2	7,8	< LOQ
4&5 Methyl-benzotriazole	n.d	n.d	n.d	< LOQ	< LOQ	< LOQ	< LOQ	< LOQ	759,7	758,4	809,9	929,5	1082,9
Alachlor	< LOQ	< LOQ	< LOQ	< LOQ	< LOQ	< LOQ	< LOQ	< LOQ	< LOQ	< LOQ	< LOQ	< LOQ	< LOQ
Amisulpride	n.d	n.d	n.d	< LOQ	< LOQ	< LOQ	< LOQ	< LOQ	122,6	122,3	134,5	171,7	200,9
Atrazine	< LOQ	< LOQ	< LOQ	< LOQ	< LOQ	< LOQ	< LOQ	3,2	< LOQ	< LOQ	< LOQ	< LOQ	< LOQ
Atrazine-2-hydroxy	< LOQ	< LOQ	< LOQ	< LOQ	< LOQ	< LOQ	1,6	3,1	1,4	1,8	1,4	< LOQ	< LOQ
Atrazine-desethyl	< LOQ	< LOQ	< LOQ	< LOQ	< LOQ	< LOQ	< LOQ	3,8	< LOQ	< LOQ	< LOQ	< LOQ	< LOQ
Atrazine-desisopropyl	< LOQ	< LOQ	< LOQ	< LOQ	< LOQ	< LOQ	< LOQ	< LOQ	< LOQ	< LOQ	< LOQ	< LOQ	< LOQ
Azoxystrobin	< LOQ	< LOQ	< LOQ	< LOQ	< LOQ	< LOQ	< LOQ	< LOQ	0,7	0,7	0,7	0,8	< LOQ
Bentazone	< LOQ	< LOQ	< LOQ	< LOQ	< LOQ	< LOQ	< LOQ	< LOQ	0,7	0,9	< LOQ	1,0	< LOQ
Benzothiazole-2-solfonic acid	n.d	n.d	n.d	< LOQ	< LOQ	< LOQ	< LOQ	< LOQ	635,8	703,0	787,4	616,8	656,5
Benzotriazole	n.d	n.d	n.d	< LOQ	< LOQ	< LOQ	< LOQ	< LOQ	3296,3	3128,9	3340,2	5042,6	5952,1
Bezafibrate	< LOQ	< LOQ	< LOQ	< LOQ	< LOQ	< LOQ	< LOQ	< LOQ	< LOQ	< LOQ	< LOQ	< LOQ	< LOQ
Bisoprolol	n.d	n.d	n.d	< LOQ	< LOQ	< LOQ	< LOQ	< LOQ	156,4	156,2	168,4	229,2	278,6
Bixafen	< LOQ	< LOQ	< LOQ	< LOQ	< LOQ	< LOQ	< LOQ	< LOQ	< LOQ	< LOQ	< LOQ	< LOQ	< LOQ
Boscalid	< LOQ	< LOQ	< LOQ	< LOQ	< LOQ	< LOQ	< LOQ	< LOQ	3,4	2,7	3,6	4,1	2,8
Carbamazepine	n.d	n.d	n.d	< LOQ	< LOQ	< LOQ	< LOQ	< LOQ	214,5	193,8	199,0	307,7	371,3
Carbendazim	< LOQ	< LOQ	< LOQ	< LOQ	< LOQ	< LOQ	2,1	3,5	16,0	16,7	15,1	19,6	10,7
Chloridazon	< LOQ	< LOQ	< LOQ	< LOQ	< LOQ	< LOQ	< LOQ	< LOQ	< LOQ	< LOQ	< LOQ	< LOQ	< LOQ
Chlorpyrifos	< LOQ	< LOQ	< LOQ	< LOQ	< LOQ	< LOQ	< LOQ	< LOQ	< LOQ	< LOQ	< LOQ	< LOQ	< LOQ
Citalopram	n.d	n.d	n.d	< LOQ	< LOQ	< LOQ	< LOQ	< LOQ	79,9	77,1	81,7	124,6	174,9
Climbazole	< LOQ	< LOQ	< LOQ	< LOQ	< LOQ	< LOQ	< LOQ	< LOQ	< LOQ	3,0	2,9	4,2	2,8
Diazinon	< LOQ	< LOQ	< LOQ	< LOQ	< LOQ	< LOQ	< LOQ	< LOQ	< LOQ	< LOQ	< LOQ	< LOQ	< LOQ
Diclofenac	< LOQ	< LOQ	< LOQ	< LOQ	< LOQ	< LOQ	< LOQ	< LOQ	346,4	383,4	377,2	697,7	442,7
Diflufenican	< LOQ	< LOQ	< LOQ	< LOQ	< LOQ	< LOQ	< LOQ	< LOQ	< LOQ	< LOQ	< LOQ	< LOQ	< LOQ
Diuron	< LOQ	< LOQ	< LOQ	< LOQ	< LOQ	< LOQ	< LOQ	< LOQ	7,8	8,1	8,5	10,1	6,5
Epoxiconazole	< LOQ	< LOQ	< LOQ	< LOQ	< LOQ	< LOQ	< LOQ	< LOQ	< LOQ	< LOQ	< LOQ	< LOQ	< LOQ

Fenofibrate	< LOQ	< LOQ	< LOQ	< LOQ	< LOQ	< LOQ	< LOQ	< LOQ	< LOQ	< LOQ	< LOQ	< LOQ	< LOQ
Florasulam	< LOQ	< LOQ	< LOQ	< LOQ	< LOQ	< LOQ	< LOQ	< LOQ	< LOQ	< LOQ	< LOQ	< LOQ	< LOQ
Fluconazole	< LOQ	< LOQ	< LOQ	< LOQ	< LOQ	< LOQ	< LOQ	< LOQ	4,6	5,3	5,0	8,2	4,5
Flufenacet	< LOQ	< LOQ	< LOQ	< LOQ	< LOQ	< LOQ	< LOQ	< LOQ	< LOQ	< LOQ	< LOQ	< LOQ	< LOQ
Flufenamic acid	< LOQ	< LOQ	< LOQ	< LOQ	< LOQ	< LOQ	< LOQ	< LOQ	5,2	5,2	4,2	8,5	4,5
Fluxapyroxad	< LOQ	< LOQ	< LOQ	< LOQ	< LOQ	< LOQ	< LOQ	< LOQ	< LOQ	< LOQ	< LOQ	< LOQ	< LOQ
Gabapentin	n.d	n.d	n.d	< LOQ	< LOQ	< LOQ	< LOQ	< LOQ	1176,5	1964,9	1495,1	1430,1	1655,5
Hydrochlorozhiazide	< LOQ	< LOQ	< LOQ	< LOQ	< LOQ	< LOQ	< LOQ	< LOQ	447,9	421,5	452,2	835,0	517,1
Imidacloprid	< LOQ	< LOQ	< LOQ	< LOQ	< LOQ	< LOQ	< LOQ	< LOQ	2,4	1,8	2,5	2,2	1,7
Indomethacin	< LOQ	< LOQ	< LOQ	< LOQ	< LOQ	< LOQ	< LOQ	< LOQ	< LOQ	< LOQ	< LOQ	< LOQ	< LOQ
Iodosulfuron-methyl	< LOQ	< LOQ	< LOQ	< LOQ	< LOQ	< LOQ	< LOQ	< LOQ	< LOQ	< LOQ	< LOQ	< LOQ	< LOQ
Irbesartan	< LOQ	< LOQ	< LOQ	< LOQ	< LOQ	< LOQ	< LOQ	< LOQ	82,4	81,8	71,4	114,8	73,0
Isoproturon	< LOQ	< LOQ	< LOQ	< LOQ	< LOQ	< LOQ	< LOQ	< LOQ	14,1	14,0	13,8	18,0	10,2
Lamotrigine	< LOQ	< LOQ	< LOQ	< LOQ	< LOQ	< LOQ	< LOQ	< LOQ	351,3	358,9	325,0	503,9	318,9
MCPA	< LOQ	< LOQ	< LOQ	< LOQ	< LOQ	< LOQ	< LOQ	< LOQ	< LOQ	< LOQ	< LOQ	< LOQ	< LOQ
Mecoprop	< LOQ	< LOQ	< LOQ	< LOQ	< LOQ	< LOQ	5,9	8,2	36,1	35,1	31,8	32,0	18,0
Mesosulfuron-methyl	< LOQ	< LOQ	< LOQ	< LOQ	< LOQ	< LOQ	< LOQ	< LOQ	< LOQ	< LOQ	< LOQ	< LOQ	< LOQ
Metalaxyl	< LOQ	< LOQ	< LOQ	< LOQ	< LOQ	< LOQ	< LOQ	< LOQ	< LOQ	< LOQ	< LOQ	< LOQ	< LOQ
Metamitron	< LOQ	< LOQ	< LOQ	< LOQ	< LOQ	< LOQ	< LOQ	< LOQ	< LOQ	< LOQ	< LOQ	< LOQ	< LOQ
Methylprednisolone	< LOQ	< LOQ	< LOQ	< LOQ	< LOQ	< LOQ	< LOQ	< LOQ	< LOQ	< LOQ	< LOQ	< LOQ	< LOQ
Metolachlor (high backgroud)	< LOQ	< LOQ	< LOQ	< LOQ	< LOQ	< LOQ	< LOQ	< LOQ	< LOQ	< LOQ	< LOQ	< LOQ	< LOQ
Metoprolol	n.d	n.d	n.d	< LOQ	< LOQ	< LOQ	< LOQ	< LOQ	171,8	164,0	182,5	273,6	340,2
Metronidazole	< LOQ	< LOQ	< LOQ	< LOQ	< LOQ	< LOQ	< LOQ	< LOQ	< LOQ	< LOQ	< LOQ	< LOQ	< LOQ
Metsulfuron-methyl	< LOQ	< LOQ	< LOQ	< LOQ	< LOQ	< LOQ	< LOQ	< LOQ	< LOQ	< LOQ	< LOQ	< LOQ	< LOQ
Nicosulfuron	< LOQ	< LOQ	< LOQ	< LOQ	< LOQ	< LOQ	< LOQ	5,3	< LOQ	< LOQ	< LOQ	< LOQ	< LOQ
O-Desmethylvenlafaxine	n.d	n.d	n.d	< LOQ	< LOQ	< LOQ	< LOQ	< LOQ	292,7	289,2	302,0	479,3	593,0
Olmasartan	< LOQ	< LOQ	< LOQ	< LOQ	< LOQ	< LOQ	< LOQ	< LOQ	110,6	114,3	105,7	140,9	88,8
PFOA (Pentadecafluorooctanoic acid)	< LOQ	< LOQ	< LOQ	< LOQ	< LOQ	< LOQ	< LOQ	< LOQ	8,0	9,2	7,2	7,4	6,7
Pirimicarb	< LOQ	< LOQ	< LOQ	< LOQ	< LOQ	< LOQ	< LOQ	< LOQ	< LOQ	< LOQ	< LOQ	< LOQ	< LOQ
Primidone	< LOQ	< LOQ	< LOQ	< LOQ	< LOQ	< LOQ	< LOQ	< LOQ	55,6	56,0	50,0	85,8	54,7
Propazine	< LOQ	< LOQ	< LOQ	< LOQ	< LOQ	< LOQ	< LOQ	< LOQ	< LOQ	< LOQ	< LOQ	< LOQ	< LOQ

Propiconazole	< LOQ	< LOQ	< LOQ	< LOQ	< LOQ	< LOQ	< LOQ	< LOQ	6,7	7,2	6,8	7,2	4,1
Prosulfuron	< LOQ	< LOQ	< LOQ	< LOQ	< LOQ	< LOQ	< LOQ	< LOQ	< LOQ	< LOQ	< LOQ	< LOQ	< LOQ
Pyraclostrobin	< LOQ	< LOQ	< LOQ	< LOQ	< LOQ	< LOQ	< LOQ	< LOQ	< LOQ	< LOQ	< LOQ	< LOQ	< LOQ
Simazine	< LOQ	< LOQ	< LOQ	< LOQ	< LOQ	< LOQ	< LOQ	< LOQ	< LOQ	< LOQ	< LOQ	< LOQ	< LOQ
Sitagliptin	n.d	n.d	n.d	< LOQ	< LOQ	< LOQ	< LOQ	< LOQ	1648,1	1625,5	1705,4	2823,6	3555,7
Sotalol	n.d	n.d	n.d	< LOQ	< LOQ	< LOQ	< LOQ	< LOQ	15,2	19,5	19,2	23,3	33,3
Sulfamethazine	< LOQ	< LOQ	< LOQ	< LOQ	< LOQ	< LOQ	< LOQ	< LOQ	< LOQ	< LOQ	< LOQ	< LOQ	< LOQ
Sulfamethoxazole	n.d	n.d	n.d	< LOQ	< LOQ	< LOQ	< LOQ	< LOQ	143,5	152,7	158,2	244,2	266,2
Sulpiride	n.d	n.d	n.d	< LOQ	< LOQ	< LOQ	< LOQ	< LOQ	48,2	51,2	51,8	83,6	81,0
Tebuconazole	< LOQ	< LOQ	< LOQ	< LOQ	< LOQ	< LOQ	< LOQ	1,1	5,8	6,2	5,5	6,8	4,3
Telmisartan	< LOQ	< LOQ	< LOQ	< LOQ	< LOQ	< LOQ	< LOQ	< LOQ	109,1	113,0	100,6	141,2	83,5
Terbuthylazine	< LOQ	< LOQ	< LOQ	< LOQ	< LOQ	< LOQ	< LOQ	6,3	< LOQ	< LOQ	< LOQ	< LOQ	< LOQ
Terbuthylazine-2-hydroxy	< LOQ	< LOQ	< LOQ	< LOQ	< LOQ	< LOQ	8,2	13,9	27,7	27,4	24,7	25,7	16,6
Terbutryn	< LOQ	< LOQ	< LOQ	< LOQ	< LOQ	< LOQ	< LOQ	< LOQ	21,4	21,3	21,3	25,2	16,3
Thiamethoxam	< LOQ	< LOQ	< LOQ	< LOQ	< LOQ	< LOQ	< LOQ	< LOQ	< LOQ	< LOQ	< LOQ	< LOQ	< LOQ
Torsemide	< LOQ	< LOQ	< LOQ	< LOQ	< LOQ	< LOQ	< LOQ	< LOQ	63,4	65,6	63,6	98,8	56,3
Tramadol	n.d	n.d	n.d	< LOQ	< LOQ	< LOQ	< LOQ	< LOQ	167,4	167,0	170,0	257,8	313,8
Triclosan	< LOQ	< LOQ	< LOQ	< LOQ	< LOQ	< LOQ	< LOQ	< LOQ	< LOQ	< LOQ	< LOQ	< LOQ	< LOQ
Trimethoprim	n.d	n.d	n.d	< LOQ	< LOQ	< LOQ	< LOQ	< LOQ	27,5	24,7	26,4	42,0	25,8
Venlaflaxine	n.d	n.d	n.d	< LOQ	< LOQ	< LOQ	< LOQ	< LOQ	149,4	146,5	150,1	248,0	309,5
Xipamide	< LOQ	< LOQ	< LOQ	< LOQ	< LOQ	< LOQ	< LOQ	< LOQ	6,2	7,7	7,9	43,3	41,1

Table A.4: Measured concentration (ng/L) time-series by auto–sampler 1 at measuring station 1; Samples collected by auto-samplers. Measured concentrations were reprinted (adapted) with permission from Markus Schmitt (Schmitt et al., 2021. Copyright 2021 American Chemical Society). Auto-sampler (AS); Limit of quantification (LOQ); PFOA –Pentadecafluorooctanoic acid; B2SA – Benzothiazole-2-solfonic acid; 4&5 M-benzo – 4&5 Methyl-benzotriazole; O-Dems – O-Desmethylvenlafaxine. T-2-H – Terbuthylazine-2-hydroxy.

	Order of the samples taken by auto–sampler 1																			
Name	1	2	3	4	5	6	7	8	9	10	11	12	13	14	15	16	17	18	19	20	21
2-Aminobenzothiazole	8,7	9,4	10,2	9,3	7,9	8,3	8,4	10,0	9,0	9,5	8,2	8,6	7,7	9,5	9,7	9,6	8,2	9,0	8,4	8,5	9,3
4&5 M-benzo	698,9	799,3	745,0	740,9	720,0	685,9	614,8	816,4	902,7	697,7	728,3	664,4	666,7	736,9	734,4	684,9	695,3	701,9	672,5	832,3	885,2
Amisulpride	118,4	121,8	124,1	117,9	130,9	127,1	127,1	148,0	151,5	136,5	142,4	144,6	144,5	145,5	146,7	142,4	142,1	131,8	129,1	137,6	138,0
Atrazine-2-hydroxy	< LOQ	1,3	1,6	1,7	1,2	1,5	1,6	1,5	1,8	1,5	1,4	1,3	1,3	< LOQ	1,3	1,5	1,6	1,4	1,5	1,5	1,6
Azoxystrobin	0,7	0,8	0,7	0,7	0,8	0,8	0,7	0,7	0,9	0,9	0,8	0,7	0,6	0,7	0,7	0,7	0,8	0,8	0,7	0,7	0,8
Bentazone	< LOQ	0,6	0,6	0,7	0,7	0,6	0,8	0,7	0,9	0,9	0,6	0,8	0,6	< LOQ	0,7	0,8	0,7	0,7	0,5	0,8	1,0
B2SA	1024,1	979,7	670,6	681,3	674,5	515,9	603,2	672,5	661,2	616,5	529,1	681,8	838,0	995,4	1150,9	1009,2	919,6	739,2	1096,7	1003,2	921,2
Benzotriazole	2784,0	2886,3	2976,7	2947,8	3087,8	3054,6	3010,0	4368,0	4465,7	3989,2	3923,7	3533,4	3487,3	3562,0	3595,5	3486,5	3107,4	3101,7	2865,4	3512,4	3727,9
Bisoprolol	149,4	171,4	171,7	170,0	168,8	156,8	150,1	215,7	205,4	186,9	189,2	187,2	200,4	206,1	208,6	190,7	170,5	158,6	151,6	166,1	168,5
Boscalid	1,8	2,9	3,1	3,7	2,6	2,7	2,6	3,0	3,4	3,3	2,7	3,2	2,8	2,5	3,5	2,4	2,4	2,9	3,2	2,3	3,0
Carbamazepine	179,5	209,6	221,6	219,0	228,2	214,5	198,6	275,9	290,2	250,4	253,0	235,0	255,1	260,3	273,0	259,1	217,5	220,6	233,1	259,2	282,4

Carbendazim	12,7	15,6	15,1	15,4	14,7	13,5	13,3	17,0	17,7	15,8	14,5	14,2	13,9	13,9	15,4	14,5	13,9	12,1	12,3	13,3	15,1
Citalopram	65,3	76,7	88,0	70,8	72,3	71,9	66,8	103,8	116,1	104,2	106,3	96,0	106,2	86,5	96,8	89,6	75,2	80,8	72,5	80,8	90,1
Climbazole	1,8	2,2	2,6	2,7	2,8	2,5	2,3	3,5	3,5	3,0	2,9	2,7	3,3	3,2	3,4	3,1	2,8	2,5	2,6	2,9	3,5
Diclofenac	325,2	416,6	437,5	410,3	451,0	427,9	450,8	621,1	495,7	390,3	411,4	437,7	481,9	461,8	526,0	448,5	431,9	433,0	410,6	434,1	351,5
Diuron	4,6	5,3	7,5	5,8	6,4	6,8	6,4	8,3	8,9	8,5	7,3	6,7	5,7	6,6	7,6	7,1	7,6	7,5	5,9	8,1	8,2
Fluconazole	3,1	5,3	5,1	5,9	5,3	5,2	5,5	8,1	8,6	7,8	6,5	7,2	8,5	7,4	6,9	6,9	6,1	6,4	5,2	7,0	7,0
Flufenamic acid	3,9	6,0	5,7	5,5	5,0	4,6	5,3	6,2	6,0	4,5	4,8	5,7	5,4	6,1	5,8	5,9	5,1	6,2	5,0	6,0	5,4
Gabapentin	895,5	1136,7	886,7	1185,5	1034,9	1232,8	1073,7	1401,9	1351,1	1103,3	900,8	1110,6	1026,1	1140,5	1455,6	1104,3	874,6	877,4	821,0	869,2	1041,4
Hydrochlorozhiazide	443,7	595,4	577,9	583,3	628,6	600,9	580,9	775,4	707,4	522,1	601,6	607,4	689,8	687,8	820,1	666,4	635,2	659,1	610,9	613,5	530,5
Imidacloprid	1,8	2,2	1,9	2,2	2,1	2,2	2,2	2,4	2,1	2,4	2,2	2,3	2,1	2,1	2,1	2,4	2,1	2,1	2,0	2,5	2,2
Irbesartan	64,1	79,2	85,8	87,5	87,7	83,0	77,5	109,2	104,5	94,2	90,3	88,6	88,0	84,5	91,4	88,7	78,6	82,9	80,2	80,3	94,3
Isoproturon	9,6	12,3	12,0	12,0	11,4	12,1	12,1	16,5	16,2	16,6	14,4	13,6	12,0	12,3	12,8	11,8	11,6	10,0	11,3	11,1	13,1
Lamotrigine	303,7	344,6	349,8	390,9	377,8	354,4	372,5	503,5	524,7	461,4	443,7	434,1	460,5	459,2	449,5	433,4	406,8	402,1	385,2	420,5	477,5
Mecoprop	16,0	29,6	30,5	31,8	24,4	24,6	21,4	28,3	25,8	22,9	20,7	23,8	18,7	11,4	26,8	28,0	21,1	22,4	21,3	24,2	24,6
Metoprolol	157,1	165,2	180,0	174,8	185,1	173,8	168,0	259,0	254,5	213,7	219,2	205,7	220,0	226,5	222,7	220,1	197,4	175,3	182,2	195,0	198,4
O-Dems	283,6	314,2	328,4	312,6	323,8	318,9	308,1	422,6	447,5	396,2	391,9	389,0	393,5	384,8	402,6	379,0	351,8	328,1	320,7	378,3	388,9
Olmasartan	85,0	100,1	116,0	119,8	123,6	110,0	107,3	141,5	133,5	122,6	119,4	111,4	107,0	116,6	121,9	112,7	112,7	109,4	111,1	117,2	136,9
PFOA	7,1	7,6	8,1	8,1	7,5	7,7	7,3	7,7	9,9	7,2	8,0	9,0	7,0	6,4	7,2	7,6	6,1	7,6	6,8	7,3	7,7
Primidone	36,1	50,8	57,6	59,4	58,6	57,8	52,3	71,9	71,2	66,8	68,4	63,4	65,2	63,5	69,5	66,9	61,4	62,4	63,2	68,1	74,7
Propiconazole	6,3	7,3	6,2	7,2	6,3	5,4	5,0	6,6	7,6	7,4	6,1	7,0	6,0	5,6	7,1	7,4	5,8	5,6	6,3	6,0	7,2
Sitagliptin	1607,0	1900,8	1922,5	1825,5	1823,2	1871,3	1678,5	2496,4	2679,2	2362,8	2466,1	2352,7	2313,1	2300,9	2286,2	2253,5	1949,5	1838,1	1820,4	2167,6	2274,4
Sotalol	11,8	17,5	17,1	12,0	13,9	14,8	15,2	20,5	22,0	23,3	15,9	18,4	20,4	17,4	20,6	16,3	17,3	15,4	17,1	21,8	18,8
Sulfamethoxazole	148,2	158,2	152,4	173,6	127,9	163,1	173,5	205,0	228,6	221,8	192,7	255,5	250,4	178,0	197,8	187,2	181,4	152,7	157,4	166,8	237,5
Sulpiride	42,9	55,6	51,7	50,7	49,6	55,0	46,2	65,1	66,2	65,8	57,0	60,1	54,3	60,1	70,2	52,3	52,6	48,6	55,9	60,6	62,0
Tebuconazole	3,8	5,0	5,1	5,3	5,4	4,7	4,6	5,7	6,0	5,6	4,8	5,2	4,6	4,6	5,0	5,0	4,2	4,3	4,2	4,7	5,1
Telmisartan	84,9	104,5	111,9	106,6	102,1	94,4	96,6	131,8	151,2	120,6	130,0	115,7	114,7	108,6	110,9	106,0	96,9	95,0	91,7	108,9	114,6
T-2-H	21,9	25,6	27,1	26,7	23,9	22,5	22,0	26,0	26,1	23,8	22,0	21,9	24,1	25,2	25,3	24,1	23,7	21,8	22,5	23,3	25,9
Terbutryn	13,4	15,9	16,8	18,1	17,4	16,5	16,9	21,4	24,0	22,0	20,1	18,9	17,8	17,4	19,6	19,2	20,5	19,9	18,3	21,2	25,7
Torsemide	44,1	61,6	58,6	63,8	62,1	60,2	61,7	90,1	93,1	82,3	78,1	72,1	70,6	66,9	77,7	72,6	66,8	65,1	67,0	71,5	83,2
Tramadol	160,1	175,3	182,0	174,1	183,6	166,6	155,4	230,4	233,4	204,7	215,9	203,9	214,5	212,7	210,3	211,5	189,9	181,0	171,4	195,6	196,9
Trimethoprim	21,6	24,8	26,4	28,6	24,7	23,4	25,4	32,8	37,1	33,0	30,0	29,5	31,2	29,8	32,9	30,8	26,5	25,5	24,2	27,4	31,8
Venlaflaxine	142,3	158,2	157,9	157,1	155,0	153,3	157,9	211,8	218,0	195,8	205,6	199,4	202,6	200,0	204,3	196,2	180,4	170,6	167,7	179,6	180,7
Xipamide	24,3	38,8	39,3	41,3	44,2	40,4	39,5	36,0	13,1	6,2	13,3	24,9	40,3	40,9	43,2	39,1	34,0	38,7	25,8	15,0	4,7

Table A.5: Measured concentration (ng/L) time-series by auto–sampler 2 at measuring station 2; Samples collected by auto-samplers. Measured concentrations were reprinted (adapted) with permission from Markus Schmitt (Schmitt et al., 2021. Copyright 2021 American Chemical Society). Auto-sampler (AS); Limit of quantification (LOQ); PFOA –Pentadecafluorooctanoic acid; B2SA – Benzothiazole-2-solfonic acid.

	Order of the samples taken by auto–sampler 2														
Name	1	2	3	4	5	6	7	8	9	10	11	12	16	17	18
2-Aminobenzothiazole	9,0	8,3	8,6	8,2	8,7	9,3	7,9	8,2	7,7	9,4	9,4	9,0	7,9	9,9	10,0
4&5 Methyl-benzotriazole	698,8	648,6	687,5	530,7	904,3	882,5	770,2	731,8	685,1	620,1	697,9	756,4	749,1	777,2	919,2
Amisulpride	124,2	115,0	115,1	124,7	153,9	140,1	135,5	128,9	137,2	143,3	141,6	146,0	124,7	130,7	122,6
Atrazine-2-hydroxy	1,3	1,8	1,7	1,3	1,2	< LOQ	1,9	1,5	1,6	1,7	1,7	1,4	< LOQ	1,5	1,4
Azoxystrobin	0,7	0,8	0,7	0,5	0,8	0,7	0,7	0,7	0,6	0,7	0,6	0,7	0,7	0,7	0,7
Bentazone	0,8	0,9	0,6	0,7	1,0	1,1	0,7	1,0	1,0	1,0	0,9	0,9	< LOQ	0,9	0,5
B2SA	722,5	753,5	728,6	479,4	617,4	723,4	462,3	579,9	654,1	957,2	1066,0	1076,7	773,4	1009,1	1170,0
Benzotriazole	2977,8	2942,7	3067,3	2924,5	4712,9	4465,2	4004,2	3786,3	3577,0	3414,0	3466,4	3539,2	2908,6	3304,7	3679,8
Bisoprolol	146,2	142,0	143,5	133,8	212,2	175,6	153,4	166,5	175,7	186,4	173,9	178,8	140,6	129,5	123,1
Boscalid	3,8	3,5	2,5	2,8	4,5	4,2	3,7	3,9	3,2	3,6	3,2	3,8	3,1	2,9	3,3
Carbamazepine	210,2	219,9	221,6	206,7	281,6	295,6	274,6	253,8	255,8	270,8	268,3	256,4	229,5	232,4	255,7
Carbendazim	15,5	13,5	14,5	12,9	18,1	17,3	15,6	14,8	13,5	13,5	14,6	14,6	9,0	13,8	13,1
Citalopram	69,3	59,6	65,2	62,5	83,6	90,4	74,8	76,4	81,9	85,0	73,0	75,2	66,8	58,4	60,2
Climbazole	2,3	2,5	1,8	2,2	3,2	3,2	3,0	2,8	2,8	2,5	2,5	2,4	1,1	2,7	2,5
Diclofenac	437,6	464,8	468,6	424,8	512,2	312,6	247,1	334,3	381,3	414,9	473,8	514,7	344,0	309,3	210,2
Diuron	7,3	6,6	6,7	7,2	8,1	8,6	9,0	7,1	5,9	6,1	6,7	6,8	5,9	8,8	7,6
Fluconazole	5,7	6,3	6,5	5,2	8,2	6,8	8,4	6,9	6,4	6,3	6,9	7,0	1,8	6,7	7,0
Flufenamic acid	5,7	4,9	4,8	4,7	5,6	4,2	3,9	3,6	4,3	5,2	5,5	6,1	5,7	4,5	4,7
Gabapentin	1026,9	1045,3	891,7	1032,6	1378,3	1193,7	1059,1	1093,7	973,7	1098,8	1116,3	1068,8	692,6	808,8	929,6
Hydrochlorozhiazide	595,5	648,3	667,3	560,4	665,3	468,6	405,3	475,7	556,5	659,9	686,1	750,7	442,0	444,9	321,1
Imidacloprid	2,3	2,3	1,9	2,1	2,3	1,8	2,3	2,1	1,8	1,8	1,8	2,4	2,1	2,0	2,0
Irbesartan	87,3	81,1	87,5	73,2	104,5	92,8	91,0	84,6	79,9	83,0	90,4	90,9	36,2	84,1	83,0
Isoproturon	13,1	13,5	13,6	12,9	16,1	16,1	14,5	14,4	11,4	11,2	11,9	12,4	5,6	11,8	11,3
Lamotrigine	410,8	367,6	393,9	375,1	478,2	496,3	457,1	441,3	430,7	419,3	440,2	462,0	210,0	441,9	460,9
Mecoprop	32,2	28,7	23,1	24,5	31,0	25,1	21,2	20,9	19,8	21,5	23,9	28,0	9,8	22,3	18,1
Metoprolol	163,9	155,3	152,6	144,7	227,7	200,2	187,0	194,9	198,3	199,4	197,4	205,4	147,4	135,1	132,8
O-Desmethylvenlafaxine	304,3	302,1	298,4	287,4	423,9	401,4	371,2	381,7	382,1	379,0	375,3	377,2	311,0	306,6	317,1
Olmasartan	119,4	102,9	114,6	103,6	131,6	121,9	106,7	111,1	105,6	104,7	107,6	130,1	60,5	127,8	116,6
PFOA	8,3	7,5	6,7	7,3	8,4	8,7	8,2	6,4	7,8	10,5	8,3	6,7	2,9	8,5	7,0
Primidone	41,9	49,1	51,3	42,9	66,6	54,5	59,1	53,1	50,3	56,2	62,6	58,7	22,0	52,1	49,9
Propiconazole	7,2	6,4	6,8	5,1	6,9	6,1	7,4	5,5	5,8	5,3	6,2	5,1	4,8	7,2	6,7
Sitagliptin	1845,5	1733,5	1716,1	1628,7	2681,6	2330,3	2469,8	2056,8	2155,3	2115,2	1960,2	2295,0	1965,2	2075,7	2435,2
Sotalol	18,0	14,7	10,1	14,3	22,0	24,0	14,4	16,8	17,6	17,2	15,4	17,5	13,9	13,8	12,7
Sulfamethoxazole	123,3	151,2	137,7	146,5	209,1	229,6	206,9	220,7	195,8	210,7	224,1	170,2	158,3	166,9	212,0
Sulpiride	47,1	54,6	45,5	49,8	68,0	70,2	61,3	62,0	56,3	52,7	58,3	60,0	54,4	59,7	66,0
Tebuconazole	5,5	5,2	4,6	4,8	6,7	6,2	5,9	4,9	5,2	4,7	4,9	4,7	3,6	5,2	4,5

Telmisartan	110,0	100,5	102,2	95,7	137,2	143,1	116,5	106,8	107,3	98,5	103,0	113,5	87,3	109,1	118,4	
Terbuthylazine-2-hydroxy	22,5	22,9	22,6	19,7	26,0	23,7	21,8	22,0	20,0	21,2	23,2	23,8	9,1	22,8	23,9	
Terbutryn	16,2	15,4	15,5	17,4	21,6	20,8	18,4	18,1	15,6	15,0	17,2	17,2	15,1	22,0	21,5	
Torsemide	65,2	61,7	66,4	65,5	88,4	84,1	75,9	79,3	72,8	69,5	71,1	76,5	43,4	73,7	74,9	
Tramadol	164,4	167,0	157,6	145,0	219,4	198,7	190,5	204,9	213,4	201,6	208,4	207,3	150,6	141,6	148,8	
Trimethoprim	26,5	22,8	24,1	23,3	34,2	33,3	31,0	27,5	26,6	26,8	28,5	31,1	15,1	27,1	26,6	
Venlaflaxine	139,7	135,8	138,9	129,2	192,5	182,9	177,1	181,5	189,7	187,8	186,0	184,9	137,8	130,0	132,0	
Xipamide	39,7	40,5	38,8	29,4	10,6	1,0	1,6	6,0	17,1	36,8	51,0	54,2	14,1	3,5 < LOQ		

Table A.6: Measured concentration (ng/L) time-series by auto–sampler 3 at measuring station 3; Samples collected by auto-samplers. Measured concentrations were reprinted (adapted) with permission from Markus Schmitt (Schmitt et al., 2021. Copyright 2021 American Chemical Society). Auto-sampler (AS); Limit of quantification (LOQ); PFOA –Pentadecafluorooctanoic acid; B2SA – Benzothiazole-2-solfonic acid.

	Order of the samples taken by auto–sampler 3															
Name	1	2	3	4	5	6	7	8	9	10	11	12	13	14	15	16
2-Aminobenzothiazole	9,2	7,4	8,2	8,9	8,5	8,4	9,2	9,8	8,1	9,0	9,4	9,2	8,1	8,7	8,4	9,7
4&5 Methyl-benzotriazole	657,2	689,2	865,2	802,8	776,8	723,6	681,0	658,4	699,9	691,6	706,9	676,4	686,4	655,6	750,3	805,9
Amisulpride	115,6	117,4	133,9	124,1	125,0	124,4	125,6	125,0	134,4	136,0	141,4	133,6	125,5	115,6	107,4	103,1
Atrazine-2-hydroxy	1,4	1,2	1,5	1,6	1,3	1,6	1,7	1,2	1,5	1,2	1,6	1,3	1,1	1,4	1,3	1,7
Azoxystrobin	0,6	0,7	0,8	0,7	0,6	0,8	0,8	0,7	0,6	0,7	0,6	0,7	0,6	0,5	0,6	0,6
Bentazone	0,9	0,9	1,0	1,2	0,8	1,0	1,0 < LOQ		0,8	0,8	0,9	0,6	0,8	0,8	1,0	1,0
B2SA	770,9	432,0	522,6	477,7	605,4	411,4	533,7	752,5	687,5	882,6	887,3	890,4	833,9	681,3	889,2	725,1
Benzotriazole	2940,0	3209,4	4584,4	4383,3	3763,1	3819,6	3472,2	3231,9	3106,8	3287,8	3244,0	3125,3	2955,8	2805,4	3003,3	3503,0
Bisoprolol	119,6	129,1	157,5	130,2	129,9	124,7	140,8	157,5	160,7	162,6	153,0	144,9	121,4	103,0	89,5	79,8
Boscalid	3,5	3,6	4,6	3,8	3,3	3,5	4,7	4,4	3,3	3,4	4,0	4,4	2,6	3,4	3,9	4,5
Carbamazepine	212,7	205,3	283,4	288,7	255,1	263,1	252,2	242,7	250,9	273,2	274,0	248,3	247,5	229,6	228,5	259,1
Carbendazim	14,2	14,6	17,8	18,1	15,8	14,4	14,4	13,7	14,6	13,7	14,8	14,4	11,4	12,6	13,0	14,1
Citalopram	53,1	46,9	57,6	53,9	67,3	73,9	72,0	67,9	53,1	46,9	57,6	53,9	67,3	73,9	72,0	67,9
Climbazole	1,8	2,3	2,7	2,6	3,1	2,7	2,6	2,4	2,3	1,8	2,3	2,3	1,9	1,5	2,2	2,6
Diclofenac	385,2	346,0	270,8	204,7	213,9	294,7	398,9	467,3	470,0	481,9	518,1	429,7	299,7	277,6	141,1	130,8
Diuron	6,4	7,2	9,4	8,7	8,6	7,4	6,2	6,7	5,8	6,2	6,9	8,1	6,9	7,9	8,9	8,2
Fluconazole	5,5	6,1	8,3	8,7	8,8	8,9	8,2	8,5	7,1	7,1	7,6	6,0	6,9	6,7	6,8	7,5
Flufenamic acid	4,0	4,1	3,3	3,0	2,9	3,7	4,6	5,1	5,3	4,7	5,8	5,2	3,9	3,8	3,2	2,5
Gabapentin	887,1	945,2	1201,9	1117,2	952,1	795,9	798,4	858,9	1018,7	1081,7	955,9	939,0	876,3	783,7	707,8	777,7
Hydrochlorozhiazide	496,6	446,4	442,1	309,5	335,5	435,8	614,4	617,9	672,4	714,8	742,5	609,8	433,9	416,0	245,2	219,5
Imidacloprid	1,9	1,8	2,1	2,2	2,3	1,8	2,1	2,1	1,8	2,0	2,2	2,6	1,8	2,0	1,3	1,9
Irbesartan	82,7	82,6	103,8	95,4	89,9	82,6	88,3	86,2	89,8	88,3	90,0	83,5	71,0	71,4	74,0	80,0
Isoproturon	13,0	13,5	16,0	16,1	15,0	14,5	12,7	11,2	12,6	11,8	12,4	12,4	10,9	12,0	11,9	10,7
Lamotrigine	360,9	407,8	525,3	490,8	448,6	438,1	440,0	472,4	443,9	450,6	452,6	453,9	369,2	390,5	404,6	452,0
Mecoprop	26,4	25,5	30,9	28,5	21,5	24,9	22,9	14,8	26,7	24,7	25,8	21,4	22,5	21,7	20,6	24,6
Metoprolol	120,0	125,9	157,8	158,4	141,7	167,6	179,6	187,0	185,2	186,5	175,2	168,1	126,0	93,6	70,8	72,4
O-Desmethylvenlafaxine	284,5	289,2	353,3	359,5	362,2	380,9	386,0	369,6	370,2	367,7	365,1	351,1	307,8	284,3	234,5	235,1
Olmasartan	112,0	104,7	135,1	128,0	123,3	96,8	115,4	107,1	114,7	111,3	121,9	119,1	105,6	95,5	103,0	115,2
PFOA	8,7	8,6	10,0	10,8	8,2	7,4	8,4	8,0	6,9	8,4	8,5	8,2	7,2	7,1	8,6	8,8
Primidone	50,8	57,6	73,7	72,6	69,5	64,8	73,0	62,6	65,4	61,9	68,7	65,8	59,4	61,5	57,8	69,1
Propiconazole	5,2	5,1	6,4	6,5	6,1	8,4	6,1	6,6	5,9	5,3	7,0	6,5	5,0	5,4	5,5	5,0
Sitagliptin	1724,9	1789,1	2326,6	2511,3	2247,7	1906,5	1874,9	1730,3	2032,3	1905,1	2018,8	1912,8	1874,8	1864,7	1896,9	2205,1
Sotalol	14,0	14,5	17,2	14,1	14,8	15,9	17,3	19,5	19,2	15,5	23,2	19,8	18,1	13,2	8,1	10,4
Sulfamethoxazole	138,3	182,3	255,5	218,2	187,0	192,2	207,7	180,5	199,9	209,5	173,7	186,2	182,3	163,9	159,8	222,9
Sulpiride	50,3	56,5	66,9	65,1	64,1	57,1	54,8	61,0	60,9	59,8	58,9	69,3	62,2	56,6	53,5	57,1
Tebuconazole	4,9	5,3	6,2	6,0	5,9	5,6	5,9	4,9	4,9	4,8	5,1	4,7	4,3	4,9	4,1	5,1
Telmisartan	94,7	107,4	139,0	135,8	123,5	116,5	109,7	97,1	107,7	95,4	95,9	102,2	87,4	88,6	97,7	121,4
Terbuthylazine-2-hydroxy	22,1	23,3	26,9	27,2	24,0	22,9	24,0	23,9	24,1	23,9	25,4	23,8	22,2	22,7	24,2	25,3
Terbutryn	15,2	15,9	14,2	16,7	13,8	17,5	21,2	20,8	16,2	21,6	15,5	17,4	15,4	20,8	18,4	18,1
Torsemide	63,2	72,3	90,7	89,2	76,8	74,2	79,1	64,9	74,2	73,3	75,4	70,1	59,4	61,2	67,8	74,5
Tramadol	138,7	134,2	166,9	162,7	176,6	207,3	219,3	202,2	196,7	192,6	196,8	180,5	157,7	121,3	97,2	100,5
Trimethoprim	22,7	26,8	33,7	34,5	28,5	26,1	25,2	26,3	26,9	26,2	28,3	23,9	22,2	23,5	23,5	28,1
Venlaflaxine	114,7	114,2	138,1	127,0	150,0	171,6	177,6	174,1	173,5	170,5	163,9	157,7	132,7	101,7	79,2	84,0
Xipamide	21,4	7,3 < LOQ		< LOQ		< LOQ	1,8	15,0	33,8	47,5	52,6	54,2	41,1	14,4	4,6 < LOQ	< LOQ

Table A.7: Molecular weight and inhibitory concentration 10 of the detected compounds. PFOA – Pentadecafluorooctanoic acid.

DTXSID	Names	MW (g/mol) (US EPA Comptox)	AhR IC10 (Exp) (M)	PPARγ IC10 (Exp) (M)	ERα IC10 (Exp) (M)	AR IC10 (Exp) (M)	GR IC10 (Exp) (M)	AREc32 IC10 (Exp) (M)
1024467	2-Aminobenzothiazole	150,2	not active	not active	not active	not active	not active	not active

1038743	4&5 Methyl-benzotriazole	133,154	5,59E-04					4,60E-04
5042613	Amisulpride	369,48	not active	not active	not active	3,13E-05	not active	not active
6037807	Atrazine-2-hydroxy	197,242						
0032520	Azoxystrobin	403,394	2,77E-07	3,15E-05	2,29E-05	1,21E-05	3,54E-05	1,97E-04
0023901	Bentazone	240,28	1,18E-03	not active	not active	not active	not active	7,57E-04
80240528	Benzothiazole-2-sulfonic acid	215,24	5,11E-04	9,50E-04				not active
6020147	Benzotriazole	119,127	1,68E-03	not active	not active	5,17E-05	not active	3,68E-03
6022682	Bisoprolol	325,449						
6034392	Boscalid	343,21	4,84E-06	not active	not active	6,79E-05	not active	2,72E-05
4022731	Carbamazepine	236,274	1,78E-04	not active	not active	not active	not active	1,52E-04
4024729	Carbendazim	191,19	5,10E-06	not active	not active	4,8E-05	not active	2,55E-06
8022826	Citalopram	324,399						1,23E-04
6046555	Climbazole	292,76	3,21E-05	not active	not active	1,68E-05	not active	1,69E-04
6022923	Diclofenac	296,15	6,62E-05	4,10E-05				4,78E-05
0020446	Diuron	233,09	5,90E-05	not active	not active	not active	not active	6,42E-05
3020627	Fluconazole	306,277	not active	not active	not active	not active	not active	not active
7023063	Flufenamic acid	281,234	not active	3,58E-05	3,84E-05	2,98E-05	4,09E-05	8,96E-05
0020074	Gabapentin	171,24	not active	not active	not active	not active	not active	not active
2020713	Hydrochlorothiazide	297,73	not active	not active	not active	not active	not active	not active
5032442	Imidacloprid	255,66	1,99E-04	not active	not active	not active	not active	5,98E-04
0023169	Irbesartan	428,54	1,95E-05	not active	not active	not active	not active	not active
1042077	Isoproturon	206,289	8,64E-05	not active	not active	not active	not active	5,55E-05
2023195	Lamotrigine	256,09	2,62E-04	4,39E-04	not active	not active	not active	2,74E-04
9024194	Mecoprop	214,65	not active	not active	not active	not active	not active	not active
2023309	Metoprolol	267,369	4,00E-05	2,31E-04				7,89E-04
40869118	O-Desmethylvenlafaxine	263,381						
2040571	Olmesartan	446,511						
8031865	PFOA	414,07	1,98E-04	not active	not active	not active	7,03E-05	not active
7023510	Primidone	218,256	not active	not active	not active	not active	not active	not active
8024280	Propiconazole	342,22	not active	not active	not active	1,61E-05	not active	not active
70197572	Sitagliptin	407,32						
0023589	Sotalol	272,36	not active	not active	not active	2,44E-05	not active	
8026064	Sulfamethoxazole	253,28	2,35E-03	not active	not active	not active	not active	2,43E-03
1042574	Sulpiride	341,43	not active	not active	not active	3,59E-05	5,36E-05	not active
9032113	Tebuconazole	307,82	2,38E-05	6,02E-05	6,34E-05	2,83E-05	not active	4,67E-05
8023636	Telmisartan	514,629	not active	2,84E-05	not active	not active	not active	3,07E-05
20216888	Terbuthylazine-2-hydroxy	211,269						
3024318	Terbutryn	241,36	3,72E-05	not active	6,68E-05	4,17E-05	not active	7,05E-05
2023690	Torsemide	348,42	not active	1,84E-04	not active	not active	not active	1,10E-03
90858931	Tramadol	263,381						
3023712	Trimethoprim	290,323	1,57E-04	not active	not active	not active	not active	not active
6023737	Venlafaxine	277,408	not active	2,11E-04	not active	not active	not active	4,51E-04
5023744	Xipamide	354,81						

Table A.8: Effect concentration 10 of the detected compounds and their half-lives (source: https://comptox.epa.gov/dashboard). PFOA – Pentadecafluorooctanoic acid.

DTXSID	Names	AhR EC10 (Exp) (M)	PPARγ EC10 (Exp) (M)	ERα EC10 (Exp) (M)	AR EC10 (Exp) (M)	GR EC10 (Exp) (M)	AREc32 ECIR1.5 (Exp) (M)	Half-life (day)
1024467	2-Aminobenzothiazole	1,92E-05	not active	not active	not active	not active	8,79E-05	7,5
1038743	4&5 Methyl-benzotriazole	2,56E-04					not active	2,53
5042613	Amisulpride	not active	not active	not active	not active	not active	not active	3,35
6037807	Atrazine-2-hydroxy							3,94
0032520	Azoxystrobin	not active	not active	not active	not active	not active	not active	5,69
0023901	Bentazone	not active	not active	not active	not active	not active	not active	4,9
80240528	Benzothiazole-2-sulfonic acid	1,48E-04	8,91E-05				8,63E-05	11,2
6020147	Benzotriazole	6,07E-04	not active	not active	not active	not active	not active	3,99
6022682	Bisoprolol							4,29
6034392	Boscalid	not active	not active	not active	not active	not active	not active	5,99
4022731	Carbamazepine	not active	not active	not active	not active	not active	not active	6,54
4024729	Carbendazim	not active	not active	not active	4,46353E-05	not active	not active	4,47
8022826	Citalopram						3,58E-05	3,55
6046555	Climbazole	2,02E-06	not active	not active	not active	not active	1,68E-04	4,9
6022923	Diclofenac	not active	8,56E-07				not active	4,68
0020446	Diuron	1,94E-06	not active	not active	not active	not active	3,52E-05	4,51
3020627	Fluconazole	not active	not active	not active	not active	not active	not active	4,52
7023063	Flufenamic acid	not active	not active	not active	not active	not active	not active	3,55
0020074	Gabapentin	not active	not active	not active	not active	not active	not active	3,72
2020713	Hydrochlorothiazide	not active	not active	not active	not active	not active	not active	7,22
5032442	Imidacloprid	not active	not active	not active	not active	not active	not active	3,54
0023169	Irbesartan	not active	1,20E-05	not active	not active	not active	not active	34,8
1042077	Isoproturon	8,74E-06	not active	not active	not active	not active	4,26E-05	4,34
2023195	Lamotrigine	not active	1,02E-04	not active	not active	not active	not active	6,23
9024194	Mecoprop	not active	not active	not active	not active	not active	not active	3,53

2023309	Metoprolol	not active	not active				not active	4,47
40869118	O-Desmethylvenlafaxine							4,71
2040571	Olmesartan							14,6
8031865	PFOA	not active	not active	not active	not active	not active	not active	4,94
7023510	Primidone	not active	not active	not active	not active	not active	not active	3,34
8024280	Propiconazole	not active	not active	not active	not active	not active	not active	4,25
70197572	Sitagliptin							3,55
0023589	Sotalol	not active	not active	not active	not active	not active		3,35
8026064	Sulfamethoxazole	not active	not active	not active	not active	not active	not active	3,35
1042574	Sulpiride	not active	not active	not active	not active	not active	not active	4,23
9032113	Tebuconazole	not active	not active	not active	not active	not active	not active	3,18
8023636	Telmisartan	1,56722E-05	1,43E-07	not active	not active	not active	not active	37
20216888	Terbuthylazine-2-hydroxy							4,62
3024318	Terbutryn	not active	not active	not active	not active	not active		3,36
2023690	Torsemide	not active	5,19E-05	not active	not active	not active	not active	3,36
90858931	Tramadol	8,56E-06	not active					3,36
3023712	Trimethoprim	not active	not active	not active	not active	not active	1,97E-04	4,24
6023737	Venlafaxine	not active	not active	not active	not active	not active	not active	3,36
5023744	Xipamide							5,67

Table A.9: Effect concentration 10 and inhibitory concentration 10 of the whole water sample. Units in relative enrichment factor (REF). NCT – No cytotoxicity; NotAct – Not active.

	AhR-CALUX				PPARγ-GeneBLAzer				ERα-GeneBLAzer				ARE32			
	EC10	std err EC10	IC10	std err IC10	EC10	std err EC10	IC10	std err IC10	EC10	std err EC10	IC10	std err IC10	ECIR1.5	std err ECIR1.5	IC10	std err IC10
AS1 1	5,82	0,29	98,9	29,2	5,27	0,74	NCT		11,68	0,74	70,51	14,12	21,1	2,66	NCT	
AS1 2	4,07	0,201	40,6	6,26	5,64	0,63	36,05	3,55	8,1	0,22	31,27	4,3	24,5	2,25	NCT	
AS1 3	4,6	0,177	47,7	4,94	4,13	0,56	40,19	3,55	8,45	0,41	33,14	2,68	15,5	1,01	NCT	
AS1 4	4,83	0,146	41,7	4,01	2,81	0,27	31,85	3,43	8,23	0,35	27,4	2,27	15	1,02	90,3	33,4
AS1 5	5	0,16	27,1	2,84	5,15	0,61	39,92	3,34	7,36	0,76	37,1	5,81	10,8	0,556	67	14,3
AS1 6	4,36	0,175	25,9	2,3	3,43	0,46	56,23	13,08	7,83	0,26	19,84	1,37	9,79	0,903	67,6	26
AS1 7	3,8	0,299	30,5	3,4	4,31	0,56	39,66	3,49	9,71	0,43	30,85	2,6	24,4	1,57	NCT	
AS1 8	3,43	0,143	29,8	2,95	4,07	0,98	28,94	2,17	7,88	0,37	25,17	1,59	7,24	0,67	47,4	7,73
AS1 9	3,04	0,145	26,6	1,76	4,47	0,73	22,99	1,4	7,24	0,41	22,7	1,28	7,1	0,485	46,7	8,52
AS1 10	4,5	0,15	24,8	1,74	3,37	0,58	26,61	1,32	7,97	0,45	23,35	1,43	12,5	0,65	36,5	3,81
AS1 11	3,68	0,21	25	1,48	4,19	0,45	25,84	2,4	6,83	0,29	15,08	1,45	9,82	1,77	34,3	4,36
AS1 12	3,87	0,214	19,7	3,97	4,97	0,74	30,04	1,88	6,45	0,48	24,18	1,74	12,7	0,886	28,9	2,47
AS1 13	2,68	0,161	29,7	4,07	4,79	0,45	30,47	3,3	8,06	0,4	24,7	2,3	8,15	0,918	47	11,8
AS1 14	3,74	0,183	32,8	2,61	4,33	0,66	24,88	1,25	8,82	0,58	21,43	1,36	10,7	0,968	43,4	8,69
AS1 15	4,27	0,342	32	2,39	4,22	0,79	27,82	1,84	9,1	0,59	24,68	1,91	17	1,25	61,5	18
AS1 16	3,38	0,317	26,9	2,15	2,43	0,46	24,1	1,85	8,52	0,52	21,89	1,62	8,35	0,686	41,4	7,42
AS1 17	3,3	0,18	22,2	1,48	3,13	0,34	28,46	2,15	10,17	0,64	27,3	2,31	12,2	0,861	31,3	3,31
AS1 18	3,56	0,299	27,8	2,03	4,64	0,8	24,97	2,28	9,77	0,52	23,23	1,49	11,6	0,633	33,7	5,64
AS1 19	3,6	0,217	20,8	1,81	2,87	0,41	29,72	2,19	13,43	1,4	24,84	1,09	7,69	0,569	30,8	3,86
AS1 20	2,86	0,0892	29,8	2,42	4,55	0,26	29,93	2,56	12,73	0,75	23,74	1,42	6,97	0,563	40,2	5,32
AS1 21	4,51	0,179	40,4	3,8	4,48	0,6	26,59	2,11	14,52	1,36	22,2	1,24	18,1	1,47	55,5	13,1
AS2 1	4,06	0,319	35,8	3,4	4,25	0,41	33,46	2,27	12,1	0,76	29,05	1,9	7,79	0,571	45,4	9,93
AS2 2	4,74	0,219	28,9	1,52	4,78	0,69	28,93	3,56	10,93	0,79	22,52	1,34	8,41	0,581	42,2	6,59
AS2 3	5,49	0,158	22,8	1,61	4,05	0,5	31,49	1,84	11,46	0,84	25,83	1,9	9,86	0,693	37	3,29
AS2 4	3,96	0,435	23,8	3,48	6,56	1,45	NCT		14,1	1,01	38,53	5,15	13,8	2,07	84	37,4
AS2 5	2,07	0,188	30,6	3,3	2,72	0,47	34	6,83	8,86	0,62	23,91	1,41	16,2	1,65	55,5	14
AS2 6	3,07	0,41	29,9	2,47	16,88	3,46	85,68	40,72	32,22	2,9	72,51	19,19	10,9	1,01	62,9	20,7
AS2 7	3,25	0,251	26,5	2,32	5,1	0,95	29,39	2,68	10,51	0,67	23,81	1,5	17,6	1,87	75	27,1
AS2 8	3,37	0,213	22,5	3,51	3,97	0,5	36,02	2,8	9,88	0,42	32,39	3,99	13,1	1,25	51,3	9,75
AS2 9	4,27	0,199	25,8	1,91	2,53	0,34	30,68	2,72	9,12	0,45	25,85	1,13	13,8	1,43	62,1	18,6
AS2 10	2,79	0,245	16,5	2,93	5,09	0,37	28,16	2,06	12,24	1,03	26,29	2,39	8,2	1,23	35,6	5,16
AS2 11	3,06	0,279	27,1	2,19	2,55	0,33	34,78	7,87	10,8	0,8	25,77	2,16	10,4	0,76	35,2	4,24
AS2 12	3,26	0,17	27	2,3	1,81	0,46	24,52	2,39	8,67	0,58	21,92	1,24	7,9	0,608	44,3	8,36
AS2 13																
AS2 14																
AS2 15																
AS2 16	4,58	0,226	35,3	3,08	9,1	1,06	47,58	7,88	13,11	0,79	42,28	7,11	12,7	0,647	69,8	17,3
AS2 17	4,33	0,166	25	1,57	4,93	0,8	27,52	2,58	15,03	1,11	21,82	1,23	9,71	0,855	42,8	7,57
AS2 18	3,57	0,167	21,8	1,44	3,74	0,64	31,18	1,68	15,59	1,66	30,33	3,98	13,4	0,498	52,6	11,2
AS3 1	3,71	0,19	38,5	8,68	4,97	0,6	53,44	17,98	15,87	1,54	26,2	2,57	11,3	0,686	78,4	37,3
AS3 2	2,99	0,0955	77,6	28,8	2,73	0,4	27,89	1,66	15,9	1,4	22,82	1,3	13,1	0,669	56,3	15,6
AS3 3	4,92	0,483	102	37,9	2,76	0,33	29,53	1,78	13,34	0,93	22,73	1,19	12,5	0,783	NCT	
AS3 4	3,7	0,25	37,2	6,02	5,42	0,74	26,6	2,45	13,52	1,13	20,93	1,1	7,62	0,58	87,6	31,6
AS3 5	3,35	0,352	28,7	3,83	3,48	0,36	31,92	1,98	9,77	0,37	27,03	2,84	7,89	0,5	39,1	5,01
AS3 6	3,83	0,325	37	4,57	5,22	0,97	26,07	2,16	9,24	0,53	23,89	1,19	10,7	0,56	58,1	14

AS3 7	3,52	0,174	35,9	4,46	4,7	0,57	25,93	2,08	13,07	0,83	26,15	1,73	16,4	1,02	NCT	
AS3 8	10,5	1,27	NCT		10,45	0,97	61,32	12,42	24,4	2,37	42,27	6,06	29,2	2,02	70,9	19,1
AS3 9	4,34	0,496	24,9	1,66	5,59	0,81	27,8	2,24	11,78	0,99	21,87	1,54	12,4	0,71	30	2,78
AS3 10	5,64	0,665	21,3	1,26	2,89	0,47	31,07	2,43	13,16	1,1	23,54	1,76	11,5	0,887	25	2,26
AS3 11	5,09	0,353	23,1	1,63	4,83	0,71	28,53	3,48	10,79	0,9	21,77	1,27	10,7	0,786	26,7	3,23
AS3 12	4,58	0,331	17,6	2,48	4,94	0,61	29,56	1,9	11,9	1,04	23,23	1,6	8,66	0,802	20,6	1,33
AS3 13	5,69	0,713	25,3	1,96	4,86	0,47	25,15	2,41	10,49	0,57	24,55	1,14	9,83	0,818	25,6	1,69
AS3 14	3,27	0,0735	18,7	3,33	5,5	0,64	28,11	1,65	11,29	0,85	27,87	2,17	8,86	0,874	22,5	2,16
AS3 15	3,22	0,182	24,5	3,06	2,15	0,31	37,18	7,91	18,2	1,43	24,28	1,87	9,39	0,67	27,8	3,2
AS3 16	3,47	0,257	27,3	1,81	3,34	0,39	28,07	1,48	11,51	0,78	25,89	2,47	11,8	0,685	43,3	6,28
blank 1	NotAct		50,4	11,6	88,39	23,31	NCT		NotAct		NCT		NotAct		NCT	
blank 2	NotAct		63,9	17,3	NotAct		NCT		NotAct		NCT		NotAct		NCT	
blank 3	NotAct		60,7	17,2	no active		NCT		NotAct		NCT		NotAct		NCT	
blank AS1	37,5	2,54	81,3	23,1	36,13	3,08	NCT		NotAct		NCT		NotAct		NCT	
blank AS2	24,6	1,41	91,9	24,2	18,31	2,59	NCT		NotAct		74,29	12,51	76,5	5,59	NCT	
blank AS3	29,6	1,51	63,5	14,4	88,22	26,72	NCT		NotAct		61,96	8,43	78,7	7,43	NCT	
grab cross 1 MS1	4,76	0,343	14,8	2,78	2,3	0,31	28,81	1,37	18,25	1,5	26,27	1,73	22,5	3,96	30,3	3,59
grab cross 2 MS1	1,36	0,137	27,7	3,53	2,67	0,21	25,95	1,47	NotAct		21,83	0,94	11,2	0,951	28,1	3,77
grab cross 3 MS1	4,57	0,796	27,5	1,76	3,38	0,44	22,8	1,25	NotAct		22,68	1,24	12,4	1,23	38,1	8,25
grab Ehr 1	NotAct		15,1	2,14	3,02	0,49	38,39	4,65	NotAct		27,26	3,66	NotAct		20,2	2,82
grab Mühl 1	2,47	0,0797	24,4	5,46	2,39	0,3	23,39	1,09	14,64	1,35	21,57	1,36	16,8	2,07	27,6	4,44
grab up 1	NotAct		34,5	4,99	6,09	0,78	35,9	2,67	NotAct		32,83	3,3	NotAct		43,6	11,8
grab WWTP	21,4	2,56	75,9	13,4	10,5	0,91	90,75	17,68	45,81	3,05	NCT		59,1	4,07	NCT	
spike 1	68,7	14	NCT		63,53	9,51	NCT		NotAct		NCT		NotAct		NCT	
spike 2	NotAct		99	40,6					NotAct		NCT		NotAct		NCT	

Table A.10: Normalized root-mean-square error: Goodness of fit for individual compounds and electrical conductivity at measuring station 2 and 3. Derivation: eq. A.15.

Name	MS2	MS3
2-Aminobenzothiazole	0.324545	0.324253
4&5 Methyl-benzotriazole	0.150374	0.212796
Amisulpride	0.165413	0.146543
Atrazine-2-hydroxy	0.39374	0.357831
Azoxystrobin	0.247064	0.33757
Bentazone	0.406576	0.295027
Benzothiazole-2-solfonic acid	0.184396	0.268231
Benzotriazole	0.102021	0.091749
Bisoprolol	0.141978	0.133837
Boscalid	0.199916	0.309741
Carbamazepine	0.197588	0.128591
Carbendazim	0.132609	0.071623
Citalopram	0.203516	0.462843
Climbazole	0.209829	0.121256

Diclofenac	0.211187	0.169818
Diuron	0.182424	0.153544
Fluconazole	0.19217	0.24853
Flufenamic acid	0.251369	0.219495
Gabapentin	0.152889	0.147962
Hydrochlorozhiazide	0.194067	0.133427
Imidacloprid	0.317005	0.217726
Irbesartan	0.169491	0.118317
Isoproturon	0.163565	0.103359
Lamotrigine	0.172825	0.149023
Mecoprop	0.219674	0.214449
Metoprolol	0.184971	0.188239
O-Desmethylvenlafaxine	0.170918	0.211639
Olmasartan	0.202801	0.254664
PFOA (Pentadecafluorooctanoic acid)	0.216907	0.306165
Primidone	0.230103	0.265994
Propiconazole	0.359626	0.363439
Sitagliptin	0.163589	0.173976
Sotalol	0.238153	0.210718
Sulfamethoxazole	0.210253	0.180281
Sulpiride	0.144587	0.247814
Tebuconazole	0.133246	0.213788
Telmisartan	0.141125	0.120503
Terbuthylazine-2-hydroxy	0.195498	0.204933
Terbutryn	0.158957	0.455512
Torsemide	0.155104	0.13495
Tramadol	0.230789	0.178641
Trimethoprim	0.135999	0.119122
Venlaflaxine	0.224642	0.198435
Xipamide	0.16923	0.126968
Electrical conductivity	0.0093	0.0084

Table A.11: Goodness of fit for EU_{bio} and the mean TU_{bio} at measuring station 2 and 3

Normalized root-mean-square error: Goodness of fit for EU_{bio} from four bioassays and the mean TU_{bio} of the four bioassays at measuring station 2 and 3. Derivation: eq. A.15

EU_{bio}	MS2	MS3
AhR-CALUX	0.2244	0.3067
PPARγ-GeneBLAzer	0.2597	0.2830
ERα-GeneBLAzer	0.2701	0.3305
ARE32	0.4648	0.3107
TU_{bio} mean	0.3401	0.2476

Appendix B

Supplementary information for chapter 3

B.1 Field campaign

The detailed sampling campaign procedure could be found in Glaser et al., 2020. The sampling map was illustrated in Figure B.1.

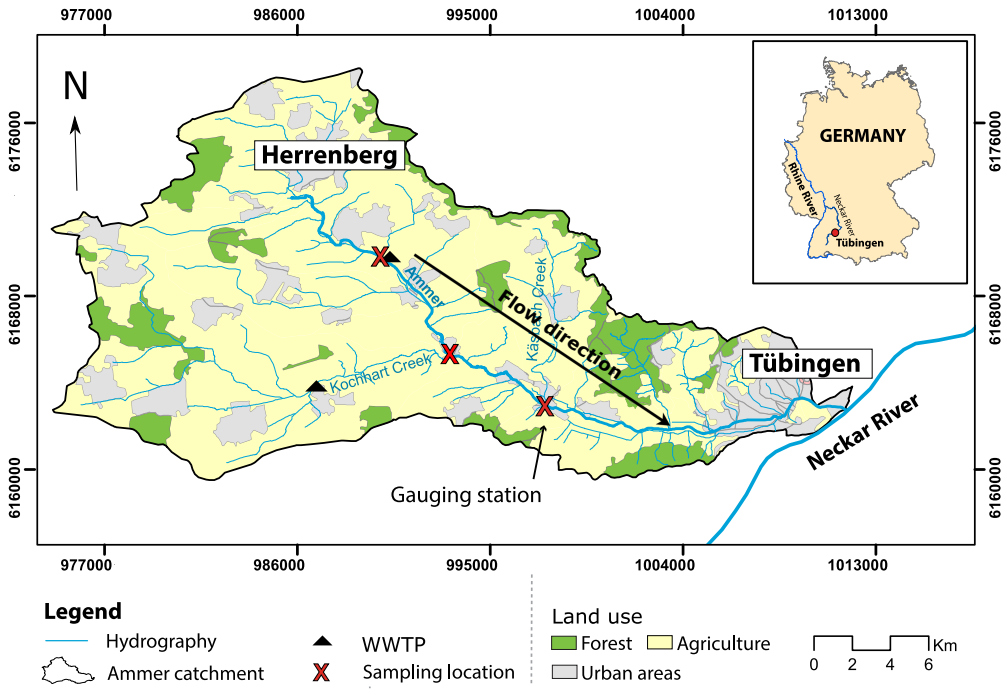

Figure B.1: Sampling map. MS1 was at sampling location near Herrenberg. MS2 was next to the Gauging station. The MS in the middle was not used. The Ammer river flows from the city of Herrenberg towards Tübingen. Abbreviation: MS – measuring station. Map made by Victor Carvalho Cabral.

Two measuring stations (MS) were set at 8 km apart from each other. The Ammer river

flows from Herrenberg towards Tübingen. MS1 was 200 m upstream to the wastewater treatment plant (WWTP) next to the main Ammer river channel. Time-series measurements were conducted at both MSs using Lagrangian sampling scheme.

B.2 The transient discharge: flood routing model

Upstream rating curve. The discharge Q time series was computed using the empirical upstream rating curve in eq. B.1,

$$Q(t) = (1 - P)(10.316 \cdot h(t)^2) - 2.537 \cdot h(t) - 0.4074) + P(2.2777 \cdot h(t)^2) + 0.0172 \cdot h(t) - 0.3019) \tag{B.1}$$

where P is the plant growth factor, h [m] the relative water level (relative to the height of the measuring instrument), t [s] the sampling time point.

The hydrological data is shown in Figure B.2.

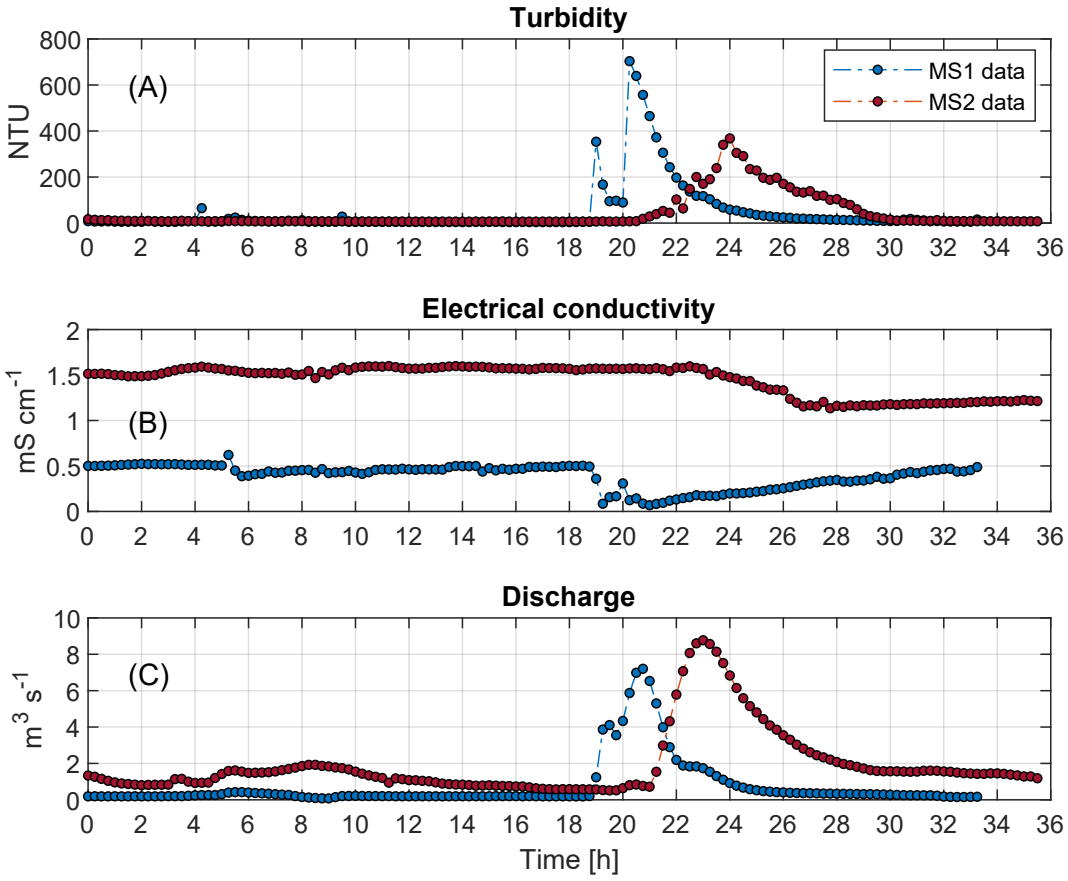

Figure B.2: Observations of turbidity, electrical conductivity, and discharge. Abbreviation: MS-measuring station.

B.3 Transfer functions for lateral inflow approximation.

We tested two transfer functions suggested by Aron and Borrelli, 1973. The first transfer function (eq. B.2) contains only one lumped parameter R [$s^{-1/2}$]. The original expression of R includes field parameters such as soil transmissivity and specific yield (Naney et al., 1978), which are cumbersome to obtain. The modeled to discharge results using eq. B.2 was illustrated in Figure B.3.

$$q(t) = 2R^2 \sum^{\infty} \exp\left(\frac{-\pi n^2 R^2 t}{4}\right) \tag{B.2}$$

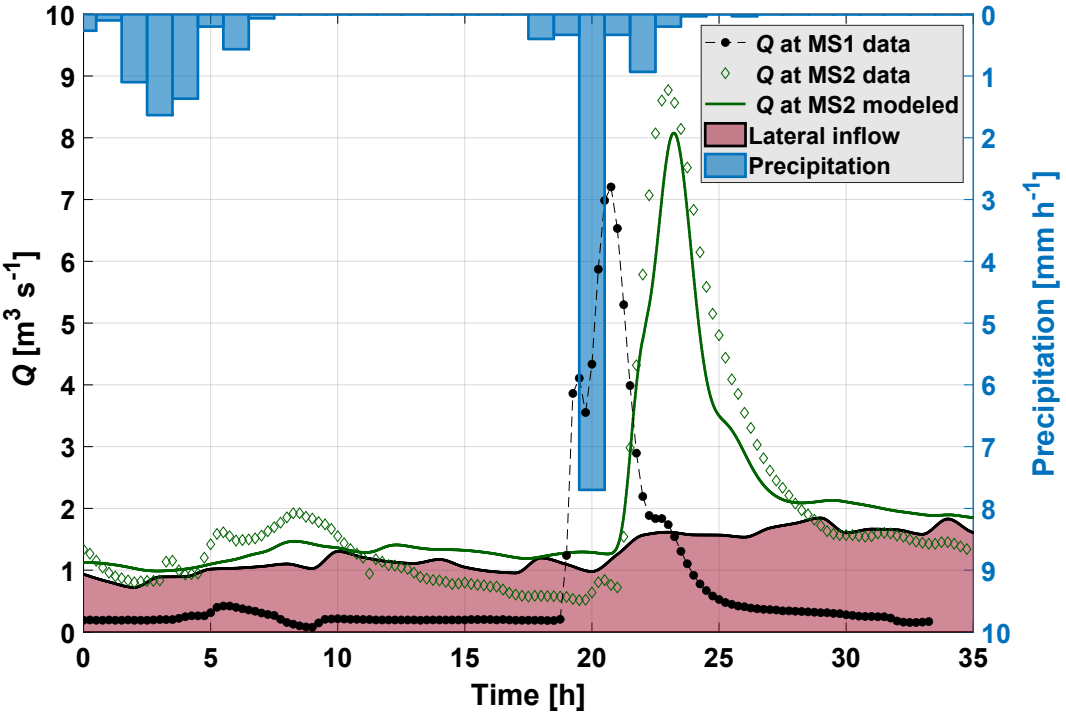

Figure B.3: Modeled transient discharge. The lateral inflow was computed using the transfer from Aron and Borrelli, 1973.

B.4 Transient velocity

The modeled transient flow velocity (Q/A) is shown in Figure B.4.

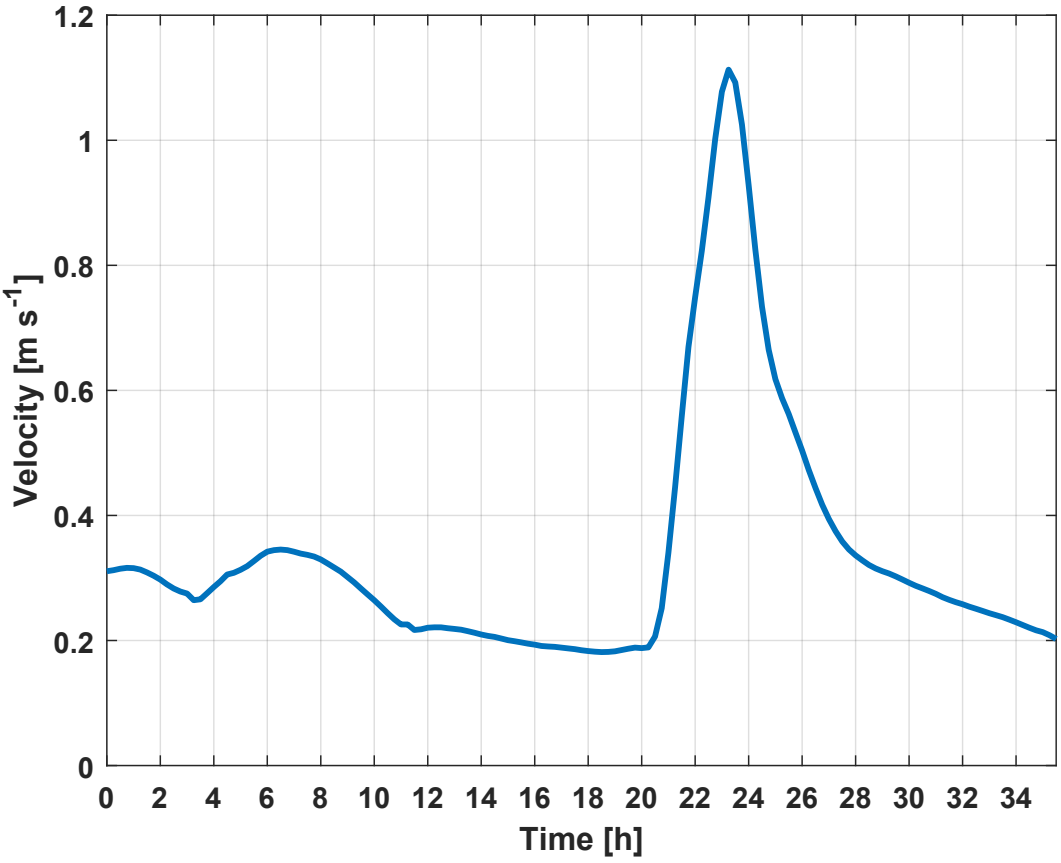

Figure B.4: Modeled transient flow velocity

B.5 Electrical conductivity.

The electrical conductivity (ECd) has been used in various previous studies (Cirpka et al., 2007; Glaser et al., 2020; Vogt et al., 2010) as conservative tracer. In our study, the main wastewater treatment plant (WWTP) was situated between the two measuring stations (MS) (Figure B.1). Figure B.2B showed that the ECd at MS2 was constantly higher than that of the MS1 over the sampling period, suggesting the ECd signal were heavily influenced by the WWTP release. To correctly simulate the ECd dynamics, a clear signal from the WWTP was needed. The model boundary condition needed to be constructed using mixing scheme (mixing of signals from the upstream inflow and WWTPs). There were no measurements conducted at both WWTPs outlet. Thus, the WWTPs ECd signals were estimated using the existing observations. We assumed the in-stream processes of the ECd was governed by the conservative transient transport model (eq. B.3).

$$\frac{\partial ECd}{\partial t} = -v(t)\frac{\partial ECd}{\partial x} + D(t)\frac{\partial^2 ECd}{\partial x^2} \tag{B.3}$$

The WWTP outlet signal was approximated based on the inflow signal at MS1 in eq. B.4,

$$\boldsymbol{ECd}(x=0,t) = \boldsymbol{ECd}_{\mathrm{MS1}} + ECd_{\mathrm{source}} + \begin{bmatrix} \boldsymbol{\sigma}(t_1) \\ \boldsymbol{\sigma}(t_2) \\ \dots \\ \boldsymbol{\sigma}(t_n) \end{bmatrix} \sim \mathcal{N}(0, 0.05 * ECd_{\mathrm{source}}) \tag{B.4}$$

$$\boldsymbol{ECd}_{\mathrm{MS1}} = f(\boldsymbol{t}) \sim \mathcal{N}(\mu(\boldsymbol{t}), \Sigma) \tag{B.5}$$

The initial condition distributions for the electrical conductivity is shown in Figure B.5

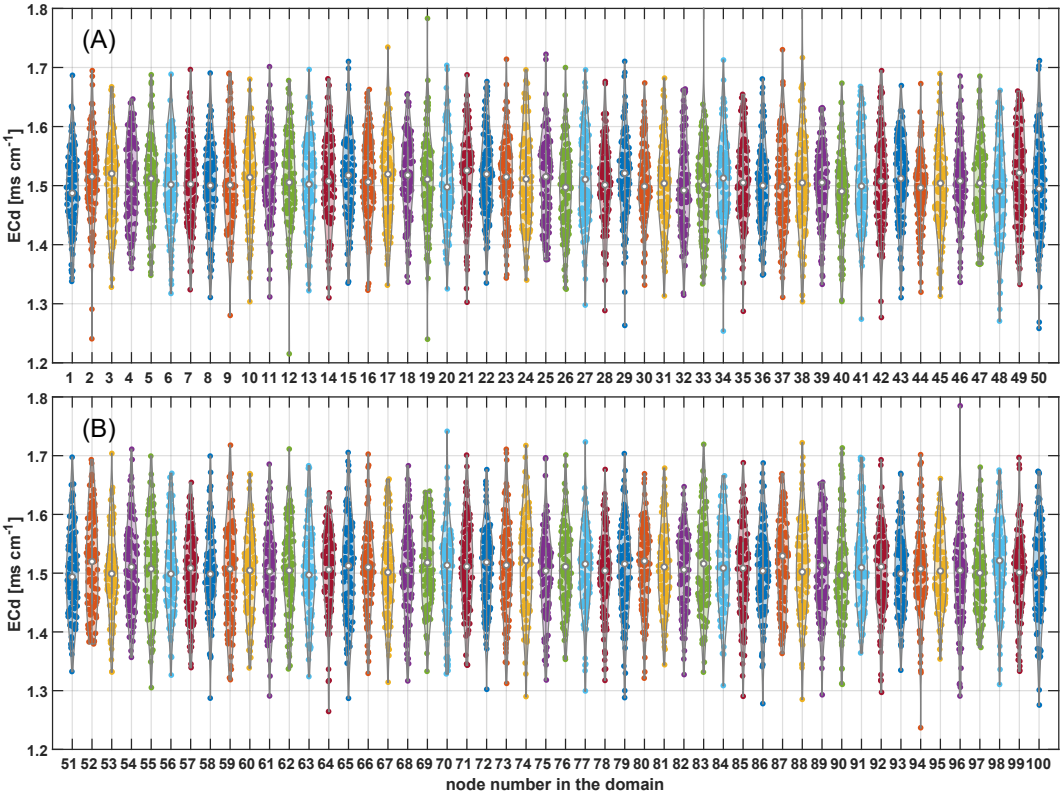

Figure B.5: The initial condition distributions of the electrical conductivity in the domain.

The modeled electrical conductivity is shown in Figure B.6

B.6 Model input quantification: Gaussian process regression

The ensemble model input is shown in Figure B.7.

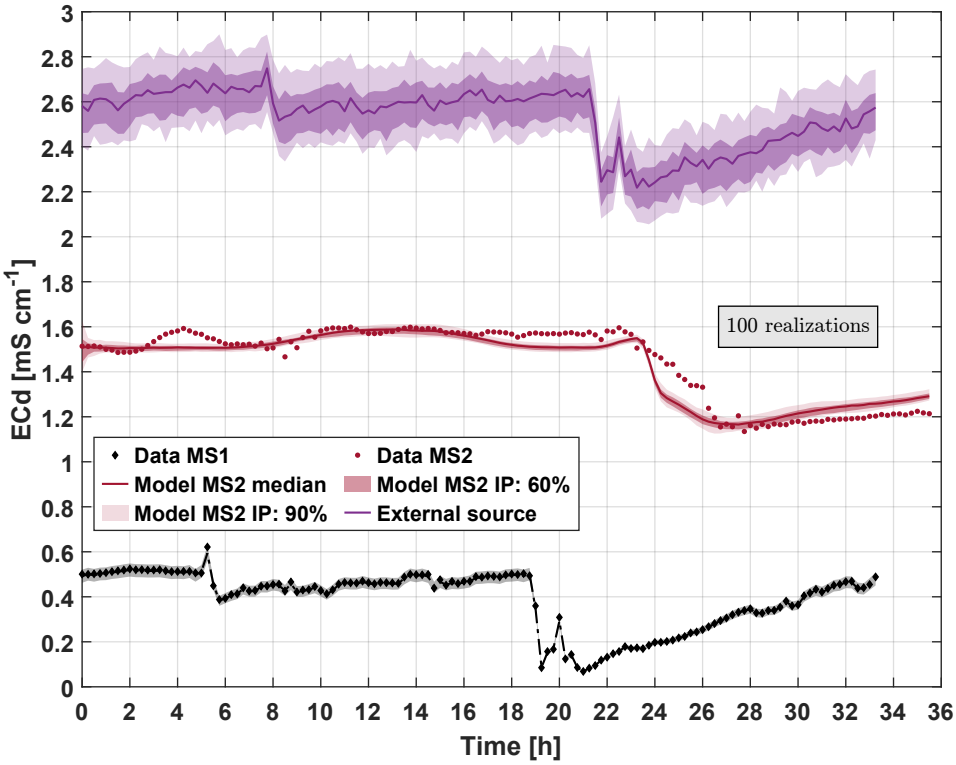

Figure B.6: The modeled electrical conductivity.

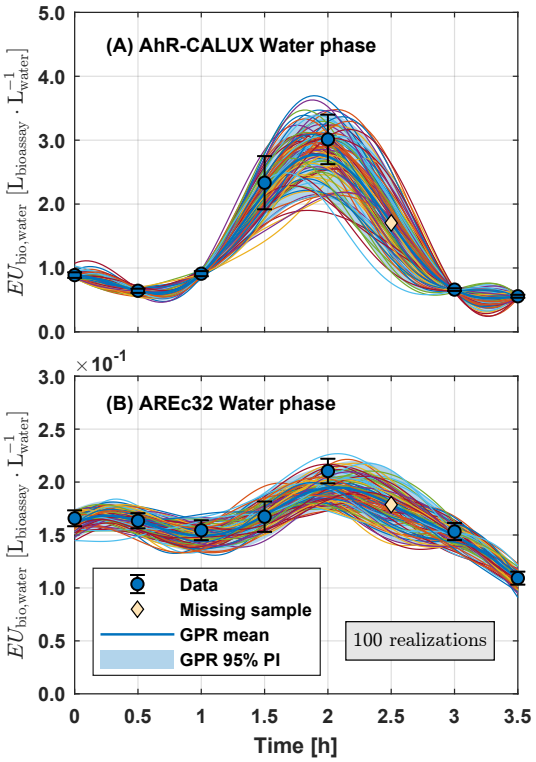

Figure B.7: 100 realizations of the mixture effects time series at measuring station 1 (MS1). Posterior distributions were obtained through Gaussian process regression (GPR).

Appendix C

Supplementary information for chapter 4

C.1 The sampling site map.

The sampling site map is shown in Figure C.1.

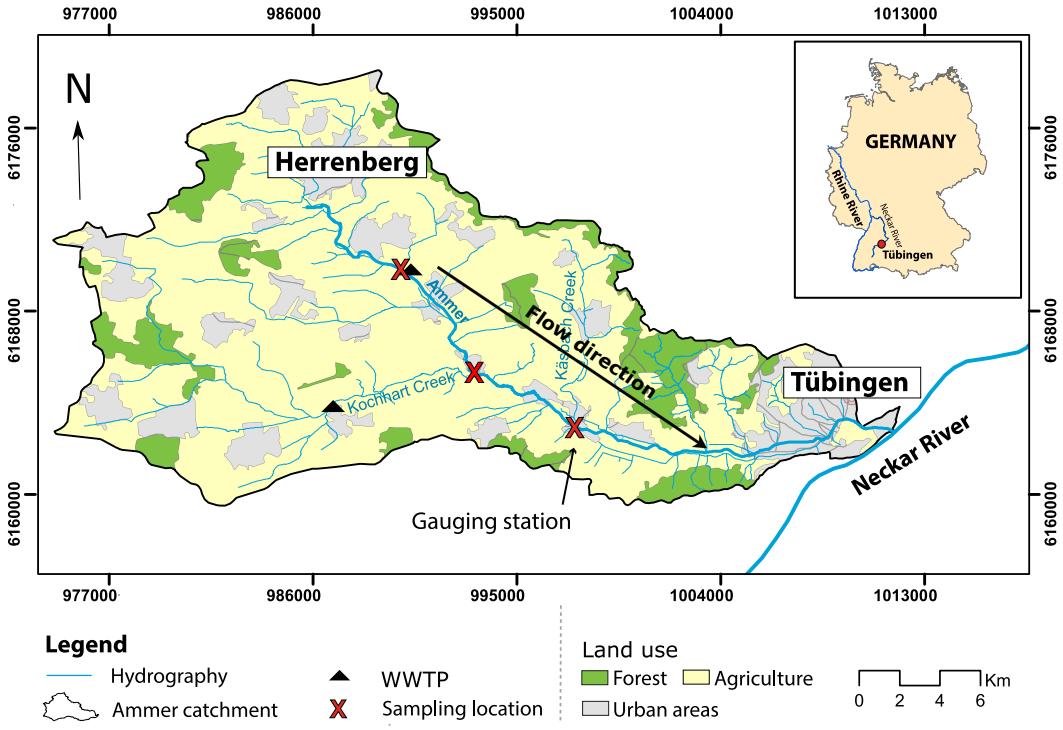

Figure C.1: Ammer River sampling site. Water in the Ammer river flows from northwest (near Herrenberg) to southeast, merging into the Neckar River in the city of Tübingen.

C.2 Prior and neural posterior distributions.

AhR-CALUX The prior and neural posterior distributions of parameters for mixture effects EU_{bio} in AhR-CALUX in segment 1 and 2 are show in Figure C.2.

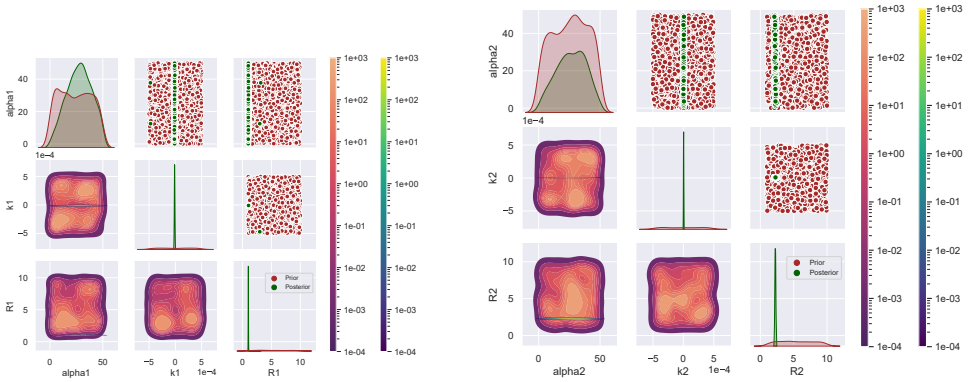

(A) Segment 1 **(B)** Segment 2

Figure C.2: Prior and posterior of EU_{bio} in AhR-CALUX in segment 1 (A) and segment 2 (B) from SBI. The light red and green probability density functions in the main diagonals are the prior and posterior distributions, respectively. The upper and lower corners show the individual 1000 samples and their kernel density estimation for the three parameters, respectively. α_i [m] is the dispersivity; k_i [s $^{-1}$] the first-order dissipation constant; R_i [-] the retardation factor ($i \in \{1, 2\}$.)

ERα–GeneBLAzer The prior and neural posterior distributions of parameters for mixture effects EU_{bio} in ERα–GeneBLAzer in segment 1 and 2 are show in Figure C.3.

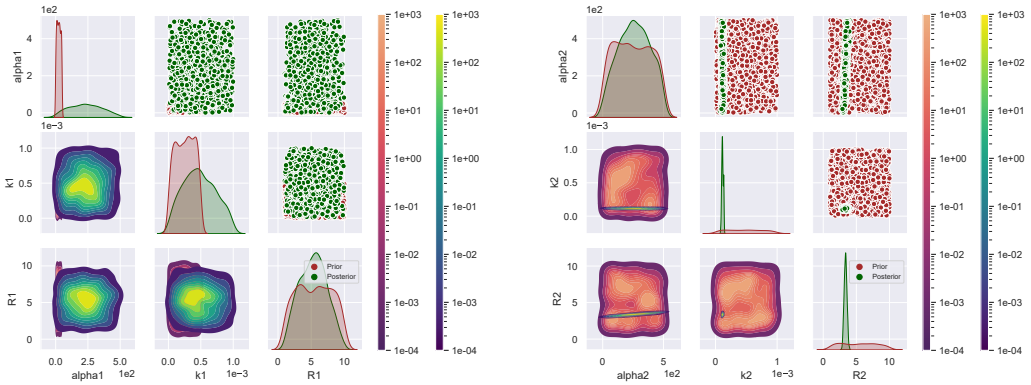

(A) Segment 1 **(B)** Segment 2

Figure C.3: Prior and posterior of EU_{bio} in ERα–GeneBLAzer in segment 1 (A) and segment 2 (B) from SBI. The light red and green probability density functions in the main diagonals are the prior and posterior distributions, respectively. The upper and lower corners show the individual 1000 samples and their kernel density estimation for the three parameters, respectively. α_i [m] is the dispersivity; k_i [s $^{-1}$] the first-order dissipation constant; R_i [-] the retardation factor ($i \in \{1, 2\}$.)

C.3 Simulation-based inference & Gaussian process aided reactive transport.

The mean root mean square error in Table C.1 is expressed in eq. C.1,

$$\overline{\mathrm{RMSE}} = \frac{1}{m}\sum_{j=1}^{m}\sqrt{\frac{1}{n}\sum_{i=1}^{n}(y_i - \hat{y}_i)^2} \tag{C.1}$$

where y is the observation; $\hat{y}$ the modeled result; i the index for observations and corresponding modeled results; n number of observations; j the index for input realizations from the Gaussian process regression; m number of input realizations.

The mean normalized root mean square error in Table C.1 is expressed in eq. C.2,

$$\overline{\mathrm{NRMSE}} = \frac{1}{m}\sum_{j=1}^{m}\frac{\sqrt{\frac{1}{n}\sum_{i=1}^{n}(y_i - \hat{y}_i)^2}}{y_{\max} - y_{\min}} \tag{C.2}$$

where y is the observation; $\hat{y}$ the modeled result; i the index for observations and corresponding modeled results; n number of observations. $y_{\max}$ and $y_{\min}$ are the maximum and minimum values of the observations, respectively. j is the index for input realizations from the Gaussian process regression; m number of input realizations.

AhR-CALUX The in-stream dynamics of EU_{bio} in AhR-CALUX are shown in Figure C.4.

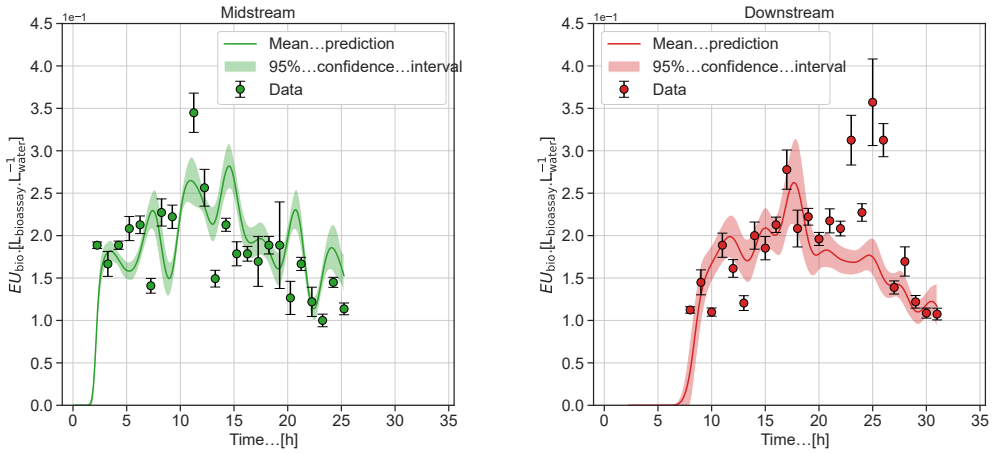

(A) EU_{bio} in AhR-CALUX at midstream site

(B) EU_{bio} in AhR-CALUX at downstream site

Figure C.4: Modeled ensemble time-series for EU_{bio} in AhR-CALUX at midstream (A) and downstream site (B). The light green and red areas represent the 95% confidence interval of the modeled ensemble from 500 realizations ($N_{\mathrm{sample}} = 500$ in algorithm 3). Analytical uncertainties (one standard error) from the measurement are shown by the error bars.

ERα–GeneBLAzer The in-stream dynamics of EU_{bio} in ERα–GeneBLAzer are shown in Figure C.5.

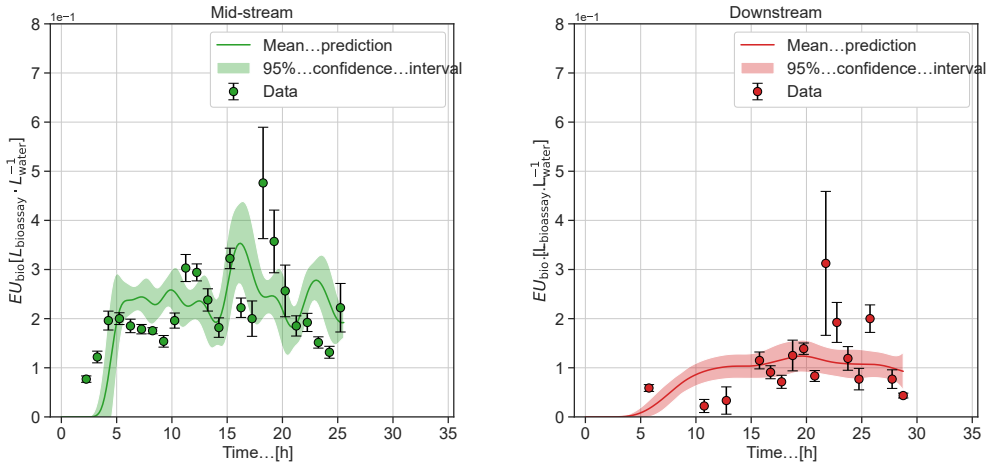

(A) EU_{bio} in ERα–GeneBLAzer at midstream site **(B)** EU_{bio} in ERα–GeneBLAzer at downstream site

Figure C.5: Modeled ensemble time-series for EU_{bio} in ERα–GeneBLAzer at midstream (A) and downstream site (B). The light green and red areas represent the 95% confidence interval of the modeled ensemble from 500 realizations ($N_{\text{sample}} = 500$ in algorithm 3). Analytical uncertainties (one standard error) from the measurement are shown by the error bars.

C.4 Performance of SBI & GPR aided reactive transport models

Table C.1: Performance of SBI & GPR aided reactive transport models: 500 realizations are used as the inflow boundary condition for forward model run.

Bioassay	Metric	Segmet 1	Segment 2
PPARγ-GeneBLAzer	$\overline{\text{RMSE}}$	3.547E-01	7.544E-02
	$\overline{\text{NRMSE}}$	4.560E-01	3.007E-01
AhR-CALUX	$\overline{\text{RMSE}}$	5.310E-02	6.781E-02
	$\overline{\text{NRMSE}}$	2.169E-01	2.727E-01
ERα-GeneBLAzer	$\overline{\text{RMSE}}$	1.615E-01	6.974E-02
	$\overline{\text{NRMSE}}$	4.045E-01	2.403E-01

C.5 PINN

AhR-CALUX The in-stream dynamics and the training loss of EU_{bio} in AhR-CALUX in segment 1 are shown in Figure C.6.

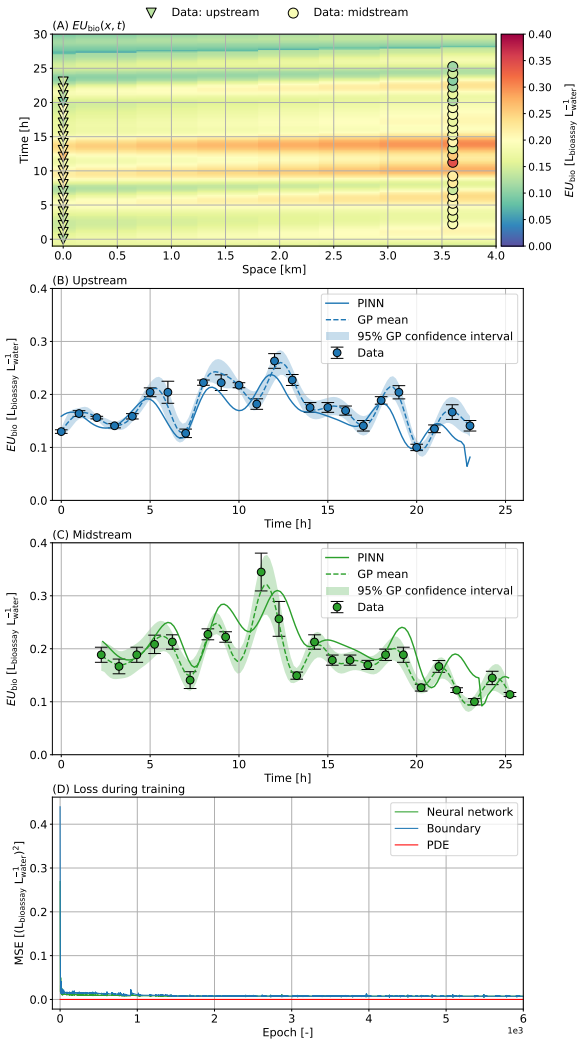

Figure C.6: Modeled ensemble time-series for EU_{bio} in AhR-CALUX in (A) segment 1 bounded by the upstream stream and midstream sites. (A) shows the distribution of EU_{bio} in the whole space-time domain. (B) and (C) show EU_{bio} at midstream and downstream sites, respectively. The light blue and green areas represent the 95% confidence interval of the Gaussian process regression on data. The training processes of the three loss functions (eqs. 4.6, 4.7, and 4.8) are shown in (D). Analytical uncertainties (one standard error) from the measurement are shown by the error bars.

The in-stream dynamics and the training loss of EU_{bio} in AhR-CALUX in segment 2 are shown in Figure C.7.

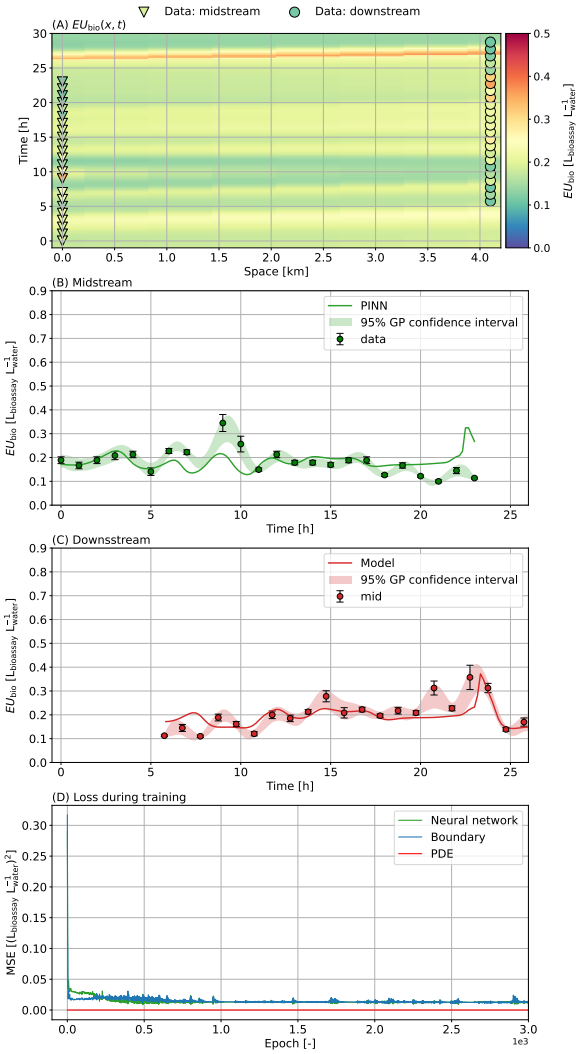

Figure C.7: Modeled ensemble time-series for EU_{bio} in AhR-CALUX in segment 2 bounded by the midstream and downstream sites. (A) shows the distribution of EU_{bio} in the whole space-time domain. (B) and (C) show EU_{bio} at midstream and downstream sites, respectively. The light green and red areas represent the 95% confidence interval of the Gaussian process regression on data. The training processes of the three loss functions (eqs. 4.6, 4.7, and 4.8) are shown in (D). Analytical uncertainties (one standard error) from the measurement are shown by the error bars.

The three-dimensional field of EU_{bio} in AhR-CALUX in segment 1 and 2 are shown in Figure C.8.

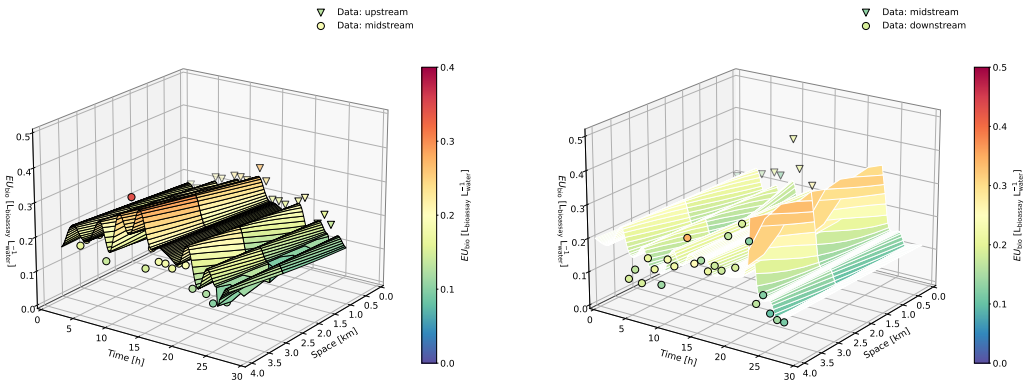

(A) EU_{bio} in AhR-CALUX in segment 1

(B) EU_{bio} in AhR-CALUX in segment 2

Figure C.8: Modeled ensemble time-series for EU_{bio} in AhR-CALUX in (A) segment 1 and (B) segment 2.

ERα–GeneBLAzer The in-stream dynamics and the training loss of EU_{bio} in ERα–GeneBLAzer in segment 1 are shown in Figure C.9.

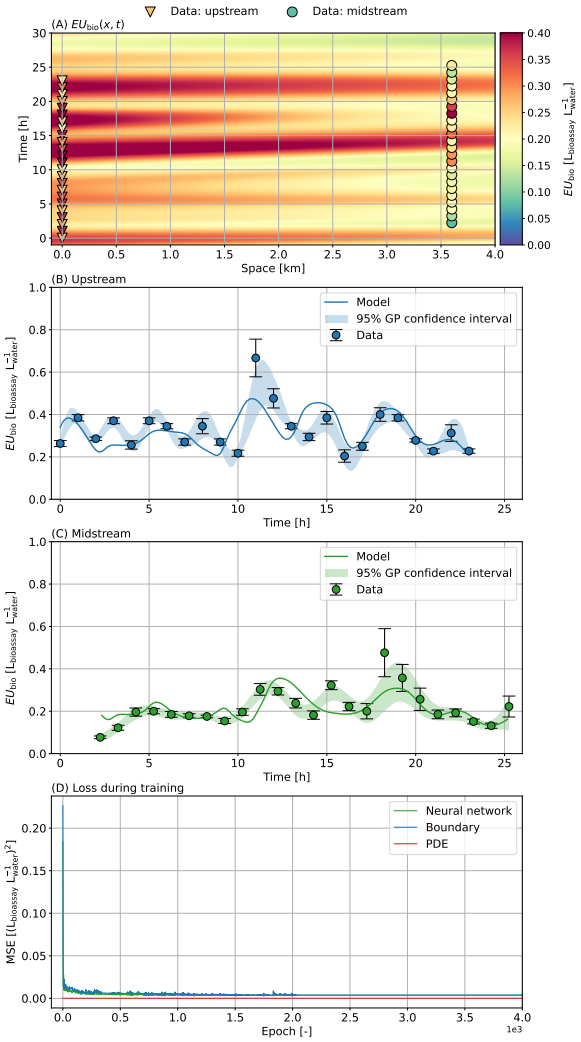

Figure C.9: Modeled ensemble time-series for EU_{bio} in ERα–GeneBLAzer in (A) segment 1 bounded by the upstream stream and midstream sites. (A) shows the distribution of EU_{bio} in the whole space-time domain. (B) and (C) show EU_{bio} at midstream and downstream sites, respectively. The light blue and green areas represent the 95% confidence interval of the Gaussian process regression on data. Analytical uncertainties (one standard error) from the measurement are shown by the error bars.

The in-stream dynamics and the training loss of EU_{bio} in ERα–GeneBLAzer in segment 2 are shown in Figure C.10.

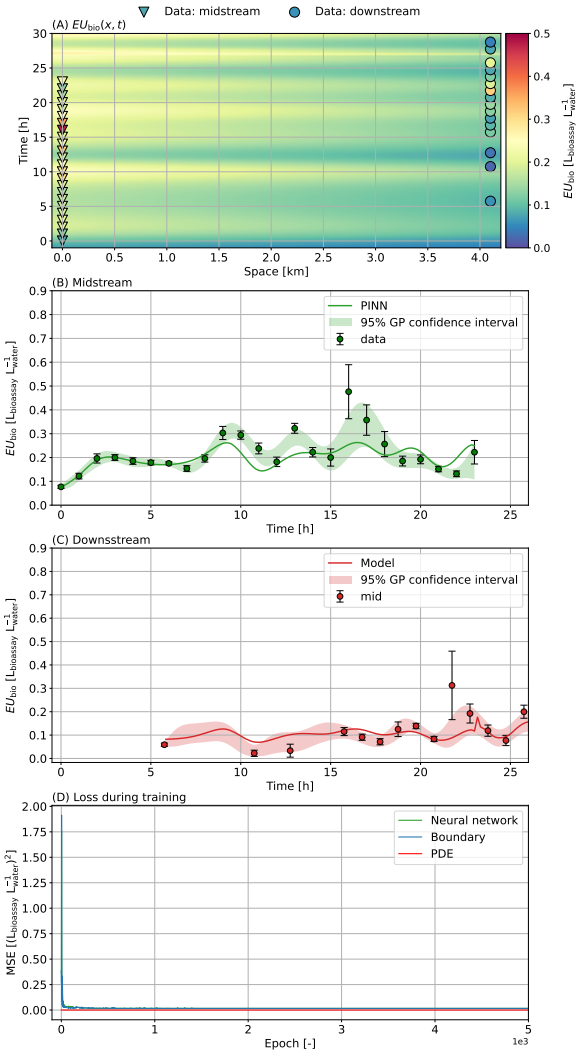

Figure C.10: Modeled ensemble time-series for EU_{bio} in ERα–GeneBLAzer in segment 2 bounded by the midstream (A) and downstream site (B). (B) and (C) show EU_{bio} at midstream and downstream sites, respectively. The light green and red areas represent the 95% confidence interval of the Gaussian process regression on data. Analytical uncertainties (one standard error) from the measurement are shown by the error bars.

The three-dimensional field of EU_{bio} in ERα–GeneBLAzer in segment 1 and 2 are shown in Figure C.11.

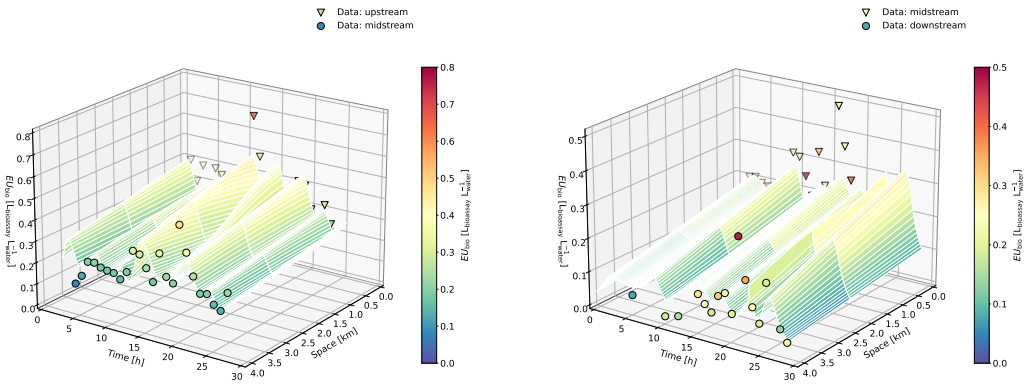

(A) EU_{bio} in EU_{bio} in segment 1

(B) EU_{bio} in EU_{bio} in segment 2

Figure C.11: Modeled ensemble time-series for EU_{bio} in ERα–GeneBLAzer in (A) segment 1 and (B) segment 2.

C.6 Performance of PINN

The root mean square error in Table C.2 is expressed in eq. C.3,

$$\text{RMSE} = \sqrt{\frac{1}{n}\sum_{i=1}^{n}(y_i - \hat{y}_i)^2} \tag{C.3}$$

where y is the observation; $\hat{y}$ the modeled result; i the index for observations and corresponding modeled results; n number of observations.

The normalized root mean square error in Table C.2 is expressed in eq. C.4,

$$\text{NRMSE} = \frac{\sqrt{\frac{1}{n}\sum_{i=1}^{n}(y_i - \hat{y}_i)^2}}{y_{\max} - y_{\min}} \tag{C.4}$$

where y is the observation; $\hat{y}$ the modeled result; i the index for observations and corresponding modeled results; n number of observations. $y_{\max}$ and $y_{\min}$ are the maximum and minimum values of the observations, respectively.

The mean squared error in Table C.2 is expressed in eq. 4.6 in chapter 4.

Table C.2: The performance metrics of PINN on the three *in vitro* bioassay data and estimated physical parameter values.

Physical parameters		PPARγ–GeneBLAzer		AhR-CALUX		ERα–GeneBLAzer		
		segment 1	segment 2	segment 1	segment 2	segment 1	segment 2	
	alpha [m]	49.586	50.000	50.000	26.129	50.000	50.000	
	R [-]	2.991	22.358	2.936	1.000	1.000	2.615	
	Lambda [1/s]	2.6364E-06	8.91E-07	0	0	3.017E-07	0	
Loss								
Weighted mean / Total	NRMSE	2.24E-01	2.20E-01	4.96E-01	6.51E-01	2.17E-01	4.55E-01	
	RMSE	1.74E-01	1.71E-01	1.21E-01	1.59E-01	8.65E-02	1.82E-01	
	MSE	3.03E-02	2.92E-02	1.47E-02	2.54E-02	7.48E-03	3.30E-02	
Neural network	NRMSE	1.63E-01	1.52E-01	3.49E-01	4.70E-01	1.54E-01	3.23E-01	
	RMSE	1.27E-01	1.18E-01	8.55E-02	1.15E-01	6.14E-02	1.29E-01	
	MSE	1.61E-02	1.40E-02	7.31E-03	1.33E-02	3.77E-03	1.66E-02	
Boundary	NRMSE	9.43E-02	1.58E-01	5.24E-01	4.86E-01	1.68E-01	4.91E-01	
	RMSE	1.20E-01	1.23E-01	8.62E-02	1.10E-01	6.09E-02	1.28E-01	
	MSE	1.43E-02	1.52E-02	7.43E-03	1.22E-02	3.71E-03	1.64E-02	
PDE	RMSE	1.23E-05	2.31E-05	2.90E-05	2.24E-05	5.81E-06	4.97E-06	
	MSE	1.52E-10	5.34E-10	8.39E-10	5.01E-10	3.38E-11	2.47E-11	
Hyperparameters								
	Epoch	3000	5000	4000	3000	4000	5000	
	Training time [min]	9.42	22	20.00	10	13.36	17	
	Neurons	20	20	20	20	20	20	
	Layers	9	9	9	9	9	9	
	Loss weights	1 1 1	1 1 1	1 1 1	1 1 1	1 1 1	1 1 1	
	Weights decay	1.00E-11	0	0.00E+00	2.00E-09	0.00E+00	0	
	Learning rate	1.00E-02	1.00E-02	1.00E-02	1.00E-02	1.00E-02	1.00E-01	